AN ABSTRACT OF THE THESIS OF

Thomas E. Tolley for the degree of Master of Science in Mechanical Engineering
presented on May 22, 2020.

Title: The Feasibility of Process Intensification of the Water-Gas Shift Reaction using Differential Temperature Microreactors

Abstract approved: _____

Brian M. Fronk

Hydrogen is an increasingly attractive low-carbon energy carrier for a variety of stationary and mobile applications. Currently, the vast majority of hydrogen in the United States is produced via the energy intensive steam reforming of natural gas. The cost and carbon emissions associated with hydrogen production can be reduced by improving the efficiency of this process. Thus, this thesis investigates the potential of differential temperature water-gas shift (WGS) microreactors to intensify the steam reforming process.

First, a COMSOL Multiphysics model of the WGS reaction is developed and compared against experimental values from the literature to validate its performance. The model is then used to evaluate improvements in the performance of the WGS reaction when operating under an optimal temperature profile when compared to the performance of a baseline model of the standard high temperature shift and low temperature shift (HTS/LTS) reactor configuration most frequently deployed in industry over a range of operating conditions. The results of this modeling effort are used to inform the design of a microreactor prototype that can be additively manufactured using a selective laser melting (SLM) process. The thermal-

hydraulic performance of this prototype is experimentally verified to further validate the modeling results. Finally, a simplified version of the developed differential temperature WGS microreactor model is implemented into a flow sheet of the overall steam reforming process and its economic benefits are evaluated through a rigorous optimization process.

The study results suggest that the implementation of a differential temperature WGS reactor operating under optimal temperature conditions significantly reduces both the required reactor volume to achieve a specific CO conversion level and the hydrogen production cost associated with the overall steam reforming process. The results also suggest that the developed prototype's performance is accurately predicted (within a maximum error of 20%) by the modeling results and that SLM processes can potentially be leveraged for the design and manufacture of WGS microreactors, though there are still a number of obstacles with these processes that must be overcome first.

The Feasibility of Process Intensification of the Water-Gas Shift Reaction using Differential Temperature Microreactors

by

Thomas E. Tolley

A THESIS

submitted to

Oregon State University

in partial fulfillment of
the requirements for the
degree of

Master of Science

Presented May 22, 2020
Commencement June 2020

Master of Science thesis of Thomas E. Tolley presented on May 22, 2020.

APPROVED:

Major Professor, representing Mechanical Engineering

Head of the School of Mechanical, Industrial, and Manufacturing Engineering

---

Dean of the Graduate School

I understand that my thesis will become part of the permanent collection of Oregon State University libraries. My signature below authorizes release of my thesis to any reader upon request.

Thomas E. Tolley, Author

ACKNOWLEDGEMENTS

I would like to express my gratitude to my advisor, Dr. Brian Fronk, for his guidance and advice across this entire process. I really appreciate the liberty he gave me in defining the scope of my own research while also acting as a mentor, source of support, and friend when needed. I would also like to express my gratitude to my labmates who frequently were able to lend their support to me by sending me papers to read, helping me assemble and troubleshoot things in the lab, or just talking through problems with me at the chalkboard. Finally, I would like to thank my family and friends. They have been a tremendous source of comfort to me during the particularly difficult periods of this process and I will be eternally grateful for their encouragement.

I acknowledge portions of this work were funded through the RAPID Institute under the U.S. Department of Energy contract (DE-EE0007888-10-4) and through the High Impact Opportunity Project program under the Oregon Innovation Council.

TABLE OF CONTENTS

TABLE OF CONTENTS (Continued)

TABLE OF CONTENTS (Continued)

LIST OF FIGURES

LIST OF FIGURES (Continued)

LIST OF FIGURES (Continued)

LIST OF FIGURES (Continued)

Figure Page

LIST OF FIGURES (Continued)

Figure Page

LIST OF FIGURES (Continued)

LIST OF TABLES

Nomenclature

Abbreviations

AM	Additive manufacturing
gge	Gasoline gallon equivalent
HTS	High temperature shift
HX	Heat exchanger
LH	Langmuir-Hinshelwood
LHV	Lower heating value [kJ/kg]
LTS	Low temperature shift
NTU	Number of transfer units
PFR	Plug Flow Reactor
PSA	Pressure swing adsorption
SLM	Selective laser melting
SMR	Steam methane reforming
SQP	Sequential quadratic programming
WGS	Water-gas shift

Greek Symbols

β Reversibility factor

χ Vapor quality

ΔH_{rxn} Heat of Reaction [kJ/mol]

ΔP Pressure drop [kPa]

ϵ Porosity (Chapters 3 and 4)/Heat exchanger effectiveness (Chapters 5 and 6)

η Catalyst pellet effectiveness factor (Chapter 2)/Efficiency (Chapter 6)

γ Specific heat ratio

κ Permeability [m^2]

μ Dynamic viscosity [Pa-s]

Ω_D Collision integral

ϕ Thiele modulus

ρ Density [kg/m^3]

σ Collision diameter [Å]

Subscripts

amb Ambient

avg Average

C Cold side

c	Coolant
cat	Catalyst
CON	Condenser
e	Effective
H	Hot side
i	Species “i”
in	Inlet
INT	Intercooler
j	Species “j”
m	Mixture
out	Outlet
p	Product
r	Reaction
u	Uncooled length
w	Reactor wall

Symbols

$\dot{m}$	Mass flow rate [kg/s]
$\dot{Q}$	Heat transfer rate [kW]

$\dot{V}$ Volumetric flow rate [m^3/s]

$\dot{W}$ Work rate [kW]

$\mathbf{u}$ Fluid velocity [m/s]

A Heat transfer area [m^2]

A_{cat} Catalyst costs converted to monthly annuity [$/month]

A_C Capital costs converted to monthly annuity [$/month]

C Concentration [mol/m^3] (Chapters 3 and 4)/Capital costs [$] (Chapter 6)

C_{min} Minimum capacity rate [kW/K]

c_p Specific heat at constant pressure [J/kg-K]

C_r Capacity rate ratio

$Cost_{H2}$ Hydrogen production cost [$/gge]

D Diffusion coefficient [m^2/s]

E_a Activation energy [kJ/mol]

F Molar flow rate [mol/s]

H Height [m]

h Specific enthalpy [kJ/kg]

I CEPCI cost index

i Interest rate

k	Thermal conductivity [W/m-K]
K_0	Pre-exponential factor [mol/kg-s]
K_{eq}	Equilibrium constant
K_i	Adsorption equilibrium constant of species i [1/bar]
k_{rds}	Reaction rate constant [mol/kg-s]
L	Length [m]
M	Molar mass [kg/mol]
N	Number of channels
n	Number of time periods
O	Monthly operating costs [$/month]
P	Pressure [kPa]
PR	Pressure ratio
R	Ideal gas constant [J/mol-K]
r	Reaction rate [mol/m^3-s]
T	Temperature [K]
U	Overall heat transfer coefficient [W/m^2-K]
V	Volume [m^3]
W	Width [m]

w	Mass fraction
X	Conversion
y	Mole fraction

For my grandfather, who fostered and influenced my interest in engineering more than he ever realized.

Chapter 1: Introduction

1.1 Background

Hydrogen is an increasingly attractive low-carbon energy carrier for transportation and stationary fuel cell systems, heating via direct combustion, and seasonal energy storage. However, in 2018, 96% of hydrogen produced worldwide was derived from fossil fuels, with 48% being produced through the steam reforming of natural gas, 30% being produced through naptha/oil reforming, and 18% being produced through coal gasification. The remaining 4% was produced through the electrolysis of water [1]. While it is desirable to transition to more renewable sources of hydrogen production in the long term to fully realize the potential of hydrogen as a low-carbon energy carrier, it is also important to initially develop low cost methods of hydrogen to encourage the formation of a market for hydrogen in the near-term.

For reference, the US Department of Energy reported that the cost of hydrogen needs to be less than $4 per gasoline gallon equivalent (gge) to be competitive with other commercially available fuel sources [2]. At present, the technologies necessary to support the required production capacity of hydrogen from renewable sources while achieving these cost targets are still not commercially viable, however. Thus, the US Department of Energy's Office of Energy Efficiency & Renewable Energy is actively funding a wide range of research efforts focused on methods and technologies to support the near-term, mid-term, and long-term production of hydrogen at commercially viable scales, as shown in Figure 1.1.

Figure 1.1 shows that the only method capable of large-scale hydrogen production in the near-term is the steam reforming of natural gas. The steam reforming of natural gas is

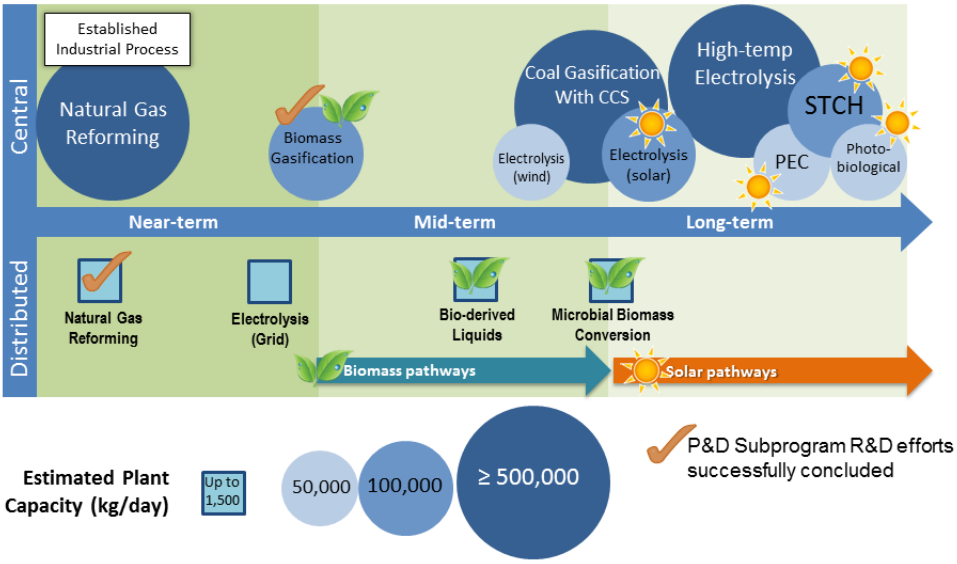

Figure 1.1: Hydrogen production pathways [3]

an industrially mature process and has proven to be the most cost effective of the fossil fuel sources of hydrogen, making it well suited to meeting near-term hydrogen needs. In the US, 95% of the hydrogen produced is currently made by the steam reforming of natural gas [4]. While this pathway still derives hydrogen from a fossil fuel resource, improvements in the efficiency of the reformation process would reduce the carbon emissions associated with hydrogen production, provide low cost hydrogen at scale, and help develop a market for hydrogen that can be produced in the the mid-term and long-term by renewable technologies. Thus, this thesis investigates how intensifying the water-gas shift reaction within the steam reforming process can help achieve this goal. The remainder of this chapter describes the steam reforming and water-gas shift reactions in more detail, discusses how microreactors can be implemented to intensify chemical processes broadly, summarizes the current state of additive manufacturing and its potential application to the development of microreactors, and outlines how the remaining chapters of this thesis will be organized.

1.2 Steam Reforming of Natural Gas

Figure 1.2 shows a heavily simplified process flow diagram of a typical natural gas steam reforming system. Natural gas enters the system and is first purified to remove trace amounts of substances such as sulfur, which can harm downstream components. Steam is then injected into the natural gas line and the mixture enters the steam methane reformer (SMR) at temperatures generally ranging between 700 °C and 950 °C. The SMR contains a catalyst which promotes the following reaction to produce hydrogen gas:

$$CH_4 + H_2O \rightleftharpoons CO + 3H_2 \tag{1.1}$$

The SMR reaction is strongly endothermic, reversible reaction with a heat of reaction of approximately $\Delta H_{rxn} = 206$ kJ/mol at standard conditions. It thus requires a significant energy input which is typically provided by the combustion of natural gas, though other energy inputs such as concentrated solar energy can be used as well [5]. The product stream from the SMR reactor is then cooled down to a temperature of approximately 350 °C and enters a high temperature shift (HTS) water-gas shift (WGS) reactor. The product stream from the HTS reactor then passes through an intercooler to lower its temperature down to approximately 200 °C and then passes through a low temperature shift (LTS) WGS reactor. The two separate WGS reactors contain two different types of catalyst that both promote the following chemical reaction to further increase hydrogen production and remove unwanted carbon monoxide from the reaction stream:

$$CO + H_2O \rightleftharpoons CO_2 + H_2 \tag{1.2}$$

For reasons explained in Section 1.3, it is industrially advantageous to split the WGS reaction into an adiabatic high temperature reactor and adiabatic low temperature reactor,

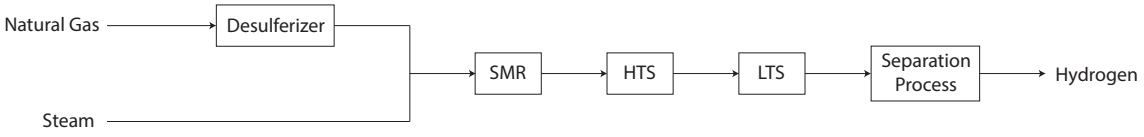

Figure 1.2: Simplified schematic of the steam reforming of natural gas

as indicated in Figure 1.2. The product stream from the LTS reactor finally passes through separation processes to remove the hydrogen from the remaining components in the gas stream. This generally includes a condenser to remove the H_2O and a pressure swing adsorption (PSA) system to extract the hydrogen gas from the remaining CO, CO_2, and CH_4, though other separation methods such as selectively permeable membranes can be used as well [6].

1.3 Water-Gas Shift Reaction

The water-gas shift reaction was first reported on in the late 1800s [7]. It was traditionally used to produce hydrogen from synthesis gas as part of the Haber-Bosch process and to produce hydrogen for petroleum refinery operation. More recently, as discussed in Section 1.2, the WGS reaction has also become a key processing step in the steam reforming of natural gas both as a method of increasing the production of hydrogen and removing unwanted CO from the reaction stream [8].

The WGS reaction, shown in equation 1.2, is a mildly exothermic, reversible reaction with a heat of reaction of approximately $\Delta H_{rxn} = -41.1$ kJ/mol at standard conditions. In accordance with Le Chatelier's principle, the product yield of the WGS reaction is thermodynamically limited at higher temperatures as the reaction will begin to favor the formation of reactants over products to maintain its chemical equilibrium state as its temperature increases. As a result, the reaction is thermodynamically favorable at lower

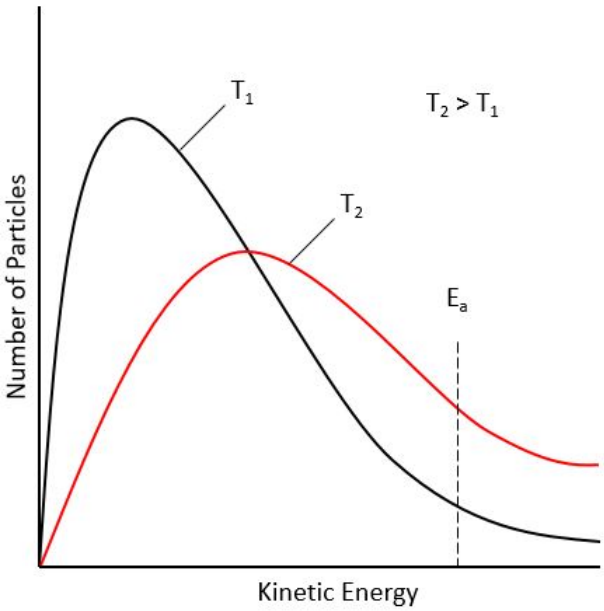

Figure 1.3: Reaction kinetics temperature dependence

temperatures. Because the reactant and product sides of the WGS reaction are equimolar, the equilibrium of the reaction is unaffected by pressure [7].

Conversely, the reaction is kinetically favorable at higher temperatures as the reaction will proceed much more quickly at higher temperatures than at lower temperatures [8]. This is a result of a larger portion of the reactant molecules having enough kinetic energy to overcome the reaction's activation energy barrier. As shown in Figure 1.3, the distribution of reacting molecules at the higher temperature features a much larger number of molecules with a kinetic energy exceeding the activation energy, E_a, at which the reaction begins than the distribution of reacting molecules at the lower temperature. As a result, more of the reactant molecules at any given instance can react to form products when at a higher temperature, resulting in a higher reaction rate.

There are a number of advantages to being able to operate the WGS reaction at a higher reaction rate. Because the WGS reaction is relatively slow at lower temperatures compared to other industrial reactions, WGS reactors are often the biggest and heaviest components within the chemical systems including them [9]. This can increase costs significantly. By operating the WGS reaction at higher reaction rates, the required reactor volume to achieve a desired product yield can be significantly less than it would be at slower reaction rates, which can significantly lower the total volume and cost of the entire chemical system as a result. However, as discussed previously, at the higher temperatures that faster reaction rates occur at, the reaction is thermodynamically limited and may not yield the desired amount of product once reaching equilibrium. As a result, achieving the desired product yield from the WGS reaction within a reasonable reactor volume becomes a matter of effectively managing the temperature of the reaction to balance the possible equilibrium position of the reaction and its rate of reaction [7]. As mentioned in Section 1.2, this is generally done in industry by splitting the WGS reaction into separate high temperature shift and low temperature shift reactors which both operate adiabatically [8]. The high temperature shift reactor takes advantage of the higher reaction rates that can be achieved at high temperatures to achieve the bulk of the reaction conversion in a lower reactor volume and the low temperature shift reactor is then used to further enhance hydrogen production.

1.4 Microreactor Technology

Recently, the design and fabrication of microreactors as part of larger process intensification efforts within chemical engineering has become a promising area of research [10]. These microreactors are miniaturized reaction systems fabricated using microfabrication techniques and precision engineering with characteristic dimensions ranging from the sub-micrometer

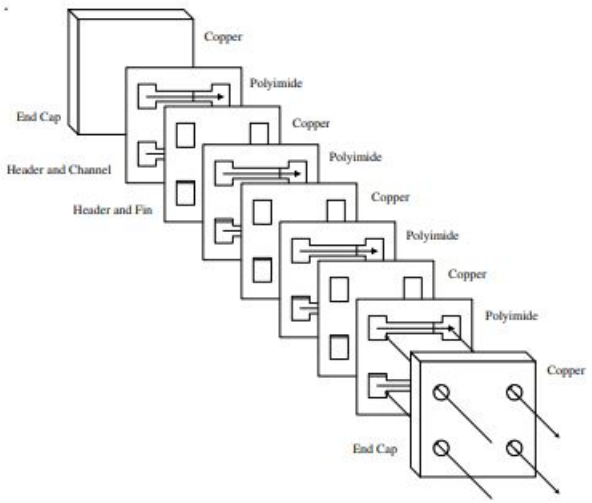

Figure 1.4: Exploded view of a typical microreactor structure [11]

to sub-millimeter range [11]. Improved microfabrication techniques have begun to make the implementation of these types of reaction systems into a variety of process engineering fields, including pharmaceutical production, fuel processing, oil refining, and chemical separation processes, a reality [12, 13]. These microfabrication techniques include bulk micromachining of monocrystalline materials, dry and wet etching processes, and micromolding among other techniques [11]. Often, a combination of these techniques will be employed to create the desired microstructures within a microreactor.

Typically, these microreactors are formed from a stack of catalytic plates with inlet and outlet headers connected by several parallel reaction channels. The stack of plates is usually contained within a housing or is sandwiched between top and bottom plates sealing the reactor [11]. Examples of a typical microreactor are shown in the exploded view in Figure 1.4 and in the picture demonstrating the small scale of microreactors in Figure 1.5. As shown in Figure 1.4, often, microreactors feature plates of different materials based on the application.

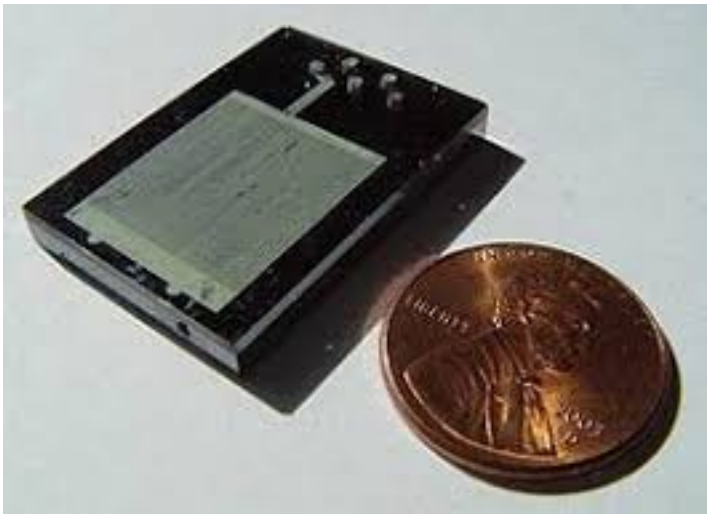

Figure 1.5: Example of the small scale of microreactors [14]

Microreactors have a number of benefits over conventional reactors. Notably, the smaller physical size of microreactors leads to superior heat and mass transfer characteristics that enhance temperature and reaction control of chemical processes and increases the safety of processes due to the low throughput of chemicals through a single microreactor. The production capacity of microreactors is easily scalable by increasing or decreasing the number of units running in parallel, allowing for significant production flexibility, quick ramp-up/ramp-down to meet production demands, and minimal down-time from component failure due to the presence of several microreactors operating simultaneously. As a result of these factors, microreactors are well-suited for use in significantly smaller chemical production plants and open the door to distributed production of chemical products which otherwise must be produced in large scale plants [11].

Although microreactor technology has a number of advantages over conventional reactor technology, much of the chemical industry in the US and Europe has been slow to adopt it due to the high capital investment costs associated with replacing existing equipment [13]. Still, as advances continue to be be made in microfabrication and additive manufacturing

techniques, it appears likely that the eventual adoption of microreactor technology across industry will hasten [13].

1.5 Additive Manufacturing Technologies

Recently, additive manufacturing (AM) technologies have become a disruptive force in the field of manufacturing across a variety of industries. Additive manufacturing is defined as the process of joining materials to make objects from 3-D model data, usually layer upon layer [15]. Unlike conventional manufacturing techniques, which are subtractive in nature and rely on the removal of material to achieve the final part shape, additive manufacturing relies only on the gradual addition of material to a part to create its final shape and form. As a result, AM lends itself to the creation of a variety of parts with complex geometries that cannot be easily machined, obviates the need for traditional design for manufacturing and assembly (DFM/DFA) principles, allows for significant part customization and on-demand manufacturing, and can significantly increase the environmental sustainability of an industrial process by reducing manufacturing waste [15, 16].

AM technologies have existed since the 1980s, but have recently become a viable, mainstream manufacturing process for a number of applications. As a result, there is also growing interest in using AM processes to produce chemical microreactors and structured catalysts for use in a variety of chemical processing industries [17]. The increasing interest in the use of these technologies across a variety of fields has spurred a significant evolution in the AM techniques available and the applications they can be used for. A diagram summarizing several of the key AM processes and their relative classification is shown in Figure 1.6, adapted from [18].

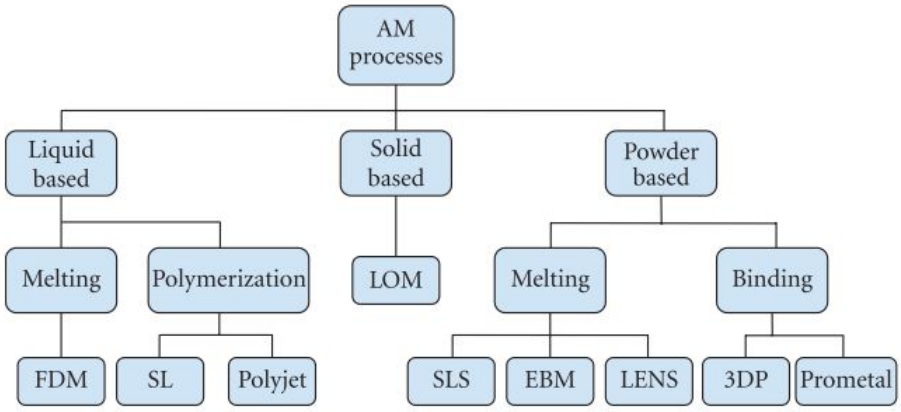

Figure 1.6: Summary of additive manufacturing processes [18]

As shown in Figure 1.6, the major AM processes are generally liquid based, solid based, or powder based. These classifications can be further broken down based on the exact nature of the process itself (e.g. melting vs. binding). The AM processes listed in Figure 1.6 include fused deposition modeling (FDM), stereolithrography (SL), polyjet/inkjet printing (IJP), laminated object manufacturing (LOM), selective laser sintering (SLS), electron beam melting (EBM), and laser engineered net shaping (LENS) [16]. Of the AM processes included in this diagram, fused deposition modeling (FDM), stereolithography (SL), polyjet/inkjet printing (IJP), and selective laser sintering (SLS)/selective laser melting (SLM) have been identified as processes that can possibly be leveraged for the production of chemical microreactors. These processes are briefly summarized as follows:

- Fused Deposition Modeling (FDM): Liquid material is extruded from a movable FDM head and deposited in thin layers onto a substrate. The material is heated to just above its melting point so that it solidifies immediately upon extrusion and cold welds to the previous layers of the print. Thermoplastics are the primary material used, but other materials are being developed as well [15, 16].

- Stereolithography (SL): A photosensitive resin and a UV laser are used to build a part layer by layer by selectively hardening sections of the resin. The process requires a support structure to attach the part to the build platform. After a single layer of the part is hardened, the build platform is lowered into the liquid resin reservoir to evenly coat the part to prepare for the next laser pass. Once the part is completed, support structures printed along with the actual part are manually removed. UV curable polymers are the primary materials used [15, 16].

- Polyjet/Inkjet Printing (IJP): A liquid phase material (the "ink") consisting of a solute dissolved or dispersed in a solvent is ejected form a nozzle through a sudden, quasi-adiabatic reduction of the chamber volume via piezoelectric action. The ejected liquid falls under the action of gravity and impinges on a substrate and dries through solvent evaporation. The liquid is then immediately cured after deposition by a UV lamp attached to the printhead carriage. The printing process itself involves the use of pre-patterned substrates at multiple layers of processing. UV curable polymers are the primary materials used [15, 16].

- Selective Laser Sintering (SLS)/Selective Laser Melting (SLM): These are powder bed methods that fuse together small particles of the build material either through sintering or melting via a high power laser. The powder bed material is heated to just below its melting point and the laser then passes over the material to fuse the material together layer by layer. The fused material forms the part while the remaining powder around the part remains in place to support the structure during the build process. Once the part is complete, the powder can be cleaned away and recycled for future prints. SLS/SLM methods are often used for a variety of plastics, metals, and ceramics [15, 16].

1.6 Thesis Goals and Organization

This thesis investigates how differential temperature microreactors can be used to intensify the WGS reaction to achieve significant reductions in both the required reactor volume for the WGS process and the overall hydrogen production cost of the steam methane reforming process. This investigation is presented from both a component design perspective, where a detailed numerical model of a WGS microreactor is developed and used to design a microreactor prototype for experimental validation, and a system level perspective, where the influence of the differential temperature WGS microreactor on the economic performance of the entire steam methane reforming is analyzed. In support of the component design analysis performed, this thesis also performs a preliminary investigation into how viable current additive manufacturing methods are for the production of WGS microreactors.

The remainder of this thesis is organized as follows:

- Chapter 2: A literature review examining the thermodynamics of the WGS reaction, the kinetics of the WGS reaction, optimal temperature profiles for the WGS reaction, the performance limitations of the conventional packed bed WGS reactors used in industry, previous studies examining the implementation of WGS microreactors, studies on the general use of additive manufacturing techniques for microreactor production, and an identification of how this study expands upon previous works
- Chapter 3: A detailed discussion of the reactor models used as part of this study, including the baseline plug flow reactor HTS/LTS model developed and the COMSOL Multiphysics model of the microreactor developed, and the approach to microreactor conversion enhancement used
- Chapter 4: A detailed presentation of the modeling results obtained from the application of the models developed in Chapter 3, including the baseline HTS/LTS reactor

performance, a verification of the COMSOL microreactor model results against experimental data found in the literature, the baseline microreactor modeling results, a general comparison of the HTS/LTS and microreactor results to evaluate the feasibility of process intensification, parametric studies examining how changing important design parameters affects microreactor performance, and general conclusions drawn

- Chapter 5: A detailed discussion of the microreactor prototype design developed and additively manufactured based on the modeling results in Chapter 4, the experimental methodology used to evaluate the thermal-hydraulic performance of the prototype, and the general agreement between the obtained experimental data and predicted model results

- Chapter 6: A detailed discussion of the flow sheets developed to evaluate how the integration of a differential temperature WGS microreactor affects system behavior, the economic analysis performed to estimate the capital and operating costs of the developed flow sheet systems, the formulation of optimization problems minimizing the hydrogen production cost of each flow sheet, and the general results of these optimization studies

- Chapter 7: A discussion of the general conclusions and contributions from this study and an identification of areas for future work

Chapter 2: Literature Review

This chapter reviews the relevant literature available on the thermodynamics of the water-gas shift reaction, the kinetics of the water-gas shift reaction, the derivation of optimal temperature profiles for the water-gas shift reaction, the existing packed bed water-gas shift reactors commonly used in industry, existing studies on the application of microreactor technology toward water-gas shift reaction process intensification, and existing studies on the application of additive manufacturing to produce chemical reactors. A summary of how the cited works are relevant to the work presented in this thesis and an explanation of how this thesis expands upon previous works is presented as well.

2.1 Water-Gas Shift Thermodynamics

As mentioned previously in Section 1.3, the WGS reaction is a mildly exothermic reaction with a heat of reaction of $\Delta H_{rxn} = -41.1$ kJ/mol at standard conditions ($P = 1 \times 10^5$ Pa , $T = 25$ °C) that becomes thermodynamically limited at higher temperatures in accordance with Le Chatelier's principle. This is reflected by the equilibrium constant, K_{eq}, of the reaction decreasing as temperature increases, as shown in the plot of WGS equilibrium constants as a function of temperature in Figure 2.1 created using data from [19].

A number of analytical and empirical expressions for the WGS equilibrium constant have been proposed in the literature [8, 19], but the empirical model proposed by Moe [20] is popular for computational models and simple design calculations due to its relative simplicity compared to other expressions:

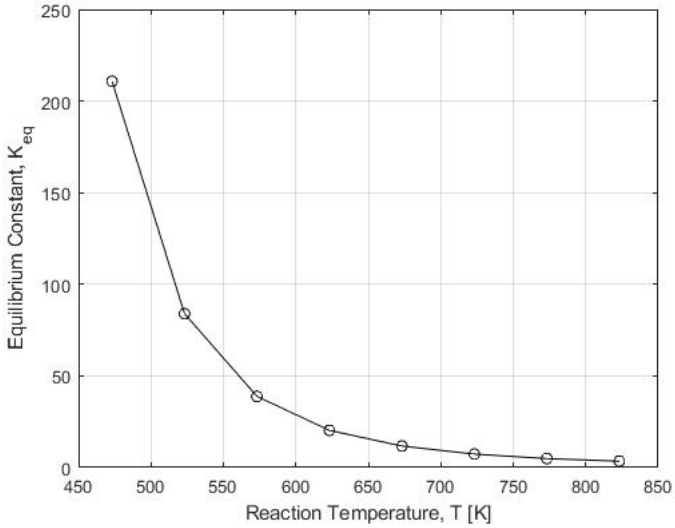

Figure 2.1: Water-gas shift equilibrium constant as a function of temperature [19]

$$K_{eq} = exp\left(\frac{4577.8}{T} - 4.33\right) \tag{2.1}$$

In equation 2.1, T is the temperature of the reaction in Kelvin. As mentioned previously in Section 1.3, because the reactant and product sides of the WGS reaction are equimolar with each other, the equilibrium of the reaction is unaffected by pressure, making it an important factor kinetically as shown in Section 2.2, but not thermodynamically.

2.2 Water-Gas Shift Kinetics

This section details relevant literature pertaining to the kinetics of the water-gas shift (WGS) reaction in the areas of catalysis and the different kinetics models used to describe the reaction.

2.2.1 Catalysis

The catalyzation of the water-gas shift reaction is a form of heterogeneous catalysis, where the phase of the catalyst material is different than that of the reactants [21]. In the context of the WGS reaction, the catalyst is a solid metal or metal oxide while the reactants are gases. Heterogeneous catalysis is particularly well-suited to continuous flow operation as the catalyst stays fixed within the operating reactor and does not require separation from the reaction product, which simply exits the reactor [21]. Without the introduction of a catalyst, the WGS reaction would occur too slowly for practical applications at the process temperatures listed in Section 1.2. The introduction of a catalyst to the reaction substantially lowers the activation energy, E_a, of the reaction, significantly increasing the reaction rate without affecting the reaction's equilibrium [21].

Catalyst selection for a particular reaction is largely driven by the Sabatier principle. The Sabatier principle states that in a heterogeneous catalytic reaction, the reactant molecules form intermediate complexes with the catalyst which go on to react in a series of elementary steps to form the final product species and that these intermediate complexes should ideally be of intermediate stability to best enhance the reaction rate. If these complexes are too stable when adsorbed to the catalytic surface, they are unlikely to react with other complexes or desorb from the catalytic surface. If they are not stable enough, they will fail to properly adsorb to the catalytic surface or react at all [21]. This is demonstrated in Figure 2.2, which shows that the reaction rate is highest in the middle range of adsorption strengths. These adsorption strengths are influenced by a number of factors, including process conditions, molecule type and geometry, and the catalyst material and surface structure, which can result in a variety of catalysts being well-suited to a particular reaction depending on the application.

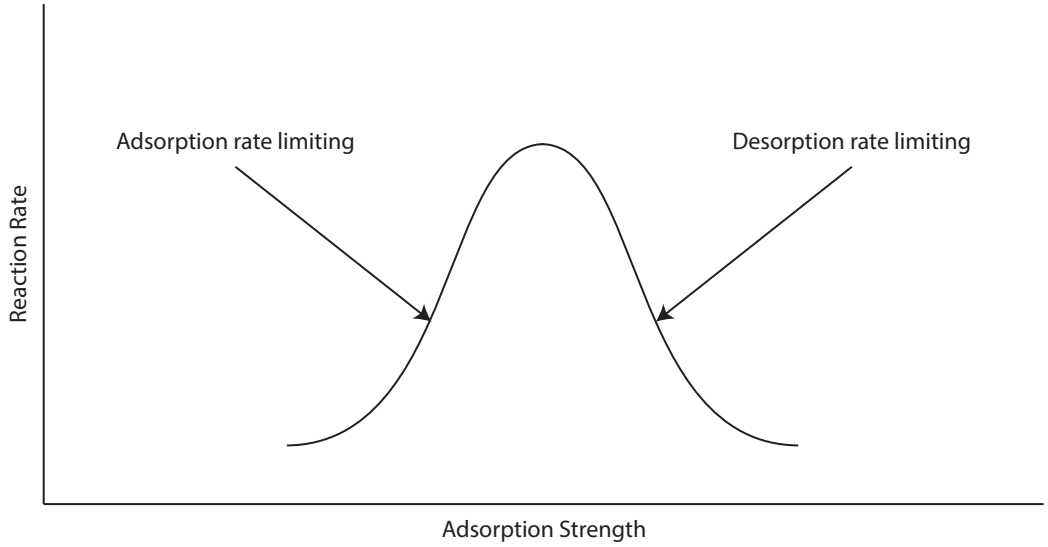

Figure 2.2: Illustration of Sabatier's principle

Catalyst development for the water-gas shift reaction is an area of ongoing research, both analytically and experimentally. Due to the thermodynamic constraints of the WGS reaction and the improvement in reaction conversion incurred by running the reaction in a high temperature reactor and low temperature reactor in series, catalysts traditionally have been developed either as high temperature shift (HTS) catalysts or low temperature shift (LTS) catalysts which operate best within a certain temperature range. Additionally, as a result of recent interest in the development of fuel cell technology, research toward developing noble metal catalysts as an alternative to HTS/LTS catalysts has increased significantly in the past few decades [8, 22, 23].

2.2.1.1 High Temperature Shift Catalysts

Traditionally, high temperature shift catalysts are ferrochrome catalysts consisting of a mixture of 80-90% iron(III) oxide (Fe_2O_3) and 8-10% chromium(III) oxide (Cr_2O_3) with the balance consisting of promoters and stabilizers like copper oxide (CuO), alumina (Al_2O_3), magnesium oxide (MgO), and zinc oxide (ZnO) [23]. In these catalyst blends, the Fe_2O_3 acts as the primary catalyzing agent while the Cr_2O_3 acts as the stabilizer and prevents the catalyst from sintering, a process in which the catalyst particles compact together due to applied heat and pressure, reducing catalyst activity and surface area. These HTS catalysts tend to operate within the temperature range of 310 °C to 450 °C. At inlet temperatures higher than this temperature range, HTS catalysts can reach maximum temperatures of approximately 550 °C at the reactor outlet, which can sinter the catalyst together and reduce its performance [7]. HTS catalysts resist poisoning from a variety of substances that LTS catalysts are sensitive to, but have been found to be poisoned by inorganic salts, boron, oils, phosphorous compounds, liquid water, and sulfur compounds at concentrations greater than 50 ppm to varying degrees [24]. At typical operating conditions and inlet conditions, reactors with HTS catalyst blends are able to reduce the concentration of CO in the reaction stream to below 3% [7].

HTS catalysts must be activated before they can be put into active service. This involves partially reducing the Fe_2O_3 to Fe_3O_4 using process gas mixtures consisting of hydrogen, nitrogen, carbon monoxide, carbon dioxide, and water vapor [7]. During this process, it is important to avoid over-reduction of the Fe_2O_3 to lower oxides, carbides, or metallic iron species as these species can promote undesirable side reactions such as methanation and the Fischer-Tropsch process and are mechanically weak, leading to catalyst structural degradation, catalyst damage, and increased pressure drop of the reactive flow across the catalyst bed [7].

2.2.1.2 Low Temperature Shift Catalysts

Traditionally, low temperature shift catalysts are a mixture of zinc oxide (ZnO), copper(II) oxide (CuO), and chromium(III) oxide (Cr_2O_3) or alumina (Al_2O_3). Typical compositions of these catalysts are reported as 68-73% ZnO, 15-20% CuO, 9-14% Cr_2O_3, and 2-5% Mn, Al, and Mg oxides for the Cr_2O_3 based catalyst [22] and 32-33% CuO, 34-53% ZnO, and 15-33% Al_2O_3 for the Al_2O_3 catalyst [25]. In these catalyst blends, the CuO is the primary catalyzing agent with ZnO and Cr_2O_3 acting as a catalyst support and Al_2O_3 aiding in dispersion and minimizing pellet shrinkage [8]. LTS catalysts typically operate within the temperature range of 200 °C to 250 °C. At higher temperatures than this operating range, the copper in the catalyst is prone to sintering, reducing the catalyst performance significantly [19]. Additionally, the catalyst is intolerant of and poisoned by sulfur, halogens, and unsaturated hydrocarbons, which can all be present in trace quantities in natural gas [24]. Sulfur reacts with the active Cu present to form Cu_2S and accumulates at the catalyst surface to block the pores and active sites, permanently inhibiting the catalyst. To prevent sulfur poisoning, the concentration of sulfur in the reaction stream must be kept below 0.1 ppm [23]. Similarly, halogen compounds such as hydrochloric acid (HCl) can react with the active Cu present in the catalyst and also facilitate the movement and sintering of the copper. To prevent halogen poisoning, the concentration of halogens in the reaction stream must be regulated even more stringently than sulfur and kept on the order of 1 ppb [23]. To help protect LTS reactors from poisoning, guard beds consisting of ZnO are placed at the inlet of LTS reactors [26]. At typical operating conditions and inlet conditions, reactors with LTS catalyst blends are able to reduce the concentration of CO in the reactive stream to as low as 0.1% CO [8].

Like HTS catalysts, LTS catalysts need to be activated before being put into active service. This involves exposing the catalyst to process stream gas with dilute hydrogen

gas. In this process, the CuO present in the catalyst is reduced to copper [7]. Because this reaction is exothermic, the process stream must be kept at temperatures below 230 °C to prevent the copper from sintering [25]. If water vapor present in the process stream condenses across the catalyst, it can deactivate the catalyst through leaching or the formation of surface carbonates. Additionally, once the catalyst is in its reduced state, it becomes extremely pyrophoric and is prone to explosions and catching fire when exposed to air, making it ill-suited to a variety of desirable processes, including on-board fuel applications for automobiles [27].

2.2.1.3 Precious Metal Catalysts

In recent decades, significant research effort has gone toward the development of precious metal catalysts for the water-gas shift reaction, specifically for use in fuel cell applications. Traditional high temperature and low temperature catalysts are not well suited to these fuel cell applications for a number of reasons. Primary concerns with these catalysts center on the relatively low activity of the LTS catalyst and correspondingly large volume and weight associated with LTS reactors, lower durability during start-up and shut-down operating conditions, and safety concerns that arise due to the pyrophoric nature of the LTS catalyst [8, 23].

For decades, precious metals have been known to have a high WGS activity, but their high prices have precluded their adoption in commercial practice [23]. These catalysts exhibit high WGS activity over the a temperature range of approximately 250 °C to 400 °C, spanning temperatures just above the standard LTS reactor temperature range to within the HTS reactor temperature range. Furthermore, these precious metal catalysts do not require pre-activation before use like HTS and LTS catalysts do and can be safely exposed

to air without exploding or experiencing a significant loss in performance, making them much better suited to fuel cell applications than the traditional HTS or LTS catalysts [23]. Recent studies on precious metal catalysts for the WGS reaction have primarily focused on precious metals such as Pt, Rh, Ru, Au, and Pd deposited on partially reducible oxides such as ceria, zirconia, titania, iron oxides, and mixed oxides of ceria [28]. A meaningful comparison of all the different precious metal catalysts reported is difficult due to the different preparation methods and experimental conditions used to evaluate them, but Thinon et al. attempted to evaluate a number of these proposed precious metal catalysts under the same process conditions to compare their relative performances with each other. They found Pt based catalysts such as $Pt/CeO_2/Al_2O_3$ and Pt/TiO_2 to be the most active of the catalysts considered at HTS WGS conditions and that Au and Cu catalysts were the most active at LTS WGS conditions [29]. They also found that Rh and Ru based catalysts promoted the undesirable methanation reaction for the process conditions used.

Ceria and titania supported platinum catalysts are emerging as the general front runners as potential water-gas shift catalysts for fuel cell applications, but are noted to have a number of disadvantages associated with them, including low activity below 250 °C, deactivation over long term operation, and the formation of hydrocarbons due to Fischer Tropsch side reactions [23]. All of the causes of deactivation for these platinum based catalysts are not fully understood, but proposed mechanisms include a loss of active catalyst surface area due to the strong adsorption of CO [30] or carbonate-like species [31] to the catalyst surface. Another study by Zalc et al. found that deactivation rates of platinum-ceria catalysts were significantly lower when hydrogen was not present in the reaction feed, suggesting that an irreversible over-reduction of ceria by hydrogen may take place under certain circumstances, permanently deactivating the catalyst [32].

2.2.1.4 Catalysis Summary

As outlined in this section, although standard catalyst blends for both HTS and LTS reactors are relatively well characterized and commercially available, they are not well suited for fuel cell applications due to a number of operating and safety concerns. As a result, a number of precious metal catalysts appropriate for the water-gas shift reaction have also been identified, with platinum based catalysts emerging as the general front runners. While these catalysts are effective, they are very expensive. In applications where it is desirable to use these types of catalysts, it thus proves beneficial to utilize them as effectively as possible and to reduce the total amount of catalyst that must be used as much as possible. The application of optimal temperature progressions, discussed in Section 2.3, in microreactors presents a unique opportunity to enhance the conversion of the water-gas shift reaction while also reducing the necessary amount of catalyst to facilitate the reaction occurring when compared to packed bed reactors, which are discussed in Section 2.4.

2.2.2 Kinetic Models

Reaction kinetics models are used to predict the rate of a reaction based on various process conditions and are thus valuable in the proper design of a reactor for a specific application [8]. These kinetic models are generally classified as either microkinetic models or macrokinetic models depending on the approach taken to model the reaction.

2.2.2.1 Microkinetic Models

In the microkinetic approach, the individual elementary steps of a reaction are modeled based on a knowledge of the energetics associated with each step. In this approach, the

surface coverage of species over the catalyst surface, reaction order, and activation energy of the reaction can all be estimated and used to predict the reaction pathway and reaction rate of the overall reaction [8]. While such methods can provide a detailed understanding of the overall progression of a reaction and accurate reaction rates, they can quickly become computationally expensive as the number of elementary steps in a model increases.

A number of microkinetic models of the WGS reaction have been proposed and favored by different authors, generally taking the form of either a redox mechanism or an associative mechanism. In the redox mechanism, the catalyzing surface is cyclically oxidized by H_2O and reduced by CO during the conversions taking place [8, 23]. In the associative mechanism, the reactant molecules adsorb to the catalyzing surface and react to form an adsorbed intermediate species which then decomposes to form products [8, 23].

Ovesen et al. proposed an eight step redox type mechanism for the WGS reaction over single crystal Cu catalyst[33]. Wang et al. similarly advocated for the redox mechanism [34] and suggested it as the dominant reaction pathway at LTS temperatures (200 °C to 250 °C). Both studies found the dissociation of water over the catalyst surface to be the rate limiting step of the reaction.

Rhodes et al. questioned whether the redox mechanism dominated the reaction at LTS conditions and suggested that the associative mechanism is also likely at these conditions, citing numerous studies experimentally showing the presence of formate ($HCOO$) on the catalyst surface at these conditions [7]. Rhodes et al. suggested that formate likely acts as an intermediate species for a separately occurring associative mechanism for the WGS reaction. Ovesen et al. later modified their redox mechanism to include additional steps to account for the associative step and the formation of $HCOO$ during the reaction [35]. Others have questioned the stability of $HCOO$ as an intermediate species and suggested other species, such as carboxyl groups, as more likely intermediate species [36–38]. Due to

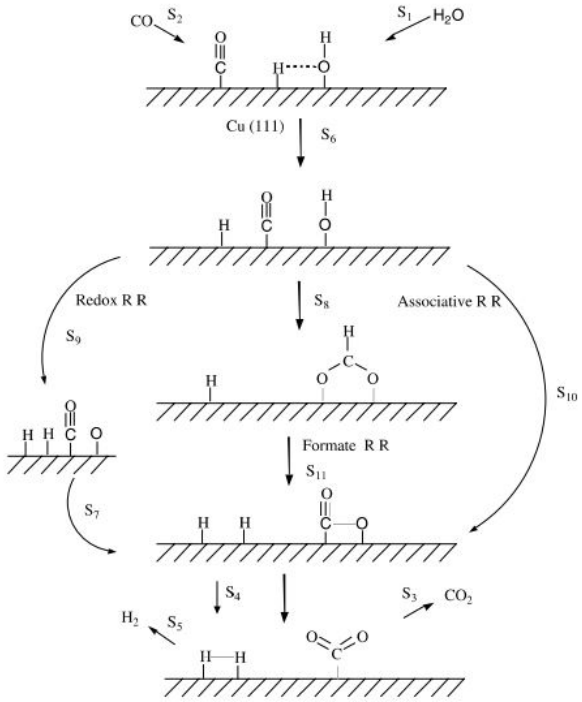

Figure 2.3: Primary reaction routes of the WGS reaction [39]

the variety of proposed associative mechanisms, a number of rate limiting steps have also been proposed.

An integrated model for the WGS over $Cu(111)$ considering a redox mechanism, associative mechanism, and formate mechanism was proposed by Fishtik and Ratta and considers each of these pathways acting in parallel with each other. These routes are illustrated in Figure 2.3, taken from [39].

This study found that the redox mechanism is the dominant reaction pathway at higher temperatures while both the formate mechanism and associative mechanisms dominated at lower temperatures [39]. A revised version of this model was later produced by Callaghan et al. with a modified redox step with similar results [25]. In the combined microkinetic model developed by Callaghan et al., a total of 16 unique elementary steps were considered, which

is very computationally demanding. The application of quasi-equilibrium and quasi-steady state approximations to several of the faster elementary steps in this model simplified it from a 16 step model to an 11 step model [25]. Within this reduced model, a number of rate limiting steps were determined to be present. The dissociation of H_2O over the catalyst surface was found to be a rate limiting step common to each mechanism, but within each reaction pathway, an additional slow step was also determined to exist. In the redox pathway, the reaction between OH and H to form O and H_2 is the rate limiting step. In the associative pathway, the reaction between CO and OH to form CO_2 and H is the rate limiting step. In the formate pathway, the reaction between CO and OH to form $HCOO$ is the rate limiting step [25]. The steps in the full microkinetic model developed by Callaghan et al. are listed in Table 2.1. For each of the steps listed, * alone indicates an open active site present on the catalyst surface that species can adsorb to and a species denoted with a superscript * indicates that the species is adsorbed to the catalyst surface.

No conclusive mechanism for the WGS has been determined yet and there is still ongoing debate about the validity and application of a number of the models discussed. Still, significant progress toward the modeling of the WGS has been made in recent decades. Existing results suggest the dominance of the redox mechanism at higher temperatures and associative mechanisms at lower temperatures with the nature and condition of the catalyst ultimately affecting the intermediate species formed and their decomposition [23].

2.2.2.2 Macrokinetic Models

In the macrokinetic approach, a single expression is used to predict the overall rate of a reaction. Generally, empirical models developed using experimental data are used to predict the overall reaction rate of a a reaction [8]. These empirical models are expressed as

Table 2.1: Multi-pathway microkinetic model of the WGS reaction [25]

Modified Redox Mechanism
$H_2O + * \rightleftharpoons H_2O^*$
$CO + * \rightleftharpoons CO^*$
$H_2O^* + * \rightleftharpoons OH^* + H^*$
$OH^* + H^* \rightleftharpoons O^* + H_2^*$
$CO^* + O^* \rightleftharpoons CO_2^* + *$
$CO_2^* \rightleftharpoons CO_2 + *$
$H_2^* \rightleftharpoons H_2 + *$
Associative Mechanism
$H_2O + * \rightleftharpoons H_2O^*$
$CO + * \rightleftharpoons CO^*$
$H_2O^* + * \rightleftharpoons OH^* + H^*$
$CO^* + OH^* \rightleftharpoons CO_2^* + H^*$
$CO_2^* \rightleftharpoons CO_2^* + *$
$H^* + H^* \rightleftharpoons H_2^* + *$
$H_2^* \rightleftharpoons H_2 + *$
Formate Mechanism
$H_2O + * \rightleftharpoons H_2O^*$
$CO + * \rightleftharpoons CO^*$
$H_2O^* + * \rightleftharpoons OH^* + H^*$
$CO^* + OH^* \rightleftharpoons HCOO^* + *$
$HCOO^* + * \rightleftharpoons CO_2^* + H^*$
$CO_2^* \rightleftharpoons CO_2 + *$
$H^* + H^* \rightleftharpoons H_2^* + *$
$H_2^* \rightleftharpoons H_2 + *$

Arrhenius models and can provide a relatively accurate, computationally light method of predicting reaction rates if the experimental data used is accurate. For the WGS reaction, empirically derived expressions are frequently used in reactor design calculations as they can provide an accurate description of the reaction rate when all kinetic parameters are properly fitted [23]. Alternatively, an overall reaction rate expression can be obtained from microkinetic models through successive substitution of the individual elementary rate expressions into the rate expressions of other steps. These Langmuir-Hinshelwood (LH)

type expressions can capture the essential reaction behavior of a microkinetic model without needing to model every elementary step, but also tend to be extremely non-linear, which can complicate solution methods considerably.

Empirically derived rate expressions for the WGS reaction frequently take the form of a power law expression as follows :

$$r = kP_{CO}^{l}P_{H2O}^{m}P_{CO2}^{n}P_{H2}^{q}(1-\beta) \tag{2.2}$$

In equation 2.2, k is the reaction rate constant, P_{CO}, P_{H2O}, P_{CO2}, and P_{H2} are the partial pressures of CO, H_2O, CO_2, and H_2 respectively, β is the reversibility factor of the reaction, and l, m, n, and q are exponents evaluated from a curve fitting process to the experimental data. The reaction rate constant of the reaction is found from the Arrhenius expression as follows:

$$k = K_0 exp\left(-\frac{E_a}{RT}\right) \tag{2.3}$$

In equation 2.3, K_0 is a pre-exponential factor, E_a is the activation energy, R is the ideal gas constant, and T is the temperature in units of Kelvin. The temperature dependence of the reaction rate is captured in the Arrhenius expression. The reversibility factor, β, of the reaction is defined as:

$$\beta = \frac{P_{CO2}P_{H2}}{K_{eq}P_{CO}P_{H2O}} \tag{2.4}$$

The reversibility factor is a measure of how close the reaction is to its equilibrium state and approaches a value of 1 as the reaction reaches its equilibrium state, resulting in a reaction rate of 0 when the reaction reaches equilibrium [8].

A number of different power law models have been proposed for a variety of both high temperature and low temperature WGS catalysts. Frequently used expressions include those proposed by Rhodes et al., Keiski et al., and San et al. for HTS catalysts [40–42] and Choi and Stenger [43] for LTS catalysts.

A number of authors have also found that LH type rate expressions describe their experimental data well. Callaghan et al. were able to reduce the microkinetic model they developed, which was discussed in Section 2.2.2.1, into a single LH rate equation and found that it perfectly matched the prediction of their full microkinetic model and was in excellent agreement with their experimental results [25]. Germani and Schuurman experimentally evaluated the performance of a $Pt/CeO_2/Al_2O_3$ catalyst and concluded that the following LH rate expression described their data best [44]:

$$r_{CO} = \frac{k_{rds} K_{CO} K_{H2O} P_{CO} P_{H2O} (1 - \beta)}{(1 + K_{CO} P_{CO} + \sqrt{K_{H2} P_{H2}})^2 (1 + \sqrt{K_{H2O} P_{H2O}} + K_{CO2} P_{CO2})} \tag{2.5}$$

In equation 2.5, k_{rds} is the reaction rate constant of the rate determining step of the reaction mechanism and K_{CO}, K_{H2O}, K_{CO2}, and K_{H2} are adsorption equilibrium constants for each of the species participating in the reaction. The reaction rate constant is found using the Arrhenius expression, similar to the reaction rate constant in the power law expression. Similar LH expressions have been developed for HTS catalysts [19], LTS catalysts [45], and other noble metal catalysts [46, 47].

2.3 Optimal Water-Gas Shift Reaction Progression

As explained in Section 1.3, as a reversible, exothermic chemical reaction, the water-gas shift reaction exhibits improved reaction kinetics with increasing temperature, but lower equilibrium conversion. Lowering the temperature of the reaction has the effect of favoring

higher conversion, but at the cost of slower reaction kinetics which requires more catalyst and larger reactors to achieve a desired conversion. As a result, achieving the desired conversion within a reasonable reactor volume becomes a matter of effective reaction temperature management. Microreactors make such effective temperature management of the WGS reaction possible and thus offer the possibility to impose a specific temperature profile onto the reaction to maximize reaction conversion [48].

In the case of reversible, exothermic chemical reactions like the WGS reaction, it is advantageous for the reaction to start at a high temperature to take advantage of fast kinetics and to then proceed to lower temperatures to improve reaction conversion [48]. The constrained nature of such reactions implies that there is an optimal temperature progression across these reactors for this progression that maximizes the possible conversion at each reaction rate. The temperature associated with this maximum possible conversion achievable at each reaction rate can be determined by evaluating the following expression taken from [48] for T_{max}:

$$\frac{\partial r_A(X_A, T_{max}, C_{i,in})}{\partial T} = 0 \tag{2.6}$$

In equation 2.6, the reaction rate r_A is a function of the reactor conversion, X_A , of a reactant, the temperature, T_{max}, of the reaction, and the inlet composition of the reaction stream to the reactor, $C_{i,in}$. The subscript A denotes that the reaction rate and conversion are in terms of a specific reactant A.

The physical temperature profile across a reactor can be extracted by applying a mass balance to the reactor [48]. For the case of an ideal plug flow reactor, this mass balance equation reduces to the following [48]:

$$C_{A,0} u_s \frac{dX_A}{dz} = r_A(X_A, T_{max}, C_{i,0}) \tag{2.7}$$

In equation 2.7, $C_{A,0}$ is the inlet concentration of reactant A to the reactor, u_s is the flow velocity through the reactor, and z is the reactor length in the direction of flow. Integrating equation 2.7 yields the minimum reactor length, and thus volume, required to achieve a certain conversion profile and the corresponding temperature profile. TeGrotenhuis et al. developed these profiles for a plug flow reactor packed with a precious metal catalyst and for a final reactor conversion of 90% based on typical WGS inlet conditions from the steam reforming of isooctane at a 3:1 steam to carbon ratio [48]. These profiles are plotted in Figure 2.4.

As shown in Figure 2.4, for the rate expression and inlet conditions used, 82% of the reactor conversion occurs within the first third of the reactor with the remaining 8% occurring in the last two-thirds of the reactor for an ideal plug flow reactor. The optimal temperature profile to achieve this conversion requires a rapid decrease in temperature from 665 °C to 400 °C within the first 8% of the reactor length. This rapid cooling is to account for the rapid heat generation that occurs at the front of the reactor due to the heat of reaction [48].

Ideally, the reformate stream from the steam reforming process would enter the WGS reactor at the highest possible temperature. However, methane formation, coking, and catalyst sintering are all concerns that prohibit the inlet temperatures from exceeding 600 °C. For HTS reactors, temperatures are commonly limited to 350-450 °C to negate such concerns [48]. When such upper temperature limits are imposed on the temperature profile, it is advantageous to allow the reactor to operate isothermally initially through the reactor and to then follow the optimal temperature profile once it drops below the upper temperature limit. By following this alternative temperature profile, TeGrotenhuis et al found that to achieve a final conversion of 90%, the reactor only needs to increase in size by 12%, implying that following the optimal temperature profile is more important at

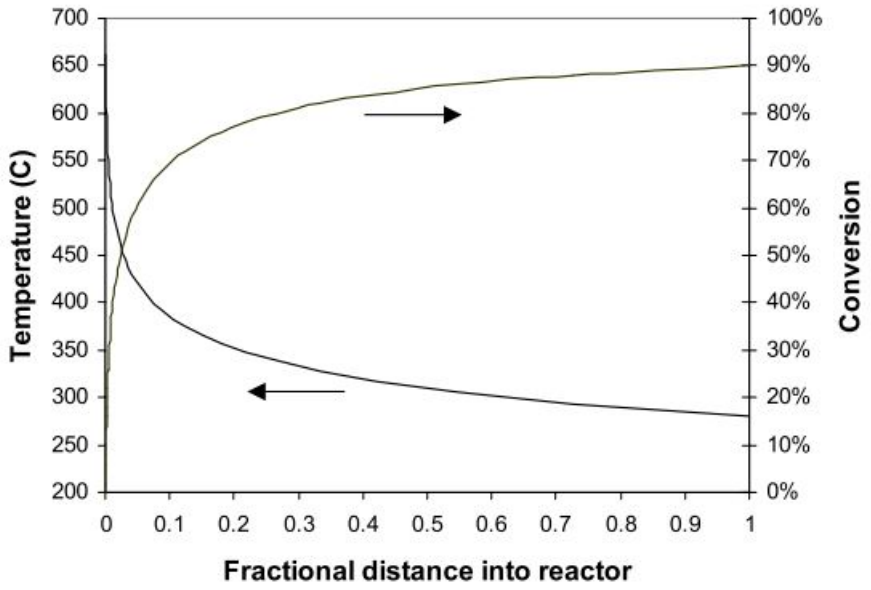

Figure 2.4: Example of an optimal temperature and conversion profile for the WGS reaction [48]

lower temperatures where reaction rates are lower [48]. When compared to the optimal temperature reactor, TeGrotenhuis et al. found that the standard two-stage WGS reactor system required approximately 2.3 times more catalyst to achieve the same conversion of 90%. Increasing the conversion rate even slightly to 93% resulted in the two-stage WGS reactor system requiring 2.5 times more catalyst than the optimal temperature reactor, implying that the optimal temperature reactor will require significantly less catalyst the higher the desired conversion rate becomes [48].

2.4 Packed Bed Reactors

As discussed previously in Sections 1.2 and 1.3, the water-gas shift reaction is generally performed in separate high temperature shift and low temperature shift reactors separated

by an intercooler in industry. These HTS/LTS reactors are generally packed bed reactors (PBR) [23] consisting of a tube filled with porous catalyst pellets through which the reacting stream passes. These pellets can come in a variety of shapes, but are often spherical or cylindrical. Within packed bed reactors, reactants first diffuse from the bulk fluid passing through the reactor to the external surface of the catalyst pellets. The reactants then diffuse into the internal pores of the pellet and react to form products on the catalytic surfaces present. The product molecules then diffuse out of the pellets, rejoin the bulk flow, and exit the reactor [49, 50].

Packed bed reactors are used in a variety of chemical processing industries and can offer number of advantages over other reactor types. Gases passing through packed beds can be approximated as plug flow, providing high contact between the reaction stream and the catalyst pellets and simplifying fluid flow analysis considerably compared to other types of reactors such as fluidized beds. Packed beds can also often provide a higher conversion per unit catalyst weight than other standard types of reactors [49].

Conversely, there are a number of disadvantages associated with using packed bed reactors. Packed bed reactors have low effective thermal conductivities, making effective temperature control of them often difficult. This can result in large packed beds with exothermic reactions running through them developing a number of hot spots, which can potentially damage catalyst pellets through sintering [49]. Additionally, packed bed reactors are prone to plugging as trace compounds present in reaction streams can deposit and collect in the void spaces between the catalyst pellets. This can result in significant pressure drops across the reactor bed, driving up operating costs significantly [49]. In the case of the WGS reaction, these compounds tend to be steam-volatile components that collect in the HTS reactor bed [23].

When considering the rate at which packed bed reactors can convert reactants to products, the relative rates of the different phenomena occurring must be considered. Often in packed bed reactors, the actual chemical reaction in the conversion process is the fastest step by several orders of magnitude while the diffusion of reactants and products into and out of the porous pellets is much slower. Packed bed reactors where these pore diffusion processes are significantly slower than the chemical reaction are termed mass transfer limited. In situations where the reactor becomes mass transfer limited, efforts at enhancing reactor performance must focus on reducing the resistance to mass transfer in the bed as opposed to increasing the reaction rate.

The extent to which a packed bed reactor is mass transfer limited can be quantified in terms of a porous pellet effectiveness factor [49, 50]. To illustrate this, a simple first-order surface reaction of a reactant, A, with a rate equation of the form $(-r")_A = k"C_A$ within a spherical pellet of radius R is considered. For this process, the effectiveness factor, η is defined as:

$$\eta = \frac{1}{\phi}\left(\frac{1}{\tanh 3\phi} - \frac{1}{3\phi}\right) \tag{2.8}$$

The effectiveness factor is a ratio of the actual mean reaction rate within the catalyst pellet's pores, $(-r_A)$, to what the reaction rate would be if the entire catalyst surface was exposed to the bulk flow concentration, $(-r_{A,s})$. The actual mean reaction rate within the catalyst of such a mass limited process can thus be expressed in terms of the the effectiveness factor and the reaction rate at the bulk flow conditions as:

$$(-r_A) = \eta(-r_{A,s}) \tag{2.9}$$

An effectiveness factor approaching 1 indicates a reaction process in which the concentration of reactant A does not drop appreciably within the pore and pore diffusion offers negligible resistance. As the effectiveness factor approaches 0, the reactant concentration drops rapidly within the pore, indicating strong pore resistance [49, 50] and inefficient utilization of the available catalyst surface. In equation 2.8, ϕ is the Thiele modulus, a measure of the relative effects of the reaction rate and mass transfer rate on a process, and is defined as the following for a spherical pellet of radius R:

$$\phi = \frac{R}{3}\sqrt{\frac{k}{D_e}} \tag{2.10}$$

In equation 2.10, k is the reaction rate constant, which can be evaluated from the surface reaction rate constant, k", the geometry of the pellet, and the catalyst density, and D_e is the effective diffusion coefficient of reactant A through the pellet. A smaller value of ϕ indicates a lower resistance to diffusion mass transfer while a large value indicates a higher resistance. The effectiveness factor as defined in equation 2.8 is plotted as a function of the Thiele modulus in Figure 2.5.

As shown in Figure 2.5, for $\phi < 0.4$, η remains close to a value of approximately 1, indicating very little pore diffusion resistance. For $\phi > 0.4$, the effectiveness factor begins to drop in value significantly, quickly approaching a value of nearly 0, indicating strong pore diffusion resistance. This chart is thus useful in determining whether a process can be considered kinetically limited or mass transfer limited based on the Thiele modulus associated with the process.

A study performed by Barbieri, Brunetti, Granato et al. [51] demonstrates the effect of varying the pressure and temperature on the Thiele modulus and in turn, the effect of varying the Thiele modulus on the pellet effectiveness factor for a commercial Cu/ZnO WGS catalyst, as shown in the plot taken from [51] in Figure 2.6. As expected, as the

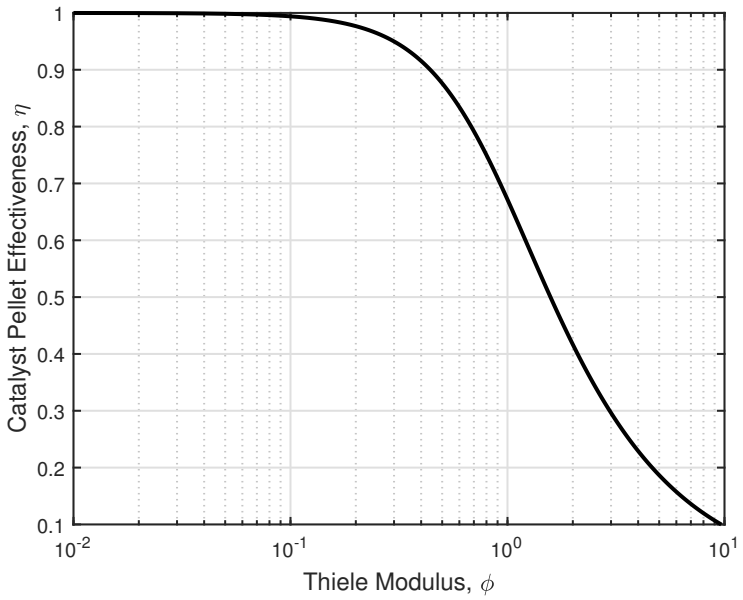

Figure 2.5: Spherical catalyst pellet effectiveness factor for a first order reaction as a function of Thiele modulus

Thiele modulus increases, the pellet effectiveness factor drops significantly, indicating the growing influence of the diffusive resistances in the catalytic pellet [51]. At the 250 °C upper limit to the catalyst's operating range, the effectiveness factor takes on a value as low as approximately 0.5, indicating significant diffusive resistances within the packed bed. At the lower 185 °C limit, the pellet effectiveness factor approaches a value of 1, indicating that the reaction kinetics are instead the limiting factor in the process over the mass transfer process. Given the standard operating temperatures of the WGS reaction, significant mass transfer limitations would thus be expected at nearly all operating conditions outside of the lowest possible LTS temperatures for the catalyst considered. This result would also be expected for other types of catalyst pellets as well.

A separate study by Germani, Alphonse, Courty et al. [52] suggested similar mass transfer limitations within WGS packed bed reactors at higher temperatures. After comparing

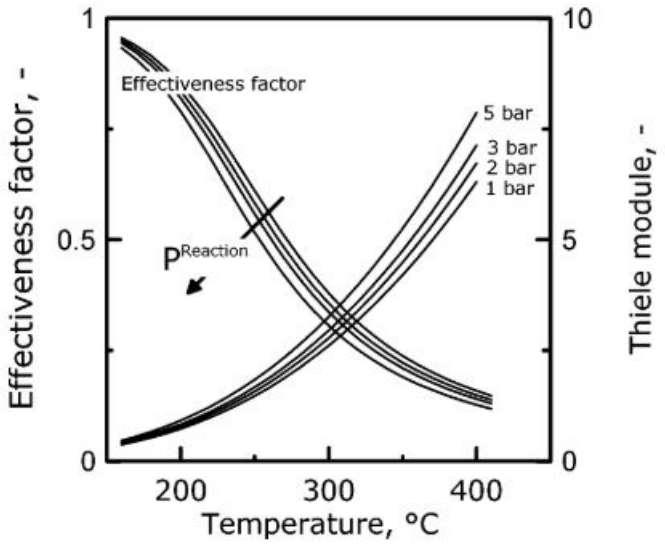

Figure 2.6: Effectiveness factor and Thiele modulus for the WGS reaction as a function of temperature [51]

the performance of a $Pt/CeO_2/Al_2O_3$ catalyst in both a packed bed reactor and a catalyst washcoated microreactor, they found that at temperatures above 290 °C, the packed bed reactor CO conversion was significantly lower than it was for the waschoated microreactor. They attributed this to diffusion limitations inside the pellets as the pellet size of 250 μm was significantly larger than the equivalent diameter of 37 μm of the washcoat layer in the microreactor and conclude that the microreactors used in their experiments were better able to utilize catalysts than the packed bed reactors used. Tonkovich et al. [53] reach similar conclusions in their study of a Ru/ZrO_2 catalyst in a microreactor. They note that fixed-bed reactors do not scale well and quickly become both heat and mass transfer limited, limiting the observed kinetics of a reaction. They conclude that microreactors are able to remove such heat and mass transfer limitations and allow for the potential miniaturization of WGS reactors by up to two orders of magnitude compared to conventional fixed bed reactors.

2.5 Existing Water-Gas Shift Microreactor Studies

A number of studies have been performed investigating the implementation of microreactors to enhance the conversion of the water-gas shift reaction. These studies typically focus on the effects of imposing external temperature profiles on a WGS reaction stream or parametrically evaluate how changing the value of certain process or reactor variables will affect reactor performance.

2.5.1 Microreactor Imposed Temperature Profile Studies

Several studies have explored the influence of imposing isothermal temperature profiles on a WGS microreactors to evaluate the improvement in reactor performance compared to adiabatic reactors. Bac et al. [54] analyzed the operation of a WGS microreactor washcoated with $Pt/CeO_2/Al_2O_3$ catalyst and integrated air coolant channels using a 2D model developed in ANSYS Fluent. Their model uses the Langmuir-Hinshelwood expression shown in equation 2.5 to model the reaction kinetics and examined a single "unit cell" of a WGS microreactor, consisting of half of a reaction channel, half of a coolant channel, and the wall separating them, as shown in Figure 2.7.

Bac et al. noted that the heat exchange integrated microreactor was capable of maintaining a nearly isothermal operating condition within the WGS reaction stream, effectively negating the expected temperature rise observed for the simulated adiabatic reactor, as shown in Figure 2.8, and increasing the CO conversion from 67.4% for the simulated adiabatic reactor to 77.6% for the isothermal reactor for the conditions simulated [54].

Rebrov et al. [55] noted that although isothermal reactors are capable of achieving higher conversions than their adiabatic counterparts, they operate at lower conversion levels near their inlets due to the slightly reduced reaction kinetics before eventually surpassing the

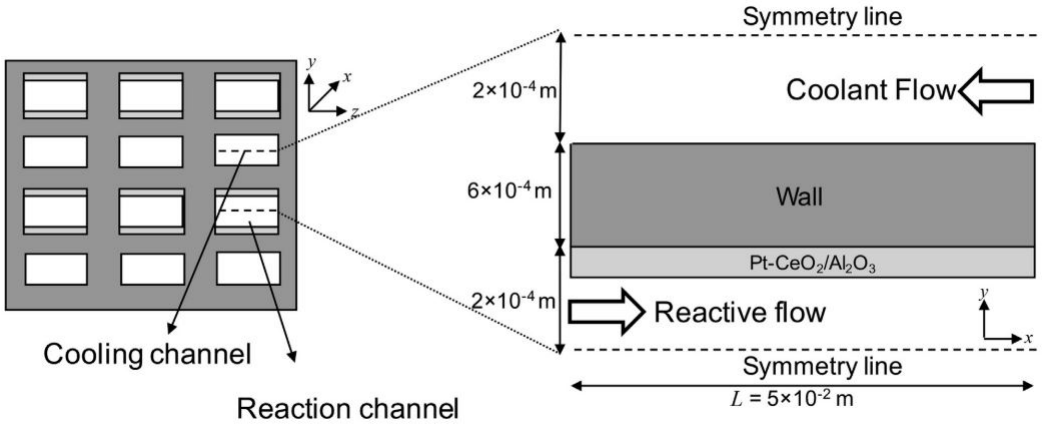

Figure 2.7: Unit cell of cooled microreactor channel modeled by Bac et al [54]

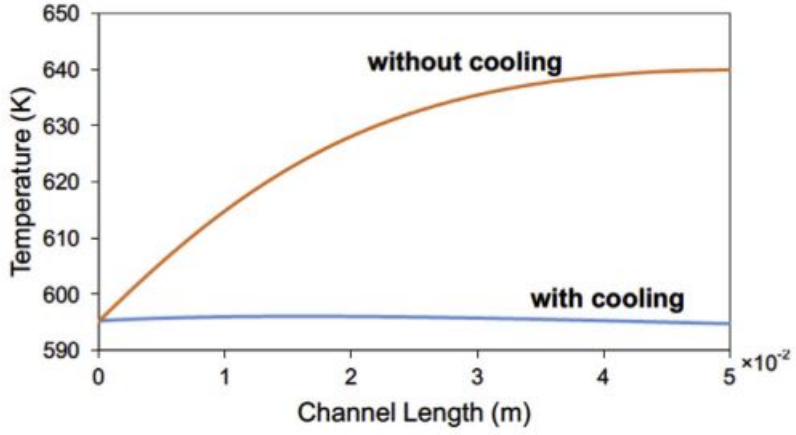

Figure 2.8: Comparison of adiabatic and cooled microreactor [54]

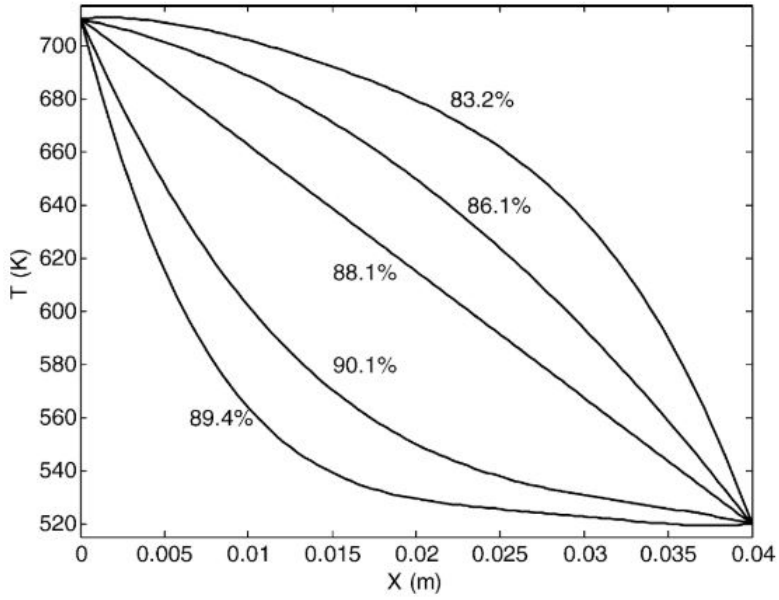

Figure 2.9: Kim et al. study on the effect of temperature profile on microreactor conversion [56]

more thermodynamically limited adiabatic reactors. Tonkovich et al. [53] demonstrated the application of microreactors in achieving an isothermal WGS reaction conditions and noted that the efficient heat transfer possible in such reactors is necessary to maintain isothermal conditions and thus achieve higher conversions. They also note that maintaining isothermal reactor operation prevents hotspots, thermal runaway, and possible explosions.

Outside of studies focused on isothermal WGS microreactor performance, a number of studies also examine WGS microreactor performance when operating under externally applied, varying temperature profiles. Kim et al. [56] performed one such study by simulating a single microreactor channel and varying the varying the applied temperature profiles from concave to linear to convex, as shown in Figure 2.9.

As shown in Figure 2.9, as the temperature profiles imposed on the reaction varied from concave to linear to convex, the reactor CO conversion increases to a maximum value before

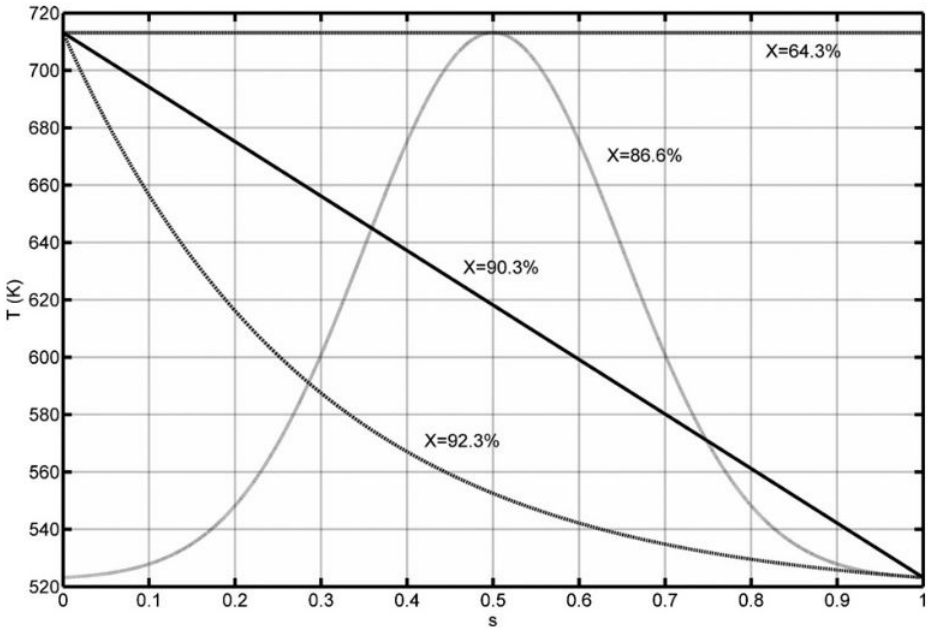

Figure 2.10: Romero study on the effect of temperature profile on microreactor conversion [57]

decreasing again. This implies the existence of an optimal temperature profile, with the convex temperature profiles applied in this study more closely matching the temperature distributions discussed in Section 2.3. Romero and Wilhite [57] performed a similar study by imposing linear, convex, and Gaussian temperature distributions to a single microchannel and comparing the results to the isothermal temperature results, as shown in Figure 2.10.

As shown in Figure 2.10, the convex temperature profile in this study resulted in the highest reactor CO conversion, similar to the Kim et al. study. All of the varying temperature profiles result in CO conversions that are 24-30% higher than the isothermal conversion reported. Romero and Wilhite go on to report, however, that although their analysis indicates that decreasing convex temperature profiles are capable of achieving the highest outlet conversions, decreasing linear temperature profiles are the most volume

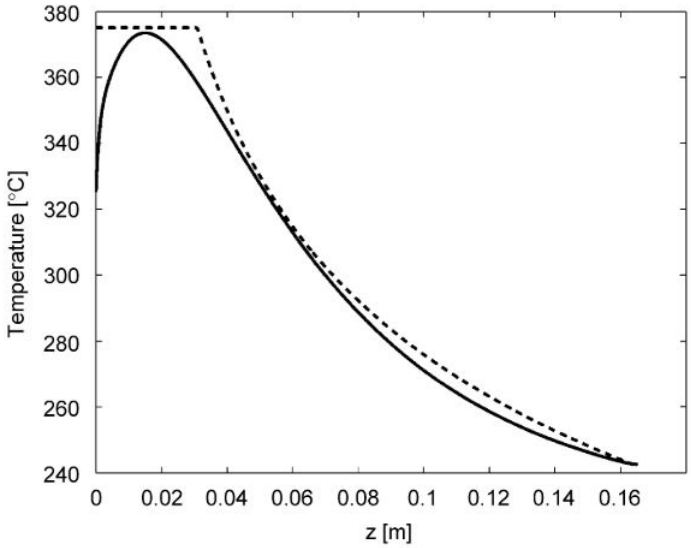

Figure 2.11: Comparison of simulated reaction (solid line) and optimal reaction (dashed line) in optimized WGS reactor [58]

efficient, requiring the least increase in reactor size in order to optimally exploit the applied temperature gradient [57].

Finally, other studies have focused on attempting to emulate an optimal reaction temperature profile across a microreactor based on the particular inlet composition and catalyst combination used. Baier and Kolb [58] studied how the optimal temperature profile for the WGS reaction can be approximated to a good degree in a single step WGS reactor by controlling the temperature in a counter flow microreactor. An optimal reaction temperature profile was developed using equation 2.6 and then modified to not exceed a maximum temperature to avoid harming the catalyst. By adjusting the coolant flow rate, coolant inlet temperature, and reactor length while keeping the number of channels and channel cross-sectional area constant, Baier and Kolb were then able to optimize the efficiency of the reactor. This optimization process resulted in the the reaction temperature profile shown in Figure 2.11 and the reaction CO mole fraction profile shown in Figure 2.12.

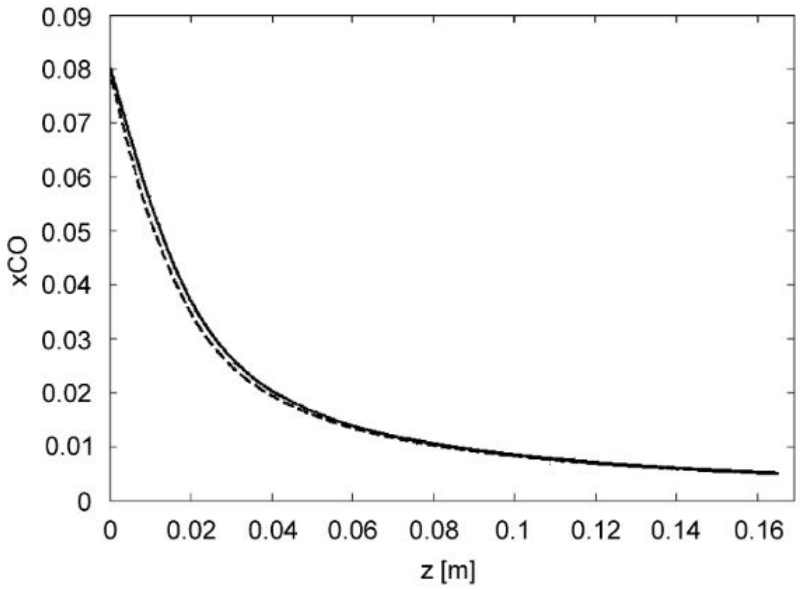

Figure 2.12: Simulated reaction (solid line) and optimal reaction (dashed line) CO mole fraction across reactor [58]

Examining Figure 2.11, it can be seen that the largest deviation between the simulated and optimal temperature profiles occurs near the inlet of the reactor, but after a length of approximately 24% the total reactor length, the temperature profiles become similar for the remaining length of the reactor. The deviations in the temperature profiles minimally affect the reactor CO conversion, with the optimal reactor only being approximately 12% shorter than the simulated reactor to achieve an outlet mole fraction of 0.5% CO and mole fraction of CO across the simulated reactor being nearly identical to the mole fraction of CO across the optimal reactor, as shown in Figure 2.12 [58].

Table 2.2: Parameter ranges to achieve 85% CO conversion for air coolant [56]

Parameter	**Parallel**	**Counter Flow**
Thermal Conductivity [W/m-K]	0.006-0.3	0.015-200
Heat Exchange Fluid Temperature [K]	298-496	472-592
Heat Exchange Fluid Fluid Velocity [m/s]	0.39-4.8	0.43-12
Reactant Temperature [K]	621-710	540-710
Reactant Velocity [m/s]	0.245-0.41	0.245-0.41

2.5.2 Microreactor Parametric Studies

Studies examining how varying process and reactor parameters will affect WGS microreactor performance have been conducted by several authors. Kim et al. [56] simulated a single microreactor channel and evaluated how varying reactor parameters, including reactor material thermal conductivity, reaction and coolant inlet temperatures, and reaction and coolant flow velocities and compiled the results for both parallel flow and counter flow operating modes. Kim et al. concluded that there were appropriate operating ranges for each of these parameters to achieve higher than 85% CO conversion across the reactor for both parallel and counter flow configurations for the reaction composition considered with air as the coolant. These values are summarized in Table 2.2, adapted from [56].

Based on the thermal conductivity ranges for the parallel and counter flow configurations shown in Table 2.2, Kim et al. conclude that the counter flow configuration can tolerate a much wider range of thermal conductivities while still achieving at least 85% CO conversion. As a result, they also conclude that the counter flow configuration lends itself much more to being manufactured out of standard high temperature materials such as stainless steel and Inconel compared to the parallel flow configuration, which would require a very low conductivity reactor material [56].

Based on the reactant inlet temperature ranges reported in Table 2.2, Kim et al. conclude that parallel flow reactors have a higher, narrower range of acceptable temperatures than

the counter flow reactor. The lower sensitivity of the counter flow orientation to changes in inlet temperature is desirable for microreactor design [56]. The acceptable range of reaction flow velocities for both the parallel flow and counter flow configurations are reported to be identical, suggesting similar behavior between the two configurations when the reactant flow is varied, at least for the CO conversions considered.

Based on the heat exchange fluid inlet temperature ranges reported in Table 2.2, Kim et al. conclude that a lower, wider range of acceptable temperatures is observed for the parallel flow configuration than for the counter flow configuration. The lower heat exchange temperatures required for the parallel flow configuration suggest the potential for higher thermodynamic reactor efficiency and easier heat capture from the reaction [56]. Conversely, the parallel flow configuration is more sensitive to the velocity of the heat exchange fluid than the counter flow configuration is, suggesting that more sensitive flow control is required for parallel flow reactors than counter flow reactors [56].

Kim et al. also investigated the effect of coolant type on reactor performance by simulating liquid water as the coolant as opposed to air. For a reactor cooled with liquid water, they found that flow velocity and coolant inlet temperature have little effect on the reactor CO conversion and a phase change in the water coolant stream is possible at high coolant inlet temperatures and low coolant flow rates. They also conclude that the reactor thermal conductivity needed to maintain high conversion levels needs to be below approximately 0.005 W/m-K for both the parallel and counter flow configuration with the conversion dropping off sharply as the reactor wall thermal conductivity increases [56]. This acts as a restrictive condition that is difficult to meet, making using water as a coolant difficult practically.

Finally, Kim et al. investigated the effect of the reactor wall thickness on CO conversion. The results indicated that wall thickness has little influence on the CO conversion, suggesting

that the wall thickness of these reactors should be reduced as much as possible to decrease the overall reactor size as part of a larger hydrogen fuel cell process intensification effort [56].

Based on the results of all their simulations, Kim et al. conclude that the counter flow microreactor configuration is preferable to the parallel flow configuration when using air coolant due to the much wider range of acceptable thermal conductivities that the reactor can be while still maintaining high CO conversion. This allows the microreactor to be made from traditional engineering materials, lowering costs and improving manufacturability. They also conclude that compared to conventional packed-bed reactors, microreactors with integrated cooling can be significantly more compact, requiring less than 50% of the catalyst required to achieve a CO conversion of 90% [56].

As part of their own WGS microreactor simulations, Bac et al. performed similar parametric studies to the ones conducted by Kim et al., varying the reaction inlet temperature, coolant inlet temperature, wall thickness, and reactor wall material in their own model to observe the effect on CO conversion. As shown in Figure 2.13, they found CO conversion to be strongly dependent on reaction inlet temperature for the range of values considered. CO conversion initially increases as the reaction inlet temperature increases from 565 K to 595 K, but then decreases as the reaction becomes equilibrium limited for the higher inlet temperature conditions simulated [54]. The effect of inlet coolant temperature on reactor CO conversion in Figure 2.13 is shown to be limited for the range of coolant inlet temperatures considered, which range in values from 10 K below the reaction inlet temperature to 20 K below the reaction inlet temperature, with very little variation in CO conversion observed for each reaction inlet temperature considered. The influence of the coolant inlet temperature becomes more pronounced at larger inlet temperature differences, however.

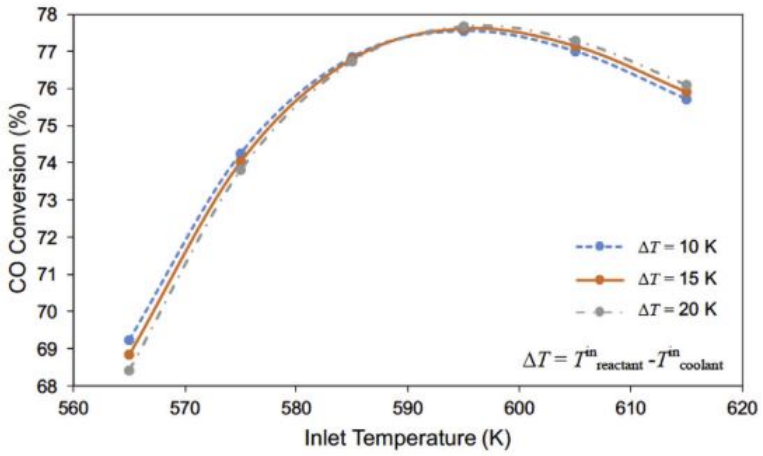

Figure 2.13: Bac et al. parametric studies on reaction and coolant inlet temperatures [54]

As shown in Figure 2.14, varying the reactor wall thickness was found to have a minor effect on the reactor temperature distribution, with a maximum variation in temperature of less than 2 K observed, and a similarly minor effect on the CO conversion. However, Bac et al. note that thicker reactor walls were found to have a more uniform temperature distribution due to the larger influence of axial conduction and the more uniform nature of the cooling over the entire reaction channel [54].

Finally, as shown in Figure 2.15, varying the reactor material between 316 SS, aluminum, and cordierite changed the temperature distribution of the reaction channel due to the varying reactor effectiveness at transferring heat away from the reaction stream. The aluminum reactor was able to operate nearly isothermally due to its high thermal conductivity, but both the 316 SS and cordierite reactors operated with noticeable hot spots due to their lower thermal conductivities and comparably lower axial conduction. Still, although hot spots are present for the simulated materials with lower thermal conductivity, no significant impact on CO conversion was reported as these temperature variations were limited to under 5 K [54].

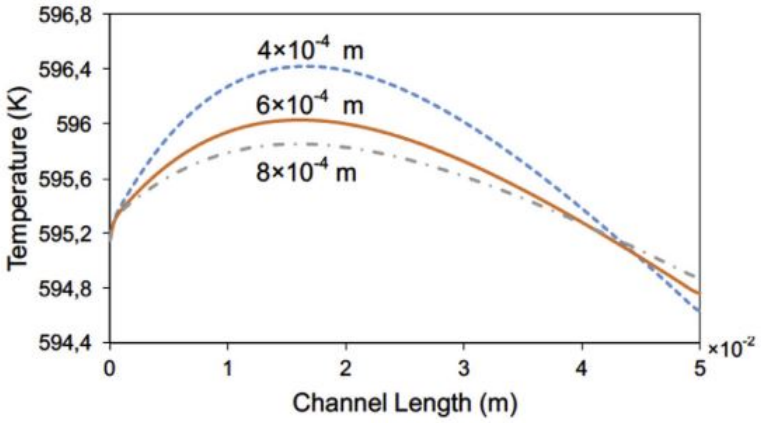

Figure 2.14: Bac et al. parametric study on reactor wall thickness [54]

Although the simulations in this study suggest that wall thickness and reactor material have a limited impact on reactor behavior at the operating conditions specified, further simulations suggest that reactor performance can be improved by using thicker walls to separate the reaction and coolant channels and by manufacturing the reactor out of materials with higher thermal conductivities. Preliminary sizing studies suggest that reactors with integrated cooling can produce the same throughput of hydrogen gas as adiabatic packed-ped reactors over a significantly reduced amount of catalyst [54].

2.6 Additive Manufacturing of Chemical Reactors

The advancement in additive manufacturing technologies over the past few decades has spurred interest in its use in the manufacturing of reactor systems, including chemical reactors and structured catalysts. Capel et al. [59] reviewed the use of AM processes for the production of reactor systems, focusing on stereolithography (SL), selective laser melting (SLM), selective laser sintering (SLS), fused deposition modeling (FDM), and multi-jet modeling (MJM), a variation of polyjet/inkjet printing utilizing several print

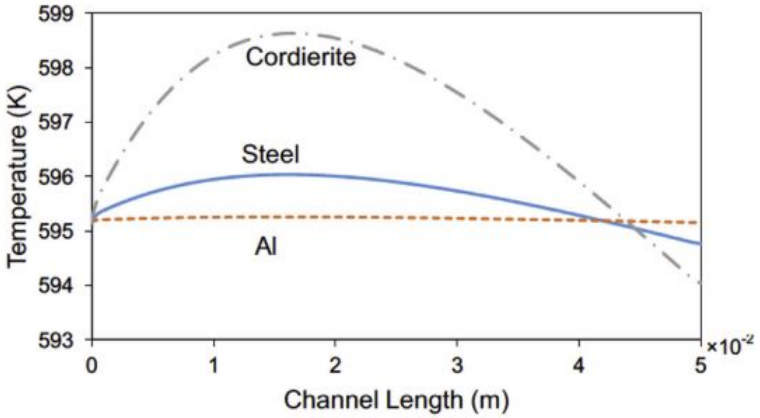

Figure 2.15: Bac et al. parametric study on reactor material [54]

heads. A number of the characteristics, advantages, and disadvantages of each of the AM processes that Capel et al. considered are listed in Table 2.3, taken from [59]. Capel et al. noted that while there are a number of prospective advantages to using AM processes to make microreactors, including the creation of complex internal geometries to enhance reaction mixing and reductions to both build time and cost in many cases, there are a number of hurdles that still need to be overcome, including limited material choices, poor printing resolution and surface finishes on parts, and the poor part mechanical and chemical properties that can result from these factors.

Cronin et al. [60] note that although the realization of configurable microscale fluidic devices through AM processes has long been an appealing idea, the existing resolution limitations with these processes have restricted the use of AM processes for this application. Although such resolution limitations exist at the micro scale, Cronin et al. demonstrate that similar milli-fluidic scale devices made from polypropylene can readily be achieved using an FDM process at very low material costs and manufacturing times. Experiments showed that the printed reactor is compatible with certain organic and inorganic chemical reactions.

The low cost and fast manufacturing of the reactor also allowed for a significant amount of iteration and fine-tuning to improve performance. A second study by Cronin et al. [61] further noted the chemical compatibility issues present with many of the current materials available for use with AM processes and the issues that arise trying to produce very small reaction channels using powder based AM processes due to difficulties with removing the unsolidified powder from the reactors. The study goes on to give a detailed procedure on how to print one such milli-fluidic reactor using FDM, outlining important considerations for CAD modeling, material choice, printer choice, and printing stages of this process and offering several troubleshooting suggestions for common issues encountered during FDM build processes.

Table 2.3: Comparison of different additive manufacturing processes [59]

AM Technique	**Materials**	**Chemical Stability**	**Thermal Stability**	**Design Limitations**	**Achievable Build Resolutions**
FDM	Thermoplastics ABS,PC,ULTEM	FDM materials range in chemical stability, however typically the ester linkages polymers like PC and ULTEM are susceptible to chemical degradation.	FDM materials range in thermal stability. ABS has a high glass transition temperature of 220 °C, whereas PC has a lower glass transition temperature of 147 °C.	Removal of support structures can be difficult from complex internal geometries. External support removal is simplistic.	Generally acceptable, with build resolutions of ± 0.3 mm possible. Needs support structures for smaller geometries.
SLS	Typically polymers such as NYLON-11 and 12, PP, PEEK, and some experimental ceramics.	Amide linkages of polymers such as NYLON-12 are susceptible to strong bases and nucleophiles. PEEK is a material widely used in flow chemistry	Wide ranging but generally stable at high temperatures. The most frequently used NYLON-12 has a heat deflection temperature of 177 °C at 66 psi.	Powder recycling and clean-up can be time consuming. Removal of un-sintered powder can be complex.	Comparable or even slightly better than FDM, with build resolutions of ± 0.2 mm possible.
SL	UV Curable Polymers, typically acrylate or epoxy backboned.	Poor chemical stability, significant degradation and swelling in stronger solvent systems due to weak epoxy and acrylate backbones	Huge range of SLA materials available, however generally very poor. Accura 60 has a low glass transition temperature of 58 °C. Accura Bluestone marketed as a high temperature material has a glass transition temperature of 83 °C.	Clean-up of un-cured resin from channels can be achieved easily with a compressed air line or pump. Secondary UV cure is also necessary.	Excellent, with build resolutions of less than ± 0.1 mm possible.
SLM	Steel, titanium, aluminum, etc.	Highly stable metal oxide layers make SLM parts chemical resistant to a wide range of chemical reagents	Thermally stable to extremely high temperatures. Aluminium is stable up to its melting point of 660 °C and titanium has a melting point of around 1660 °C	Removal of external support structures can be difficult. Often requires heavy duty machinery such as angle grinders. Part may also require polishing to achieve acceptable surface smoothness.	Excellent, with build resolutions of less than ± 0.1 mm possible. However, often requires more build process optimisation than other techniques.
MJM	UV Curable Polymers, typically acrylate or epoxy backboned.	Poor chemical stability, significant degradation and swelling in stronger solvent systems due to weak epoxy and acrylate backbones	Like SLA materials, MJM materials have poor thermal stability; however there are more limited material options.	Clean-up of un-cured resin from channels can be achieved easily with a compressed air line or pump. Secondary UV cure is also necessary.	Excellent, with build resolutions of less than ± 0.1 mm possible. Potentially slightly more accurate than SL systems.

Parra-Cabrera et al. [17] similarly identify extrusion based methods like FDM, powder based methods such as SLS and SLM, SL, and IJP as AM processes that can significantly impact the design of microreactors and structured catalysts, citing similar advantages and disadvantages to the ones stated by Capel et al. They go on to state that the possibilities associated with the ability to manufacture geometrically optimized reactors for an application using AM processes are a significant attraction. While the design of conventional reactors is often driven more by the costs and limitations associated with conventional manufacturing methods, AM processes are often not restricted in the same way and can potentially be used to fabricate geometrically optimized microreactors for specific chemical processes. Although the examples of such flow reactors are primarily confined to experimental settings, Parra-Cabrera et al. expect the use of these additively manufactured reactors to become more widespread over time due to both the possibility for more optimal reactor performance and the AM design process lending itself to a much more integrated approach to the design, modeling, manufacturing, and testing of chemical reactors.

2.7 Literature Review Summary and Research Emphasis

The information presented in this literature review generally outlines the work that has been previously done in the area of characterizing the water-gas shift reaction in terms of its thermodynamics and kinetics, demonstrates how microreactors can improve the performance of the water-gas shift reaction beyond what packed bed reactors are capable of, discusses the work that other groups have done in terms of characterizing the performance of the water-gas shift reaction in microreactors, and discusses the current state of additive manufacturing as it pertains to microreactor manufacturing. The information presented in Sections 2.1 through 2.5 informed the modeling approach taken during this study, which

is presented in Chapter 3. Similarly, the information presented in Section 2.6 informed the prototyping effort presented in Chapter 5 by helping me identify the most viable additive manufacturing method to implement for this study and the potential design and manufacturing challenges that would need to be addressed during this process.

The studies performed by other groups presented in Sections 2.5 encompass a considerable amount of work in the modeling and development of differential temperature water-gas shift microreactors and clearly demonstrate the capability of these systems to enhance conversion beyond what the standard HTS/LTS packed bed reactor systems are capable of. While these studies alone are useful from a component design perspective, they are all specified in terms of a fixed inlet condition and performed without consideration of the broader system impacts that differential temperature WGS reactor might have on the overall steam reforming process. No notable studies in the literature examine this. Furthermore, while there is broad consideration for how additive manufacturing can be used to manufacture microreactors, there is no study examining its potential application to the WGS reaction specifically. This study expands upon previous works into these areas by developing a component level model of a differential temperature WGS reactor operating under an optimal temperature profile, designing, manufacturing, and experimentally verifying the performance of an additively manufactured WGS microreactor prototype based on this component model, and implementing a simplified version of this model into a full flowsheet model of the steam reforming process to evaluate the economic benefits of differential temperature WGS reactors when considered in the broader context of actual industrial operation, to evaluate how optimal system operation is affected by the integration of a differential temperature WGS reactor, and to evaluate how this approach can better inform the operating conditions that these reactors should be designed for.

Chapter 3: Model Development

This chapter describes the modeling methodology used to quantify the baseline performance of an idealized high temperature shift and low temperature shift packed bed reactor system, to quantify the performance of a differential temperature water-gas shift microreactor that can be made using additive manufacturing, and to develop an optimal temperature progression for the water-gas shift reaction to follow within the developed microreactor model.

All of the models in this section were developed assuming a platinum based catalyst, due to the general emergence of platinum based catalysts as the front runners among the WGS catalysts available for fuel cell applications, as detailed in Section 2.2.1.3. This includes the HTS and LTS reactor baseline models, which would generally use ferrochrome and copper-zinc catalyst respectively, to better facilitate comparison with the differential temperature approach. The Langmuir-Hinshelwood kinetic expression developed by Germani and Schurrman [44] (equation 2.5) for a $Pt/CeO_2/Al_2O_3$ catalyst was used to predict the reaction rate. This expression is multiplied by the catalyst density, ρ_{cat}, to convert the rate expression from a per mass basis to a per volume basis. For the packed bed reactors, a bulk catalyst density of $\rho_{cat} = 700\ kg/m^3$ taken from Ding and Chan [47] for platinum coated alumina pellets is used. For the microreactor models where the catalyst is coated on the channel walls, a catalyst density of $\rho_{cat} = 1450\ kg/m^3$, taken from Germani and Schuurman [44] is used. The bulk catalyst density of the packed bed is significantly lower than the microreactor catalyst density due to the significantly lower packing efficiency of the catalyst pellets compared to the microreactor coating. The WGS equilibrium expression

developed by Moe [20] (equation 2.1) was used as part of this reaction rate expression and to determine the extent to which the reaction would proceed.

3.1 Baseline HTS/LTS Packed Bed Reactor Model

As discussed in Sections 1.2, 1.3, and 2.4, the water-gas shift reaction is typically performed sequentially in an adiabatic high temperature shift packed bed reactor followed by an adiabatic low temperature shift packed bed reactor in industry. These reactors are separated by an intercooler to reduce the temperature of the HTS outlet stream before it enters the LTS reactor by approximately 200-250 °C, as shown in Figure 3.1. The inlet composition and process conditions corresponding to Figure 3.1 are listed in Table 3.1. These conditions are taken from on ongoing work at Oregon State University researching ways of intensifying the distributed production of hydrogen via the natural gas reforming process.

Figure 3.1: Simplified schematic of HTS/LTS WGS process

Table 3.1: HTS and LTS process conditions used in modeling

Parameter	**Value**
Mass Flow Rate, $\dot{m}$	2.525 g/s
HTS Inlet Temperature, T_1	350 °C
HTS Inlet Pressure, P_1	5.0 bar
HTS Inlet Mole Fraction CO, $y_{CO,1}$	0.113
HTS Inlet Mole Fraction H_2O, $y_{H2O,1}$	0.244
HTS Inlet Mole Fraction CO_2, $y_{CO2,1}$	0.052
HTS Inlet Mole Fraction H_2, $y_{H2,1}$	0.546
HTS Inlet Mole Fraction CH_4, $y_{CH4,1}$	0.045
HTS Outlet Pressure. P_2	5.0 bar
LTS Inlet Temperature, T_3	200 °C
LTS Inlet Pressure, P_3	5.0 bar
LTS Outlet Pressure, P_4	5.0 bar

Both the HTS and LTS packed bed reactors in Figure 3.1 are modeled as plug flow reactors (PFR). Although plug flow reactors are an idealization of the actual process occurring, they are useful for developing a conservative estimate of the total required reactor volume in the HTS/LTS configuration. In the context of the process being simulated, the use of plug flow relations assumes the following:

- Steady state flow conditions
- Constant, uniform fluid velocity across the entire cross section of the reactor and through the entire length of the reactor
- Perfect radial mixing such that there is no variation in properties in the radial direction

- Negligible mass transfer by diffusion in the axial direction
- Negligible diffusion resistance into and out of the catalyst pellets
- Negligible heat transfer by conduction in the axial direction
- Negligible heat transfer away from the reaction stream
- The presence of the catalyst particles negligibly influences the heat transfer process
- No work is done by or on the reaction stream
- Negligible changes in the potential or kinetic energies of the reactor
- Negligible pressure drop across the reactor
- The reaction stream can be modeled as an ideal gas mixture

The implementation of these assumptions simplifies analysis considerably, removing the need for detailed fluid flow characterization and reducing both the mass transfer and heat transfer analyses to 1-D problems where the concentration of each species and the process temperature vary only in the axial direction. The rest of this section details the mass transfer and heat transfer PFR relations developed and then discusses the solution method used to evaluate the HTS/LTS reactor performance.

3.1.1 Plug Flow Reactor Mass Transfer

Figure 3.2 shows a simplified schematic of the PFR mass transfer process. As shown, only the advective mass transfer terms into and out of the reactor and the reaction rate term are considered. A differential mass balance on the reactor for each species can thus be reduced to the following ordinary differential equation:

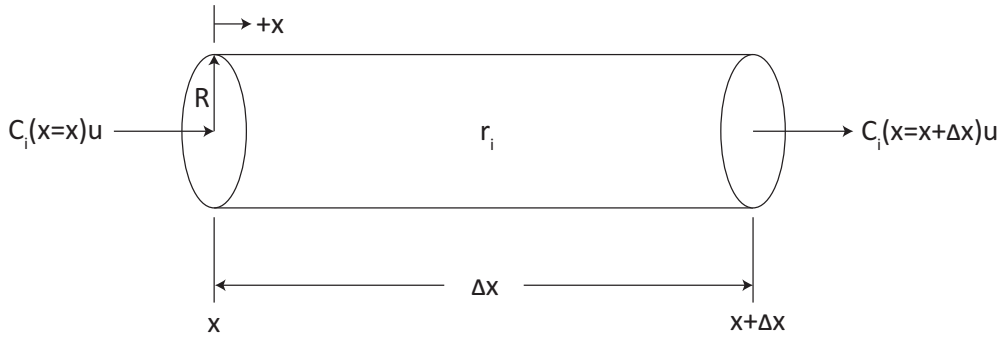

Figure 3.2: Plug flow reactor mass balance

$$\mathbf{u}\frac{dC_i}{dx} = r_i \tag{3.1}$$

In equation 3.1, $\mathbf{u}$ is the flow velocity, C_i is the concentration of species i, x is the distance in the axial direction of the reactor, and r_i is the generation/disappearance rate of species i determined from the reaction rate expression (equation 2.5). r_i is negative for the reactant species consumed by the reaction and positive for the product species generated by the reaction. r_i is dependent on the reaction temperature and the partial pressures of each species participating in the reaction. The reaction temperature is evaluated from the PFR energy balance discussed in Section 3.1.2 and the partial pressure of each chemical species can be evaluated using Dalton's law of partial pressures as:

$$\begin{aligned} P_i &= y_i P \\ P &= \sum_{i=1}^{n} P_i \end{aligned} \tag{3.2}$$

From the partial pressure of each chemical species calculated using Dalton's law, the concentration of each species can then be determined using the ideal gas law as:

$$C_i = \frac{P_i}{RT} \tag{3.3}$$

3.1.2 Plug Flow Reactor Heat Transfer

Figure 3.3 shows a simplified schematic of the PFR heat transfer process. As shown, only the enthalpy terms into and out of the reactor and the heat generation term due to the exothermic reaction are considered. A differential energy balance on the reactor can thus be reduced to the following ordinary differential equation:

$$\rho_m c_{p,m} \mathbf{u} \frac{dT}{dx} = -\Delta H_{rxn} r \tag{3.4}$$

In equation 3.4, ρ_m is the gas mixture density, $c_{p,m}$ is the gas mixture specific heat at constant pressure, ΔH_{rxn} is the heat of reaction for the WGS reaction, and r is the reaction rate. The term $-\Delta H_{rxn} r$ represents the generation of heat for exothermic reactions, which have negative heats of reaction, or the consumption of heat for endothermic reactions, which have positive heats of reaction. To evaluate the mixture properties, the following relationships for ideal gas mixtures are used:

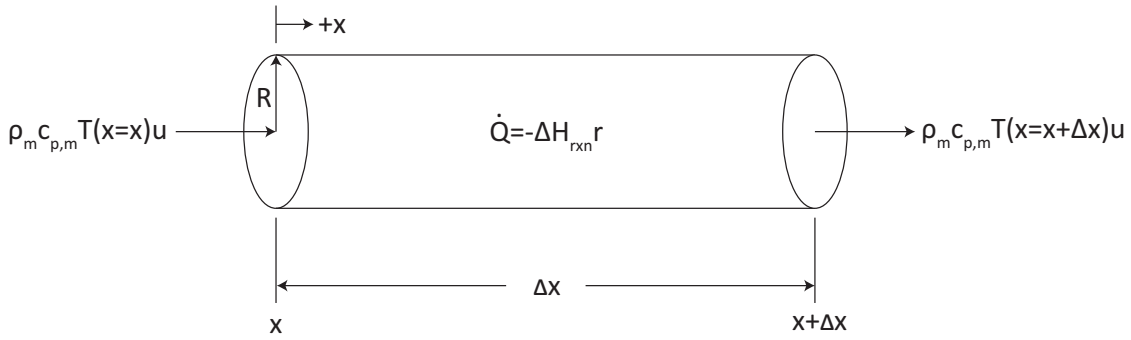

Figure 3.3: Plug flow reactor energy balance

$$\rho_m = \frac{P\bar{M}}{\bar{R}T} \tag{3.5}$$

$$c_{p,m} = \sum_{i=1}^{n} w_i c_{p,i} \tag{3.6}$$

In equation 3.5, $\bar{M}$ is the average molar mass of the gas mixture. In equation 3.6, w_i is the mass fraction of species i. The gas mixture average molar mass and the mole and mass fractions of the gas mixture can be related to each other through the following equations:

$$\bar{M} = \sum_{i=1}^{n} y_i M_i \tag{3.7}$$

$$w_i = y_i \frac{M_i}{\bar{M}} \tag{3.8}$$

3.1.3 Plug Flow Reactor Solution Process

Examining equations 3.1 and 3.4, it can be seen that they are coupled and must be solved simultaneously to obtain the axial concentration and temperature profiles across a single reactor. Equations 3.1 through 3.8 along with equations 2.1 and 2.5 represent a fully defined system of equations that can be used to evaluate the change in concentration of each species and the change in process temperature across a PFR for a given set of inlet conditions in the axial direction. These equations were solved numerically using a MATLAB script to evaluate the equilibrium conversion of each reactor and equilibrium volume of both the HTS and LTS reactors. The heat rejection from the reaction stream as it passes through the intercooler can be evaluated from an energy balance as:

$$\dot{Q}_{WGS} = \dot{m} c_{p,m} (T_2 - T_3) \tag{3.9}$$

In equation 3.9, $c_{p,m}$ is evaluated at the average temperature across the intercooler and for the HTS outlet composition obtained from the developed PFR model. The MATLAB script used to solve this system is presented in Appendix A for reference.

Although the PFR model considerably simplifies analysis, it neglects a number of effects which can potentially impact reactor performance. Notably, neglecting the resistance to diffusion into and out of the catalyst pellets overestimates the apparent reaction rate through these reactors significantly. In reality, for this assumption to be valid, the catalyst pellets would have to be much smaller than what would generally be commercially available to minimize their resistance to mass transfer. The use of such a catalyst would result in significant pressure drop across these reactors, however, making them inappropriate for industrial use. As a result, the packed bed reactor models developed in this section represent the upper limit of performance for the HTS/LTS reactor configuration and are thus a conservative baseline for the evaluation of the volume reduction possible using microreactors.

3.2 Baseline 2-D Microreactor Channel Model

As discussed in Sections 1.4 and 2.5, microreactors have been proposed as an alternative reactor style to the traditional HTS/LTS packed bed reactors and been shown to enhance WGS CO conversion for a variety of operating conditions and microreactor designs. In the context of this study, microreactors present the possibility of significantly reducing the volume of traditional WGS reactor systems by consolidating the system from three separate components (two reactors and an intercooler) into a single device that achieves the

same result more efficiently and reducing the reactor volume necessary to achieve a certain conversion level. In the interest of developing a more detailed model that can be used to evaluate the influence of integrated cooling on the WGS reaction in microreactors and to ultimately serve as a design tool in the development of such a reactor, the PFR model developed in Section 3.1 must be expanded to a two dimensional model (2-D) spatially and include a number of effects that were neglected previously. This changes the list of pertinent assumptions necessary to the formulation of a successful WGS microchannel model to the following:

- Steady state flow conditions
- Laminar flow conditions maintained within the reaction channels
- The reaction can be modeled as 2-D with negligible variation across the width of a single microchannel
- The mass transfer diffusion coefficients for a single component into the rest of the mixture can be evaluated using a mixture-averaged approach
- The occurrence of the reaction and the corresponding heat generation is limited to the catalyst volume within the reactor
- No work is done by or on the reaction stream
- Negligible changes in the potential or kinetic energies of the reactor
- The reaction stream can be modeled as an ideal gas mixture
- Negligible flow maldistribution between the microchannels making up the entirety of the reactor

Notably, assumptions that obviated the need for a rigorous momentum transfer analysis (i.e. constant, uniform fluid velocity and negligible pressure drop) or the consideration of diffusion based effects (i.e. no mass transfer by diffusion or heat transfer by thermal conduction) for the PFR models are relaxed such that these effects are no longer neglected. This section presents the geometry of the microreactor prototype considered in this study and the 2-D microchannel models developed to simplify the analysis of this prototype and develops the equations used to model the transport phenomena within these models. The inlet conditions to the HTS reactor listed in Table 3.1 (T_1, P_1, etc.) are used as the process inlet conditions to the microchannel models except where noted.

3.2.1 2-D Microreactor Model Geometry

The geometries of the 2-D models developed in this study take separate forms depending on whether the temperature progression of the reaction is controlled via external boundary conditions or through the integration of a secondary coolant fluid and whether the reaction temperature is actively managed over the entire length of the channel or if an adiabatic inlet length is specified. If the model is run using either a prescribed wall temperature or insulation boundary condition, the 2-D microchannel geometry shown in Figure 3.4 is used. This geometry consists of a single microchannel of length L and height H . Although not shown in the schematic, the microchannel is also of width W into the page. Thin layers of catalyst of height H_{cat} are deposited onto the upper and lower surfaces of the microchannel. For prescribed boundary condition models, separate adiabatic and wall temperature conditions can be applied, allowing for the development of the adiabatic inlet condition previously specified.

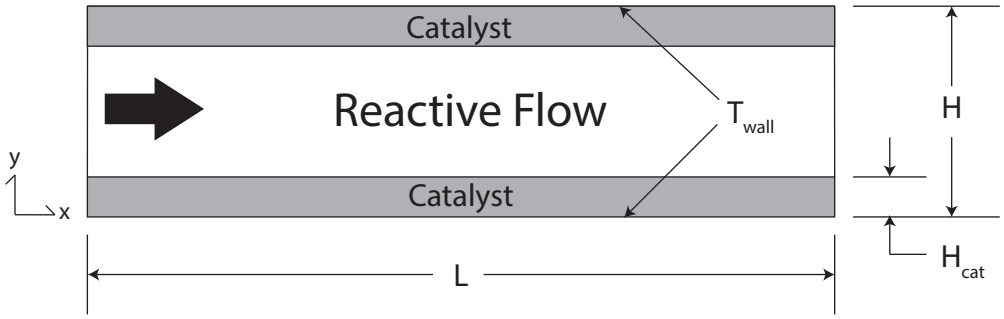

Figure 3.4: Prescribed boundary conditions microchannel geometry

For more realistic models which include the influence of coolant channels, the geometry shown in Figure 3.5 is used. This geometry consists of a "unit cell", or the smallest repeating structure, of the microreactor with applied symmetry boundary conditions. This consists of half of a reaction channel, half of a coolant channel, and the reactor wall separating the channels. This model is the same length L and width W as the 2-D model shown in Figure 3.4, but only includes half of the height of each channel (H and H_c). The reactor wall separating the channels is a height of H_w. For geometries featuring an adiabatic reaction inlet, the geometry in Figure 3.5 is slightly modified to the geometry shown in Figure 3.6, where a length L_u at the reaction channel inlet is not actively cooled.

The values listed in Table 3.2 are used as the baseline condition for the geometries of these 2-D models. For models featuring an adiabatic reaction inlet without active cooling, the uncooled length L_u is specified on a model by model basis depending on the inlet condition to the reactor. The baseline microreactor prototype considered consists of 200 reaction channels and 200 coolant channels with walls made from Inconel 718 and air used as the coolant fluid. As mentioned previously, it is assumed that there is negligible flow maldistribution between these channels such that inlet reaction and coolant streams to the device split evenly between all of the channels.

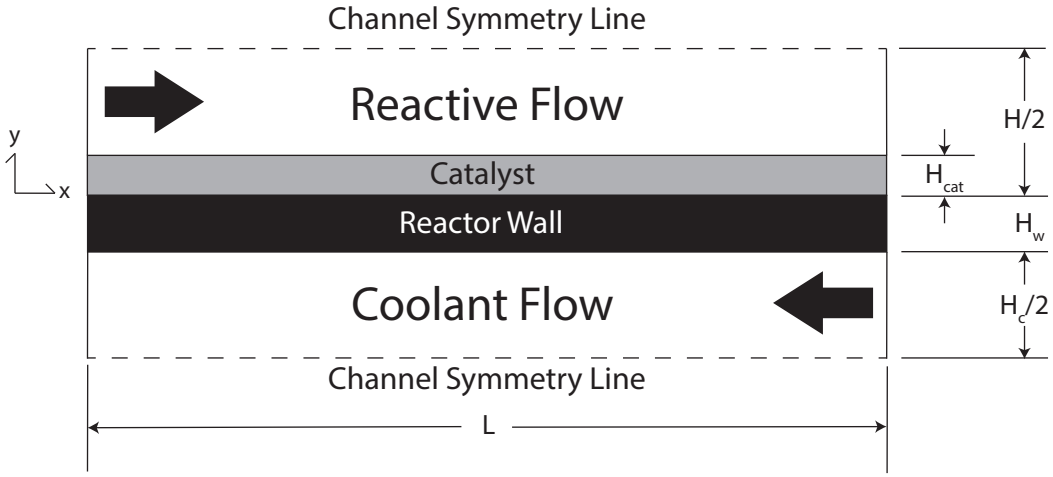

Figure 3.5: Integrated coolant channel microchannel geometry

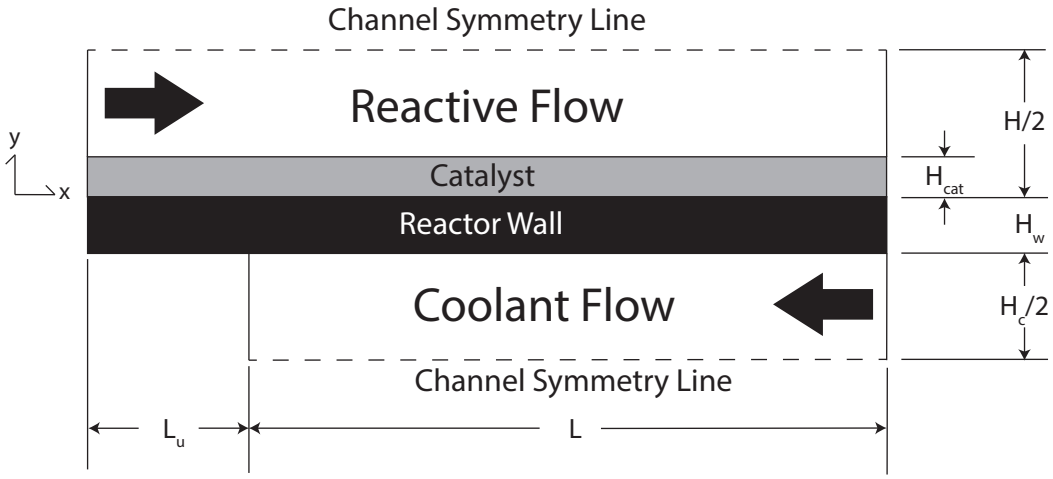

Figure 3.6: Integrated coolant channel microchannel geometry without applied cooling at reaction inlet

Table 3.2: 2-D model baseline parameters

Parameter	Value
Reaction Channel Length, L	200 mm
Reaction Channel Height, H	1 mm
Reaction Channel Width, W	80 mm
Catalyst Layer Height, H_{cat}	0.05 mm
Coolant Channel Height, H_c	0.5 mm
Reactor Wall Thickness, H_w	0.5 mm
Number of Reaction Channels, N_r	200
Number of Coolant Channels, N_c	200

3.2.2 2-D Microreactor Momentum Transfer

As mentioned in Section 3.1, the use of PFR relations obviates the need for a detailed momentum transfer analysis as the model assumes a constant, uniform velocity profile and negligible pressure drop through the reactor. By expanding to a 2-D reactor model that include these effects, the variation in flow velocity and pressure drop through both the open channel and porous catalyst phases of the reactor must be modeled, as shown in Figure 3.7.

In the open channel phase of a reaction channel, a general form of the Navier-Stokes equations for the compressible flow of a gas with varying viscosity is used to characterize the velocity profile and and pressure drop of the flowing reaction stream. For the 2-D model developed, this form of the Navier-Stokes equations is:

$$\rho_m(\mathbf{u}\cdot\nabla)\mathbf{u} = -\nabla P\mathbf{I} + \nabla\cdot(\mu_m(\nabla\mathbf{u} + (\nabla\mathbf{u})^T) - \frac{2}{3}\mu_m(\nabla\cdot\mathbf{u})\mathbf{I}) \tag{3.10}$$

In the porous catalyst phase of the reaction channel, the effect that the catalyst has on the gas flow must be considered. This is done using the Brinkman equations, which are used to model moderate velocity fluid flows through porous media. In addition to the terms considered in the Navier-Stokes equations, the Brinkman equations also account for the dissipation of kinetic energy due to viscous shear in the porous media, which results in

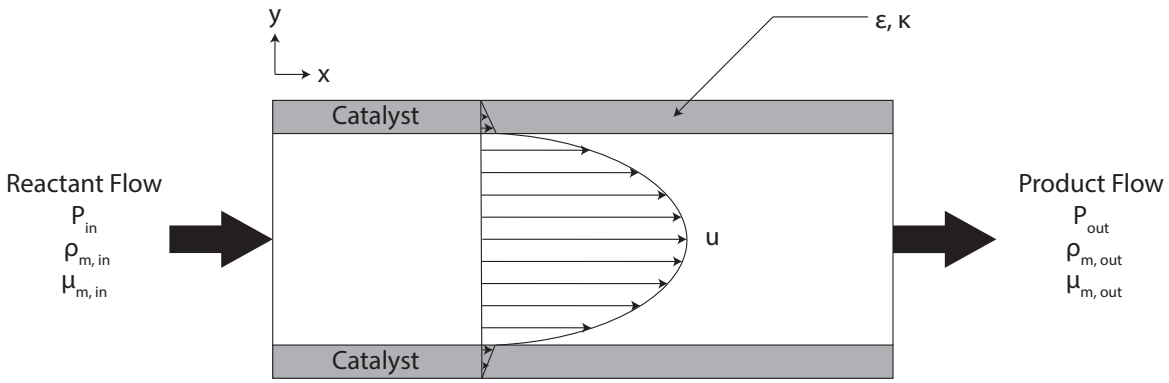

Figure 3.7: 2-D reaction channel model momentum transport

higher pressure drops and lower flow velocities through the catalyst, as visually indicated in Figure 3.7. For the 2-D model developed, the form of the Brinkman equations used is:

$$\frac{1}{\epsilon}\rho_m(\mathbf{u}\cdot\nabla)\mathbf{u}\frac{1}{\epsilon} = -\nabla P\mathbf{I} + \nabla\cdot(\frac{\mu_m}{\epsilon}(\nabla\mathbf{u}+(\nabla\mathbf{u})^T) - \frac{2}{3}\frac{\mu_m}{\epsilon}(\nabla\cdot\mathbf{u})\mathbf{I}) - \frac{\mu_m}{\kappa}\mathbf{u} \tag{3.11}$$

In both equations 3.10 and 3.11, μ_m is the gas mixture dynamic viscosity and P is the fluid pressure. In equation 3.11, ϵ is the catalyst porosity and κ is the catalyst permeability. The catalyst porosity indicates the unoccupied space within the catalyst and the permeability is a measure of how easily a fluid can pass through the catalyst phase. To evaluate the mixture dynamic viscosity, the following relationship developed by Wilke [62] is used:

$$\mu_m = \sum_{i=1}^{n} \frac{\mu_i}{1 + \frac{1}{y_i} \sum\limits_{\substack{j=1 \\ j \neq i}}^{n} y_j \phi_{i,j}}$$
$$\phi_{i,j} = \frac{\left(1 + \left(\frac{\mu_i}{\mu_j}\right)^{0.5} \left(\frac{M_j}{M_i}\right)^{0.25}\right)^2}{\left(\frac{4}{\sqrt{2}}\right)\left(1 + \frac{M_i}{M_j}\right)^{0.5}} \tag{3.12}$$

In equation 3.12, μ_i and μ_j are the dynamic viscosities of components i and j, respectively, and $\phi_{i,j}$ is a dimensionless parameter developed by Wilke for this equation.

The void fraction of the catalyst is assumed to be $\epsilon = 0.4$, a typical value for catalysts, and the catalyst permeability is evaluated using the following expression:

$$\kappa = \frac{H_{cat}^2}{150} \frac{\epsilon^3}{(1-\epsilon)^2} \tag{3.13}$$

which Bac et al. [54] also used to estimate the permeability of the catalyst layer in their study.

For the models which also include coolant channels, the same general form of the Navier-Stokes equations used to model the momentum transfer within the open channel phase of the reaction channels is also used to model the momentum transfer within the coolant channels:

$$\rho_c(\mathbf{u}_c \cdot \nabla)\mathbf{u}_c = -\nabla P_c \mathbf{I} + \nabla \cdot (\mu_c(\nabla \mathbf{u}_c + (\nabla \mathbf{u}_c)^T) - \frac{2}{3}\mu_c(\nabla \cdot \mathbf{u}_c)\mathbf{I}) \tag{3.14}$$

In equation 3.14, ρ_c is the density of the coolant, $\mathbf{u}_c$ is the velocity of the coolant, P_c is the pressure of the coolant, and μ_c is the dynamic viscosity of the coolant. For all cases considered as part of this study, the coolant is taken as air.

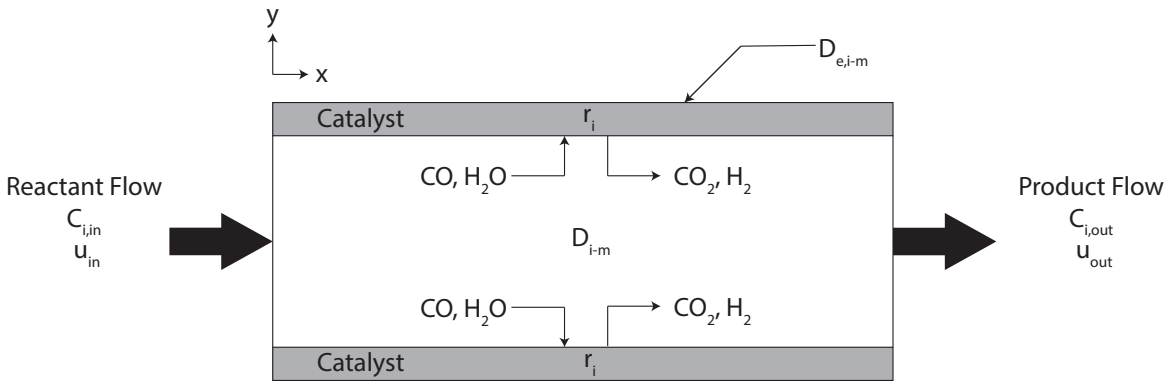

Figure 3.8: 2-D reactor model mass transport

3.2.3 2-D Microreactor Mass Transfer

A simplified schematic showing the 2-D microreactor mass transfer process is shown in Figure 3.8. As shown in Figure 3.8, both the convective and diffusive mass transfer terms into and out of the reactor in both the x and y directions are now considered. Like the momentum transfer process discussed in Section 3.2.2, the mass transfer process through both the open channel and porous catalyst phases must be modeled.

In the open channel phase of a reaction channel, a differential mass balance for each species reduces to the following partial differential equation:

$$\nabla \cdot (D_{i-m} \nabla C_i) - \nabla \cdot (\mathbf{u} C_i) = 0 \tag{3.15}$$

In the porous catalyst phase of a reaction channel, the effect that the presence of the catalyst has on the diffusion process must be considered and the occurrence of the chemical reaction must be accounted for as well. As a result, the differential mass balance for each species in the porous catalyst phase reduces to the following partial differential equation, which differs slightly from the mass balance developed for the open channel phase:

$$\nabla \cdot (D_{e,i-m} \nabla C_i) - \nabla \cdot (\mathbf{u} C_i) + r_i = 0 \tag{3.16}$$

In equation 3.15, $D_{i,m}$ is the diffusion coefficient of a species i into the rest of the gas mixture. These mixture diffusion coefficients are evaluated using a mixture averaged approach using the following expression:

$$D_{i,m} = \frac{1 - y_i}{\sum\limits_{\substack{j=1 \\ j \neq i}}^{n} \frac{y_j}{D_{i,j}}} \tag{3.17}$$

Equation 3.17 is used to calculate the diffusion coefficient of species "i" into the rest of the gas mixture consisting of n species as a weighted average of the diffusion coefficient of each species pair, $D_{i,j}$, based on the mixture composition. This approach assumes unimolecular diffusion of species "i" through a stagnant mixture of the other gas components, greatly simplifying the multicomponent diffusion coefficients that can be developed from the Stefan-Maxwell equations, which are a function of both the mixture composition and the molar flux of each species considered. The diffusion coefficient of each species pair $D_{i,j}$ is calculated using the following expression, which is derived using kinetic gas theory:

$$D_{i,j} = 2.6628 \times 10^{-22} \frac{\sqrt{\frac{T^3 (M_i + M_j)}{2 \times 10^3 M_i M_j}}}{P \sigma_i \sigma_j \Omega_D} \tag{3.18}$$

In equation 3.18, σ_i and σ_j are the collision diameters of chemical species i and j from the Lennard-Jones potential and Ω_D is the collision integral from the Lennard-Jones potential. The presence of Knudsen diffusion through the porous catalyst phase is neglected such that the effective diffusion coefficient through the porous catalyst is calculated as:

$$D_{e,i-m} = \epsilon^2 D_{i,m} \tag{3.19}$$

3.2.4 2-D Microreactor Heat Transfer

A simplified schematic showing the 2-D microreactor heat transfer process for a microchannel without external cooling is shown in Figure 3.9. Like the mass transfer process discussed in Section 3.2.3, both convective and diffusive heat transfer terms into and out of the reactor in both the x and y directions are now considered. Like the momentum and mass transfer processes previously discussed, the heat transfer process in both the open channel and porous catalyst phases must be modeled.

In the open channel phase of a reaction channel, a differential energy balance reduces to the following partial differential equation:

$$\nabla \cdot (k_m \nabla T) - \nabla \cdot (\rho_m c_{p,m} \mathbf{u} T) = 0 \tag{3.20}$$

In the porous catalyst phase of a reaction channel, the effect that the presence of the catalyst has on the thermal conduction process must be considered and the heat generation due to the occurrence of the chemical reaction must be accounted for as well. As a result, the differential energy balance for this process reduces to the following partial differential

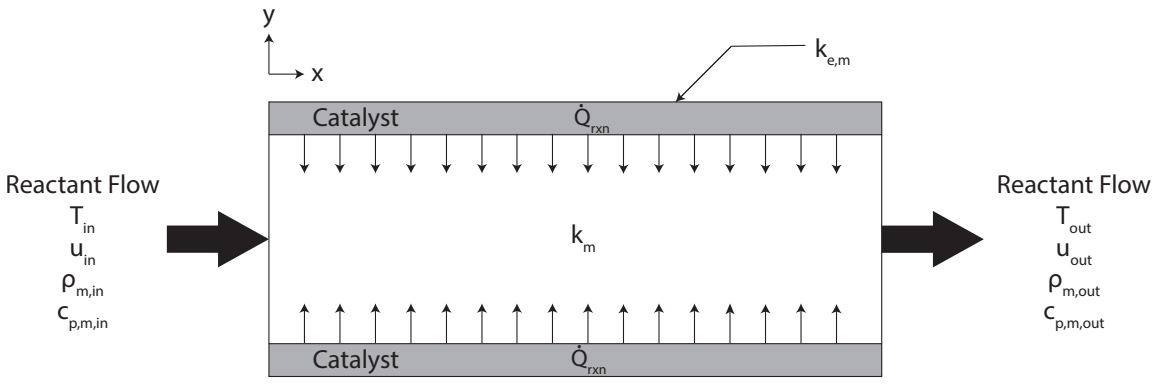

Figure 3.9: 2-D reactor model heat transport without external cooling

equation, which differs slightly from the energy balance developed for the open channel phase:

$$\nabla \cdot (k_{e,m} \nabla T) - \nabla \cdot (\rho_m c_{p,m} \mathbf{u} T) + (-\Delta H_{WGS})(r_{WGS}) = 0 \tag{3.21}$$

In equation 3.20, k_m is the thermal conductivity of the reaction gas mixture. This mixture thermal conductivity is evaluated using the following expression:

$$k_m = \frac{1}{2}\left[\sum_{i=1}^{n} y_i k_i + \left(\sum_{j=1}^{n} \frac{y_j}{k_j}\right)^{-1}\right] \tag{3.22}$$

In equation 3.21, $k_{e,m}$ is the effective thermal conductivity of the porous catalyst phase. The effective thermal conductivity is taken as the volume average of the mixture thermal conductivity, k_m and the solid catalyst thermal conductivity, k_{cat}:

$$k_{e,m} = \epsilon k_m + (1 - \epsilon) k_{cat} \tag{3.23}$$

The catalyst thermal conductivity is assumed to be that of alumina (Al_2O_3), a primary component of the catalyst and treated as a constant value evaluated at the reactor inlet temperature using version 10.644 of Engineering Equation Solver (EES), an equation solving software package with built-in properties for a variety of common materials.

The 2-D heat transfer process for the microchannel with external cooling is slightly different than for the geometry shown in Figure 3.9 as it includes the external coolant and the wall separating the channels, as shown in Figure 3.10. The reaction channel equations developed for the model without external cooling remain the same in this model, but additionally, the heat transfer through the wall separating the reaction and coolant channels and through the coolant channel are modeled. The heat transfer through the wall is by conduction only and is modeled by the general form of the heat equation as:

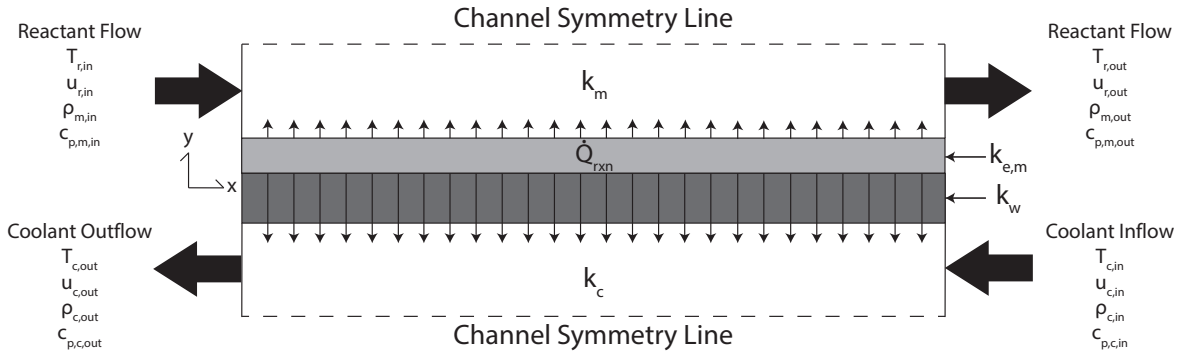

Figure 3.10: 2-D reactor model heat transport with external cooling

$$\nabla \cdot (k_w \nabla T) = 0 \tag{3.24}$$

In equation 3.24, k_w is the thermal conductivity of the wall material. For all cases considered in this study, this is evaluated as the thermal conductivity of Inconel 718 from the property values listed in EES. The differential energy balance in the coolant channel reduces to the following partial differential equation:

$$\nabla \cdot (k_c \nabla T) - \nabla \cdot (\rho_c c_{p,c} \mathbf{u}_c T) = 0 \tag{3.25}$$

where k_c is the thermal conductivity of the coolant fluid, ρ_c is the density of the coolant fluid, $c_{p,c}$ is the specific heat of the coolant fluid, and u_c is the coolant fluid velocity. Equation 3.25 is identical to the energy conservation equation developed for the open channel phase of the reaction channel, but using the coolant fluid properties instead of the reaction gas mixture properties. For all cases considered as part of this study, the coolant fluid is taken as air.

3.2.5 2-D Microreactor Solution Process

The momentum transfer, mass transfer, and heat transfer equations developed in Sections 3.2.2, 3.2.3, and 3.2.4 are all strongly coupled, with both the momentum transfer and mass transfer processes exhibiting a significant dependence on reaction temperature. This system of equations was solved numerically using version 5.4 COMSOL Multiphysics, a commercial finite element software package that can be used to solve coupled systems of partial differential equations, to evaluate the pressure drop, conversion profile, and temperature profile across each of the developed microreactor models.

In COMSOL, the Chemistry and Thermodynamics modules were used to evaluate the mixture properties and kinetics of the process, the Laminar Flow module was used to solve the momentum transfer equations, the Transport of Concentrated Species module was used to solve the mass transfer equations, and the Heat Transfer in Fluids module was used to solve the heat transfer equations. Information on the COMSOL model developed, including a more detailed discussion of the physics modules used, how the model was meshed, and the solver type used are presented in Appendix B.

From the calculated temperature distribution and thermal properties in the developed COMSOL model solutions, the total heat rejection from the microreactor models can be evaluated from an overall energy balance as:

$$\dot{Q}_{WGS} = \dot{m} c_{p,m} (T_{in} - T_{out}) + \dot{Q}_{rxn} \tag{3.26}$$

In equation 3.26, T_{in} and T_{out} are the inlet and outlet temperature from the reaction channel and $\dot{Q}_{rxn}$ is the total heat generation by the reaction.

3.3 Approach to Reaction Enhancement

As discussed in Section 2.3, the optimal temperature profile for a reversible, exothermic reaction can be evaluated using equation 2.6 [48]. This equation sets the partial derivative of the reaction rate with respect to temperature equal to zero and can be used to evaluate what the optimal temperature at a specified CO conversion level will be. The resulting locus of maximum conversion points represents the reaction progression that achieves the maximum CO conversion in the lowest possible reactor volume. The CO conversion across the reactor is defined as:

$$X_{CO} = \frac{F_{CO,i} - F_{CO}(x)}{F_{CO,i}} \tag{3.27}$$

where $F_{CO,i}$ is the inlet molar flow rate of CO to the reactor and $F_{CO}(x)$ is the molar flow rate of CO along the reactor axially. Equation 2.6 is a function of the inlet composition and, to a lesser extent, the inlet temperature to the reactor and thus unique optimal temperature profiles exist for each inlet condition. Applying equation 2.6 to the reaction rate expression developed by Germani and Schuurman in equation 2.5, it can be seen that the reaction rate constant, partial pressure terms, and reversibility factor are all temperature dependent, complicating the evaluation of equation 2.6 for this reaction rate expression significantly. The 2019 version of Maple, a mathematical software package that can be used to symbolically evaluate a variety of complex mathematical expressions, was used to evaluate this partial derivative. The resulting expression was then numerically solved to evaluate the corresponding optimal temperature associated with each conversion level for the HTS inlet condition specified in Table 3.1. These results are shown in 3.11 along with several contour lines of constant reaction rate for reference.

As shown in Figure 3.11, the optimal temperature progression passes through the

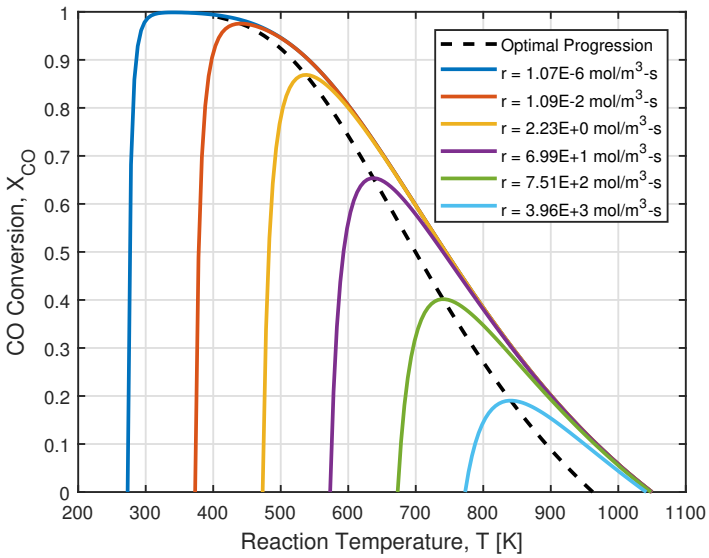

Figure 3.11: Optimal WGS progression with lines of constant reaction rate for the reaction rate expression developed by Germani and Schuurman

maximum CO conversion point on each of the lines of constant reaction rate shown. Notably, each of the lines of constant reaction rate also converges to the same curve as the temperature increases. This curve corresponds to the equilibrium curve of the reaction, which represents the maximum possible CO conversion achievable at each reaction rate and is entirely dependent on the thermodynamics of the reaction. The optimal temperature progression shown is unique to the inlet condition listed in Table 3.1. Ideally, for this inlet condition, the reactants should enter the reactor at a temperature of 962 K and then be cooled in a manner that follows this progression to the desired CO conversion level. The physical temperature profile can thus be obtained by applying a mass balance to the reactor, as discussed previously in Section 2.3. This mass balance reduces to equation 2.7 for plug flow reactors and can be numerically solved to relate the prescribed CO conversion and temperature values from Figure 3.11 to the cumulative reactor volume necessary to facilitate the process. Simplifying this mass balance for the 2-D reaction channel model is complicated

both by the presence of partial derivatives with respect to the x and y directions and by the fact that the reaction does not occur uniformly across the entire reaction channel domain, being limited to the catalyst layers. However, a sufficiently accurate optimal temperature profile for the 2-D model can still be obtained by using equation 2.7 with the "effective" reaction rate of the reactor, which is taken as:

$$r_e = \left(\frac{V_{cat}}{V_r}\right) r \tag{3.28}$$

In equation 3.28, r_e is the effective reaction rate, V_{cat} is the catalyst volume coated on the walls of the reactor, and V_r is the total reactor volume. By multiplying the calculated reaction rate by the ratio of the catalyst volume to total reactor volume, the effective reaction rate becomes a reaction rate expressed in terms of the entire reactor volume rather than just the catalyst volume where the reaction actually takes place. For packed bed reactors, the entire reactor volume is taken as the catalyst volume and the effective reaction is the same as the reaction rate. The optimal CO conversion and temperature profiles developed for the 2-D model using equations 2.7 and 3.28 for 90% total reactor CO conversion are shown in Figures 3.12 and 3.13.

Figure 3.12 shows that the optimal conversion and temperature profiles are identical in distribution to the results by TeGrotenhuis et al. [48] shown in Figure 2.4, with a rapid conversion of CO near the inlet of the reactor due to the rapid reaction rates possible at higher temperatures accompanied by a drastic reduction in temperature. Figure 3.13 shows that these conversion and temperature profiles exactly follow the optimal conversion profile developed in Figure 3.11 up to the desired outlet CO conversion of 90%.

The COMSOL model geometries described in Section 3.2.1 were developed with the intent of directly applying the optimal temperature profile to a microreactor channel using boundary conditions and evaluating practically achievable temperature profiles that can

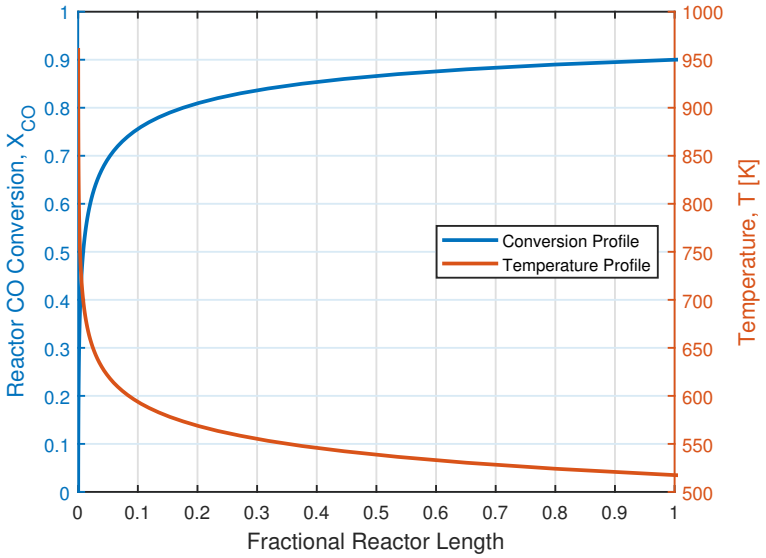

Figure 3.12: Optimal CO conversion and temperature profiles developed for microreactor model

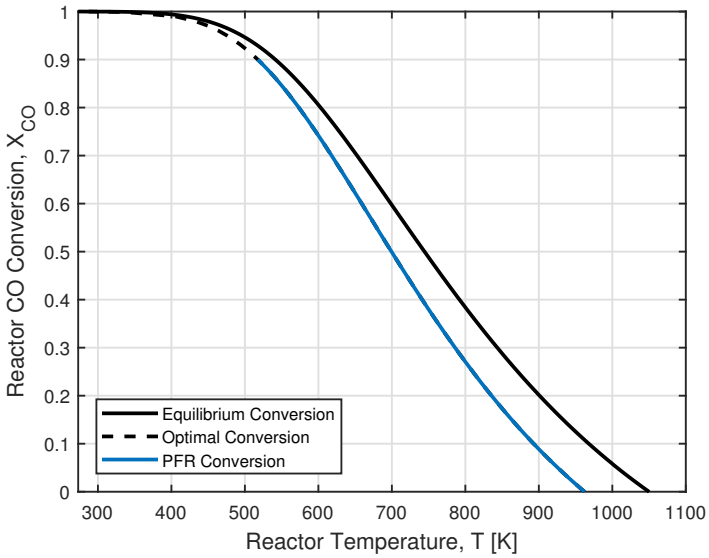

Figure 3.13: Optimal CO conversion plotted as a function of reaction temperature developed for microreactor model

closely emulate these optimal temperature profiles using integrated coolant. In nearly all practical applications of the WGS reaction, it is not possible for reactants to come into the reactor at the ideal temperature of 962 K. As a result, it proves beneficial for the reaction channels to have uncooled inlet lengths that allow the reaction to increase its temperature by generating heat until it approaches the optimal temperature profile and to then apply cooling such that the reaction temperature follows the optimal temperature profile. This is shown and discussed in much further detail in Chapter 4.

Chapter 4: Modeling Results

This chapter presents the results produced using both the HTS/LTS plug flow reactor MATLAB model and the microreactor COMSOL Multiphysics model introduced in the previous chapter. The results generated from the HTS/LTS PFR model are presented first. The COMSOL microreactor model is validated against experimental data from the literature. The validated model is then used to evaluate reactor performance for both the prescribed boundary condition and integrated coolant channel geometries outlined in Section 3.2.1 for the baseline conditions and model geometry specified in Tables 3.1 and 3.2 and for parametric sweeps of important design parameters.

4.1 Baseline HTS/LTS Packed Bed Reactor Modeling Results

The HTS/LTS PFR model developed in MATLAB as described in Section 3.1 was used to evaluate the CO conversion, mole fraction, and temperature profiles across both the HTS and LTS reactors, the total reactor volume required to achieve these conversion levels, the total heat rejection across the intercooler, and to compare the actual reaction progression through the reactors to the optimal progress developed in Section 3.3. The model provides an idealized baseline volume of an adiabatic reactor that could be compared to the differential temperature reactor geometries. The results from running this model are presented in Figures 4.1, 4.2, 4.3, and 4.4.

Figure 4.1 shows that the HTS reactor achieves an equilibrium CO conversion value of approximately 0.598 in a reactor volume of approximately $1.81 \times 10^{-4}\ m^3$, while the LTS reactor achieves an equilibrium CO conversion of 0.928 in a reactor volume of approx-

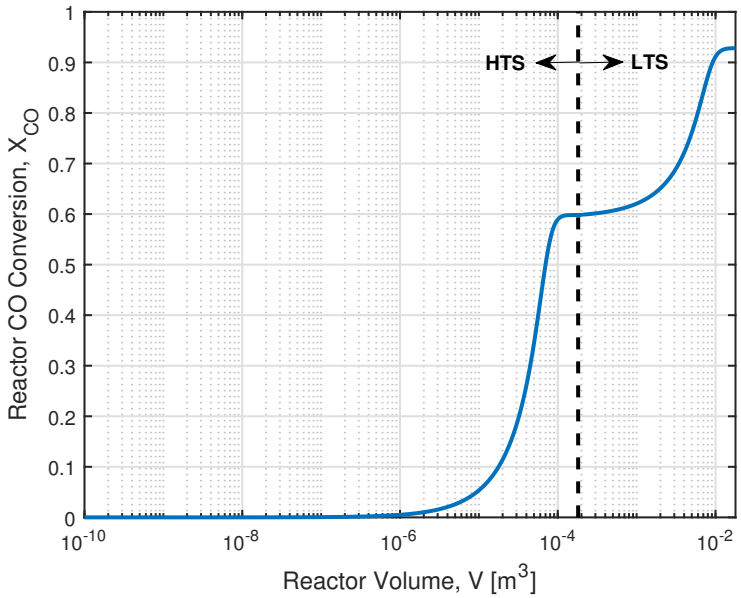

Figure 4.1: CO conversion profile across HTS/LTS reactor system

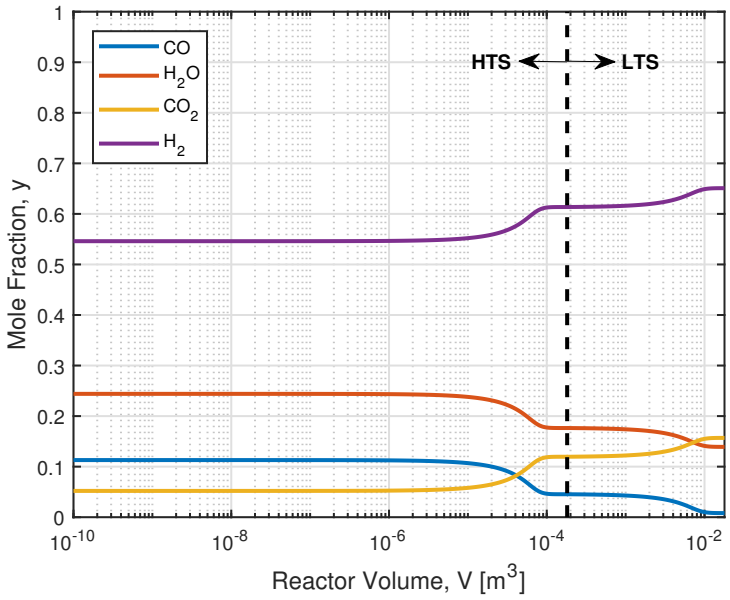

Figure 4.2: Mole fractions of chemical species across HTS/LTS reactor system

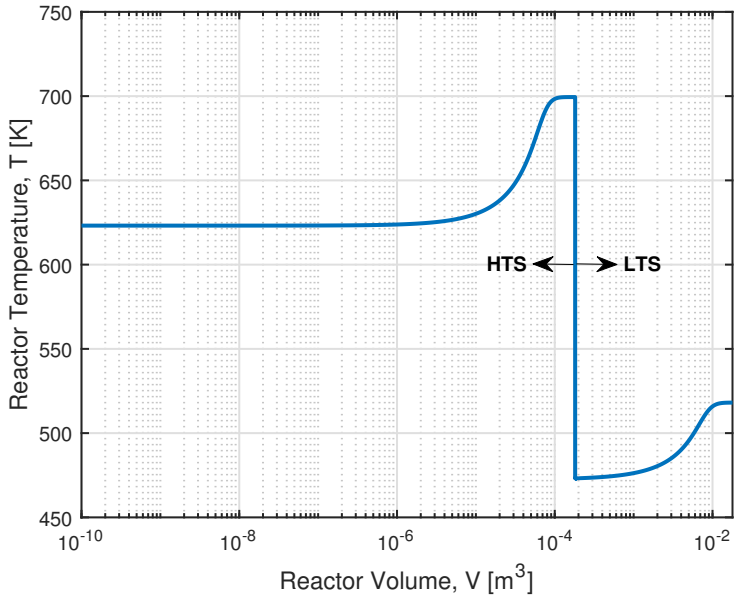

Figure 4.3: Temperature profile across HTS/LTS reactor system

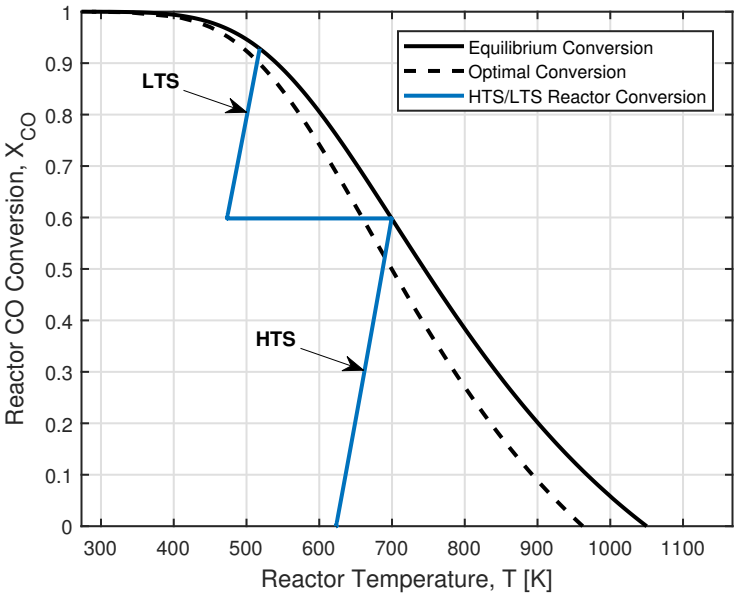

Figure 4.4: Comparison of HTS/LTS conversion profile to optimal progression

imately $1.77 \times 10^{-2}\ m^3$ for a total cumulative reactor volume total of $1.79 \times 10^{-2}\ m^3$. The HTS reactor achieves the bulk of the CO conversion in a significantly lower reactor volume due to the enhanced reaction kinetics at higher operating temperatures, only constituting approximately 1% of the total reactor volume, but is also more thermodynamically limited, reaching an equilibrium CO conversion level that is ultimately lower than desired. Conversely, the LTS reactor is able to achieve a much higher CO conversion value as the equilibrium shifts toward product formation at lower temperatures, but also requires a significantly larger reactor volume to facilitate this process due to the slower reaction kinetics. This is further demonstrated by the results shown in Figure 4.2, which show the CO mole fraction dropping to an acceptably low value of 0.82%. As noted previously in Section 3.1, the reactor volumes calculated from this model represent the minimum possible values for the HTS/LTS system and are thus a conservative, idealized baseline for comparison against. This is primarily a result of the assumption neglecting mass transfer resistance into and out of the catalyst pellets. The required packed bed reactor volumes for this process would thus be expected to be significantly larger in reality.

Figure 4.3 shows that the HTS reactor increases in temperature from 623.15 K up to 700 K and that the LTS reactor increases in temperature from 473.15 K up to 518 K. The sudden discontinuity in the temperature profile that occurs between the HTS and LTS reactors occurs due to the heat rejection that occurs across the intercooler, which is calculated to be approximately 1.65 kW based on the reaction stream mass flow rate, the desired inlet/outlet temperatures to and from the intercooler, and the reaction mixture's specific heat.

Finally, Figure 4.4 compares the HTS/LTS reactor progression to the optimal conversion progression. Notably, both the HTS and LTS reactor CO conversions increase linearly with temperature until hitting the equilibrium curve, where the net reaction rate goes to 0.

From the PFR relations shown in equations 3.1 and 3.4, the following expression for the derivative of CO conversion with respect to temperature can be derived:

$$\frac{dX_{CO}}{dT} = \frac{-\rho_m c_{p,m}}{C_{CO,i}\Delta H_{rxn}} \tag{4.1}$$

In equation 4.1, $C_{CO,i}$ is the initial concentration of CO entering the HTS reactor. This relationship indicates that the slopes of the HTS and LTS conversion lines in Figure 4.4 are a function of the reaction mixture density, reaction mixture specific heat, the inlet concentration of CO, and the heat of reaction. Although a number of these properties vary across the reactors due to changes in composition and temperature, none of the properties vary by more than 10% such that the HTS and LTS conversion lines are essentially parallel to each other. For exothermic reactions, which have negative heats of reaction, these lines have positive slopes, as exhibited in Figure 4.4 for the WGS reaction, while the slopes of these lines for endothermic reactions, which have positive heats of reaction, would be negative. Notably, the HTS/LTS reaction progression does not match the optimal progression well at all. Splitting the reaction into HTS and LTS reactors does have the desired effect of increasing the overall reactor CO conversion beyond what could be achieved in a single HTS reactor, but the large deviation of this reactor configuration's performance from the optimal conversion progression suggests that even larger improvements in performance can be achieved if the reaction temperature can be better controlled and forced to follow the optimal reaction progression.

4.2 2-D Microreactor Model Validation

Before using the 2-D Microreactor COMSOL model developed to predict reactor performance over a wide range of operating conditions, it was first compared to experimental data

in the literature to validate that its predictions agreed well enough to produce meaningful results. The experimental data compared to was collected by Germani and Schuurman [44]. These results were part of a study they conducted for the development of the Langmuir-Hinshelwood reaction rate expression shown in equation 2.5 for a $Pt/CeO_2/Al_2O_3$ catalyst. To facilitate this comparison, the geometry and operating conditions of the model were adjusted to emulate the conditions used in the study by Germani and Schuurman.

The experiment conducted by Germani and Schuurman used a reactor consisting of six microstructured, stainless steel platelets stacked on each other and sealed in an outer housing. Each platelet was 50 mm x 50 mm x 1 mm and had a total of 49 microchannels etched into it, resulting in a total of 294 microchannels being used in the reactor. Each microchannel was 0.4 mm deep, 0.6 mm wide, and spanned the entire 50 mm length of the plate. Each microchannel was washcoated with catalyst such that a single layer would deposit on its bottom surface. On average, 2.16 mg of catalyst deposited in each microchannel. With the listed catalyst density of $\rho_{cat} = 1450\ kg/m^3$, this results in an average catalyst layer thickness of approximately 0.05 mm in each channel.

The reaction stream fed into the reactor during the experiments was at a pressure of 1 bar and had a composition of 10% CO, 20% H_2O, 10% CO_2, 30% H_2 and 30% Ar on a molar basis. The feed rate of the reaction stream was fixed at 0.1 SLPM referenced to a pressure of 101.3 kPa and a temperature of 0 °C. In their experimental study, Germani and Schuurman varied the inlet temperature to the reactor from 200 °C to 340 °C in 20 °C increments and used cartridge heaters to maintain nearly isothermal conditions within the reactor for each inlet temperature tested.

To simulate the experiments conducted by Germani and Schuurman, the prescribed boundary condition model described in Section 3.2.1 was modified to operate with the microchannel geometry and process conditions outlined in this section. These values are

Table 4.1: Experimental process conditions used by Germani and Schuurman [52]

Experiment Parameter	**Value**
Inlet Temperature, T_{in}	200-340 °C
Pressure, P	1.0 bar
Reaction Flow Rate, $\dot{V}$	0.1 SLPM
Inlet Mole Fraction CO, $y_{CO,in}$	0.10
Inlet Mole Fraction H_2O, $y_{H2O,in}$	0.20
Inlet Mole Fraction CO_2, $y_{CO2,in}$	0.10
Inlet Mole Fraction H_2, $y_{H2,in}$	0.30
Inlet Mole Fraction Ar, $y_{Ar,in}$	0.30

Table 4.2: Experimental microchannel geometry used by Germani and Schuurman [52]

Reactor Dimensions	**Value**
Reaction Channel Length, L	50 mm
Reaction Channel Height, H	0.4 mm
Reaction Channel Width, W	0.6 mm
Catalyst Layer Height, H_{cat}	0.05 mm
Number of Reaction Channels, N	294

summarized in Tables 4.1 and 4.2. The wall temperatures in this verification model were prescribed as constant values set at the inlet temperatures to the reactor for each case considered to enforce isothermal operating conditions for each simulation performed. The average outlet CO conversion was calculated for each inlet temperature and compared directly to the experimental results produced by Germani and Schuurman, as shown in Figure 4.5.

Figure 4.5 shows that there is generally good agreement between the experimental results and the COMSOL model results. The model accurately replicates the behavior of the experimental data over the entire range of reactor inlet conditions examined, with the largest percent error between the experimental and modeled results being 30.8% at an inlet temperature of 493 K and the mean average percent error between the modeled and experimental results over the entire range of temperatures evaluated over being 7.72%.

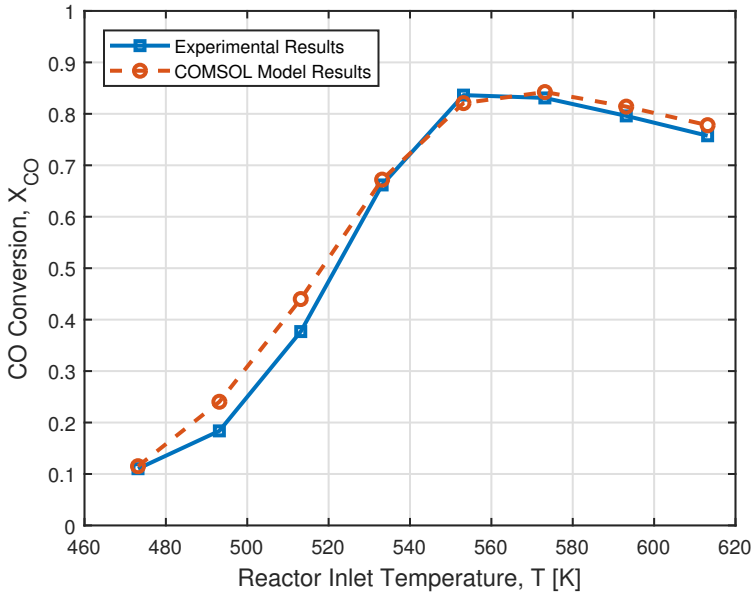

Figure 4.5: Comparison of 2-D COMSOL model results and experimental results from Germani and Schuurman [44]

This provides confidence that the subsequently performed analyses using the COMSOL model provide physically meaningful results.

The results in Figure 4.5 also show that the CO conversion initially increases fairly rapidly as the reactor inlet temperature is increased. However, at reactor inlet temperatures higher than 553 K, the CO conversion begins to decrease. This indicates a shift from the reactor being kinetically limited at lower temperatures to being thermodynamically limited at higher temperatures. This is better demonstrated in Figure 4.6, which compares the modeled results to the equilibrium curve for the reaction. Figure 4.6 shows that at the lower inlet temperatures modeled, the CO conversion does not reach the equilibrium conversion curve. This indicates that the reaction proceeds slowly enough through the reactor that it is unable to reach equilibrium and that the reactor is kinetically limited. As the reactor inlet temperature is increased, these kinetic limitations are reduced and at an inlet temperature

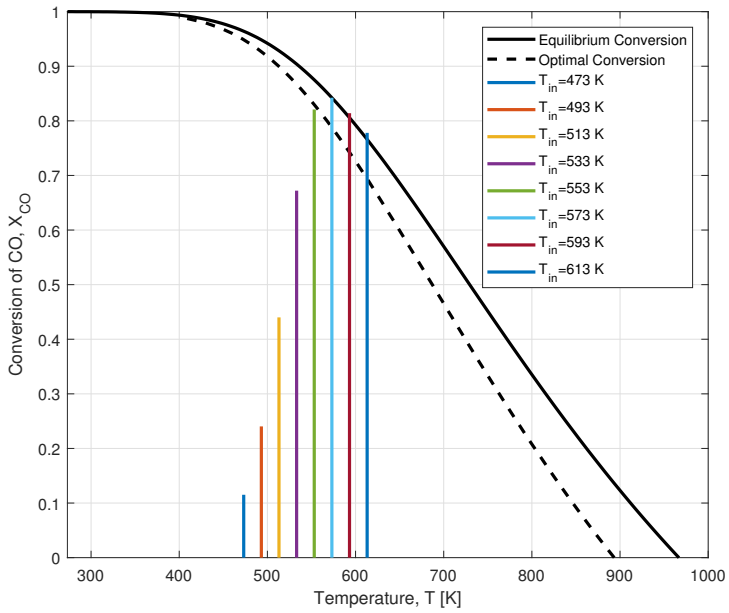

Figure 4.6: Isothermal COMSOL model results for varying reactor inlet temperatures

of 573 K, the reaction finally hits the equilibrium conversion curve, achieving the highest CO conversion value of any of the inlet temperatures evaluated. As the reactor inlet temperature continues to increase, the reaction continues to hit the equilibrium conversion curve. Because the equilibrium conversion decreases as the reaction temperature continues to increase, the reactor's CO conversion also begins to decrease, indicating a shift in the reactor's performance toward being thermodynamically limited as opposed to kinetically limited. It is also worth noting that both the equilibrium curve and optimal progression in Figure 4.6 are different than the ones shown in Figure 3.13. This is a direct result of the inlet reaction mixture composition used for these simulations being different than the baseline composition that was used to generate the curves shown in Figure 3.13. This demonstrates the sensitivity of these curves to the inlet condition to the reactor, as discussed in Section 3.3.

4.3 Baseline 2-D Microreactor Modeling Results

The performance of both the prescribed boundary condition and integrated coolant models described in Section 3.2.1 were evaluated with the developed momentum, mass, and heat transfer equations presented in Section 3.2. The adiabatic performance of the prescribed boundary condition model was first established as a baseline by applying an insulation boundary condition along the entire length of the channel wall. This boundary condition was then modified to include a prescribed wall temperature length to directly control the reaction temperature such that it would follow the optimal temperature progression as closely as possible. The results of this prescribed wall temperature model were then used to iteratively evaluate coolant inlet flow and temperature values that emulated the optimal temperature progression as closely as possible. The results generated from each of these models for the baseline case, including the CO conversion profiles, temperature profiles, velocity profiles, and pressure drop, are shown in Figures 4.7 through 4.12.

Figure 4.7 shows the CO conversion profiles along the center line for the adiabatic, prescribed wall temperature, and integrated coolant microreactor cases. While the adiabatic model has an insulated boundary condition applied over its entire length, both the prescribed wall temperature and integrated coolant models operate with adiabatic inlet sections followed by differential temperature sections where the reaction stream temperature is actively managed via an applied temperature boundary condition or coolant flow. For the integrated coolant results presented in Figure 4.7, the total air coolant flow rate and inlet temperature were taken as 1.09×10^{-2} kg/s and 560.7 K, which were determined via an iterative process to yield the highest CO conversion for the reaction stream conditions used. These differential temperature sections increase the reactor conversion significantly beyond what the adiabatic reactor can achieve. While the adiabatic reactor model only achieves a final CO conversion value of 0.613 for the reactor volume considered, the pre-

scribed temperature model and integrated coolant models achieve conversions of 0.826 and 0.821, respectively, over a 34% increase. For a significant portion of the reactor volume considered, the adiabatic model operates at equilibrium and thus this portion of the reactor does not significantly contribute to the overall reactor CO conversion. By actively cooling this section of the reactor such that it follows the optimal temperature progression developed in Section 3.3, CO conversion can be significantly increased. As discussed in Section 3.3, although the reaction stream would ideally enter the reactor at 962 K for the inlet composition simulated, this is a temperature that is too high to be practical in actual application as WGS reactants generally enter these reactors at temperatures between 310 °C and 450 °C (583.15 K to 723.15 K) based on the needs of the overall system operation. To facilitate operation at more standard inlet conditions, it thus proves beneficial for these differential temperature reactors to operate with an adiabatic inlet section, where the heat generated by the reaction goes toward increasing the temperature of the reaction stream, followed by differential temperature sections, where the reaction stream is actively cooled to increase CO conversion beyond what is possible in purely adiabatic conversion. The lengths/volumes of the adiabatic and differential temperature sections of the microreactor model, as indicated on the figures, were evaluated by identifying the point at which the adiabatic reactor curve intersects the optimal conversion curve in Figure 4.9 and the corresponding length/volume at which this intersection occurs on Figures 4.7 and 4.8.

Comparing the prescribed temperature model and integrated coolant model CO conversion curves on Figure 4.7, the prescribed temperature model curve always exceeds the conversion achieved by the integrated coolant model, though both curves converge to very similar outlet values. This can be better explained by examining Figure 4.9. Figure 4.9 shows that while the prescribed temperature model is able to instantly switch from adiabatic operation to differential temperature operation and very closely follow the optimal

conversion curve, the integrated coolant model deviates from this progression, operating nearly isothermally initially before eventually converging onto the optimal conversion curve. Figure 4.8 more directly shows the difference in the temperature profiles along the center lines of these models, with the prescribed temperature model reaching a maximum temperature of approximately 685.5 K and the integrated coolant model only reaching a maximum temperature of approximately 637.3, a difference of nearly 50 K. While the adiabatic section of prescribed temperature model identically follows the adiabatic reactor temperature progression, the integrated coolant reactor remains at a significantly lower temperature until eventually converging to a a similar temperature progression as the prescribed temperature model in the differential temperature section. The difference in the exhibited temperature progressions is primarily due to the occurrence of axial conduction through the microreactor wall in the integrated coolant model. While the prescribed temperature model assigns a perfect insulation boundary condition over its adiabatic section, this section of the reaction channel would be in contact with the reactor wall material in reality and would not not operate perfectly adiabatically as desired. Rather, heat will conduct through this portion of the wall to the cooled section, ultimately resulting in lower temperatures, slower reaction kinetics, and lower CO conversion in this section of the model compared to both the adiabatic and prescribed temperature models. From energy balances on the prescribed temperature and integrated coolant reactor models, the heat rejections from these microreactor models are both calculated to be approximately 1.24 kW. While the majority of this heat rejection (approximately 63.6%) is from the exothermic reaction, a sizable portion is from the sensible energy change of the reaction stream as it is cooled to follow the optimal temperature progression.

Figure 4.10 shows the velocity profiles across each of the microreactor models halfway along the reactor length (0.10 m). The velocity profiles for each model are generally

parabolic in shape, which is characteristic of laminar flow profiles, but also flatten out to extremely low velocities at the edges. This is a result of the presence of the porous catalyst layers on the edges of the microreactor models, which have very high resistances to flow and thus very low flow velocities through them. For thicker catalyst layers, the obstruction to flow through the channel would increase, increasing both the flow velocity and pressure drop through the reaction channel. Notably, while the prescribed temperature and integrated coolant models exhibit nearly identical velocity profiles, reaching maximum flow velocities of approximately 0.22 m/s along the centerline of the reaction channel, the adiabatic reactor model reaches a slightly higher maximum flow velocity of 0.26 m/s. This is primarily a result of the higher gas temperatures of the adiabatic model increasing the bulk fluid velocity slightly due to the commensurate reduction in density that occurs. Figure 4.11 better shows this as it plots the change in the center line velocity along the length of the reaction channel for each model. The results show a notable deceleration in the flow velocity of both the prescribed temperature and integrated coolant models along the lengths of their differential temperature sections as a result of the reduction in flow temperature. Figure 4.12 shows similar trends with the pressure drops for each of the microreactor models. While the adiabatic reactor model exhibits a pressure drop of 12.7 Pa along its entire length, both the prescribed temperature and integrated coolant models exhibit a pressure drop of approximately 9.9 Pa. The reduction in pressure drop for the differential temperature models is primarily a result of the lower flow velocities along their differential temperature sections as well as the decrease in mixture viscosity as the temperature decreases, lowering the resistance to flow.

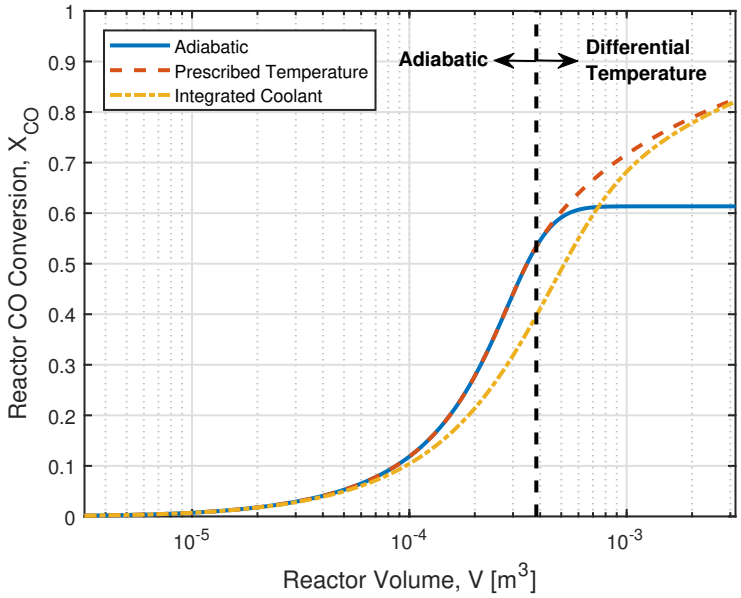

Figure 4.7: Comparison of CO conversion profiles for each microreactor model

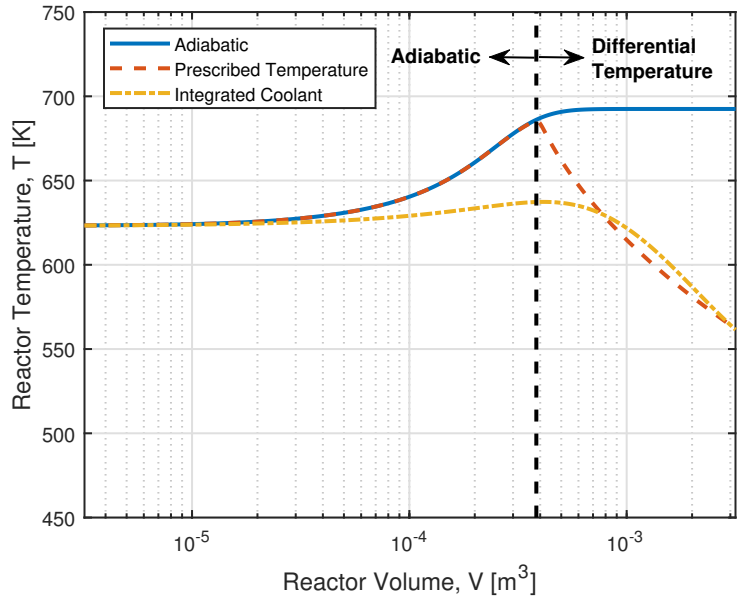

Figure 4.8: Comparison of temperature profiles for each microreactor model

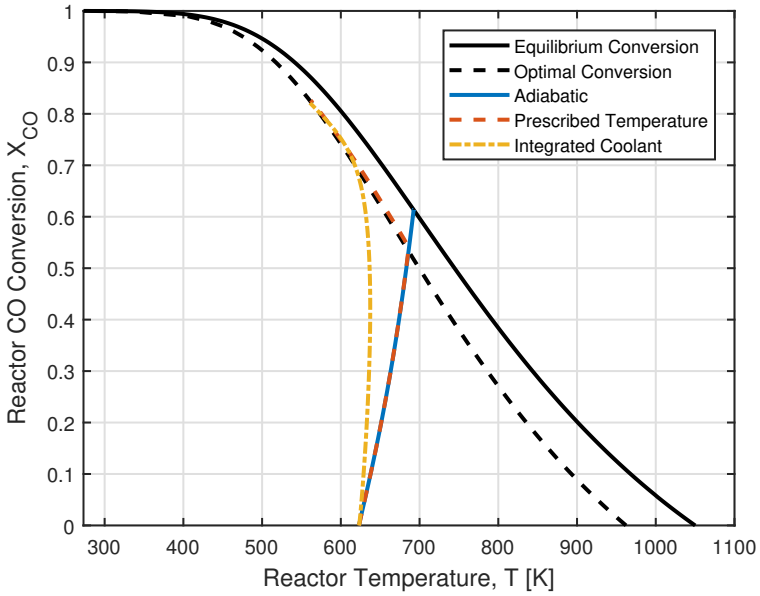

Figure 4.9: Comparison of microreactor models to optimal progression

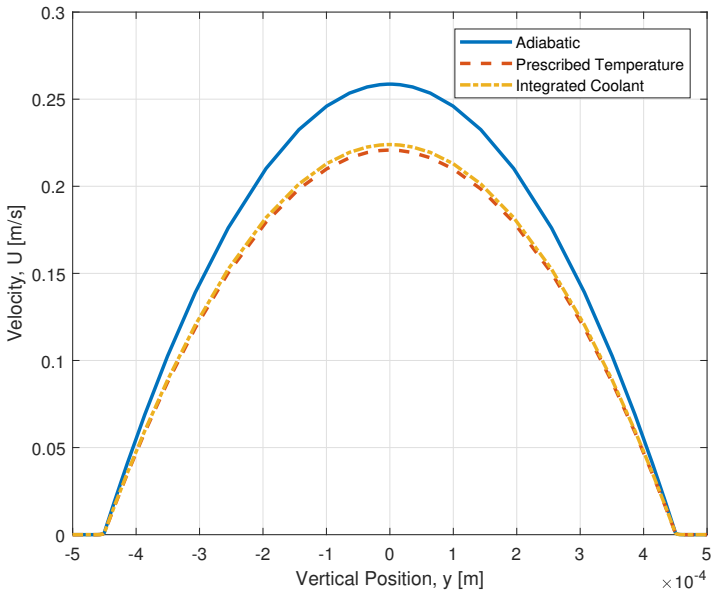

Figure 4.10: Comparison of velocity profiles for each microreactor model

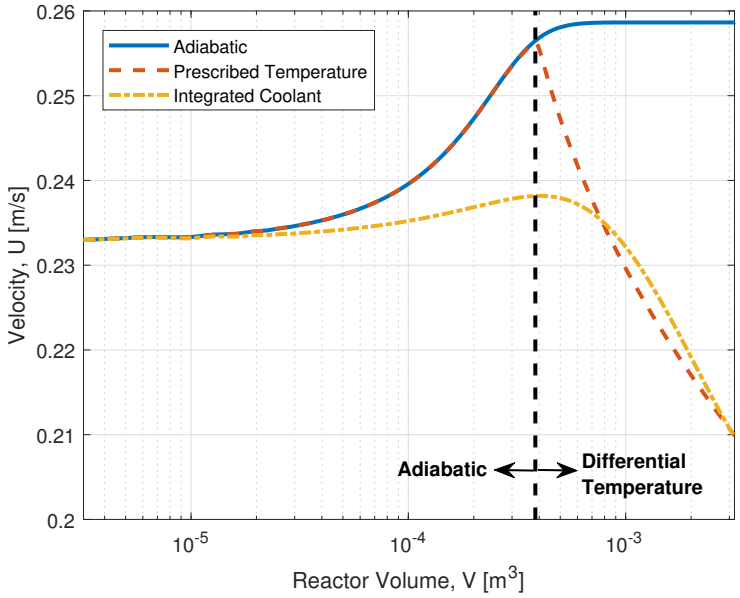

Figure 4.11: Comparison of the change in flow velocity for each microreactor model

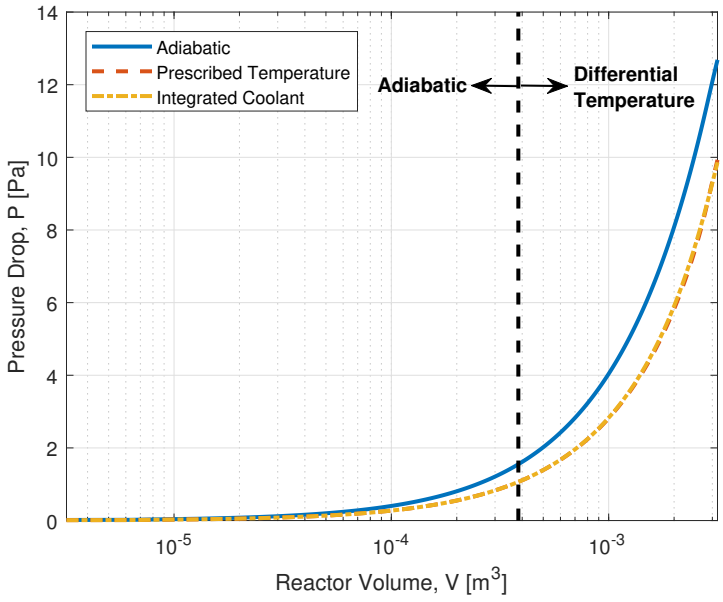

Figure 4.12: Comparison of pressure drop values for each microreactor model

4.4 Comparison of HTS/LTS Packed Bed Reactor and 2-D Microreactor Modeling Results

Figures 4.13 through 4.15 directly compare the CO conversion and temperature profiles of the HTS/LTS packed bed reactor and the differential temperature microreactor models. Figure 4.13 shows that both of the differential temperature microreactors increase conversion beyond what the HTS/LTS reactor configuration is capable of in the approximate reactor volume range of 5.09×10^{-4} m^3 to 3.20×10^{-3} m^3. Notably, the HTS packed bed reactor exhibits significantly faster reaction kinetics than the microreactor models, reaching its final conversion value in a significantly lower reactor volume. This is primarily because the microreactor models have substantially less catalyst present within them than the packed bed reactor does and because of the assumption neglecting mass transfer resistance into and out of the catalyst pellets of the packed bed reactor. While the packed bed reactors are assumed to be completely packed with catalyst such that the reaction takes place homogeneously throughout the entire reactor volume, the microreactor models only have catalyst coated on their walls. As a result, the packed bed reactors have approximately 4.83 times as much catalyst present within them compared to the microreactor models for the same reactor volume for the baseline geometry considered. When assuming 100% packed bed catalyst effectiveness, this facilitates higher reaction rates than are possible for the microreactors at the same operating temperatures while in adiabatic operation. It is again worth noting, however, that the presented HTS/LTS results represent the best possible performance of the packed bed reactor system and that even for this conservative baseline, there are conditions over which the microreactor exhibits better performance, suggesting that even larger improvements can be achieved in reality.

While the microreactor geometries perform worse than the HTS packed bed reactor due to slower reaction kinetics, they initially show better conversion than the LTS packed bed reactor since their temperatures are not immediately shifted to a significantly lower temperature, as shown by the temperature profiles plotted in Figure 4.14, with the microreactor models following the optimal conversion profile plotted in Figure 4.15 relatively closely. However, the lower amount of catalyst present in the microreactor appears to impede the reaction kinetics enough for the LTS conversion curve to appear to exhibit better conversion again as the reactor volume continues to increase. Had longer microreactor channels been considered, it appears as if the LTS conversion would eventually overtake the microreactor conversion once again. Still, for the range of reactor volumes mentioned, the prescribed temperature and integrated coolant microreactor models achieve 21.6% and 13.9% reductions in reactor volume compared to the HTS/LTS packed bed reactor configuration, respectively. More notably, these reductions in reactor volume are achieved using 83.8% and 82.2% less catalyst than the HTS/LTS packed bed reactor uses, respectively. This is a significant reduction in the total amount of catalyst used for the WGS reaction that, when coupled with the commensurate reduction in reactor volume required, could significantly reduce the costs associated with these reactor systems. Although the differential microreactor models suggest worse performance compared the HTS packed bed reactor for lower catalyst amounts used, these results also suggest that larger savings could potentially be achieved by these reactors depending on the operating conditions chosen and the relative costs of the catalyst and reactor used. The implications of this finding are explored more in Section 4.5 of this chapter and the optimization study conducted in Chapter 6.

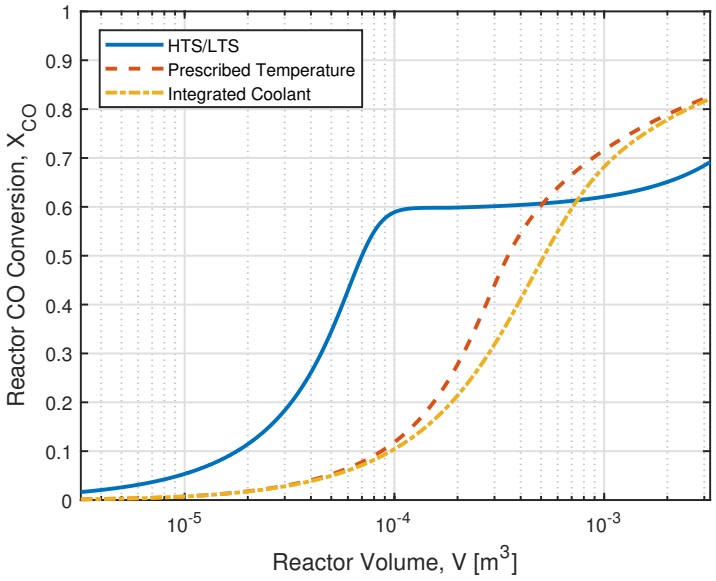

Figure 4.13: Comparison of HTS/LTS and differential temperature model CO conversion profiles

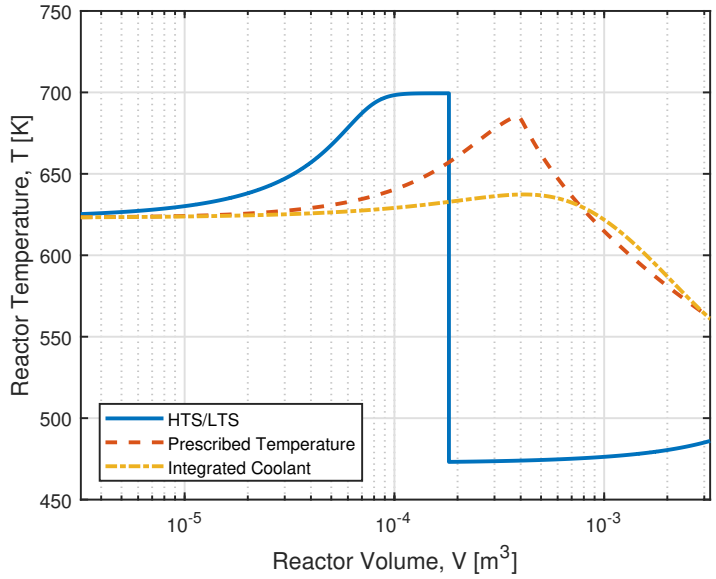

Figure 4.14: Comparison of HTS/LTS and differential temperature model temperature profiles

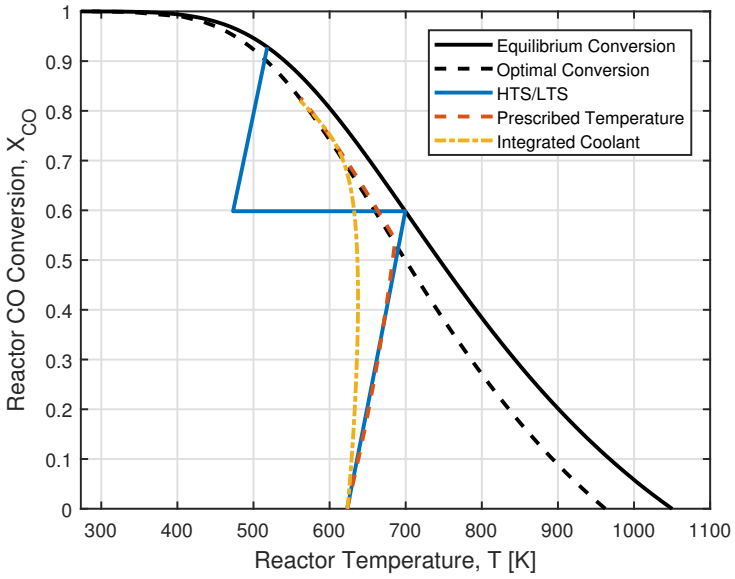

Figure 4.15: Comparison of HTS/LTS and differential models to optimal progression

4.5 2-D Microreactor Parametric Studies

The microreactor modeling results discussed in Section 4.3 for the baseline condition analyzed suggest that there are situations where WGS microreactors operating under optimal temperature progression conditions can achieve significant reductions in both the reactor volume and the amount of catalyst required for this process. To better characterize how the performance of these microreactor models changes for different operating conditions and geometries and to evaluate situations in which these microreactors perform at a significant advantage to the standard HTS/LTS reactor configuration, I performed parametric studies varying the reactor inlet temperature, catalyst layer thickness, and applied cooling length and compared the results from the microreactor and packed bed reactor models. The results of these parametric studies are presented in this section.

4.5.1 Varying Inlet Temperature

Process conditions of the overall steam reforming process dictate the inlet temperature to the WGS reaction, but higher inlet temperatures can be beneficial to the initial kinetics of the reaction and can help facilitate performance that is closer to the optimal temperature progression developed in Section 3.3. To explore the influence of the inlet temperature on reactor performance, I varied the value of this parameter from 573 K to 823 K for both the prescribed temperature and integrated coolant models while maintaining all other process and design parameters at their baseline values. This corresponds to the general range of inlet temperatures that would commonly be used in actual system operation up to a higher temperature limit where catalyst sintering or degredation would be expected to occur. The general results of this parametric study are summarized in Table 4.3 along with the results from the HTS/LTS PFR model evaluated over the same reactor volume for reference. For the HTS/LTS PFR model, the inlet temperature to the LTS reactor was still taken as 200 °C for each HTS inlet temperature evaluated. The tabulated results indicate that both differential temperature reactor models exhibit better CO conversion than the HTS/LTS configuration for all of the temperatures considered for a total reactor volume of V_{WGS} = 0.0032 m^3. As previously indicated in Section 4.4, this is done using over 80% less catalyst than is used for the HTS/LTS reactors, a very significant reduction. Conversely, the HTS/LTS configuration always exhibits higher heat rejection than the differential temperature reactors, though this difference decreases at higher inlet temperatures.

Figures 4.16, 4.17, and 4.18 show how the prescribed temperature model performance changes as the inlet temperature is increased. Figure 4.16 shows that the conversion process improves as the inlet temperature is increased, with the 573 K inlet temperature achieving a final CO conversion of 0.810 and the 823 K inlet temperature achieving a final CO conversion of 0.832. This increase in CO conversion is realized as a result of the reaction

following the optimal temperature progression over a greater portion of the reactor length, as shown in Figure 4.17, since the the reaction is able to more quickly approach the optimal temperature progression near the inlet of the reactor. Figure 4.18 shows that as the inlet temperature increases, the temperature progressions begin to converge to the same curve. This curve corresponds to the optimal temperature progression derived in Section 3.3.

Figures 4.19, 4.20, and 4.21 show similar results for the integrated coolant differential temperature microreactor at varying inlet temperatures. While the general trends in the CO conversion profiles shown in Figure 4.19 are identical to the trends shown for the prescribed temperature model in Figure 4.16, it is noteworthy that the integrated coolant models achieve lower CO conversion than the prescribed temperature models for each case. This is primarily a result of the integrated coolant model not being able to follow the optimal temperature progression as closely as the prescribed temperature model, as shown in Figures 4.20 and 4.21. Notably, the deviations from the optimal temperature progression at the higher inlet temperatures actually result in lower CO conversions, with the 723 K inlet temperature case actually achieving the highest conversion and the 823 K inlet temperature case performing notably worse than other cases over significant lengths of the reactor. To more accurately emulate the optimal temperature progression practically, it appears as if it would be necessary to cool the reaction stream down across different cooling stages such that the flow rates and inlet temperatures of each stage could be controlled separately. This significantly increases the design and operation complexity of the reactor, however, and would appear to incur relatively little benefit as the single coolant stage design modeled still appears to achieve very similar results to the idealized prescribed temperature models in all cases.

Figures 4.22 and 4.23 compare the CO conversion profiles for the HTS/LTS and differential temperature reactor models at the lowest inlet temperature evaluated (573 K)

and the highest inlet temperature evaluate (823 K) respectively. These figures generally demonstrate that the differential temperature reactor models perform better than the HT-S/LTS model does at higher inlet temperatures, with the prescribed wall temperature and integrated coolant models respectively achieving 65.5% and 61.2% reduction in the required reactor volume compared to the HTS/LTS configuration at 80% CO conversion for an inlet temperature of 823 K. At an inlet temperature of 573 K, the design range over which the differential temperature reactor models require less volume than the HTS/LTS to achieve a certain CO conversion appears significantly reduced. This suggests that if it is desirable to operate at these lower reactor temperatures, than it may be beneficial to have thicker catalyst layers on the reactor walls than the 5×10^{-5} m thickness used in this parametric sweep as the kinetic limitations of the differential temperature reactors are too great in this operating range for there to be a reduction in the required reactor volume. Still, even at conditions that would require larger overall reactor volumes than the HTS/LTS configurations, differential temperature reactors can achieve significant reductions in the required catalyst to facilitate the process, indicating a potential advantage in applications where larger reactor volumes are acceptable, but a reduction in the catalyst used is desired.

Table 4.3: Results from parametric sweep of reactor inlet temperatures

	Inlet Temperature, T [K]	**CO Conversion, X_{CO}**	**Heat Rejection, $\dot{Q}_{WGS}$ [kW]**
HTS/LTS	573	0.75	1.37
	623	0.692	1.65
	673	0.632	1.93
	723	0.571	2.22
	773	0.512	2.51
	823	0.455	2.81
Prescribed Temperature	573	0.810	0.801
	623	0.826	1.24
	673	0.830	1.62
	723	0.831	1.99
	773	0.832	2.36
	823	0.832	2.74
Integrated Coolant	573	0.802	0.795
	623	0.821	1.24
	673	0.828	1.62
	723	0.830	1.99
	773	0.829	2.36
	823	0.826	2.74

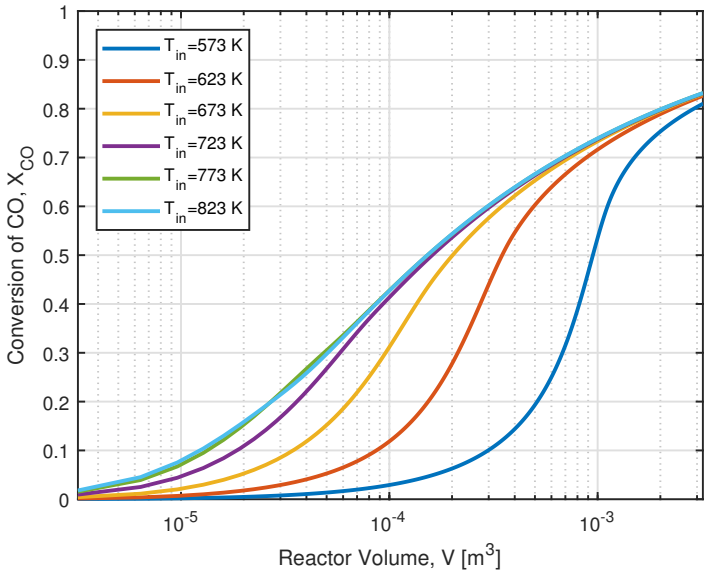

Figure 4.16: Differential temperature microreactor CO conversion profiles at varying inlet temperatures for prescribed boundary conditions

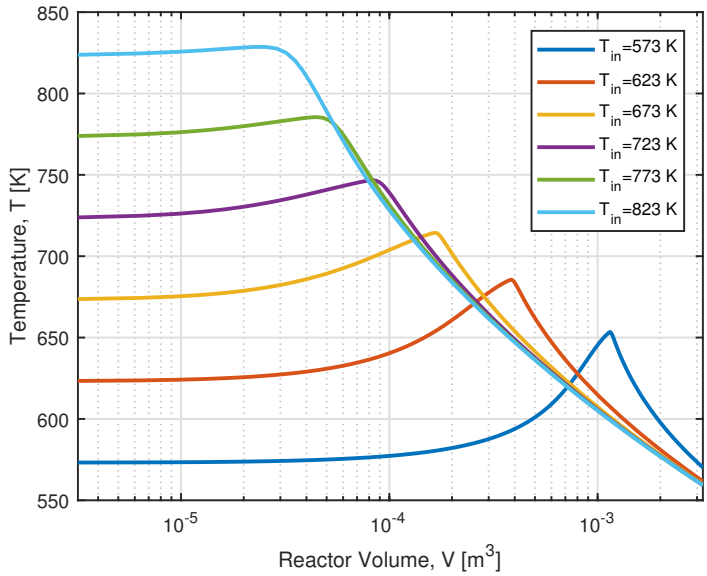

Figure 4.17: Differential temperature microreactor temperature profiles at varying inlet temperatures for prescribed boundary conditions

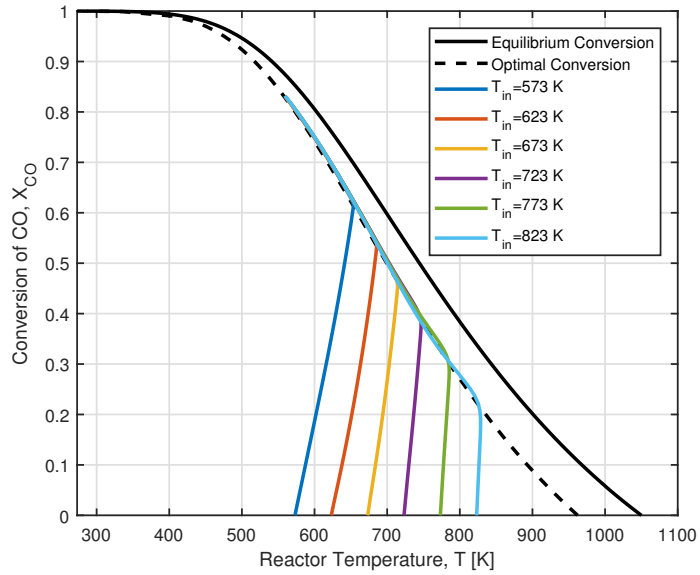

Figure 4.18: Comparison of differential temperature microreactor models to optimal progression at varying inlet temperatures for prescribed boundary conditions

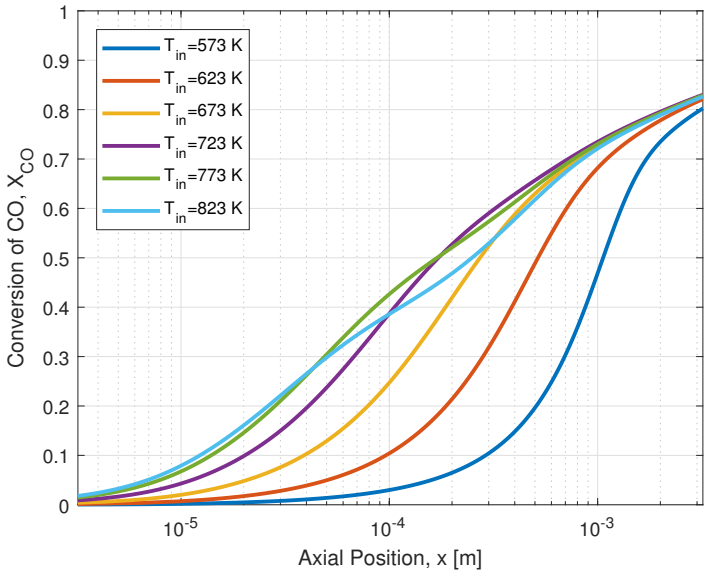

Figure 4.19: Differential temperature microreactor CO conversion profiles at varying inlet temperatures for integrated cooling

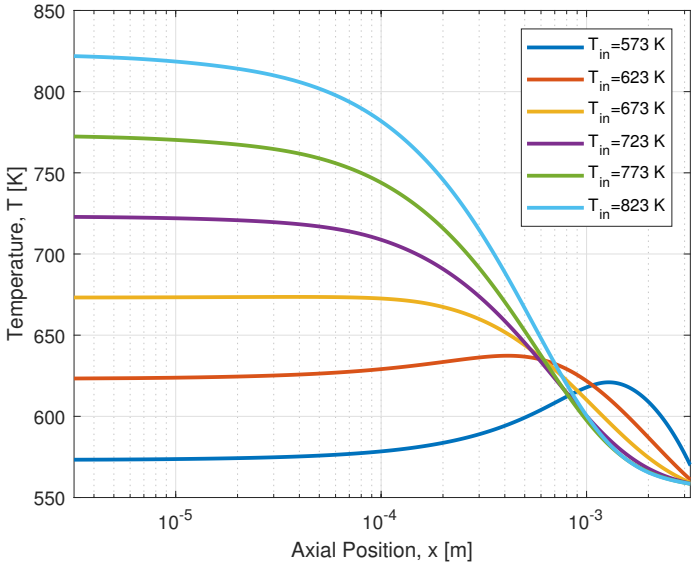

Figure 4.20: Differential temperature microreactor temperature profiles at varying inlet temperatures for integrated cooling

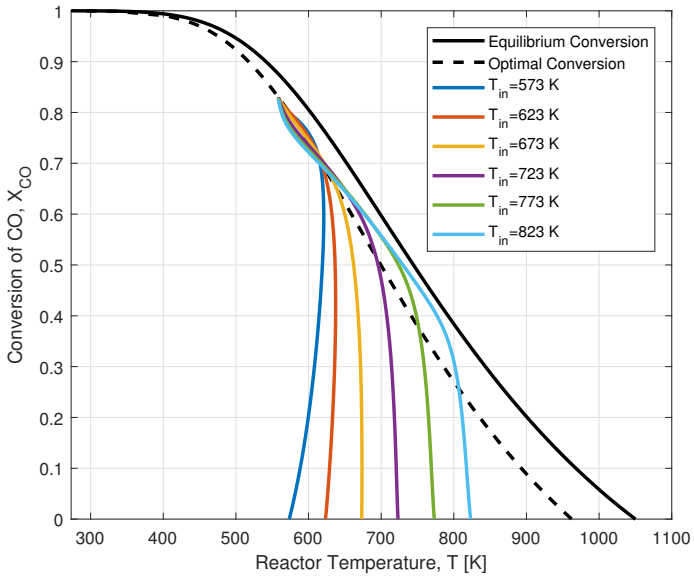

Figure 4.21: Comparison of differential temperature microreactor models to optimal progression at varying inlet temperatures for integrated cooling

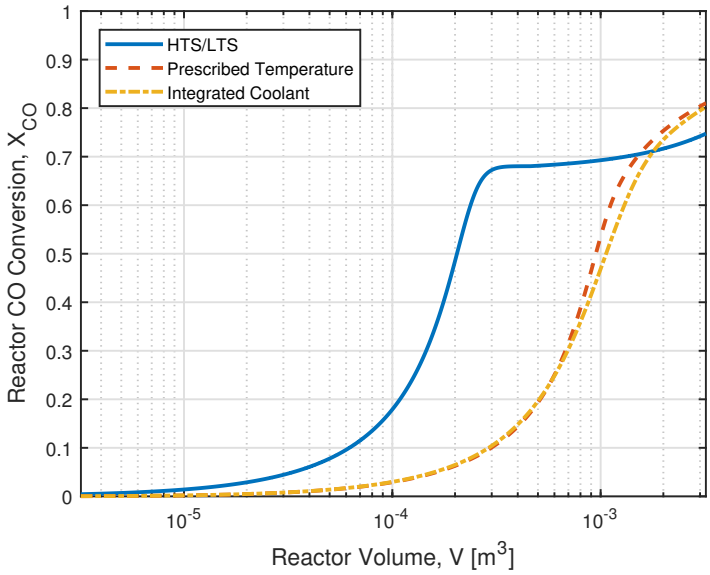

Figure 4.22: Comparison of HTS/LTS and differential temperature reactor CO conversion profiles for an inlet temperature of 573 K

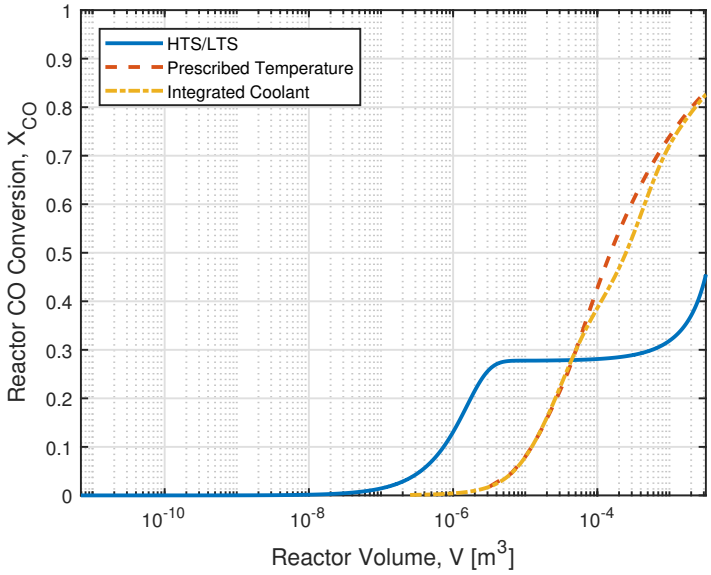

Figure 4.23: Comparison of HTS/LTS and differential temperature reactor CO conversion profiles for an inlet temperature of 823 K

4.5.2 Varying Catalyst Thickness

Inserting more catalyst into the reactor facilitates faster reaction kinetics, which can reduce the required reactor volume, but at the expense of incurring higher catalyst costs and higher pressure drop through the reactor due to the higher resistance to flow. To explore the influence that the amount of catalyst within the reactor has on its performance, I varied the thickness of the deposited catalyst layer from 5×10^{-5} m to 5×10^{-4} m for both the prescribed temperature and integrated coolant models while maintaining all other process and design parameters at their baseline values. The 5×10^{-4} m thickness corresponds to a packed bed reactor configuration where the reactor volume is completely filled with catalyst. The general results of this parametric study are summarized in Table 4.4 along with the results from the HTS/LTS PFR model evaluated over the same reactor volume for reference. The HTS/LTS model was still assumed to use a bulk catalyst density of $\rho_{cat} = 700$ kg/m^3 and the microreactor model was still assumed to use a catalyst density of $\rho_{cat} = 1450$ kg/m^3, even for the fully packed microreactor condition. Additionally, the catalyst in the microreactor was still assummed to operate at 100% effectiveness, even though the mass transfer resistance would be expected to increase as the catalyst layer thickness increases. These tabulated results indicate that the packed bed configurations of the differential temperature models achieve approximately 25% higher CO conversions than the HTS/LTS PFR model does over a reactor volume of 0.0032 m^3 and that differential temperature reactors following the optimal temperature progression operate more effectively. The heat rejection from the reaction also increases with increasing catalyst thickness, both as a result of the increase heat generation from the reaction and the higher change in the sensible energy of the reaction stream.

Figures 4.24, 4.25, and 4.26 show how the prescribed temperature model performance changes as the catalyst layer thickness is varied. Figure 4.24 shows that the conversion

process improves as the catalyst content is increased, with the 5×10^{-5} m thickness model achieving a final CO conversion of 0.826 and the 5×10^{-4} m thickness model, which corresponds to packed bed conditions, achieving a final CO conversion of 0.936. This increase in conversion is realized primarily due to both the reaction following the optimal temperature progression over a greater portion of the reactor length due to the enhanced reaction kinetics and the change in the heat transfer characteristics of the model as the catalyst thickness is increased. Equation 3.21 in Section 3.2.4 shows that the heat transfer process in the porous catalyst phase is influenced by conduction, convection, and heat generation processes. Figure 4.32 shows that flow velocity through the porous catalyst phase is generally quite low, never exceeding 0.10 m/s for any thickness value studied, leading to conduction being the dominant mode of heat transfer through the catalyst layer. As a result, increasing the catalyst layer thickness increases the influence of conduction on the overall heat transfer process, leading to lower rises in temperature over the length of the adiabatic section and a more uniform temperature distribution throughout the reactor. This is shown by Figures 4.25 and 4.26.

Figures 4.27, 4.28, and 4.29 show similar results for the integrated coolant differential temperature microreactor at varying catalyst thickness values. The general trends in the CO conversion profiles shown in Figure 4.27 are identical to the trends shown for the prescribed temperature models in Figure 4.24, though the integrated coolant model achieves a slightly lower conversion for each case as it is not able to follow the optimal temperature progression as closely as the prescribed temperature model can. This can be more directly seen by comparing Figure 4.29 to Figure 4.26 and by examining how the temperature progressions shown in Figures 4.28 and 4.25 differ from each other.

Figure 4.27 compares the CO conversion profiles for the HTS/LTS and differential temperature reactor models for the 5×10^{-4} m catalyst layer thickness corresponding to packed

bed conditions. This figure indicates that both differential temperature reactor models exceed the HTS/LTS reactor CO conversion over the entire reactor volume considered, achieving outlet CO conversions of approximately 0.933 while the HTS/LTS reactor configuration only reaches a conversion of 0.692 and is even further limited to a final equilibrium conversion of 0.928. The higher catalyst density used for the microreactor model leads to this model exhibiting faster reaction kinetics over the entire reactor volume, as would be expected. Compared to the baseline results in Figure 4.13, the achievable reductions in total reactor volume can be much larger, with the prescribed temperature model achieving a volume reduction of 91.5% and the integrated coolant model achieving a volume reduction of 90.0% for 80% CO conversion. These results also indicate a similar reduction in the required catalyst as for the baseline case considered. It is worth noting that the presence of the catalyst in the microreactor models, in addition to altering the chemical process occurring, also changes the heat transfer process. Figure 4.31 indicates that the HTS reactor exhibits a much larger increase in temperature compared to either differential temperature reactor, which have nearly constant temperature inlets. As mentioned previously, this is a result of conduction through the porous catalyst phase dominating the heat transfer process. Because the PFR model neglects diffusive effects and thus the influence that conduction through the catalyst has on heat transfer through the reactor, it predicts higher temperature increases through the HTS reactor. This discrepancy is a result of the general limitations of the PFR model developed and is not an accurate characterization of what the actual reactor performance would be for the simulated conditions. The actual system performance would likely be closer to the performance predicted by the differential temperature reactor models, which evaluated the heat transfer in a more rigorous fashion. Still, the PFR model provides a reasonable enough estimate which can still be applied as a conservative estimate of the actual reactor performance as shown.

While the results of this parametric study indicate improved conversion at higher catalyst loading, they also indicate significant increases in pressure drop across the reactor model. This is shown in Figure 4.33, which indicates a substantial increase in the pressure drop across the reactor from 10.0 Pa for a catalyst thickness of 5×10^{-5} m to 1.39×10^{5} Pa for packed bed conditions. This is primarily a result of the increased resistance to flow through the reactor as more catalyst is coated onto the reactor walls. This also has the effect of increasing the maximum flow velocity through the reactor, as indicated in Figure 4.32, which plots the velocity profiles for each catalyst thickness. In the case of the packed bed reactor case studied, the velocity profile no longer has the parabolic distribution that is characteristic of open channel laminar flow and is instead a nearly uniform velocity profile. This is primarily a result of the increased viscous dissipation through the porous catalyst phase, as indicated in the Brinkman equations shown in equation 3.11. Significant increases in the pressure drop through the reactor would drive up parasitic pumping costs costs, a consideration that should be taken into account in addition to the potential reduction in the apparent kinetics of the process due to mass transfer limitations should it be desirable to operate a packed bed reactor utilizing more catalyst.

Table 4.4: Results from parametric sweep of catalyst thickness

	Catalyst Thickness, H_{cat} [m]	**CO Conversion, X_{CO}**	**Heat Rejection, $\dot{Q}_{WGS}$ [kW]**
HTS/LTS	Packed Bed	0.692	1.65
Prescribed Temperature	5×10^{-5}	0.826	1.24
	1×10^{-4}	0.868	1.46
	2×10^{-4}	0.899	1.65
	3×10^{-4}	0.914	1.75
	4×10^{-4}	0.923	1.83
	5×10^{-4}	0.936	1.89
Integrated Coolant	5×10^{-5}	0.821	1.24
	1×10^{-4}	0.865	1.46
	2×10^{-4}	0.898	1.66
	3×10^{-4}	0.913	1.76
	4×10^{-4}	0.922	1.83
	5×10^{-4}	0.933	1.89

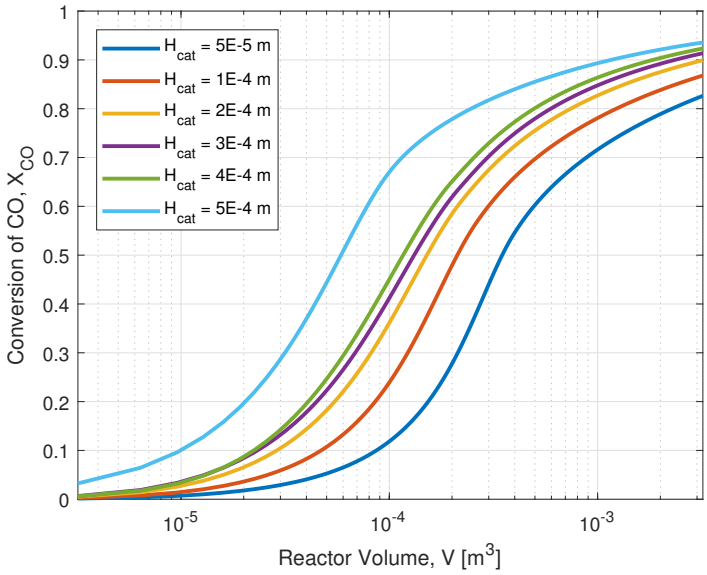

Figure 4.24: Differential temperature microreactor CO conversion profiles at varying catalyst layer thicknesses for prescribed boundary conditions

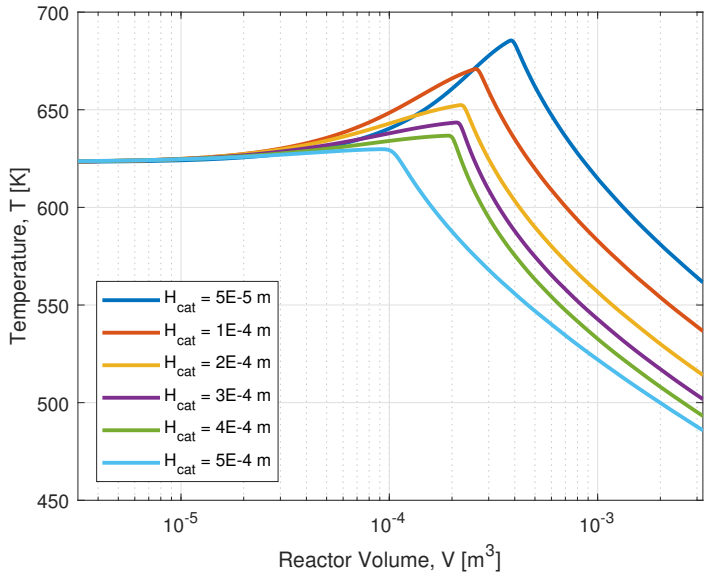

Figure 4.25: Differential temperature microreactor temperature profiles at varying catalyst layer thicknesses for prescribed boundary conditions

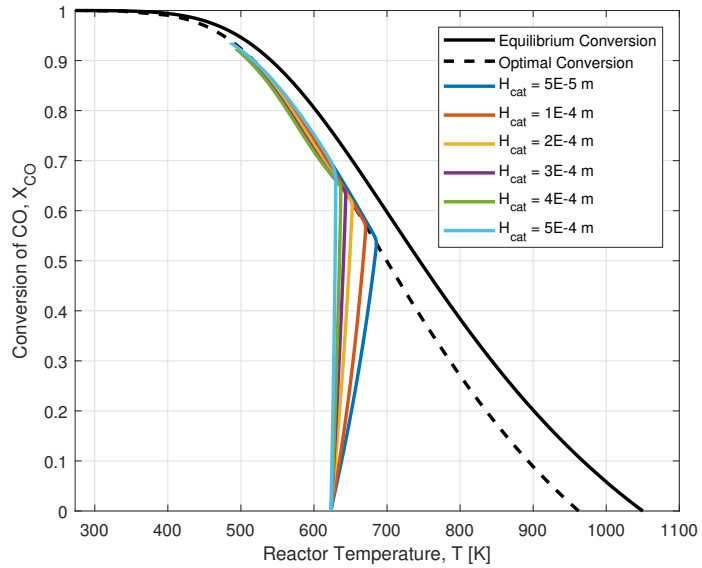

Figure 4.26: Comparison of differential temperature microreactor models to optimal progression at varying catalyst layer thicknesses for prescribed boundary conditions

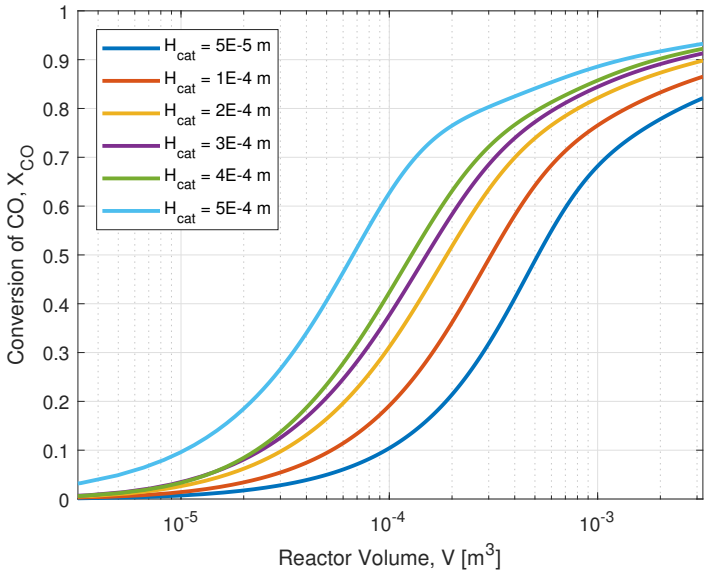

Figure 4.27: Differential temperature microreactor CO conversion profiles at varying inlet catalyst layer thicknesses for integrated coolant

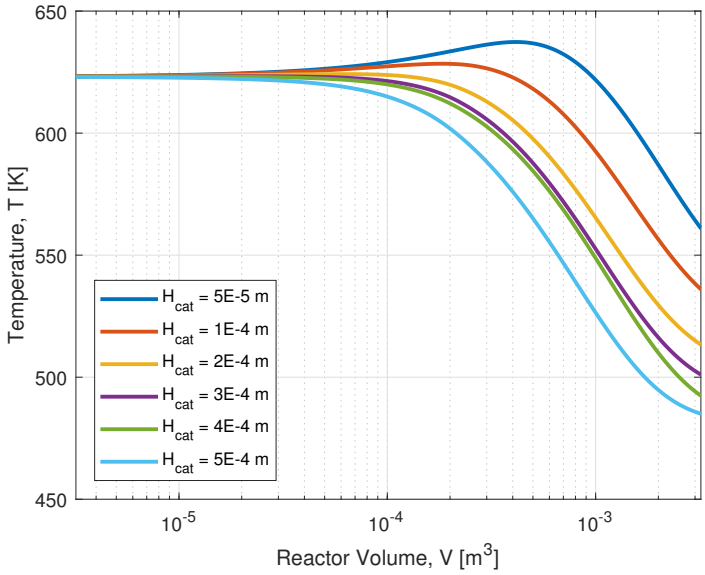

Figure 4.28: Differential temperature microreactor temperature profiles at varying catalyst layer thicknesses for integrated coolant

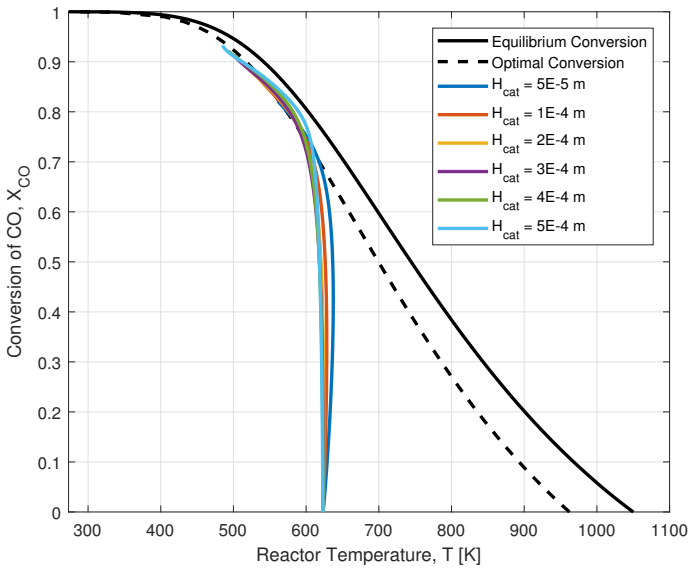

Figure 4.29: Comparison of differential temperature microreactor models to optimal progression at varying catalyst layer thicknesses for integrated coolant

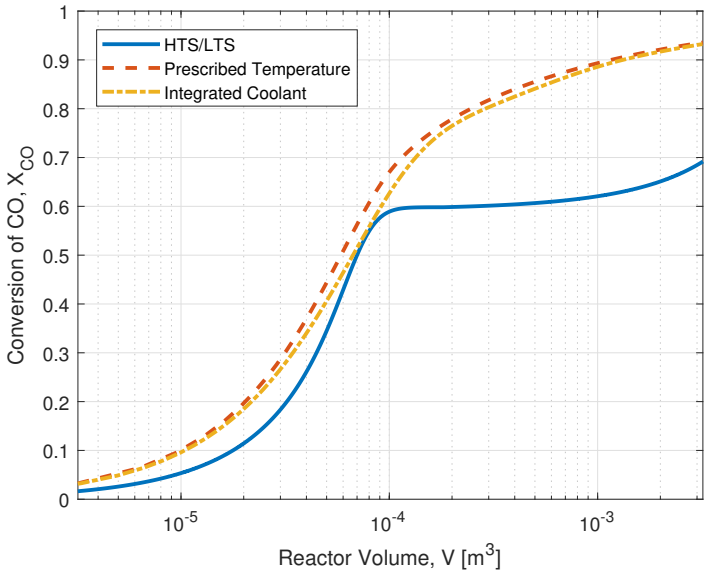

Figure 4.30: Comparison of HTS/LTS and differential temperature reactor CO conversion profiles for a catalyst thickness of 5×10^{-4} m

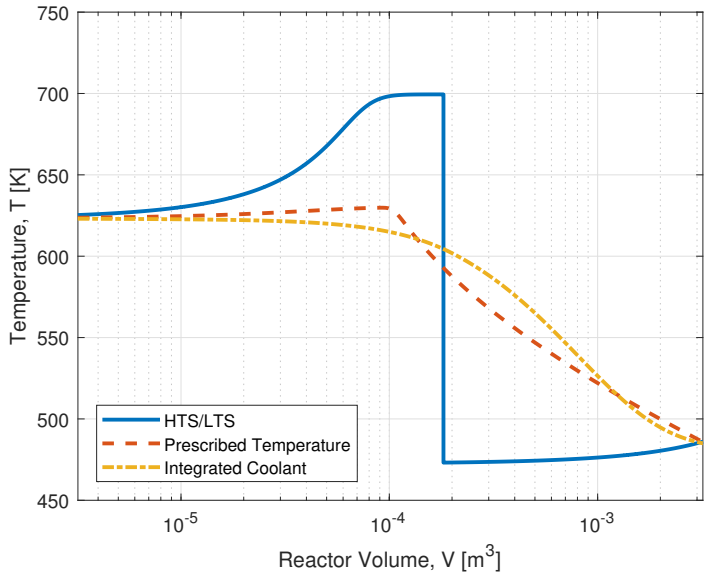

Figure 4.31: Comparison of HTS/LTS and differential temperature reactor temperature profiles for a catalyst thickness of 5×10^{-4} m

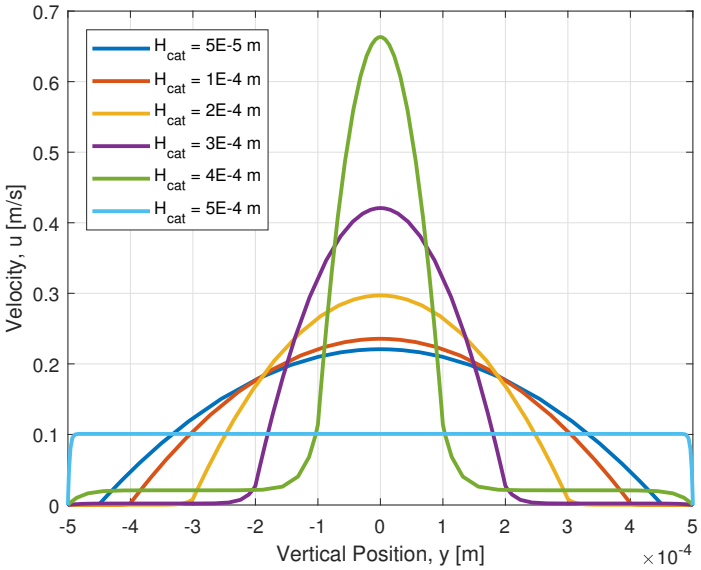

Figure 4.32: Comparison of velocity profiles at varying catalyst layer thicknesses for prescribed boundary conditions

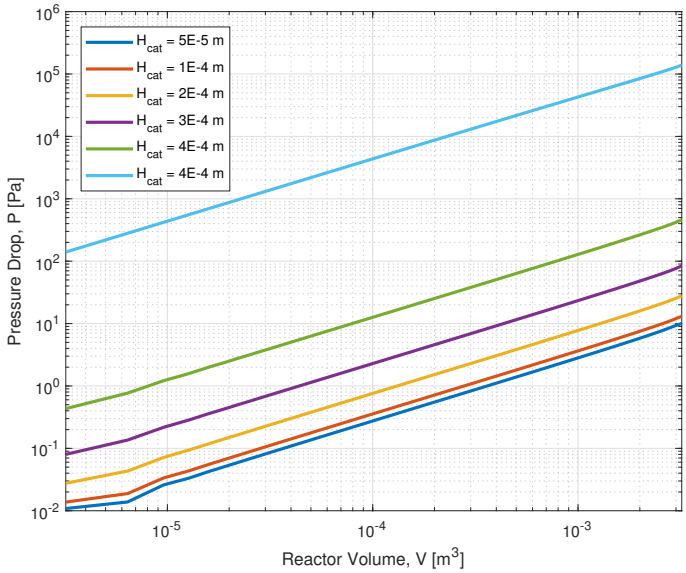

Figure 4.33: Comparison of pressure drop values at varying catalyst layer thicknesses for prescribed boundary conditions

4.5.3 Varying Cooling Length

The applied cooling length in the integrated coolant models is an important parameter affecting the overall conversion process and one of the most directly controllable microreactor design variables that can be varied in the development of an actual microreactor design. While it is assumed in the baseline integrated coolant model that the uncooled inlet section should correspond directly to the adiabatic inlet section evaluated for the prescribed temperature model, in this study, I varied the uncooled inlet section length from 0 mm to 150 mm in 50 mm increments in the manner indicated in Figure 3.6 while maintaining all other process and design parameters at their baseline values and compared the results to the baseline integrated coolant and prescribed temperature model results. The general results of this parametric study are summarized in Table 4.5. These tabulated results generally indicate very similar performance for each cooling length considered, with conversions between 0.791 and 0.821 and heat rejections between 1.20 and 1.24 kW achieved. Notably, for the coolant flow rate used, the model with cooling applied over the entire reaction channel length achieves the highest conversion while the model with the shortest cooling length achieves the lowest conversion.

Figures 4.34, 4.35, and 4.36 show how the integrated coolant model performance changes as the cooling length is increased. Figure 4.34 shows that the conversion process worsens as the cooling length decreases, though none of the integrated coolant models are able to perform better than the idealized prescribed temperature model. Like for other parametric studies performed, this is because the models with longer cooling lengths are better able to following the optimal temperature progression, as shown in 4.36. The models with adiabatic inlets of L_{ad} = 100 mm and 150 mm exhibit short plateaus in their conversion profiles where they reach equilibrium before the applied cooling is able to increase conversion. Figure 4.35 compares the temperature progressions of these models to the prescribed

temperature model and shows that the models with the shortest cooling lengths exhibit the highest temperature spikes before rapidly decreasing toward the coolant inlet temperature. Notably, for the coolant flow rate used, the reaction temperature for each cooling length considered approaches the same an outlet temperature wihin 2 °C of the coolant inlet temperature. This is primarily due to axial conduction through the reactor wall cooling the adiabatic inlet section, as previously discussed in Section 4.3. While the reaction stream in each of these studies is highly influenced by the coolant flow, higher reaction stream flow rates would prevent the reaction stream from approaching the coolant inlet temperature as closely as it does for the conditions considered since its residence time in the reactor would decrease. Counterintuitively, the model with cooling applied over its entire channel length reaches a higher maximum temperature than the model with the 24 mm adiabatic inlet section and exhibits a temperature profile closer to the ideal prescribed temperature profile. This is primarily because the fully cooled model mitigates the effects of axial conduction in the inlet section by actually transferring heat back into the reaction stream. This is better shown in Figure 4.37. Due to the heat generation from the reaction, the coolant stream actually exits the reactor at a higher temperature than the reaction inlet stream temperature. As a result, the coolant initially absorbs a significant amount of heat near the outlet of the reaction, but then transfers a small amount of this heat back into the reaction stream near the reaction inlet, resulting in slightly higher temperatures than are achieved by the models where cooling is not applied over this length. Care should be taken in selecting an appropriate coolant flow rate for reactors with full length cooling, however, as excessive cooling of the reaction stream at the inlet of the reactor can significantly reduce the reaction rate of the process and thus impede the conversion process. Still, these results suggest that satisfactory conversion and heat recovery performance can be achieved across a multitude of cooling lengths, which lends a degree of flexibility to how these differential

temperature microreactors can be designed and in the allowable coolant process conditions that can be used.

Table 4.5: Results from parametric sweep of cooling length

	Uncooled Inlet Length, L_u [m]	**CO Conversion, X_{CO}**	**Heat Rejection, $\dot{Q}_{WGS}$ [kW]**
Prescribed Temperature	0.024	0.826	1.24
Integrated Coolant	0	0.822	1.24
	0.024	0.821	1.24
	0.050	0.821	1.24
	0.100	0.812	1.23
	0.150	0.791	1.20

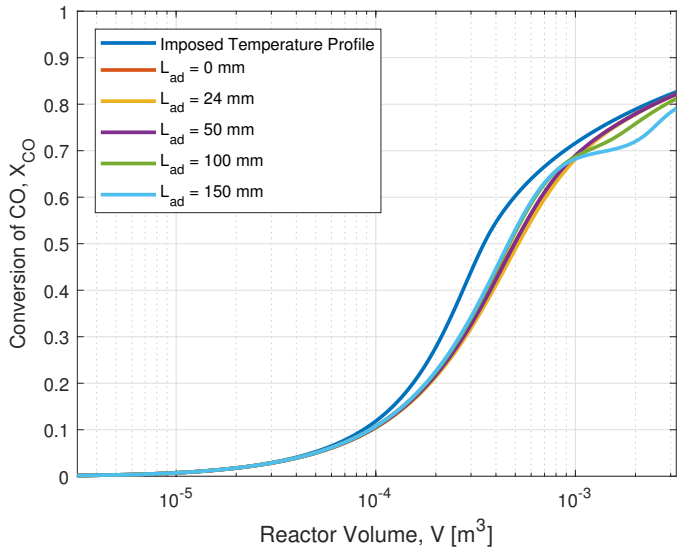

Figure 4.34: Differential temperature microreactor CO conversion profiles for varying cooling lengths

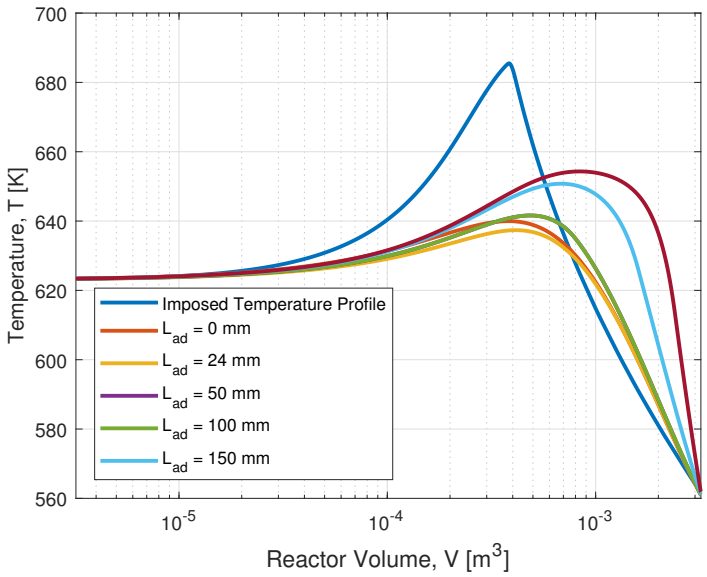

Figure 4.35: Differential temperature microreactor temperature profiles for varying cooling lengths

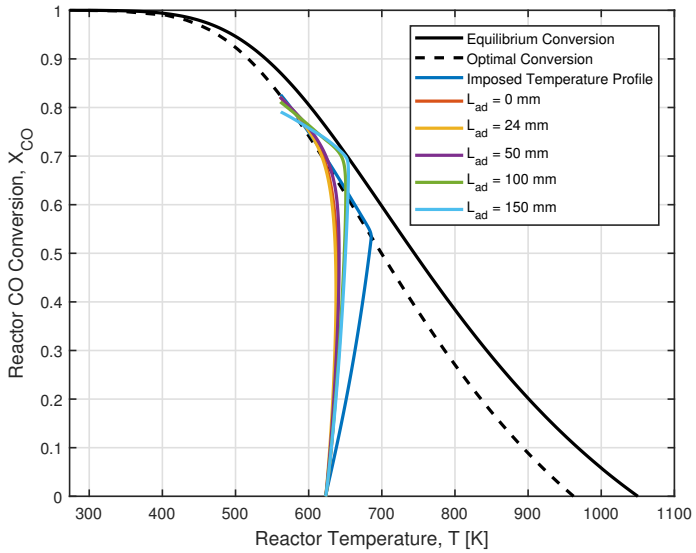

Figure 4.36: Comparison of differential temperature microreactor models to optimal progression at varying cooling length

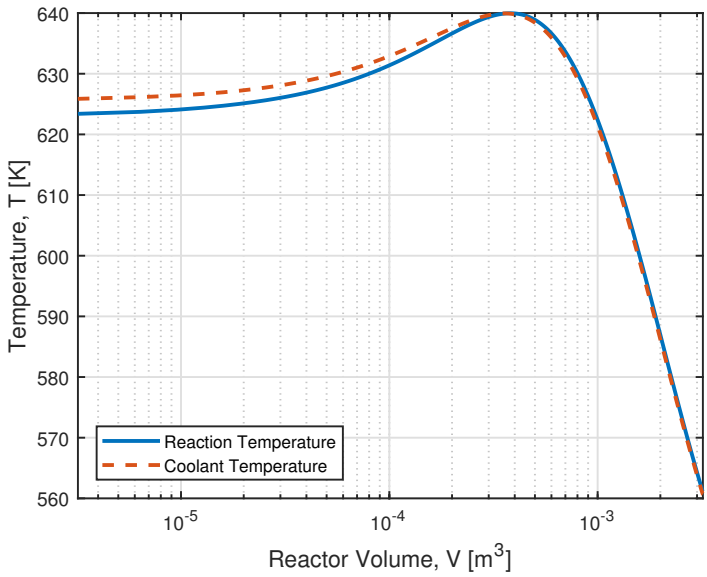

Figure 4.37: Comparison of reaction and coolant stream temperatures for the integrated coolant model with full length cooling

4.6 Modeling Results Summary

The modeling results presented in this chapter indicate that differential temperature WGS reactors appear practically capable of enhancing CO conversion beyond what the standard HTS/LTS reactors can achieve. For the baseline conditions modeled, the integrated coolant model achieves a 13.9% reduction in the required reactor volume and a 82.2% reduction in the required amount of catalyst compared to the HTS/LTS reactors to achieve a CO conversion of 80% despite kinetic limitations that arise due to there being less catalyst in the reactor with even large volume reductions possible at higher reactor catalyst loadings. These results are for a highly conservative model of the HTS/LTS process, however, and represent the minimum possible volume and catalyst reductions possible. In reality, even larger reductions in the reactor volume and required amount of catalyst are likely possible. A

parametric study examining the effects of inlet temperature on reactor performance suggests that larger reductions in reactor volume/catalyst can be achieved for reactors operating at higher temperatures, although there are diminishing returns to the practical benefits achieved as higher inlet temperatures are used. A second parametric study examining the effects of the total catalyst used in the reactor suggests that increasing the catalyst packing reduces kinetic limitations significantly, as would be expected, reducing the total required reactor volume, though at the cost of increased pressure drop through the reactor. It is also worth noting that care would have to be taken doing this as the introduction of additional catalyst could lead to larger mass transfer limitations in the process. Finally, a third parametric study examining the effects of cooling length on reactor performance suggests that microreactors with longer longer applied cooling lengths are capable of achieving better CO conversion and heat recovery performance, but also indicates that satisfactory results can be achieved over a variety of cooling lengths as well and that care must be taken to avoid excessive cooling of the reaction stream near its inlet to avoid impeding the reaction kinetics. The general influence of these process and design parameters on reactor performance is important in determining an appropriate reactor design and each of these factors was considered in the development of an initial WGS microreactor prototype, which is discussed in greater detail in Chapter 5.

Chapter 5: Prototype Design and Experimental Verification

Previous chapters show the potential of differential temperature WGS microreactors to intensify the production of hydrogen. To realize this potential, physical design and fabrication methods for differential temperature WGS microreactors must be developed. Thus, this chapter presents an additively manufactured microreactor prototype design developed using the modeling results presented in the previous chapters as part of an initial evaluation of the potential of additive manufacturing for this purpose. While the prototype is designed based on a reacting flow model, insertion of catalyst and evaluation of reacting flow was outside of the scope of this study. As a first step, the thermal-hydraulic performance of the reactor design without catalyst was evaluated to validate the fabrication approach and modeling methods. Therefore, this chapter also presents the experimental and data reduction approach used to verify if the of thermal-fluid portion of the modeling performed in Sections 3 and 4 can predict the actual performance of the device with sufficient accuracy. Future work will build on the modeling and fabrication approaches demonstrated here to produce a differential temperature WGS microreactor with integrated catalyst.

5.1 Microreactor Prototype Design

I used the results generated from the modeling effort presented in Chapters 3 and 4 to develop a differential temperature WGS microreactor prototype design capable of achieving 80% CO conversion for the reaction stream composition listed in Table 3.1 at approximately a sixth scale of the listed production capacity. In collaboration with an additive manufacturing vendor (i3D in Bend, Oregon), an iterative process was used to produce a prototype

design that met this performance requirement and could be manufactured using Inconel 718 and a selective laser melting (SLM) additive manufacturing technique. Figure 5.1 shows the general footprint of this design and Figures 5.2 through 5.4 show section views of the internal features of the design. The prototype consists of two inlets and two outlets for the coolant flow and reaction flow to enter and exit the device. The fluid streams first enter into header chambers and then split to flow through multiple identical parallel rectangular flow channels. The streams then re-converge at an outlet header chamber and then exit the device. The channels operate primarily in counter flow, but the configuration of the inlet and outlet chambers induces a lateral motion to the flow that is more similar to cross flow, as indicated on Figure 5.4.

The prototype was fabricated out of Inconcel 718 using a selective laser melting (SLM) process, which was discussed in Sections 1.5 and 2.6. Outside of the SLM process which fully formed the body of the prototype in a single manufacturing step, the only other required manufacturing step was to tap the inlets and outlets of the device with NPT threads so that the prototype could be mated with tube fittings and plumbed into the test facility discussed in Section 5.2.1. Figure 5.1 shows this finished prototype. The design consists of 25 reaction channels, each with a height of 1 mm, a length of 100 mm, and a width of 80 mm, and 25 coolant channels, each with a height of 0.5 mm, a length of 100 mm, and a width of 80 mm. The walls separating the channels each have a thickness of 0.5 mm. While several of these values directly correspond to the baseline modeling parameters listed in Table 3.2, the channel lengths and the number of channels differ due to manufacturing constraints. Furthermore, a catalyst coat was not applied to the reaction channels as only the thermal-hydraulic performance of the device was evaluated as part of this experimental study. Had a thin $H_{cat} = 5 \times 10^{-5}$ m coat of platinum catalyst been applied to the walls of the channels in this prototype, modeling results suggest that the device would be capable

of producing approximately 4 kg of hydrogen per day, which would scale up to 24 kg of hydrogen per day for actual distributed production conditions. When acting just as a heat exchanger for non-reacting flow conditions, modeling results suggest that the prototype is capable of operating over a range of heat exchanger effectiveness values varying from approximately 0.6 to 0.85 for expected operating conditions, allowing for good temperature control over one stream by varying the flow and temperature conditions of the other stream as is desired for the actual reactor operation.

The size of the powder bed used for the SLM manufacturing process limited the possible overall length and height of the prototype, necessitating the manufacturing of a scaled down version of the design proposed in the baseline modeling conditions. The prototype was manufactured out of Inconel 718 primarily due to the better resistance nickel alloys display at higher temperature and corrosive operating conditions compared to stainless steels, but also because it significantly reduced the manufacturing cost associated with the prototype. This is a result of the Inconel 718 powder used being much coarser than the stainless steel powders available from the vendor, which corresponds to significantly reduced print times and thus lower overhead manufacturing costs, but also a rougher surface finish and worse printing resolution. These disadvantages are consistent with what the studies cited in Section 2.6 suggest.

Notably, although Table 2.3 suggests that SLM manufacturing processes are capable of achieving very good build resolutions of ± 0.1 mm, this is highly dependent on the size of the powder used in the process. For the developed prototype, which was manufactured using a coarser powder, resolutions much smaller than ± 0.5 mm were not possible as it would have made it too difficult to remove the unmelted powder from the internal features of the device once the printing process was completed. While advances in additive manufacturing are beginning to relax these manufacturing limitations, they still posed a notable challenge in

the development of this prototype, simultaneously limiting both the minimum characteristic lengths within the reaction channels to a larger scale than was initially desired and the maximum allowable prototype footprint to a smaller size than initially desired due to the size of the powder bed used to manufacture the device. Still, the relative simplicity of the SLM manufacturing process in terms of the number of manufacturing steps required is appealing since the only major post-processing steps that would be required are integrating catalyst into the device and installing the reactor into the system, though the former task is non-trivial and more work needs to be done to facilitate easier catalyst integration into these devices due to the lack of interior access to the channels.

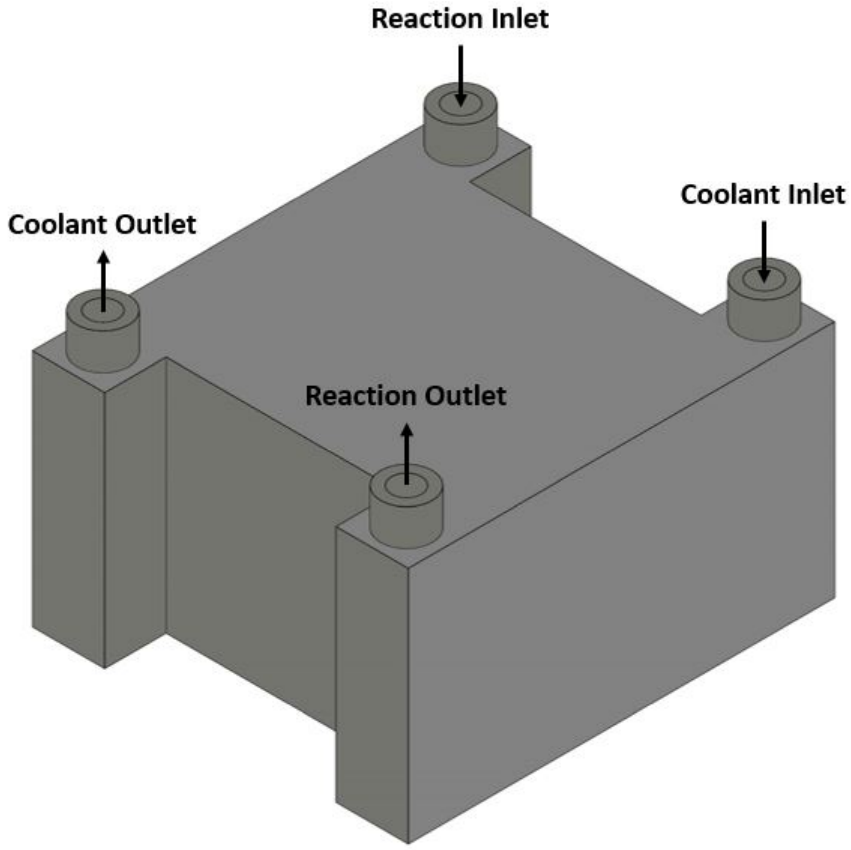

Figure 5.1: Rendered view of microreactor prototype considered

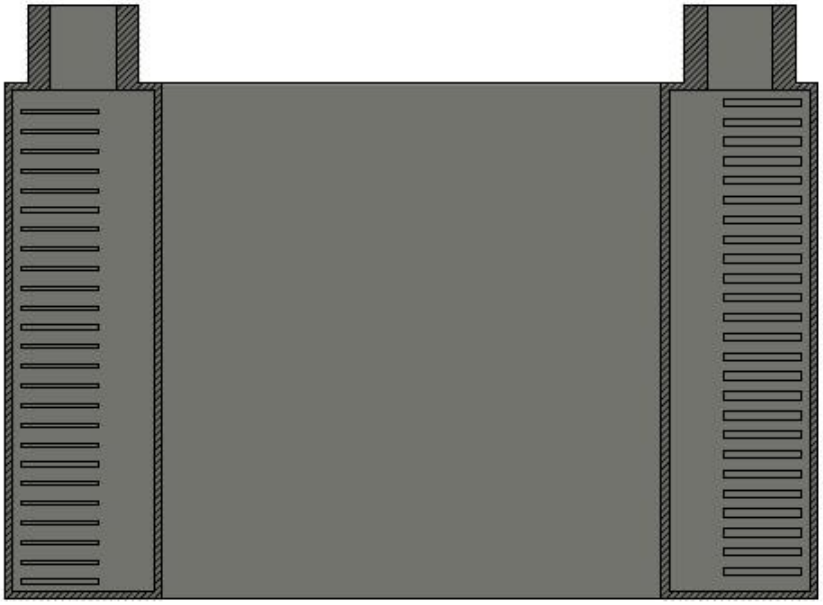

Figure 5.2: Section view of interior of prototype header chambers

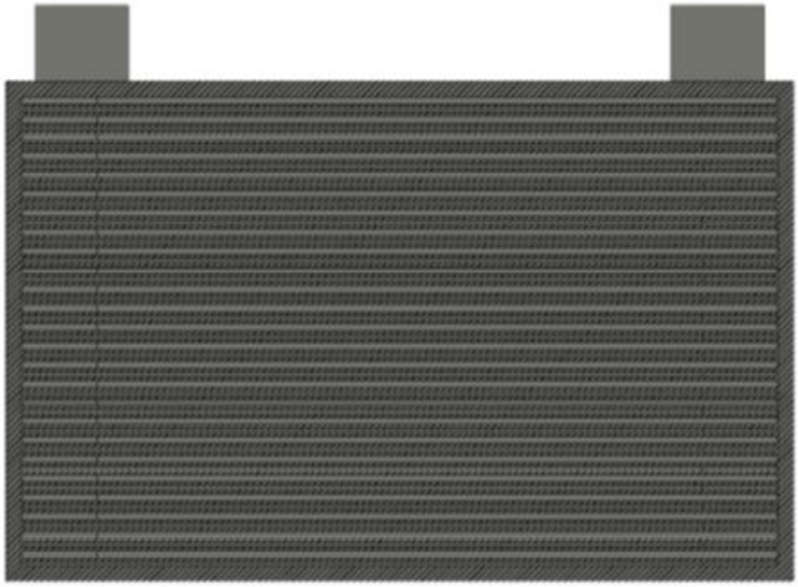

Figure 5.3: Section view of interior of prototype channels

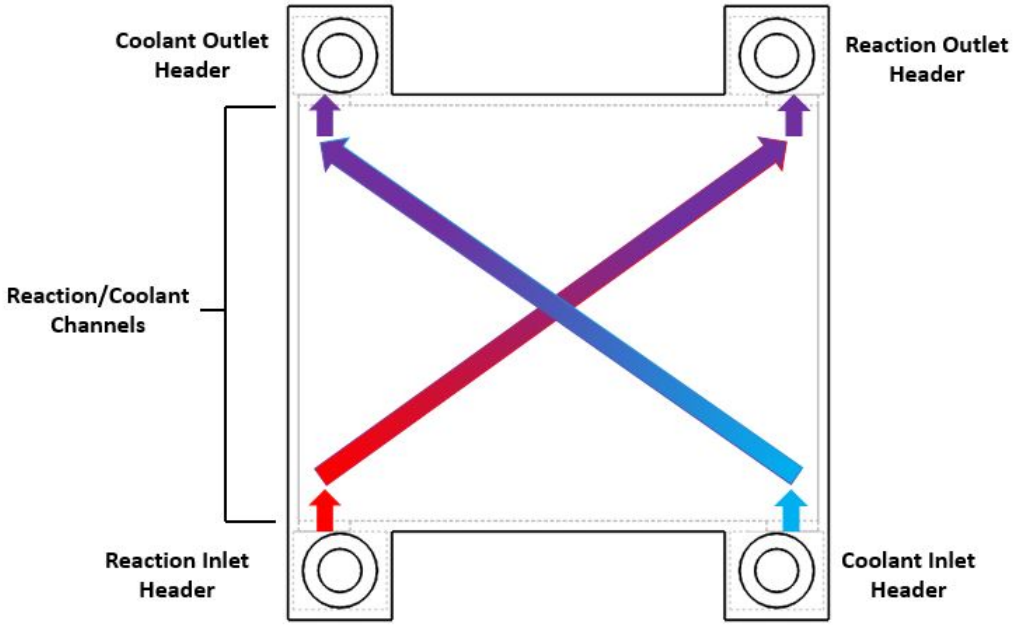

Figure 5.4: Flow paths of reaction and coolant channels

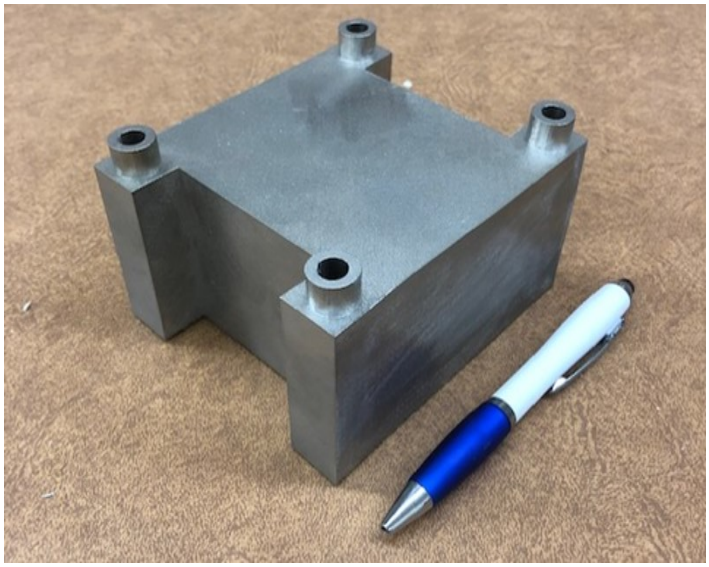

Figure 5.5: Finished prototype with pen for scale

5.2 Experiment Design

This section outlines the experimental approach used to determine the heat exchanger effectiveness of and the pressure drop through the prototype under different operating conditions as part of a general evaluation of its thermal-hydraulic performance. The design and layout of the test facility used for the experiments, the general experimental procedure used, and the required calculations necessary to evaluate these parameters are all presented in detail.

5.2.1 Test Facility and Data Acquisition System

A labeled picture of the test facility used for this study is shown in Figure 5.6 and a piping and instrumentation diagram (P&ID) of the test facility is shown in Figure 5.7. In this flow arrangement, instrument air acts as the working fluid. The instrument air enters the facility through a Norgren pressure regulator that can maintain the inlet pressure at values up to approximately 80 psig. The air then passes through a Norgren 5 μm filter to prevent any oil or condensed water present in the instrument air from entering the system. At the outlet of the air filter, the tubing changes from 1/4" 316 stainless steel to 1/4" Teflon to reduce the pressure drop through the facility and to allow for flexibility in how the connection to downstream components is made. The instrument air then splits through a tee to form the hot and cold side streams that flow through the reactor prototype. On the hot side, a needle valve and Micro Motion Coriolis flow meter are used to control and measure the mass flow. After the flow meter, the tubing changes from 1/4" Teflon to 3/8" 316 SS and next passes through a 1 kW Tutco Farnam process air heater that heats the air to the desired inlet temperature to the prototype. The heater power is controlled using a silicon controlled rectifier (SCR). Omega Type K thermocouples are inserted into the

flow at both the inlet and outlet of the hot side to measure the change in air temperature across the prototype. A Rosemount absolute/differential pressure transducer is connected to the inlet and outlet of the hot side of the prototype to measure the inlet static pressure and the pressure drop across the prototype. After exiting the hot side of the prototype, the air stream immediately vents to the atmosphere. On the cold side, the component arrangement is nearly identical to the hot side arrangement with the exception of the flow meter and pressure transducers used. Instead of a Coriolis mass flow meter being used, a Dwyer rotameter is used to directly measure the volumetric flow rate. Instead of a single absolute/differential Rosemount transducer, separate Omega static and Rosemount differential pressure transducers are used to measure the inlet pressure and the pressure drop across the cold side of the prototype.

As shown in Figure 5.7, the electrical signals from all of the measurement instruments except the rotameter are sent to a data acquisition (DAQ) system, where they are conditioned and then sent to a computer to be read and recorded in LabVIEW. A more detailed diagram showing how these electrical signals are transmitted, conditioned, and recorded is shown in Figure 5.8. All thermocouple signals are sent to an NI 9214 Thermocouple module from National Instruments. This DAQ card applies a cold junction correction to the received voltage signals, filters and amplifies these signals, and then performs a 24-bit analog to digital conversion on these signals so that they can be read and recorded by the computer. This DAQ card also features open thermocouple detector (OTD) circuits to detect faulty signals from broken thermocouples. The signals from the pressure transducers and Coriolis flow meter are sent to an NI 9208 Analog Input module. Although the pressure transducer signals can be sent directly to this DAQ card, the Coriolis flow meter signal requires a separate transmitter. This DAQ card amplifies the signals from these instruments and performs a 24-bit analog to digital conversion for the signal to be read and recorded

by the computer. The data collected using LabVIEW was collected at a frequency of 1 Hz. Because I am only interested in the steady state operating data for the prototype, faster sampling rates are unnecessary as there is no need to rapidly resolve changes in the data with time. All readings from the Dwyer flow meter are manually recorded. The major pieces of instrumentation used in this study are summarized in more detail in Table 5.1.

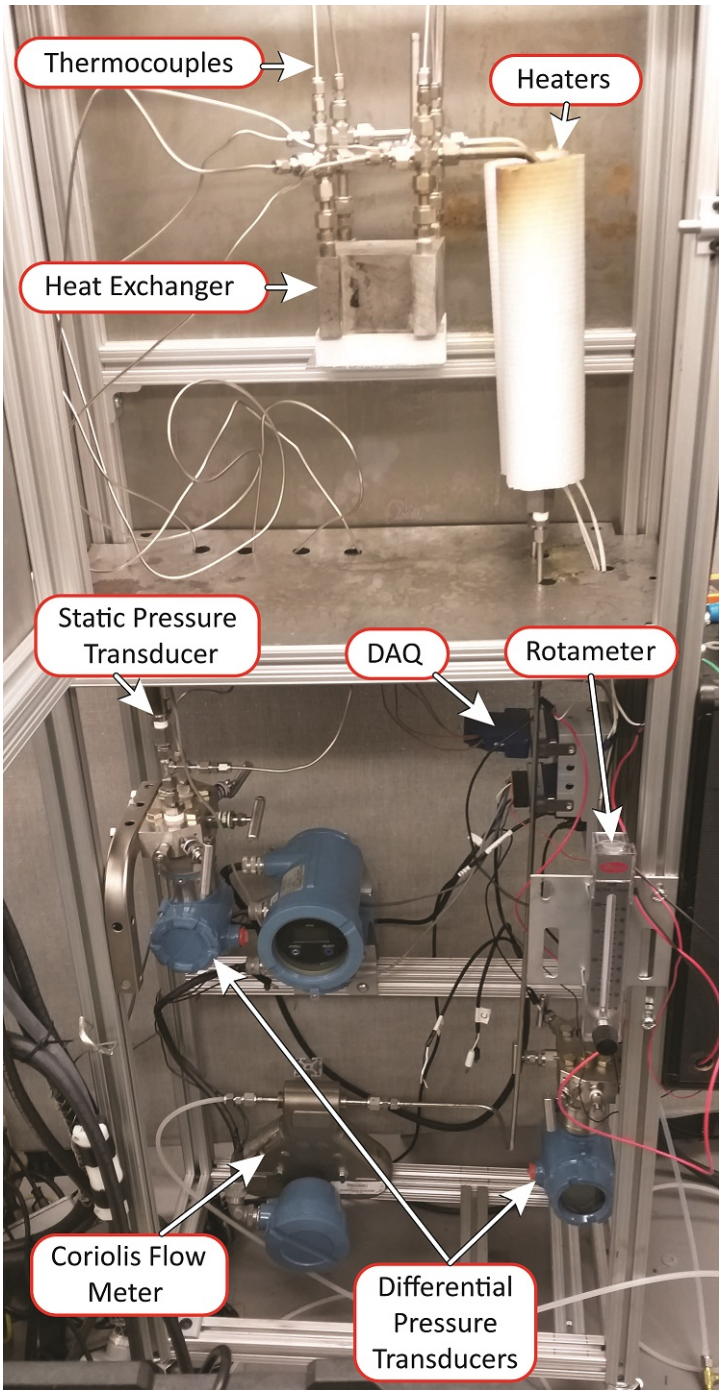

Figure 5.6: Labeled test facility picture

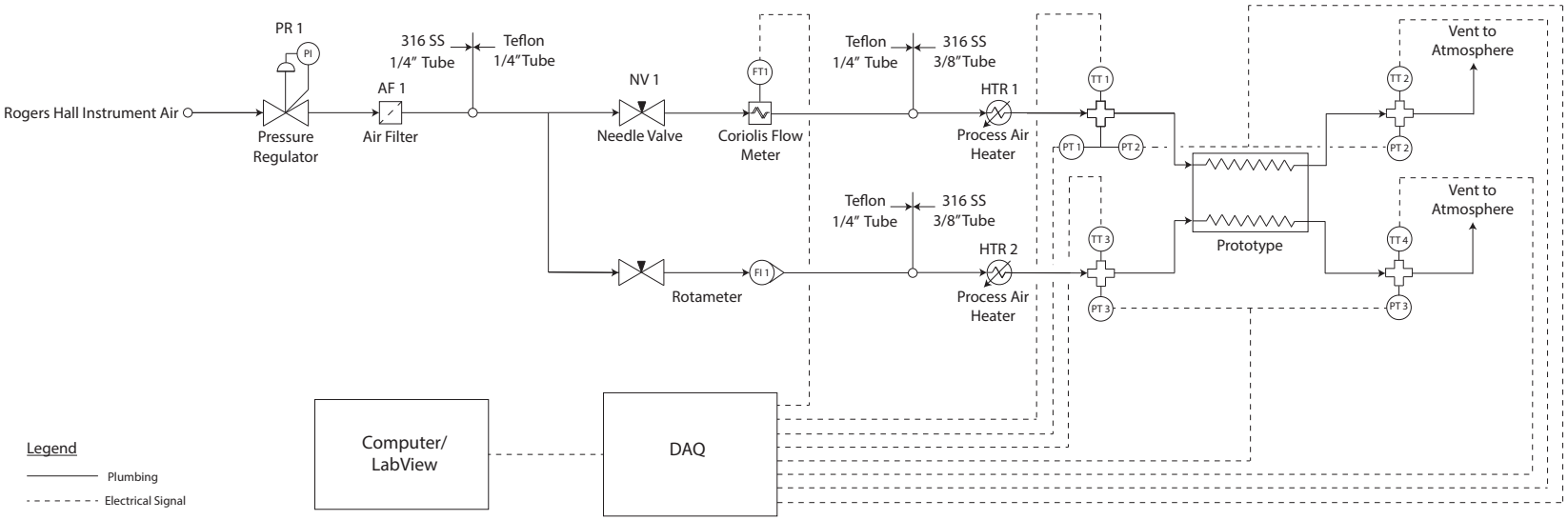

Component	Description	Quantity
PR 1	Norgren Pressure Regulator, 50-150 psia	1
AF 1	Norgren Air Filter, 5 micron	1
NV 1	Swagelok Integral Bonnet Needle Valve	1
FT 1	Micro Motion Coriolis Flow Meter	1
FI 1	Dwyer Rotameter, SS Valve, 20-200 SCFH	1
HTR 1,2	Tutco Farnam Heat Torch Process Air Heater, 1000 W	2
TT 1-4	Omega Type K Thermocouple, Ungrounded	4
PT 1	Omega Static Pressure Transducer, 0-300 psia	1
PT 2	Rosemount Differential Pressure Transducer, -62.2 to 62.2 kPa	1
PT 3	Rosemount Absolute/Differential Pressure Transducer, 0.5-3626 psia static pressure range, -2.5 to 2.5 bara differential pressure range	1

Figure 5.7: Piping and instrumentation diagram of experimental facility

Table 5.1: Summary of important instrumentation and equipment used in test loop

Instrument	**Manufacturer**	**Part Number**	**Range/Capacity**	**Measurement Uncertainty**
Coriolis Flow Meter	Micro Motion	CMF010M323NQBUEZZZ	0 to 5.3 g/s (air)	±0.0032% reading
Rotameter	Dwyer	RMB-54-SSV	20 to 200 SCFH (air)	±2% full scale
Heat Torch Process Air Heater	Tutco Farnam	HT075-1000-208-1/4F-3/8F-X	1 kW, 250 °F to 1300 °F	n/a
Silicon Controlled Rectifier	Payne Controls	18D-2-10i	2.4 kVA @ 208 VAC	n/a
Absolute/Differential Pressure Transducer	Rosemount	3051SMV5M23A4N2A11A1AM5	Static: 0.5 to 3626 psia Differential: -2.5 bara to 2.5 bara	±0.04% reading
Absolute Pressure Transducer	Omega	PX209-300AI	0 to 300 psi	±0.25% reading
Differential Pressure Transducer	Rosemount	3051CD2A02A1AS5	-62.2 to 62.2 kPa	±0.14% reading
Type K Thermocouple	Omega	KMQXL-125U-12	-200 °C to 1250 °C	±2.2 °C

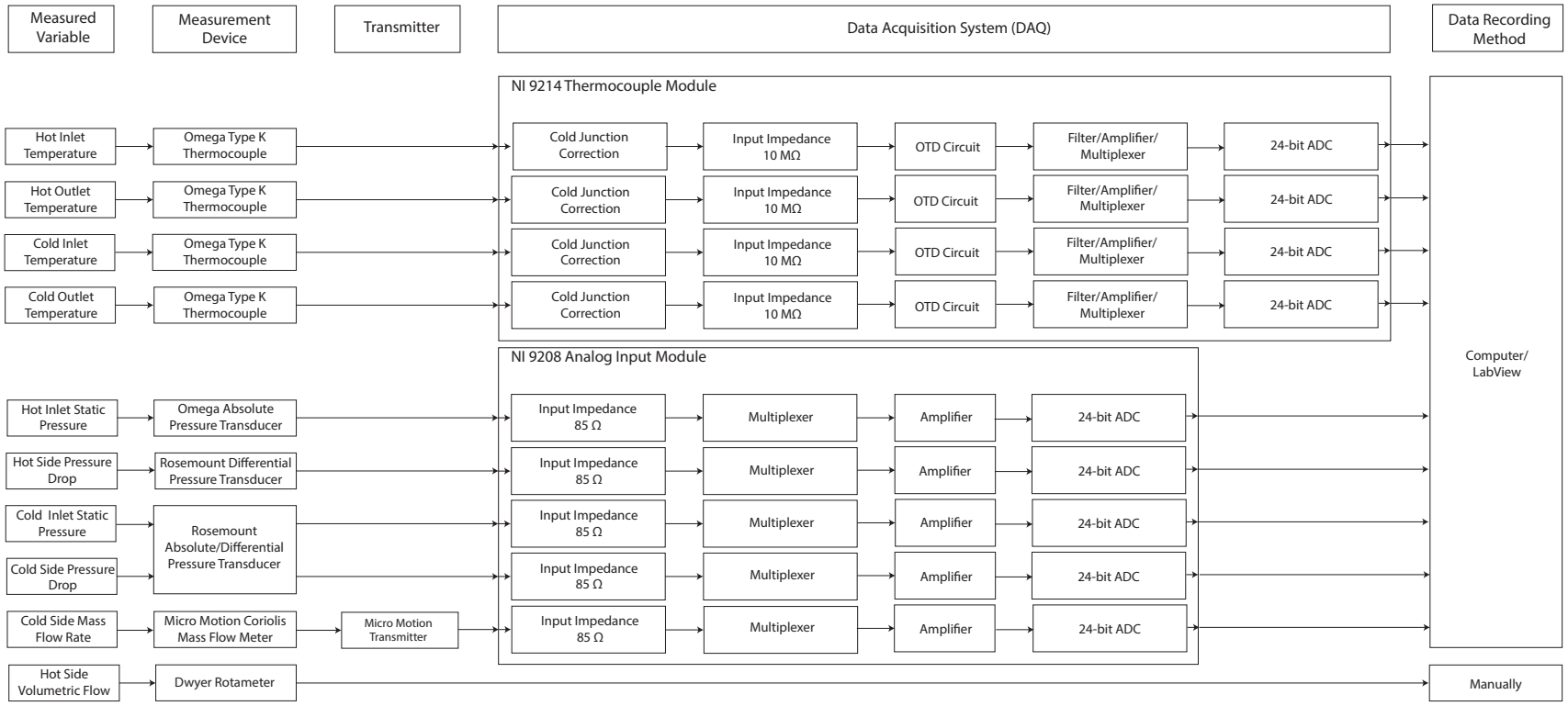

Figure 5.8: Data acquisition system signal processing

5.2.2 Experimental Procedure

To collect data from the test loop, all instruments in the test loop are first turned on and allowed to run for about 15 minutes so that they can properly warm up. LabVIEW is then opened and used to verify that all instruments are reading correctly for ambient conditions. Air flow through the system is then turned on by opening the instrument air regulator and setting it to a value of 75 psig. The needle valves on both the hot and cold sides of the test loop are then used to adjust the flow rates to the desired set points. The SCRs are then adjusted to set the inlet temperatures of both streams to the desired set points. Once the inlet temperatures are set to the desired values, the entire system is then allowed to reach steady state. In the context of the testing being performed, this is defined as the point at which the outlet temperatures from the prototype were observed to change by less than 1 °C over a period of 20 minutes or longer. This can take several hours to reach for each data point. Once steady state is achieved, LabVIEW is used to record data from the system for several minutes and several volumetric flow rate readings from the rotameter are manually recorded.

Using the procedure outlined above, I obtained data for a hot side mass flow rate sweep, where the mass flow rate on the hot side was incrementally adjusted across several data points, and for a cold side inlet temperature sweep, where the cold side inlet temperature was adjusted across several data points. For the hot side mass flow rate sweep, I maintained the cold side flow rate at a constant value of 80 SCFH and the hot and cold side inlet temperatures at 150 °C and 100 °C, respectively, while varying the hot side flow rate between approximate values of 0.4, 0.8, 1.0, and 1.2 g/s. For the cold side inlet temperature sweep, I maintained the hot side inlet temperature at 100 °C and the hot and cold side flow rates at 0.8 g/s and 80 SCFH, respectively, while varying the cold side inlet temperature between approximate values of 25 °25, 50 °C, and 75 °C. For the tests conducted, the hot

side of the device corresponded to the coolant channels of the device and the cold side corresponded to the reaction channels of the device.

5.2.3 Data Processing

While it is possible to directly measure the pressure drop across both sides of the prototype using differential pressure transducers, it is necessary to calculate the heat exchanger effectiveness of the device from the collected experimental data. The average temperature and pressure of the hot and cold streams ($T_{H,avg}$, $T_{C,avg}$, $P_{H,avg}$, $P_{C,avg}$) can be determined from the measured temperature and pressure data ($T_{H,i}$, $T_{H,o}$, $T_{C,i}$, $T_{C,o}$, $P_{H,i}$, $P_{C,i}$, ΔP_H, ΔP_C) and subsequently used to evaluate the average specific heat at constant pressure of each stream ($c_{p,H}$,$c_{p,C}$) using the built in property evaluation functions in Engineering Equation Solver (EES). From these values, the heat duties of the two streams are evaluated as:

$$\begin{aligned} \dot{Q}_H &= \dot{m}_H c_{p,H}(T_{H,i} - T_{H,o}) \\ \dot{Q}_C &= \dot{m}_C c_{p,C}(T_{C,o} - T_{C,i}) \end{aligned} \tag{5.1}$$

Although the hot side mass flow rate is measured directly using a Coriolis flow meter, as discussed in Section 5.2.1, the cold stream mass flow rate is not directly measured. Instead, a rotameter is used to measure the cold side volumetric flow rate due to equipment/cost limitations. The cold side mass flow rate is calculated from this measured value as:

$$\dot{m}_C = \rho_{C,i}\dot{V}_{C,i} \tag{5.2}$$

In equation 5.2, the density of the cold fluid is evaluated from the ideal gas law as:

$$\rho_{C,i} = \frac{P_{C,i}}{RT_{amb}} \tag{5.3}$$

In equation 5.2, T_{amb} is the temperature of unheated cold side air flowing through the rotameter, which is measured using the cold inlet thermocouple before the heaters are turned on. From the flow rate measurements and evaluated specific heats, the capacity rates of both streams are evaluated as:

$$\begin{aligned} C_H &= \dot{m}_H c_{p,H} \\ C_C &= \dot{m}_C c_{p,C} \\ C_{min} &= min(C_H, C_C) \end{aligned} \tag{5.4}$$

In equation 5.4, the minimum capacity rate, C_{min} , is evaluated as the lower of the calculated capacity rates for the hot and cold sides, C_H and C_C. From the minimum capacity rate and the inlet temperatures, the maximum possible heat duty for the prototype at a specific operating condition is evaluated as:

$$\dot{Q}_{max} = C_{min}(T_{H,i} - T_{C,i}) \tag{5.5}$$

Finally, using the calculated hot side heat duty and the maximum possible heat duty value, the effectiveness of the prototype at a certain operating condition is evaluated as:

$$\epsilon = \frac{\dot{Q}_H}{\dot{Q}_{max}} \tag{5.6}$$

As discussed in Section 5.3, the hot side heat duty is used to evaluate the effectiveness in equation 5.6 because there is less uncertainty associated with this value than there is with the cold side heat duty due to the different flow measurement devices used.

5.3 Uncertainty Analysis

To evaluate the uncertainty in the calculated values listed in Section 5.2.3 from the uncertainties in the measured values, a propagated uncertainty analysis was conducted. I used the method proposed by Kline and McClintock [63] to calculate the uncertainty for most values as explicit partial derivatives could be taken in most cases. I used the sequential perturbation method to evaluate the uncertainty in the specific heat values, however, as these values were evaluated using Engineering Equation Solver (EES) and not using explicit equations. Figure 5.9 generally shows how all of the measured sources of uncertainty relate to the uncertainty in the calculated heat exchanger effectivness and demonstrates the particular importance of the uncertainty in the measured flow rates and temperatures to this top level uncertainty. Notably, the uncertainty associated with the C_{min} value depends on which fluid has the minimum capacity rate at each data point considered.

In the uncertainty calculations, the nominal value for each measured variable was taken as the average value of the recorded measurements. Each measured value had a bias uncertainty U_b, and a precision uncertainty, U_p, associated with it. The bias uncertainty for each measured value was estimated as the instrument uncertainty and included the uncertainty associated with the instrument itself and the uncertainty associated with the DAQ when necessary. The precision uncertainty was evaluated from the collected experimental data at 95% confidence using the student t-distribution as:

$$U_p = t_{95}\frac{S}{\sqrt{n}} \tag{5.7}$$

where n is the total number of measurements taken for a variable, S is the standard deviation of that variable, and t_{95} is the student t value at 95% confidence for $n-1$ degrees of freedom. To reduce the influence of precision uncertainty on the collected experimental

results, a large amount of data was collected for each experimental steady-state operating point. Generally, more than 700 data points were collected for each operating point tested. As a result, during data processing, the precision uncertainty was always several orders of magnitude less than the bias uncertainty.

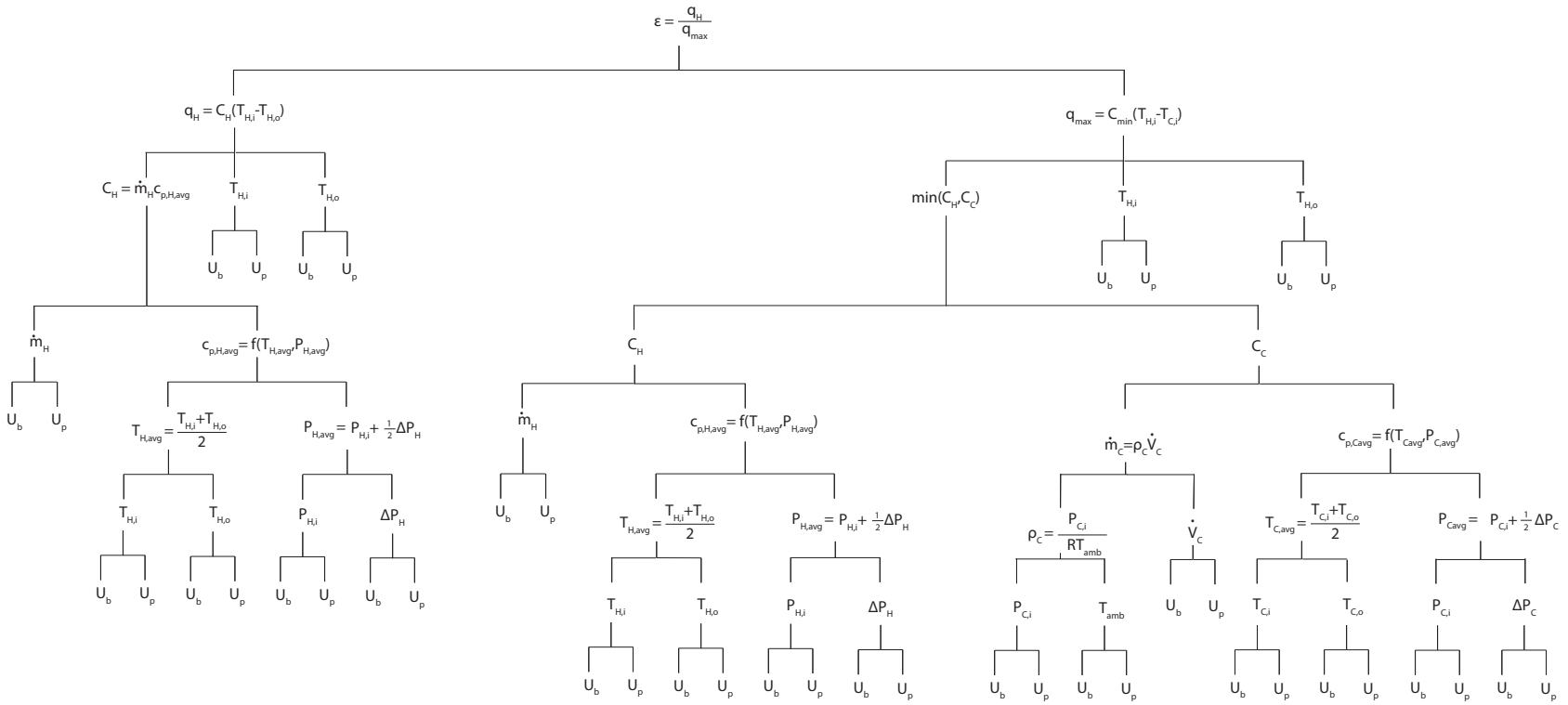

Figure 5.9: Uncertainty tree

5.4 Experimental Results

The experimental results evaluated from the data recorded using the experimental procedure presented in Section 5.2.2 and the equations presented in Section 5.2.3 are outlined in this section. These experimental results are also directly compared to results generated using a thermal-hydraulic model of the prototype in COMSOL Multiphysics operating at the same inlet conditions to evaluate how well the model agrees with the experimental results by applying equations 3.14 and 3.25 for air as the working fluid on both sides of the device.

5.4.1 Hot Side Flow Rate Sweep

The results of the hot side flow rate sweep are presented in this section. As a first check of the validity of the collected data, the heat duty for the hot and cold streams were calculated using equation 5.1 and compared to ensure a reasonable energy balance. Figure 5.10 shows how the heat duty of both the hot and cold streams vary as a function of the hot side mass flow rate. Here, the average percent difference in measured heat duty between the streams was 5.39%, with a maximum percent difference of 6.53%. However, the heat duty for the hot and cold side were within experimental uncertainty for all points. In general, the uncertainty in the hot side heat duty is lower due to the lower uncertainty in measured mass flow compared to the analogous uncertainty in the measured volumetric flow for the cold side. Thus, the hot-side heat duty is used in all subsequent effectiveness calculations.

Figure 5.11 shows how the measured pressure drop across the hot and cold sides of the prototype vary as the hot side mass flow rate is increased and compares these results to the pressure drops predicted using the developed COMSOL model. These results indicate a linear increase in the hot side pressure drop as the hot side mass flow rate increases and a nearly constant trend in the cold side pressure drop. Here, there is an average percent

difference of 19.6% and a maximum percent difference of 45.4% between the experimental pressure drop and the COMSOL model pressure drop for the hot side and an average percent difference of 7.08% and a maximum percent difference of 7.63% between the experimental pressure drop and the COMSOL model pressure drop for the cold side. While the maximum percent difference appears fairly large for the hot side comparison, this data point occurs for the lowest nominal pressure drop reported and only corresponds to a difference of 0.90 kPa between the experimental and model results. Notably, the modeled value nearly falls within the uncertainty bars of this experimental point as well. Excluding this point immediately drops the maximum percent difference down to only 15.8%, a value that appears more reasonable. The observed increase in the hot side pressure drop is primarily a result of the higher friction losses, which increase linearly with flow velocity for the laminar flow conditions that would be expected within the thin flow channels of the prototype. While the cold side pressure drop does appear constant, it does increase slightly as the hot side flow rate is increased. This is primarily due to slight changes in the fluid properties of the cold stream as a result of its varying temperature profile. The COMSOL simulation results appear to reasonably predict the experimental pressure drop values, with the cold side pressure drops falling within the experimental error bars and the hot side pressure drops nearly falling within the uncertainty bars for each case. Discrepancies between the modeled and the experimental pressure drops are likely at least partially attributable to the model not correctly calculating the pressure drop in the inlet/outlet chambers of the prototype, where there would likely be more turbulence and circulation contributing to pressure drop. Given the very consistent trend of the model overpredicting the hot side pressure drop and slightly underpredicting the cold side pressure drop, it also appears possible that the hot side channels may be slightly larger than the ones specified in the COMSOL model, resulting in slightly less obstruction to flow and thus less pressure drop.

A similar argument could be made for the opposite case with the cold side, which may have slightly smaller channels than specified in the COMSOL model or even powder from the manufacturing process that could not be removed obstructing its flow path, though there is less compelling evidence of this since the modeled results agreed within the experimental uncertainty bars for each point. Since the prototype was made from a high temperature melting process, it is reasonable to suspect that thermal expansion/contraction of the part during its manufacturing could have resulted in part dimensions slightly different than the ones specified in the model used to make it, but without physically cutting into the part and measuring the channels, it is not possible to conclusively claim that this is the reason for the observed differences between the experimental data and model results.

Figure 5.12 shows how the experimental heat exchanger effectiveness of the prototype varies as the hot side mass flow rate is increased and compares these results to the effectiveness values predicted by the developed COMSOL model. The experimental results indicate a variation in the effectiveness from a minimum value of 0.565 ± 0.065 to a maximum value of 0.722 ± 0.076 for the range of hot side mass flow rates tested. The minimum observed effectiveness corresponds to the condition at which both the hot side and cold side mass flow rates are approximately equal to each other. As the hot and cold streams become more unbalanced such that they take on significantly different values, the effectiveness values increase. The COMSOL simulation results exhibit an identical trend, but appear to consistently overpredicted the experimental effectiveness values. Here, there is an average percent difference of 9.52% and a maximum percent difference of 12.8% between the experimental effectiveness and COMSOL effectiveness values based on the calculated heat duty for the hot side of the device. This indicates generally good agreement which is further shown by the modeled values falling within the experimental data uncertainty bars for three of the four test points considered, giving confidence that the model results are predicting the

actual performance of the prototype with a satisfactory degree of accuracy. The model does notably overpredict the experimental effectiveness at each test point, however. This is most likely a result of the thermal properties of the actual reactor material differing from the properties input to the model, which are for Inconel 718 that has not gone through a powder bed melting process. The Inconel forming the prototype body likely has a slightly reduced thermal conductivity compared to normally treated Inconel as a result of the SLM process, slightly reducing the heat exchange between the streams and thus the device effectiveness compared to the model prediction. Along the same line of reasoning, it is also possible that the hydrodynamic conditions within the actual channels of prototype induce a higher resistance to heat transfer between the streams than predicted by the model, though it would again be difficult to assess if this is the case without access to the interior of the device's flow channels.

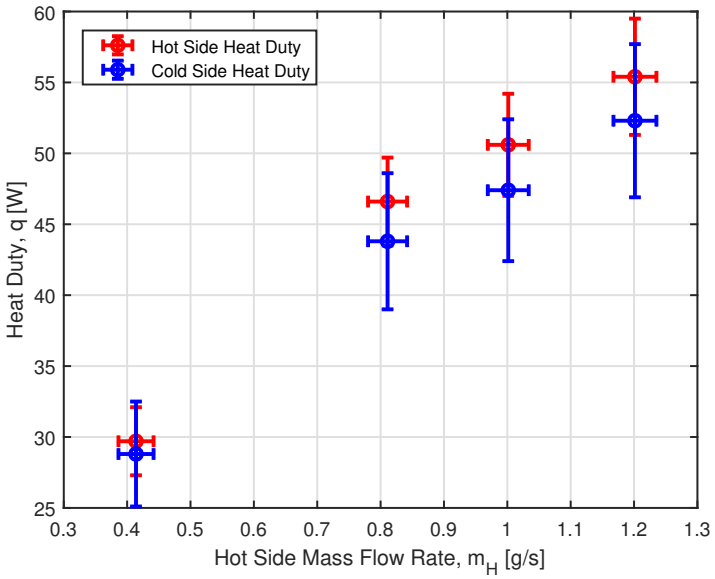

Figure 5.10: Energy balance comparison of hot and cold side of prototype for flow rate sweep

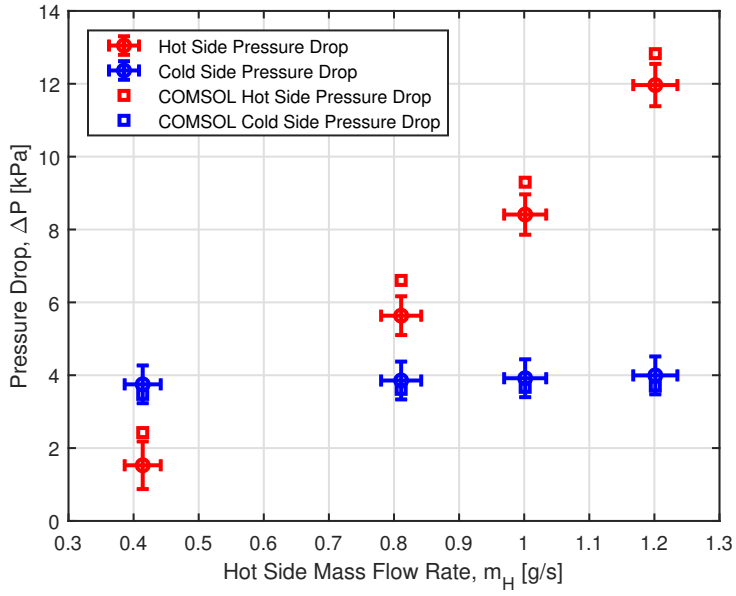

Figure 5.11: Pressure drop comparison of hot and cold side of prototype for flow rate sweep

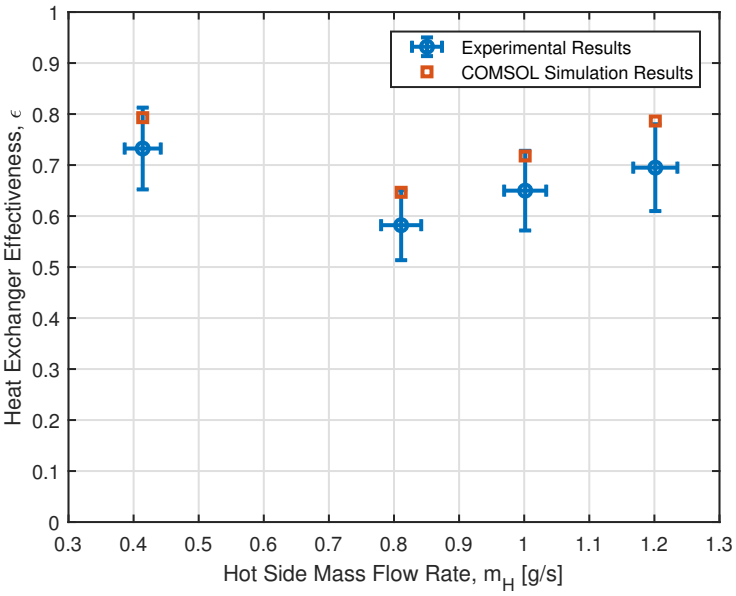

Figure 5.12: Prototype effectiveness for flow rate sweep

5.4.2 Cold Side Inlet Temperature Sweep

The results of the cold side inlet temperature sweep are presented in this section. As was done for the other test sweep done, the heat duty for the hot and cold streams were compared to ensure there was a reasonable energy balance. Figure 5.13 compares the heat duties of the hot and cold streams as a function of the cold side inlet temperature. Here, the average percent difference in measured heat duty between the streams was 11.4% with a maximum percent difference of 24.5%. While the maximum percent difference in the heat duty appears quite large, the heat duties for the hot and cold side are still within the experimental uncertainty at each point, indicating consistent energy balances. As noted previously, the uncertainty in the hot side heat duty is lower than the uncertainty in the cold side heat duty due to the lower uncertainty in the measured mass flow so it is again used in all subsequent effectiveness calculations.

Figure 5.14 shows how the measured pressure drop across the hot and cold sides of the prototype vary as the cold side inlet temperature is increased and compares these results to the pressure drops predicted using the developed COMSOL model. These results indicate a fairly constant pressure drop across all test points with only slight increases observed as the cold side inlet temperature is increased. Here, there is an average percent difference of 18.5% and a maximum percent difference of 20.0% between the experimental pressure drop and the COMSOL model pressure drop for the hot side and an average percent difference of 12.8% and a maximum percent difference of 14.8% between the experimental pressure drop and the COMSOL model pressure drop for the cold side, indicating relatively good agreement. The modeled cold side pressure drop particularly agrees within the experimental uncertainty bars for each test point considered. As was the case for the cold side pressure drop in the hot side flow rate study, increases in the pressure drop of both the hot and cold side streams of this study are primarily a result of slight changes in fluid properties

due to varying temperature profiles. As was the case for the hot side mass flow sweep, the COMSOL model consistently overpredicts the hot side pressure drop and underpredicts the cold side pressure drop, further suggesting that the difference in the experimental and modeled pressure drops may be due to the prototype's channel sizes differing slightly from what was specified in the model.

Figure 5.15 shows how the experimental heat exchanger effectiveness of the prototype varies as the cold side inlet temperature is increased and compares these results to the effectiveness values predicted by the COMSOL model. The experimental results indicate a variation in the effectiveness from a minimum value of 0.572 $\pm$ 0.073 to a maximum value of 0.64 $\pm$ 0.15. Since the heat exchanger remains relatively balanced for each test point considered, the measured effectiveness values for this test sweep vary less than they did for the mass flow rate sweep. Notably, the uncertainty bars for the effectiveness grow significantly as the cold side inlet temperature is increased. This is a result of the uncertainty expression for the effectiveness featuring $\dot{Q}_{max}$ in the denominator of both its uncertainty terms. As the cold side inlet temperature increases, $\dot{Q}_{max}$ decreases, ultimately increasing the overall uncertainty. Here, there is an average percent difference of 7.02% and a maximum percent difference of 12.0% between the experimental effectiveness and COMSOL effectiveness values based on the calculated heat duty for the hot side of the device. This indicates relatively good agreement which is further shown by all of the modeled values falling within the experimental data uncertainty bars, giving confidence that the model results are predicting the actual performance of the prototype with good accuracy. Again, the model does overpredict the effectiveness, though to a lesser extent than it did for the hot side mass flow rate sweep. This is again likely due to differences in the thermal conductivity of the actual reactor material and the specified properties in COMSOL or due to different hydrodynamic conditions within the flow channels than predicted by COMSOL.

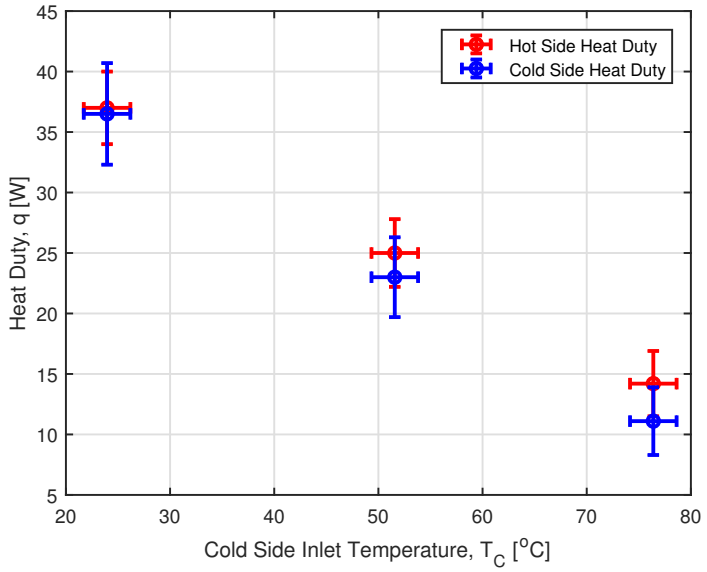

Figure 5.13: Energy balance comparison of hot and cold side of prototype for temperature sweep

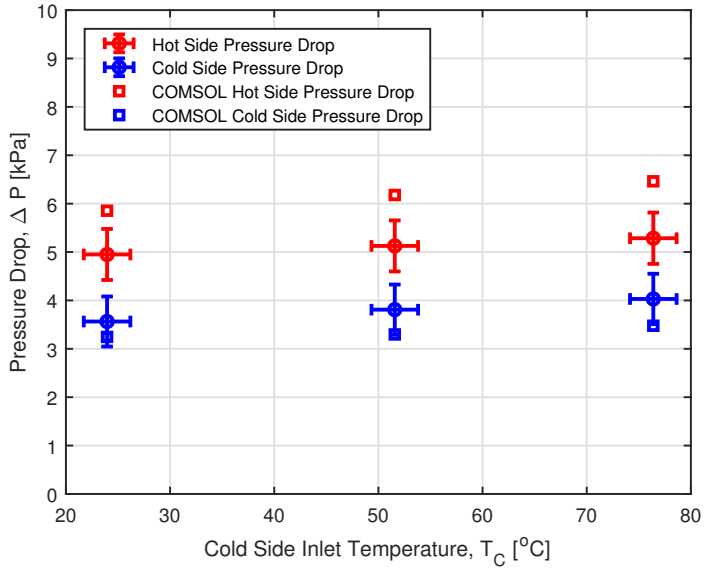

Figure 5.14: Pressure drop comparison of hot and cold side of prototype for temperature sweep

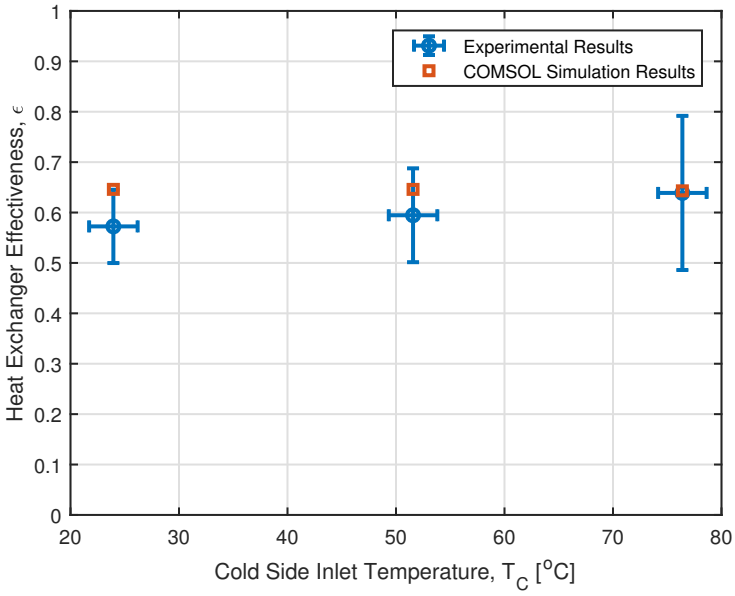

Figure 5.15: Prototype effectiveness for temperature sweep

5.5 Prototype Design and Experimental Verification Summary

The results presented in this chapter indicate that a scaled down microreactor prototype design developed from the previously presented modeling results can be successfully manufactured using a selective laser melting (SLM) additive manufacturing method. While an initial prototype was successfully manufactured using SLM, manufacturing and cost constraints regarding the size of the powder bed and powder particles that could be used altered the original design concept significantly. These constraints, along with the additional complications that result from the need to integrate catalyst into the reaction channels of these devices, still pose a significant challenge to the development of additively manufactured microreactors. Still, the successful development of this prototype and the rapid pace of innovation in the field of additive manufacturing suggest that microreactors can

be successfully manufactured using additive manufacturing and that these limitations will continue to relax over time such that even better designs can be realized.

The experimental results presented suggest that the thermal-hydraulic portion of the modeling results presented in Chapters 3 and 4 is able to predict the actual performance of the device with a reasonable degree of accuracy. For both of the experimental sweeps performed, the COMSOL model predicts pressure drops and effectiveness values that fall within or nearly fall within the calculated error bars for each experimental test point. This, along with the general agreement between the reacting flow modeling results and the experimental results from Germani and Schuurman, is a good indication that the developed COMSOL models can be used to predict how the prototype would perform under reacting flow conditions. The good agreement between these experimental and modeling results also suggest that the full 3-D temperature distribution of the prototype can be reasonably estimated from the COMSOL model. Figure 5.16 shows an example of one such temperature distribution. While this temperature distribution does indicate that the temperature primarily changes along the length of the prototype in the x direction, as desired for temperature control of the water-gas shift reaction, it also indicates significant temperature variation in the y-direction, which is less desirable for tighter temperature control over the reaction. In practice, it would desirable for for the temperature to be uniform in the y-direction so that the reaction can be better controlled to enhance conversion. This temperature distribution suggests that a higher quantity of less wide flow channels should perhaps be used to achieve a more uniform reaction temperature.

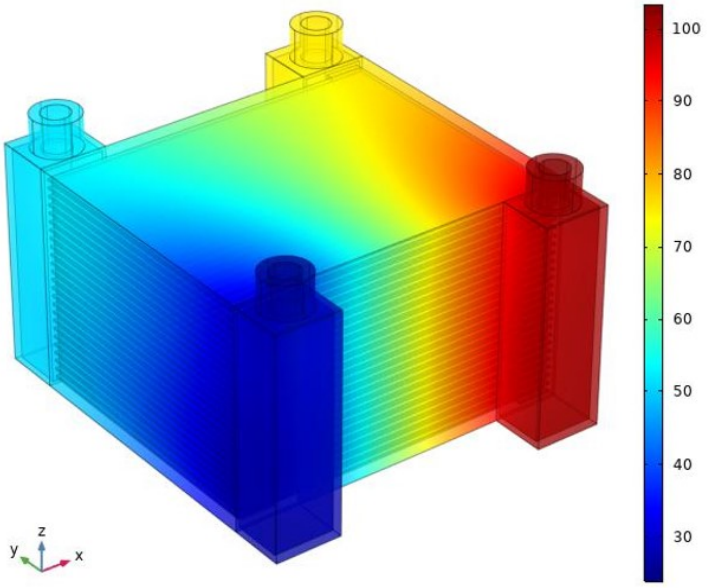

Figure 5.16: 3-D temperature distribution of prototype simulated in COMSOL

Chapter 6: Steam Methane Reforming Optimization Studies

This chapter presents optimization studies examining how the implementation of a differential temperature water-gas shift reactor can reduce the hydrogen production costs within the steam methane reforming process. While the modeling effort and results in Chapters 3 and 4 are presented from a component design perspective for specified inlet conditions, the studies performed in this chapter take a system level approach, where the optimal design for a differential temperature WGS reactor is more directly informed by the objective of reducing the cost of hydrogen production associated with the overall steam methane reforming process. Particularly, the simplified flow sheets analyzed and modeling equations used, the cost estimation and economic analysis performed, the formulation of a tractable optimization problem and the sequential quadratic (SQP) algorithm implemented to solve it, and the developed solutions are all presented in detail.

6.1 Baseline Steam Methane Reforming Flow Sheet

As part of the formulation of an optimization problem for analysis, I developed the simplified baseline flow sheet for the steam methane reforming process shown in Figure 6.1. This flow sheet is intended to operate at a production capacity of approximately 1500 kg H_2/day and is similar to the flow sheet developed by the National Renewable Energy Laboratory (NREL) as part of their H2A models for distributed hydrogen production [64]. Methane enters the system at standard conditions ($T_1 = 20$ °C, $P_1 = 101.3$ kPa) at state 1 and is compressed to state 2. Water also enters the system at standard conditions ($T_3 = 20$ °C, $P_3 = 101.3$ kPa), is pumped to state 4, is heated across the WGS intercooler to state 5, is further heated

across a heat exchanger to state 6, and is then fully boiled into saturated steam at state 7. The methane and steam streams then enter a mixing chamber and exit together as a single stream at state 8. The combined methane/steam stream next enters a recuperative heat exchanger where it is heated to a significantly higher temperature at state 9 before entering the steam methane reformer (SMR), where the stream is converted to synthesis gas by the SMR and WGS reactions (equations 1.1 and 1.2). Syngas exits the reformer at state 10 and is then cooled across the recuperative heat exchanger to state 11. The syngas is then cooled across an air cooled heat exchanger to state 12 before passing through the high temperature shift (HTS) water-gas shift reactor, which further enhances hydrogen production and removes unwanted carbon monoxide from the stream. The product stream from the HTS reactor at state point 13 is then cooled across the intercooler to state 14 where it then enters a low temperature shift (LTS) water-gas shift reactor, which again further enhances the hydrogen production and removes unwanted carbon monoxide from the stream. The product stream from the LTS reactor exits at state 15 and next passes through a condenser, which condenses the water vapor so that it can be separated from the product stream using a water knockout drum. The gas stream at state 18 continues on to the pressure swing adsorption (PSA) system, which separates the remaining CO, CO_2, and CH_4 from the hydrogen gas by selective adsorption at high pressures. The product hydrogen gas from this system at state 19 would next be sent through a compression process for storage, but that is not considered as part of this analysis. These other gases, as well as any additional hydrogen gas that could not be separated during this process, are released as the tail gas stream at state 20 at lower pressures. Depending on the system operation, the tail gas at state 21 can be rich in both H_2 gas that could not be separated into the product stream and unreacted CH_4. For energy efficiency, the tail gas is thus mixed with air to state 21 and then combusted to provide at least a portion of the heat inputs required for

the SMR and water boiling processes with the balance of the required heat inputs provided by the supplemental combustion of CH_4 as necessary. Air blowers are used to provide cooling/combustion air as necessary for states 24-26, 27-30, and 31-32.

As part of the development of this flow sheet model, the following simplifying assumptions are made:

- Steady state flow conditions
- All fluids entering the system are at standard conditions ($T = 20$ °C, $P = 101.3$ kPa)
- All gas streams can be modeled as ideal gases
- Negligible pressure drop across all components and connecting piping
- Negligible heat loss from all components
- Negligible changes in the potential and kinetic energies of the flow streams
- Constant specific heats evaluated at the average temperature across the compressor, mixers, SMR preheater, WGS intercooler, condenser, and blowers
- All turbomachinery operates at an isentropic efficiency of 75%
- The recuperative heat exchanger (HX 1 in Figure 6.1) is a shell-and-tube heat exchanger operating with a constant heat exchanger effectiveness of $\epsilon_{HX1} = 0.6$ and constant overall heat transfer coefficient of $U_{HX1} = 120$ W/m^2-K
- The WGS pre-cooler (HX 2 in Figure 6.1) is a shell-and- tube heat exchanger operating with a constant overall heat transfer coefficient of $U_{HX2} = 80$ W/m^2-K
- The intercooler is a shell-and-tube heat exchanger operating with a constant overall heat transfer coefficient of $U_{INT} = 400$ W/m^2-K

- The condenser is a shell-and-tube heat exchanger operating with a constant overall heat transfer coefficient of $U_{CON} = 130$ W/m^2-K
- The air/water heat exchanger used to provide heating to the water stream (HX 3 in Figure 6.1) is a shell-and-tube heat exchanger operating with a constant heat exchanger effectiveness of $\epsilon_{HX3} = 0.6$ and a constant overall heat transfer coefficient of $U_{HX3} = 130$ W/m^2-K
- Negligible fouling effects in all equipment
- The SMR reactor is a tubular packed bed reactor that is packed with a nickel based catalyst with a bulk density of $\rho_{cat,SMR} = 2355$ kg/m^3
- The HTS and LTS reactors are tubular packed bed reactors that are packed with a platinum based catalyst with a bulk density of $\rho_{cat,WGS}$ =700 kg/m^3
- The SMR and WGS reactors can be modeled using PFR relations
- Negligible diffusion resistance into/out of the catalyst pellets of the packed bed reactors
- The SMR and WGS reactions are the only chemical reactions occurring within the steam methane reformer
- The WGS reaction is the only chemical reaction occurring within the HTS/LTS reactors
- The water knockout system completely separates the condensed water from the gas stream
- The PSA system recovers hydrogen from the product stream with 80% efficiency
- The tail gas used to provide heat to the boiler and SMR reactor undergoes complete combustion with a stoichiometric amount of air

- In situations where the combustion of the tail gas is not enough to fully provide the heat inputs to the boiler and SMR reactor, supplemental heat inputs are provided by the complete combustion of methane fuel

While there are a number of idealizations in the listed assumptions, the developed model still enables the formulation of a coherent flow sheet for analysis and enables comparison to the differential temperature WGS flow sheet developed in Section 6.2. The remainder of this section outlines the equations used to model each of the processes indicated on the baseline flow sheet in Figure 6.1.

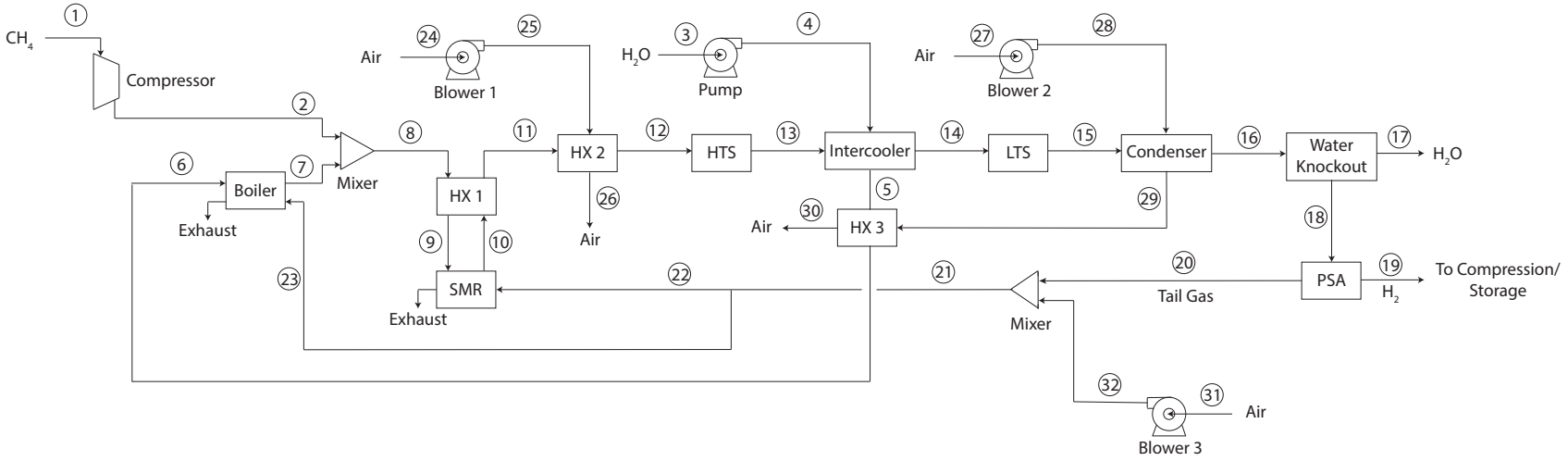

Figure 6.1: Baseline flow sheet for the steam reforming process

6.1.1 Compression/Blowing Processes

For the compression process (1-2) and blowing processes (24-25, 27-28, 31-32) indicated, the isentropic work inputs can be evaluated from energy balances as:

$$\dot{W}_s = \dot{m} c_p (T_{out,s} - T_{in}) \tag{6.1}$$

In equation 6.1, $\dot{m}$ is the mass flow rate of gas though each device, c_p is the specific heat at constant pressure, $T_{out,s}$ is the outlet temperature for an isentropic process, and T_{in} is the inlet temperature. The isentropic outlet temperature can be evaluated using the following isentropic relationship for ideal gases:

$$T_{out,s} = \left(\frac{P_{out}}{P_{in}} \right)^{(\gamma-1)/\gamma} T_{in} \tag{6.2}$$

In equation 6.1, P_{in} and P_{out} are the inlet and outlet pressures and γ is the specific heat ratio. The inlet pressure to each of these devices is defined as 101.3 kPa and the outlet pressure is evaluated using specified pressure ratios, PR . While the pressure ratio of the compressor is left as a design parameter to be varied, the pressure ratios for all blowers are specified as 1.1. The required work input for the actual operation of these devices can be evaluated from their isentropic efficiencies as:

$$\dot{W} = \frac{\dot{W}_s}{\eta_s} \tag{6.3}$$

Finally, the actual outlet temperatures from each of these devices can be evaluated from energy balances as:

$$T_{out} = \frac{\dot{W}}{\dot{m} c_p} + T_{in} \tag{6.4}$$

6.1.2 Water Pumping Process

The pumping process (3-4) is modeled in a similar fashion to the compression/blowing processes, but using specific enthalpy values, h, from a look-up table instead of specific heat values with temperatures. The work input for isentropic operation can thus be evaluated from an energy balance as:

$$\dot{W}_{3-4,s} = \dot{m}_3(h_{4,s} - h_3) \tag{6.5}$$

In equation 6.5, the inlet enthalpy h_3 can be evaluated using the prescribed inlet pressure, P_3, and temperature, T_3. The inlet entropy, s_3, can also be evaluated in this way. Using the device pressure ratio, PR_{3-4}, which is left as a design parameter to be varied, the outlet pressure P_4 can be found and used along with s_3 to evaluate the isentropic outlet enthalpy, $h_{4,s}$. The actual pump work input can be evaluated using the isentropic efficiency and equation 6.1 and the actual outlet enthalpy can be evaluated as:

$$h_4 = \frac{\dot{W}_{3-4}}{\dot{m}_3} + h_3 \tag{6.6}$$

Using h_4 and P_4, the outlet temperature from the pump, T_4, can then be evaluated using a look-up table.

6.1.3 Heat Exchanger Processes

For the recuperative heat exchanger (HX 1) and water/air heat exchanger (HX 3), the inlet temperatures of the streams entering the device at states 5, 8, 10, and 29 are either specified values in the flow sheet or calculated directly from other specified values. Additionally, for the specified range of conditions, the reactant side of HX 1 and air side of HX 3 will always

have the minimum capacity rate fluid. Using these values, the maximum possible heat transfer for these heat exchangers can be found as:

$$\dot{Q}_{max} = C_{min}(T_{H,in} - T_{C,in}) \tag{6.7}$$

and subsequently used to evaluate the actual heat transfer between the fluid streams using the specified effectiveness values as:

$$\dot{Q} = \epsilon \dot{Q}_{max} \tag{6.8}$$

In equation 6.7, $T_{H,in}$ is T_{10} and T_{29} and $T_{C,in}$ is T_8 and T_5 for HX 1 and HX 3, respectively. These heat transfer values can subsequently be used to solve for the outlet temperatures of each stream using energy balances and to find the required number of transfer units, NTU . For shell-and-tube heat exchangers, the NTU value can be evaluated as:

$$\begin{aligned} NTU &= -(1 + C_r^2)^{-1/2} \ln\left(\frac{E-1}{E+1}\right) \\ E &= \frac{2/\epsilon - (1 + C_r)}{(1 + C_r^2)^{1/2}} \end{aligned} \tag{6.9}$$

In equation 6.9, C_r is the ratio of the minimum and maximum capacity rates. From the NTU values and the specified overall heat transfer coefficients, U, the required heat transfer area for each heat exchanger can be evaluated as:

$$A = \frac{NTUC_{min}}{U} \tag{6.10}$$

The specified overall heat transfer coefficient for each heat exchanger is estimated using a thermal resistance network model at a standard operating condition.

For the WGS pre-cooler (HX 2), intercooler, and condenser, the temperatures of three of the streams entering each heat exchanger are specified or directly calculated from other specified values. In the case of the WGS pre-cooler, its inlet temperature T_{11} is directly calculated based on the heat transfer process in HX 1 and its outlet temperature T_{12} is left as a design parameter to be varied. The inlet temperature to the intercooler is directly calculated based on the HTS reactor process and its outlet temperature T_{14} is left as a design parameter to be varied. The inlet temperature to the condenser is directly calculated based on the LTS reactor process and its outlet temperature is specified as $T_{16} = 50$ °C to facilitate better separation in the PSA process, which operates more efficiently near ambient temperatures [65]. For each of these heat exchangers, the inlet temperatures of the coolants are directly calculated based on the blower/pump processes. The heat transfer between the streams in these devices can thus be calculated from energy balances and used to evaluate the outlet temperature of the other stream. The maximum heat transfer for these devices can be found using equation 5.5 and used to evaluate the effectiveness of each heat exchanger using equation 6.7, which can subsequently be used to evaluate the NTU value and required heat transfer area.

For cases where there is a phase change occurring within the heat exchangers (as is always the case for the condenser and is frequently the case for the intercooler and HX 3 in this flow sheet), the NTU value is calculated using the following equation instead of equation 6.9:

$$NTU = -\ln(1 - \epsilon) \tag{6.11}$$

6.1.4 Boiler Process

For the water boiling process (6-7), the required heat duty can be evaluated from an energy balance as:

$$\dot{Q}_{6-7} = \dot{m}_6(h_7 - h_6) \tag{6.12}$$

The enthalpy values in equation 6.12 are evaluated from a look-up table and h_7 is taken as the saturated vapor enthalpy at P_7, which is assumed to be equal to the pump outlet pressure, P_4.

6.1.5 Mixing Processes

For the mixing processes that combine the methane and water streams (2-7-8) and the tail gas and air streams (20-21-32), the total mass flow rate of the combined streams can be evaluated from mass balances as:

$$\dot{m}_{out} = \dot{m}_{in,1} + \dot{m}_{in,2} \tag{6.13}$$

In equation 6.13, $\dot{m}_{out}$ is the total mass flow exiting the mixer and $\dot{m}_{in,1}$ and $\dot{m}_{in,2}$ are the constituent streams which flow into the mixer. The compositions of the mixed streams on a mass basis can be evaluated as:

$$w_j = \frac{\dot{m}_{out,j}}{\dot{m}_{out}} \tag{6.14}$$

In equation 6.14, w_j is the mass fraction of component j in the combined stream and $\dot{m}_{out,j}$ is the mass flow of component j within the combined stream. From these mass fractions, the compositions of the streams can also be evaluated on a molar basis as:

$$y_j = w_j \left(\frac{M}{M_j} \right) \tag{6.15}$$

In equation 6.15, M is the average molar mass of the gas mixture, which can be evaluated using equation 3.7, and M_j is the molar mass of component j. Assuming an adiabatic mixing process, the temperatures of the mixed stream can be evaluated from energy balances as:

$$T_{out} = \frac{\sum_{j=1}^{n} \dot{m}_j c_{p,j} T_{j,in}}{\sum_{j=1}^{n} \dot{m}_j c_{p,j}} \tag{6.16}$$

In equation 6.16, $c_{p,j}$ is the specific heat of component j and and $T_{j,i}$ is the inlet temperature of component j entering the mixer.

6.1.6 SMR Conversion Process

Generally, the steam methane reformers used in industry are packed bed reactors consisting of several tubes packed with a nickel based catalyst that facilitates both the SMR reaction and the WGS reaction [66]. As discussed in Section 1.2, while the WGS reaction is a mildly exothermic reaction, the SMR reaction is strongly endothermic and requires a significant energy input which is generally supplied by the combustion of natural gas, though other methods can be used as well. Unlike the WGS reaction, the equilibrium of the SMR reaction heavily favors the formation of hydrogen gas at higher temperatures. As a result, it is generally advantageous from both a kinetic and thermodynamic perspective for the SMR reaction to operate at higher temperatures such that the optimal temperature profile for the reaction is isothermal at the highest allowable operating temperature. Because the product side of the SMR reaction has more moles of gas than the reactant side, increases in the process pressure shift the reaction equilibrium to favor reactant formation in accordance with Le Chatelier's principle, while the opposite occurs for decreases in pressure.

The conversion process occurring in the steam methane reformer is modeled using the same PFR relations used to model the HTS/LTS reactors in Section 3.1. Equations 3.1 and 3.4 are used to model the mass and heat transfer processes in the SMR reactor, respectively, though the heat transfer equation is modified to include a term accounting for the heat input provided to the reaction stream. Because both the SMR and WGS reactions occur simultaneously within the SMR reactor, the generation/consumption rate, r_i, of each species in the mass transfer equation is taken as the sum of the contributions from each reaction. For each species, these relative contributions are:

$$\begin{aligned} r_{CH4} &= -r_{SMR} \\ r_{H2O} &= -r_{SMR} - r_{WGS} \\ r_{CO} &= r_{SMR} - r_{WGS} \\ r_{H2} &= 3r_{SMR} + r_{WGS} \\ r_{CO2} &= r_{WGS} \end{aligned} \tag{6.17}$$

In equation 6.17, r_{SMR} is the reaction rate associated with the SMR reaction and r_{WGS} is the reaction rate associated with the WGS reaction for the nickel based catalyst packed in the reactor. Reactions consuming a species are assigned as negative terms and reactions generating a species are assigned as positive terms in these expressions. For the hydrogen generation term, the SMR reaction rate is multiplied by the stoichiometric coefficient of hydrogen in the SMR equation since three moles of hydrogen gas are produced for each cycle of this conversion process. Similarly, the net heat generation in the SMR reactor is evaluated from the net contributions of both reactions occurring as:

$$(\Delta Hr)_{net} = [(-\Delta H_{SMR})(r_{SMR})] + [(-\Delta H_{WGS})(r_{WGS})] \tag{6.18}$$

Because the SMR reaction rate is generally significantly higher than the WGS reaction rate across the entire reactor length and because the SMR reaction is very strongly endothermic, the net process in the steam reformer is also still strongly endothermic. Since isothermal operation at a high temperature is desired, the operating temperature of the SMR is left as a design parameter which is specified as T_{10}. To increase the temperature of the SMR reactant stream at state 9 to the desired reaction operating temperature, it is first preheated before entering the reacting section of the reformer. The total heat input for this preheating process can be evaluated from an energy balance as:

$$\dot{Q}_{SMR,pre} = \dot{m}_9 c_{p,SMR,pre}(T_{10} - T_9) \tag{6.19}$$

In equation 6.19, $c_{p,SMR,pre}$ is the specific heat at constant pressure of the reactant stream evaluated at the average of the inlet and outlet temperatures of the SMR reactor. The heat addition for the reacting section of the reformer ($\dot{Q}_{SMR,rxn}$) can be evaluated from equation 3.4 for isothermal operation and the total heat input to the reformer can be found as:

$$\dot{Q}_{9-10} = \dot{Q}_{SMR,pre} + \dot{Q}_{SMR,rxn} \tag{6.20}$$

The Langmuir-Hinshelwood rate expressions developed by Xu and Froment [66] for the SMR and WGS reactions can be used to predict the reaction rates for each process within the reformer as:

$$
\begin{aligned}
r_{SMR} &= \frac{\frac{k_{rds,1}}{P_{H2}^{2.5}}\left(P_{CH4}P_{H2O} - \frac{P_{H2}^{3}P_{CO}}{K_{eq,SMR}}\right)}{DEN^2} \\
r_{WGS} &= \frac{\frac{k_{rds,2}}{P_{H2}}\left(P_{CO}P_{H2O} - \frac{P_{H2}P_{CO2}}{K_{eq,WGS}}\right)}{DEN^2} \\
DEN &= 1 + K_{CO}P_{CO} + K_{H2}P_{H2} + K_{CH4}P_{CH4} + \frac{K_{H2O}P_{H2O}}{P_{H2}}
\end{aligned}
\tag{6.21}
$$

In equation 6.21, $k_{rds,1}$ and $k_{rds,2}$ are the reaction rate constants for the SMR and WGS reactions, respectively, $K_{eq,SMR}$ and $K_{eq,WGS}$ are the equilibrium constants for each reaction, and K_{CO}, K_{H2}, K_{CH4}, and K_{H2O} are adsorption constants for species that adsorb to the catalyst surface during the reaction. These rate expressions are expressed on a catalyst mass basis and are subsequently multiplied by a bulk catalyst density of $\rho_{SMR,cat}$ = 2355 kg/m^3, suggested by Jeong et al. [67] for the $Ni/MgAl_2O_4$ catalyst modeled, to evaluate the total SMR reactor volume required for the process. The equilibrium expression previously specified for the WGS reaction in equation 2.1 is used in these expressions and the following equilibrium expression developed by Dirksen and Riesz [68] for the SMR reaction is used:

$$
K_{eq,SMR} = exp\left(\frac{-26830}{T} + 30.114\right) \tag{6.22}
$$

As was done for the PFR relations developed in Section 3.1, mass transfer resistances into/out of the pellets in the SMR reactor are neglected such that the results generated from this model represent the best possible performance of an SMR packed bed reactor in terms of the volume required to facilitate the reaction.

6.1.7 HTS/LTS Conversion Process

The HTS/LTS conversion process is modeled using the relations developed in Section 3.1. Both the inlet temperature to the HTS reactor, T_{12}, and the inlet temperature to the LTS reactor, T_{14} are left as design parameters to be varied.

As discussed previously in Section 3.1, the use of PFR relations significantly simplifies the analysis required to model the SMR and WGS reactors, but neglect a number of effects which impact actual reactor performance. Still, the results presented in Section 4.5.2 comparing the performance of the PFR and COMSOL models for packed bed conditions suggest reasonable enough agreement that the PFR model can be used as a first estimate of the actual reactor performance. Given the system level nature of the type of modeling being performed in this chapter, the use of PFR relations is thus a reasonable starting point for evaluating the dynamics of the overall process and the improvements in system performance that can be realized by implementing a differential temperature WGS reactor, as outlined in the flow sheet models discussed in Section 6.2.

6.1.8 Water Knockout Process

The water knockout process separates the liquid water from the stream such that the stream exiting at state 17 contains only liquid water and the stream exiting at state 18 contains only gases without any water present. The mass flow rate of each stream can be evaluated using a mass balance as:

$$\begin{aligned} \dot{m}_{17} &= \dot{m}_{16,H2O} \\ \dot{m}_{18} &= \dot{m}_{16} - \dot{m}_{17} \end{aligned} \tag{6.23}$$

The composition of the stream at state 17 is assumed to consist of only water and the composition of the stream at state 18 can be evaluated on a dry basis using the composition of the stream entering the water knockout drum at state 16.

6.1.9 Pressure Swing Adsorption Process

The pressure swing adsorption process separates hydrogen gas from the stream entering at state 18 into the product stream at state 19 with an assumed efficiency of 80% on a molar basis, a typical value for these systems [65]. The mass flow rate of the streams exiting the PSA process can thus be evaluated from a mass balance as:

$$\begin{aligned} F_{19} &= (0.80)F_{18,H2} \\ \dot{m}_{19} &= F_{19}M_{H2} \\ \dot{m}_{20} &= \dot{m}_{18} - \dot{m}_{19} \end{aligned} \tag{6.24}$$

In equation 6.24, $F_{18,H2}$ is the molar flow rate of hydrogen into the PSA process and M_{H2} is the molar mass of hydrogen gas. The product stream at state 19 is assumed to consist of pure hydrogen and the composition of the stream at state 20 can be evaluated based on the composition of the stream at state 18 and the amount of hydrogen separated into the product stream at state 19. Pressure swing adsorption operates cyclically at high and low pressures so it is assumed that the pressure of the product hydrogen, which is allowed to flow through the PSA system while it is under high pressure, at state 19 is P_{19} = P_{18} and that the pressure of the tail gas, which flows through the PSA system at low pressure, is $P_{20} = P_{32}$, the outlet pressure of air stream that mixes with the tail gas.

6.1.10 Tail Gas Combustion Process

The tail gas combustion processes that occur across the steam reformer and boiler are assumed to undergo complete combustion with a stoichiometric amount of air such that they operate according to the following chemical equation:

$$aCH_4 + bH_2 + c(O_2 + 3.76N_2) + dCO + eCO_2 \rightarrow fCO + gCO_2 + hH_2O + iN_2 \quad (6.25)$$

Using the molar flow rates of the individual tail gas components at state 20, this equation can be balanced and used to evaluate the required molar flow rate of air for stoichiometric combustion which can in turn be used to evaluate the mass flow rate of air that must be provided by the blower ($\dot{m}_{32}$) and to subsequently obtain the composition of the stream at state 21. While there is CO present in the mixed stream, this is assumed to come entirely from the tail gas stream such that the combustion process does not create any additional CO. The heat output from the combustion process is evaluated as:

$$\dot{Q}_{tail} = \dot{m}_{21,CH4}(LHV)_{CH4} + \dot{m}_{21,H2}(LHV)_{H2} \quad (6.26)$$

In equation 6.26, $(LHV)_{CH4}$ and $(LHV)_{H2}$ are the lower heating values of methane and hydrogen, respectively. The allocation of the tail gas stream to the reformer and the boiler are evaluated based on the relative magnitudes of the required heat duties of each piece of equipment. In cases where the heat from the combusted tail gas is not enough to meet the combined heat duty of the reformer and boiler, supplemental methane is combusted in the amount necessary to supply the excess heat load, $\dot{Q}_{excess}$. This is calculated as:

$$\dot{m}_{CH4,excess} = \frac{\dot{Q}_{excess}}{(LHV)_{CH4}} \tag{6.27}$$

6.2 Differential Temperature WGS Reactor Flow sheet

Figure 6.1 shows how the baseline flow sheet in 6.2 is modified to integrate a differential temperature WGS reactor into the steam methane reforming process. The differential temperature WGS reactor replaces the HTS/LTS reactors and the intercooler originally present, but all other processes are unaltered such that the modeling equations outlined in Section 6.1 still apply. PFR relations are stilled applied to model the differential temperature WGS reactor process, but are modified to implement a differential reaction temperature profile as previously derived in Section 3.3 and demonstrated throughout Chapter 4. In this implementation, the PFR relations presented in Section 3.1 are initially applied to evaluate the adiabatic performance of the reactor, the optimal temperature profile for the reactor inlet condition is evaluated using equation 2.6, and the intersection between these two curves is evaluated. The implemented PFR model operates adiabatically up until this intersection point and is then forced to follow the optimal progression. Over this section of the reactor, the prescribed conversion and temperature progression are used in conjunction with equations 3.1 and 3.4 to evaluate the total reactor volume and heat rejection required by the process. Additionally, instead of operating as a packed bed reactor, as the HTS/LTS reactors do, the differential temperature WGS reactor implemented in this study is assumed to be a microreactor similar in form to the ones studied in Chapters 3 and 4, due to their better heat transfer characteristics and demonstrated capability of imposing the desired temperature profile onto the reaction. A catalyst loading of 20% is assumed and equation 3.28 is used to evaluate an effective reaction rate through the microreactor.

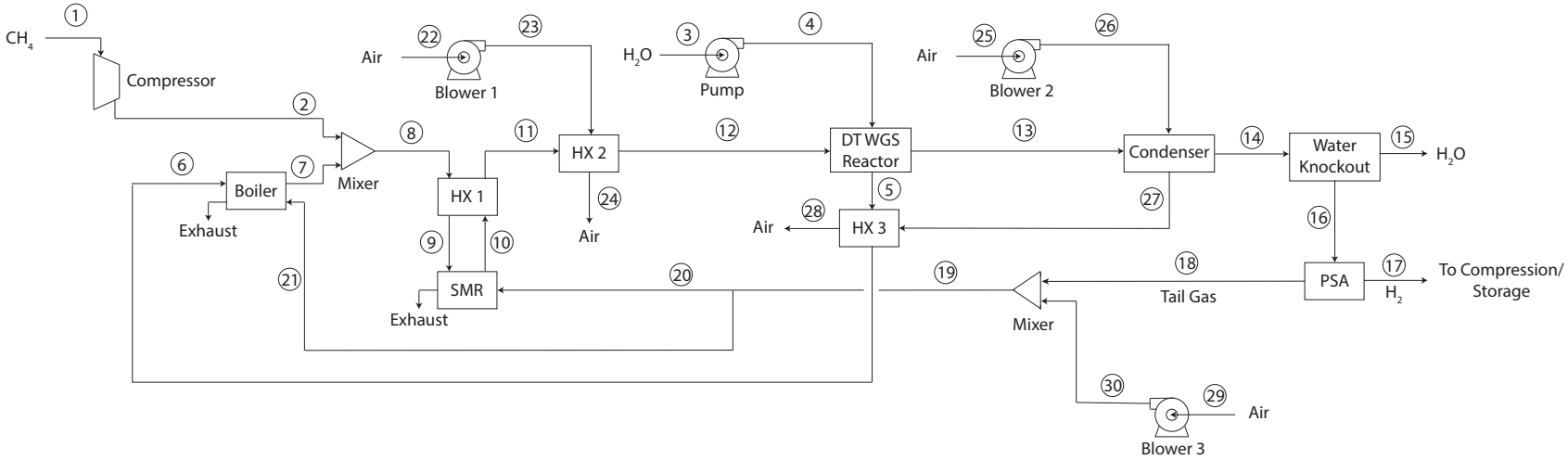

Figure 6.2: Differential temperature WGS microreactor flow sheet for the steam reforming process

6.3 Cost Estimation and Economic Analysis

This section presents the methodology I used to estimate the capital costs and operating costs associated with the flow sheet models developed in Sections 6.1 and 6.2 and the subsequent economic analysis that was performed to estimate the hydrogen production costs associated with each flow sheet.

6.3.1 Capital Cost Estimation

The capital costs associated with a project are the fixed, one-time expenses incurred at the start of the project to bring it into operation at a commercially viable scale. Such costs are generally associated with the procurement of the land, permits, and equipment necessary to operate the project and the initial construction/installation of the project. For the flow sheets analyzed, I only considered the capital costs associated with the procurement and installation of the indicated equipment in Table 6.1 such that the capital costs associated with the piping connecting all components, the mixing chamber combining the methane and water streams, and any turbomachinery necessary to deliver supplemental methane fuel to the boiler and SMR reactor for heating are all neglected. I also assumed that the cost of the water knockout drum was included in the cost of the condenser.

I estimated the capital costs of the required process equipment primarily using cost correlations taken from [69], which relate characteristic parameters for each piece of equipment that are calculated using the modeling equations presented in Section 6.1 to an approximate capital cost using a power sizing model. These power sizing models generally take the following form:

$$(Cost_2) = (Cost_1)\left(\frac{Size_2}{Size_1}\right)^n \tag{6.28}$$

Table 6.1: Capital cost functions for each flow sheet component

Component	Capital Cost Function	Ref
Natural Gas Compressor	$C_{comp} = (\$260{,}000)\left(\frac{\dot{W}_{1-2}[hp]}{300[hp]}\right)^{0.8}\left(\frac{P_2[psi]}{1000[psi]}\right)^{0.18}$	[69]
Water Pump	$C_{pump} = (\$78{,}408)\left(\frac{\dot{W}_{3-4}[hp]}{9[hp]}\right)^{0.59}$	[69]
Air Blowers	$C_{blower} = (\$22{,}500)\left(\frac{\dot{V}[ft^3/min]}{600[ft^3/min]}\right)^{0.79}$	[69]
Boiler	$C_{boiler} = (\$117{,}900)\left(\frac{\dot{Q}_{4-5}[bhp]}{400[bhp]}\right)^{0.65}$	[69]
Recuperative Heat Exchanger (HX 1)	$C_{HX1} = (\$129{,}957.41)\left(\frac{A_{HX1}[ft^2]}{300[ft^2]}\right)^{0.68}$	[69]
WGS Pre-cooler (HX 2)	$C_{HX2} = (\$86{,}565.94)\left(\frac{A_{HX2}[ft^2]}{300[ft^2]}\right)^{0.68}$	[69]
Air/Water Heat Exchanger (HX 3)	$C_{HX3} = (\$74{,}912.33)\left(\frac{A_{HX3}[ft^2]}{300[ft^2]}\right)^{0.68}$	[69]
WGS Intercooler	$C_{INT} = (\$111{,}251.09)\left(\frac{A_{INT}[ft^2]}{300[ft^2]}\right)^{0.68}$	[69]
Condenser	$C_{CON} = (\$74{,}912.33)\left(\frac{A_{CON}[ft^2]}{300[ft^2]}\right)^{0.68}$	[69]
SMR Reactor	$C_{SMR} = (\$547{,}0416)\left(\frac{\dot{Q}_{9-10}[mmBTU/hr]}{300[mmBTU/hr]}\right)^{0.7}$	[69]
HTS Reactor	$C_{HTS} = (\$111{,}251.09)\left(\frac{V_{HTS}[ft^3]}{4.6875[ft^3]}\right)^{0.68}$	[69]
LTS Reactor	$C_{LTS} = (\$111{,}251.09)\left(\frac{V_{LTS}[ft^3]}{4.6875[ft^3]}\right)^{0.68}$	[69]
PSA	$C_{PSA} = (\$54{,}750)\left(\frac{\dot{m}_{H2,product}[kg/day]}{115[kg/day]}\right)^{0.4}$	[64]

In equation 6.28, $Cost_1$ is the cost of a piece of equipment operating at Size 1, $Cost_2$ is the cost of the same piece of equipment operating at Size 2, and n is the size exponent which accounts for how the equipment cost varies as it is scaled to a different size. The correlation used to estimate the cost of the pressure swing adsorption (PSA) system was taken from the H2A hydrogen production model developed by NREL [64] and is based on data provided from a PSA manufacturer. The correlations used to estimate the capital costs for the required equipment are compiled in Table 6.1 along with the reference they were taken from.

The functions listed in Table 6.1 all account for both the cost of the equipment itself and its installation into the system. In the evaluation of these cost functions, the methane compressor is assumed to be a steel centrifugal compressor, the water pump is assumed to

be a mild steel reciprocating pump, and the blowers are assumed to be cast iron centrifugal blowers. Both the shell and tube sides of recuperative heat exchanger (HX 1) were assumed to be constructed from high temperature nickel alloys to operate at the high temperatures expected for the reformer. The tubes of the WGS pre-cooler (HX 2) were assumed to be constructed from high temperature nickel alloys while its shell side was assumed to be constructed from carbon steel as it will only have air flowing through it. The shell and tube sides of the interooler were both assumed to be constructed from 316 stainless steel since operating temperatures at this stage of the process will generally be low enough to not require high temperature alloys. The tube sides of both the condenser and the air/water heat exchanger (HX 3) were assumed to be constructed from 316 stainless steel while their shell sides were assumed to be constructed from carbon steel. The cost of the SMR reactor was estimated as a box type reformer furnace with horizontal tubes while the costs of the WGS reactors in both the baseline and differential temperature flow sheets were estimated by modifying the intercooler shell-and-tube cost correlations to use tube volume as the sizing parameter instead of heat transfer area. The costs predicted by these equations are all referenced to a purchase year of 1989 except for the PSA system, which is referenced to a purchase year of 2005. I estimated the capital cost for each piece of equipment for a purchase year of 2019 using cost indices with the following equation:

$$(C)_{2019} = (C)_{past}\left[\frac{(I)_{2019}}{(I)_{past}}\right] \tag{6.29}$$

In equation 6.29, C_{2019} is the cost of the system referenced to a purchase year of 2019, C_{past} is the cost of the system referenced to the purchase year used by the cost correlations, and I_{2019} and I_{past} are the cost indices for these years, respectively. I used the average Chemical Engineering Plant Cost Index (CEPCI) for these years ($I_{1989} = 355.4$, $I_{2005} = 468.2$, $I_{2019} = 607.5$) based on values reported by the Chemical Engineering magazine [70].

6.3.2 Operating Cost Estimation

The operating costs associated with a project are the continually recurring expenses incurred by the general operation of the project in terms of the resources consumed and required administrative/operation tasks performed. Such costs are generally associated with the costs of raw materials and utilities such as fuel and electricity and payroll administration for worker activity such as general system operation and maintenance work. For the flow sheets analyzed, I only considered the operating costs associated with the consumption of natural gas, water, and electricity and the raw material costs associated with periodically replacing the catalyst in the reactors. I assumed a standard operating schedule of 8000 hours per year, with down time evenly distributed across all months, and fixed costs of $Cost_{CH4}$ = \$0.177/kg of methane consumed, $Cost_{H2O}$ = \$0.00095/kg of water consumed, and $Cost_e$ = \$0.1088/kWhr of electricity consumed by the process billed on a monthly basis. These values approximately match the utility costs listed in the H2A production model developed by NREL [64]. The SMR and WGS catalysts are assumed to cost $Cost_{SMR,cat}$ = \$53.91/kg and $Cost_{WGS,cat}$ = \$419.26/kg, respectively, based on estimates produced using CatCost [71], a tool developed by DOE/NREL/ALLIANCE that can be used to estimate the costs of a catalyst based on its composition and the expected processing methods that would necessary to synthesize it, and assumed to require replacement every four years, based on the results indicated in a catalyst review by Ratnasamy [23]. Notably, the estimated WGS catalyst price is significantly higher than the estimated SMR catalyst price due to its platinum content.

To estimate the operating costs of the analyzed flow sheets, I used the equations compiled in Table 6.2, which convert all of the material and energy inputs to the flow sheets into costs using the evaluated costs for methane, water, electricity, and the catalysts. While each of the methane, water, and electrical costs are expressed on a monthly basis, the catalyst

Table 6.2: Operating cost functions for each flow sheet component

Component	Operating Cost Function [$]
Reaction Stream Methane	$O_{CH4} = Cost_{CH4}(\dot{m}_1)\left(\frac{2{,}400{,}000s}{1month}\right)$
Reaction Stream Water	$O_{H2O} = Cost_{H2O}(\dot{m}_3)\left(\frac{2{,}400{,}000s}{1month}\right)$
Natural Gas Compressor	$O_{comp} = Cost_e(\dot{W}_{1-2})\left(\frac{666.67hrs}{1month}\right)$
Water Pump	$O_{pump} = Cost_e(\dot{W}_{3-4})\left(\frac{666.67hrs}{1month}\right)$
Air Blower 1	$O_{blower,1} = Cost_e(\dot{W}_{24-25})\left(\frac{666.67hrs}{1month}\right)$
Air Blower 2	$O_{blower,2} = Cost_e(\dot{W}_{27-28})\left(\frac{666.67hrs}{1month}\right)$
Air Blower 3	$O_{blower,3} = Cost_e(\dot{W}_{31-32})\left(\frac{666.67hrs}{1month}\right)$
Boiler	$O_{boiler} = Cost_{CH4}(\dot{m}_{boiler,f})\left(\frac{2{,}400{,}000s}{1month}\right)$
SMR Reactor	$O_{SMR} = Cost_{CH4}(\dot{m}_{SMR,f})\left(\frac{2{,}400{,}000s}{1month}\right)$
SMR Catalyst	$O_{SMR,cat} = Cost_{SMR,cat}(\rho_{SMR,cat})(V_{SMR})$
WGS Catalyst	$O_{WGS,cat} = Cost_{WGS,cat}(\rho_{WGS,cat})(V_{WGS})$

replacement costs are treated as single events which occur every four years. The boiler and SMR costs are taken as the cost of the methane streams that must be supplied to these pieces of equipment to supplement the tail gas combustion as necessary. When the heat inputs from the combustion of the tail gas is sufficient alone, these costs go to 0.

6.3.3 Hydrogen Production Cost Estimation

Using the cost estimations developed in Sections 6.3.1 and 6.3.2, I developed the cash flow diagram shown in Figure 6.3 for the flow sheets analyzed over an assumed system lifetime of 20 years with month time periods. As shown in Figure 6.3, the total capital cost of the system (C) is paid at the onset of the project and for every month of operation after that, the total utility operating cost of the system (O) is paid. Additionally, catalyst for both the SMR and WGS reactors is purchased at the onset of the project at a cost of (O_{cat}) and is replaced every four years to maintain system operation.

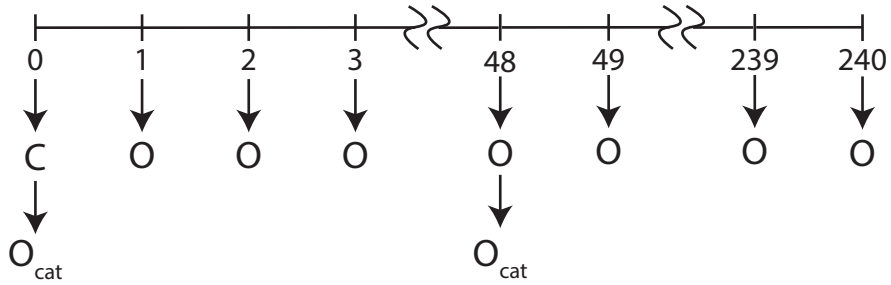

Figure 6.3: Cash flow diagram for flow sheet processes

To evaluate the hydrogen production cost of each flow sheet based on the specified cash flows, the capital and catalyst operating costs have to be converted to a monthly annuity . For the capital costs, this can be done using the following equation:

$$A_C = C(A/P, i, n) \tag{6.30}$$

In equation 6.30, $(A/P, i, n)$ is the Capital Recovery Factor, which can be expressed as:

$$(A/P, i, n) = \frac{i(1+i)^n}{(1+i)^n - 1} \tag{6.31}$$

In equation 6.31, i is the interest rate, which is assumed to be 7% APR, and n is the number of months that the problem is solved over, which corresponds to 240 for a 20 year system lifetime, the same lifetime assumed as part of the H2A model developed by NREL [64]. To convert the catalyst replacement costs into monthly annuity values, they are all first adjusted to present worth values using the following equation:

$$P_{cat} = O_{cat}[1 + (P/F, i, 48) + (P/F, i, 96) + (P/F, i, 144) + (P/F, i, 192)] \tag{6.32}$$

In equation 6.32, the $(P/F, i, n)$ terms are Present Worth Factors which convert the purchased cost of catalyst at each time to their present worth. This factor can be expressed as:

$$(P/F, i, n) = \frac{1}{(1+i)^n} \tag{6.33}$$

Subsequently, the present worth of the catalyst can be converted into monthly annuity values using the Capital Recovery Factor as:

$$A_{cat} = P_{cat}(A/P, i, n) \tag{6.34}$$

The present worth of the catalyst replacement costs can then be converted to a monthly annuity (A_{cat}) using the Capital Recovery Factor listed in equation 6.31 such that the total monthly production cost can be taken as:

$$A = O + A_C + A_{cat} \tag{6.35}$$

Using this monthly production cost, the production cost per gge of H_2 produced on a monthly basis can be evaluated as:

$$Cost_{H2} = \frac{A}{\dot{m}_{H2,p}\left(\frac{2{,}400{,}000s}{1month}\right)\left(\frac{1[gge]}{1.02kg}\right)} \tag{6.36}$$

where $\dot{m}_{H2,p}$ is the production rate of hydrogen from the system in kg/s.

6.4 Formulation of Optimization Problem and Solution Method

As noted in Section 1.1, the US Department of Energy estimates that for hydrogen to be competitive with other available fuel sources, it needs to be sold at a price less than \$4/gge. To meet this goal, it is desirable to achieve reductions in the overall hydrogen production cost of the steam reforming process. By attempting to minimize the hydrogen production costs associated with the baseline and differential temperature WGS flow sheets, as estimated in Section 6.3, better insight into how the implementation of a differential temperature WGS into the steam reforming process can reduce hydrogen production costs and how the overall operating characteristics of the system might change can be obtained. Based on this insight, more informed decisions about the process conditions that a differential temperature WGS reactor should be designed for can thus be made. This section outlines the formulation of optimization problems which attempt to minimize the hydrogen production cost associated with the presented flow sheets subject to a set of operating constraints and describes the sequential quadratic programming (SQP) algorithm implemented in MATLAB to numerically evaluate the flow sheet conditions producing this minimum production cost.

6.4.1 Optimization Problem Formulation

To properly formulate a physically meaningful optimization problem to solve, an objective function defining the value to be minimized and constraints functions defining the boundaries of the design space must be specified. In the context of this problem, the objective function is to minimize the production cost of hydrogen. The hydrogen production cost is defined in equation 6.36 and is a function of the capital and operating costs of the system and the overall rate of hydrogen production, which are in turn functions of variables related to the flow sheet process.

Constraint functions generally come from physical limitations on the system regarding acceptable flow rates, temperatures, pressures, and compositions for processes to operate under and desired production metrics. For a baseline case study examining a steam reforming process with a capacity of at least 1500 kg H_2/day, it is desirable for the methane and water mass flow rates to be constrained between values of 0 kg/s and 0.2 kg/s based on the expected hydrogen production rates from the SMR and WGS reactions. While the mass flow through the blower providing air to mix with the tail gas stream is directly calculated, the mass flow through the blowers providing cooling air to the WGS pre-cooler and condenser are specified as design variables with lower limits and upper limits of 1 kg/s and 5 kg/s, respectively, to ensure that reasonable heat exchanger areas are evaluated and to prevent the temperatures of the streams from crossing over each other, which may occur at lower air flow rates. As previously mentioned in Section 6.1.4, the outlet steam produced by the boiler is assumed to be saturated with a quality of $\chi_7 = 1$. As discussed previously in Section 6.1.6, the kinetics and equilibrium of the SMR reaction are favored at high temperatures so it is desirable for the steam reformer to operate at a high temperature between 700 °C and 950 °C. For the HTS/LTS reactors configured in the baseline flow sheet, it is desirable to maintain the inlet temperature to the HTS reactor between 350 °C and 400 °C for kinetic reasons and to maintain the inlet temperature to the LTS reactor between 200 °C and 250 °for thermodynamic reasons, as discussed in Section 1.3. For effective separation through the PSA process, which requires high operating pressures and performs better at near ambient temperatures [72], it is desirable for the reaction stream to operate between approximate pressures of 10 bar and 15 bar and at a near ambient temperature of 50 °C. Additionally, if excessive amounts of carbon monoxide enter the PSA process, it is possible that some of it will slip through into the system's product hydrogen stream. Fuel cells are generally intolerant of carbon monoxide above even trace amounts so it is desirable for

the product stream exiting the WGS reactors to contain less than 1% carbon monoxide on a molar basis to ensure that a sufficiently pure stream of product hydrogen gas can be produced. Because the pressures of the cooling air streams do not generally affect the reaction processes, the pressure ratios on all of the blowers are specified as 1.1, a typical value for these devices as they do not generate significant increases in fluid pressure.

It is conventional to formulate optimization problems in negative-null form, which expresses all inequality constraints in a form where they take on positive values when violated and all equality constraints in a form where they take on non-zero values when violated. Optimization algorithms generally require problems to be specified in this way to be solved properly. In negative-null form, the optimization problem minimizing the hydrogen production cost for the baseline flow sheet subject to the listed constraints can be expressed as:

$$
\begin{aligned}
\text{minimize} \quad & Cost_{H2} \\
\text{subject to} \quad & -\dot{m}_1 \leq 0 \\
& \dot{m}_1 - (0.2kg/s) \leq 0 \\
& -\dot{m}_3 \leq 0 \\
& \dot{m}_3 - (0.2kg/s) \leq 0 \\
& (1500kg/day) - \dot{m}_{17} \leq 0 \\
& (1kg/s) - \dot{m}_{24} \leq 0 \\
& \dot{m}_{24} - (5kg/s) \leq 0 \\
& (1kg/s) - \dot{m}_{27} \leq 0 \\
& \dot{m}_{27} - (5kg/s) \leq 0 \\
& \chi_7 - 1 = 0
\end{aligned}
$$

$$10 - PR_{1-2} \leq 0$$

$$PR_{1-2} - 15 \leq 0$$

$$10 - PR_{3-4} \leq 0$$

$$PR_{3-4} - 15 \leq 0$$

$$P_2 - P_5 = 0$$

$$P_{20} - P_{32} = 0$$

$$T_7 - T_{sat,7} = 0$$

$$(700°C) - T_{10} \leq 0$$

$$T_{10} - (950°C) \leq 0$$

$$(350°C) - T_{12} \leq 0$$

$$T_{12} - (400°C) \leq 0$$

$$(200°C) - T_{14} \leq 0$$

$$T_{14} - (250°C) \leq 0$$

$$T_{16} - (50°C) = 0$$

$$y_{CO,15} - 0.01 \leq 0$$

A similar optimization problem is formulated for the differential temperature WGS reactor flow sheet, but with an additional constraint requiring the outlet CO mole fraction from the differential temperature WGS reactor to equal the outlet CO mole fraction of the LTS reactor in the baseline flow sheet to facilitate better comparison between the performance of the WGS reactors in each flow sheet.

6.4.2 Solution Method

To solve the optimization problems formulated in Section 6.4.1, I programmed the equations presented in Sections 6.1 and 6.3 into MATLAB and used the sequential quadratic programming (SQP) algorithm embedded into the built-in "fmincon" function to evaluate the flow sheet configuration resulting in the minimum hydrogen production cost subject to the constraints developed in Section 6.4.1. SQP algorithms belong to a class of iterative, gradient based solution methods used to solve non-linear, constrained optimization problems [73]. These algorithms numerically minimize an objective function using an iterative procedure that is broken into quadratic programming and step size sub-problems based on the input of an initial guess design point. First, the quadratic sup-problem is defined as:

$$\begin{aligned} \text{minimize} \quad & \nabla f(x^k)^T d_k + \frac{1}{2} d_k^T H d \\ \text{subject to} \quad & \nabla h_i^T(x^k) + h_i(x^k) = 0 \\ & \nabla g_j^T(x^k) + g_j(x^k) \leq 0 \end{aligned} \tag{6.37}$$

and solved to evaluate the search direction at each iteration in the solution process. In equation 6.37, x^k is a vector containing all design parameters that are varied in the problem with k representing the iteration number currently being evaluated, $f(x)$ is the objective function of the problem, d_k is the search direction, H is the Hessian of the Lagrange function, h_i represents all of the equality constraints imposed on the problem, and g_j represents all of the inequality constraints imposed on the problem. The Lagrangian function of the optimization problem is defined as:

$$L(x, u, v) = f(x) + \sum_{i}^{p} v_i h_i(x) + \sum_{j}^{m} u_j [g_j(x) + s_j^2] \tag{6.38}$$

where v_i and u_j are the Lagrange multipliers for the equality and inequality constraints,

respectively, and s_j is the slack variable for the inequality constraints. It is normally too difficult to analytically evaluate the Hessian matrix at each iteration so algorithms normally approximate it using a quasi-Newton method. Particularly, the MATLAB algorithm used in this study uses the BFGS method to approximate the Hessian at each iteration.

The search direction evaluated from the quadratic sub-problem is then used in the step size problem to evaluate the new design point in the iteration process using the following equation:

$$x^{k+1} = x^k + \alpha d_k \tag{6.39}$$

In equation 6.39, is the step size in the search direction. The step size is generally evaluated by minimizing a descent function along the search direction. In the MATLAB algorithm implemented, this is done by sufficiently reducing the merit function used by Han [74] and Powell [75]. At each design point evaluated, constraint violation and convergence are checked to evaluate if the current design point violates the constraints imposed on the problem and to evaluate if the magnitude of the search direction has become sufficiently small such that the design point being considered satisfies the Karush-Kuhn-Tucker (KKT) conditions, the first-order necessary conditions for a local minimum, within acceptable tolerance levels. More details regarding the SQP algorithm implemented in MATLAB can be found in the documentation provided by Mathworks [76].

Notably, the successful implementation of the SQP algorithm can only guarantee convergence to a local minimum value and not a global minimum. The algorithm is only capable of finding the minimum in the basin of attraction that the initial guess point falls in. As a result, attempting to find the global minimum of the hydrogen production cost in the defined optimization problems is an iterative process. The “GlobalSearch” function can be used to do this more efficiently by generating a grid of trial points based on the initial guess

point, using the SQP algorithm to evaluate the the resulting local minimum for each trial point, and then reporting the global minimum as the smallest of the local minima values found. While there is still no guarantee of convergence to the global minimum value using this method, the solutions obtained can still provide useful information regarding better flow sheet operating modes. The results from the "GlobalSearch" function are taken as the optimal solution for each flow sheet and are presented and discussed in Section 6.5.

6.5 Optimization Studies Results

The optimal baseline flow sheet configuration which minimizes the hydrogen production cost for the given list of constraints is summarized in Table 6.3, the corresponding equipment operation parameters for this flow sheet are summarized in Table 6.4, and the resulting production cost parameters are summarized in Table 6.5. The results of this study indicate that the optimal operation of this flow sheet results in a hydrogen production cost of approximately \$0.98/gge. While this production cost is significantly lower than the \$4/gge selling price goal set by the US Department of Energy, it does not take into account a number of factors that would significantly increase its value, including labor/maintenance work, piping costs, and the compression/storage process that the product hydrogen must also go through among others. As a result, the predicted production costs presented in this study should be considered as just a portion of the overall production cost of hydrogen from these types of systems, while still enabling a relative comparison of the baseline and distributed WGS flow sheets.

To validate the evaluated optimal baseline flow sheet, I entered the state points summarized in Table 6.3 into Aspen HYSYS, a chemical process simulation software, to check for agreement with the MATLAB model results. The results predicted by the Aspen HYSYS

model match the results predicted by the MATLAB model within 2% at every state and for every process considered, indicating very good agreement and validating the generated optimization results. The slight discrepancies in the values between the Aspen HYSYS model and the MATLAB model are likely due to slight differences in how fluid properties are evaluated. In the developed MATLAB model, the gas streams were assumed to behave as ideal gases to simplify analysis while the Aspen HYSYS model used the Peng-Robinson equation of state, which generally produces more accurate results, especially at higher pressures where gases begin to deviate from ideal behavior more noticeably. While the results generated from the MATLAB model would have been more accurate using a more comprehensive equation of state, the relative simplification in the model achieved by assuming ideal gas behavior was advantageous computationally and still produced acceptably accurate results to draw conclusions from. The flow sheet results generally indicate that the upper water flow rate constraint, upper SMR temperature constraint, upper HTS/LTS temperature constraints, lower compressor/pump pressure ratio constraints, and lower WGS pre-cooler blower mass flow constraint are all active, indicating that the optimal solution occurs at these limits. This generally makes sense and indicates the importance of water to both reaction processes, the general reduction in turbomachinery costs and enhancement to SMR conversion at lower operating pressures, and that the capital costs of the reactors are generally influential enough that the optimal system operation point favors high temperature operation to reduce reactor volume.

The predicted capital cost ($1,630,134.45) and operating cost ($32,786.34/month) of the baseline flow sheet considered in this study agree within 7.5% and 16.8% of the capital and operating costs predicted respectively for a similar distributed production steam reforming system analyzed by the National Renewable Energy Laboratory as part of a case study for their H2A hydrogen production model [64]. The system in this case study is similarly

sized, having a production capacity of approximately 1500 kg H_2/day, and, while different in several aspects, is generally similar enough to the baseline flow sheet to serve as a good basis for validating the economic analysis performed in this study. The economic analysis performed in the H2A model is generally more comprehensive than the analysis performed in this study, which likely results in its higher predicted capital costs and higher overall hydrogen production costs. The notably higher operating cost for the baseline flow sheet in this study compared to the H2A model is primarily due to the larger number of turbomachines used to provide air for cooling throughout the system. Given the rather approximate nature of the cost estimation procedure used, the agreement between the results of this study and the H2A model is quite good and gives confidence that the optimization model produces reasonable enough results to evaluate how the implementation of a differential temperature WGS reactor will alter the performance of the overall steam reforming process being examined.

Table 6.3: Optimal baseline flow sheet state points

	State Points															
	1	**2**	**3**	**4**	**5**	**6**	**7**	**8**	**9**	**10**	**11**	**12**	**13**	**14**	**15**	**16**
Mass Flow Rate, $\dot{m}$ [kg/s]	0.0545	0.0545	0.200	0.200	0.200	0.200	0.200	0.2545	0.2545	0.2545	0.2545	0.2545	0.2545	0.2545	0.2545	0.2545
Temperature, T [K]	293.15	522.98	293.15	293.23	453.57	453.57	453.57	471.68	922.53	1223.15	855.65	673.12	751.66	523.15	565.69	323.15
Pressure, P [kPa]	101.3	1013	101.3	101.3	1013	1013	1013	1013	1013	1013	1013	1013	1013	1013	1013	1013
CH_4 Mole Fraction, y_{CH4}	1	1	0	0	0	0	0	0.2345	0.2345	0.0015	0.0015	0.0015	0.0015	0.0015	0.0015	0.0015
H_2O Mole Fraction, y_{H2O}	0	0	1	1	1	1	1	0.7655	0.7655	0.3208	0.3208	0.3208	0.2511	0.2511	0.2155	0.2155
CO Mole Fraction, y_{CO}	0	0	0	0	0	0	0	0	0	0.1153	0.1153	0.1153	0.0456	0.0456	0.01	0.01
H_2 Mole Fraction, y_{H2}	0	0	0	0	0	0	0	0	0	0.5191	0.5191	0.5191	0.5888	0.5888	0.6244	0.6244
CO_2 Mole Fraction, y_{CO2}	0	0	0	0	0	0	0	0	0	0.0433	0.0433	0.0433	0.1130	0.1130	0.1486	0.1486
N_2 Mole Fraction, y_{N2}	0	0	0	0	0	0	0	0	0	0	0	0	0	0	0	0
O_2 Mole Fraction, y_{O2}	0	0	0	0	0	0	0	0	0	0	0	0	0	0	0	0

	State Points															
	17	**18**	**19**	**20**	**21**	**22**	**23**	**24**	**25**	**26**	**27**	**28**	**29**	**30**	**31**	**32**
Mass Flow Rate, $\dot{m}$ [kg/s]	0.0825	0.1720	0.0214	0.1507	0.3414	0.3414	0	1	1	1	1.4275	1.4275	1.4275	1.4275	0.1907	0.1907
Temperature, T [K]	323.15	323.15	323.15	323.15	313.81	313.81	313.81	293.15	303.93	431.60	293.15	303.93	550.93	492.51	293.15	303.93
Pressure, P [kPa]	1013	1013	1013	111.43	111.43	111.43	111.43	101.3	111.43	111.43	101.3	111.43	111.43	111.43	101.3	111.43
CH_4 Mole Fraction, y_{CH4}	0	0.0019	0	0.0052	0.0025	0.0025	0.0025	0	0	0	0	0	0	0	0	0
H_2O Mole Fraction, y_{H2O}	1	0	0	0	0	0	0	0	0	0	0	0	0	0	0	0
CO Mole Fraction, y_{CO}	0	0.0127	0	0.0351	0.0168	0.0168	0.0168	0	0	0	0	0	0	0	0	0
H_2 Mole Fraction, y_{H2}	0	0.7959	1	0.4382	0.2094	0.2094	0.2094	0	0	0	0	0	0	0	0	0
CO_2 Mole Fraction, y_{CO2}	0	0.1894	0	0.5215	0.2492	0.2492	0.2492	0	0	0	0	0	0	0	0	0
N_2 Mole Fraction, y_{N2}	0	0	0	0	0.4125	0.4125	0.4125	0.79	0.79	0.79	0.79	0.79	0.79	0.79	0.79	0.79
O_2 Mole Fraction, y_{O2}	0	0	0	0	0.1097	0.1097	0.1097	0.21	0.21	0.21	0.21	0.21	0.21	0.21	0.21	0.21

Table 6.4: Optimal baseline flow sheet equipment parameters

Equipment Parameter	**Value**
Compressor Work, $\dot{W}_{1-2}$ [kW]	32.59
Pump Work, $\dot{W}_{3-4}$ [kW]	0.2439
WGS Pre-Cooler Blower, $\dot{W}_{24-25}$ [kW]	10.89
Condenser Blower, $\dot{W}_{27-28}$ [kW]	15.54
Tail Gas Blower, $\dot{W}_{31-32}$ [kW]	2.08
Boiler Duty, $\dot{Q}_{6-7}$ [kW]	289.17
SMR Duty, $\dot{Q}_{9-10}$ [kW]	939.21
WGS Heat Rejection, $\dot{Q}_{13-14}$ [kW]	162.24
Tail Gas Heat of Combustion, $\dot{Q}_{tail}$ [kW]	667.29
Recuperative Heat Exchanger Area, $A_{HX1}[m^2]$	9.97
WGS Pre-cooler Area, $A_{HX2}[m^2]$	4.21
Air/Water Heat Exchanger Area, $A_{HX3}[m^2]$	10.5
Intercooler Area, $A_{INT}[m^2]$	1.22
Condenser Area, $A_{CON}[m^2]$	32.4
SMR Reactor Volume, $V_{SMR}[m^3]$	7.48 $\times 10^{-4}$
WGS Reactor Volume, $V_{WGS}[m^3]$	0.251

Table 6.5: Optimal baseline flow sheet production cost parameters

Production Cost Parameter	**Value**
Total Capital Costs, C	\$1,630,134.45
Capital Cost Monthly Annuity, A_C	\$12,638.42
Catalyst Cost Monthly Annuity, A_{cat}	\$3,661.63
Monthly Operating Cost, O	\$32,786.34
Monthly Hydrogen Production Rate, $\dot{m}_{H2,p}$	51,319 kg
Hydrogen Production Cost, $Cost_{H2}$	\$0.976/gge

Similar tables showing the optimal flow sheet configuration, corresponding equipment operation parameters, and the resulting production cost parameters for the differential temperature WGS reactor flow sheet are summarized in Tables 6.6 through 6.8. Comparing the state points for the optimal differential temperature WGS reactor to the state points for the optimal baseline flow sheet, it can be seen that there is an increase in the feed rate of methane into the system due to a general increase in the CO conversion capacity of the system achieved by the differential temperature WGS reactor. The SMR operation temperature is also approximately 88 K lower. While this would be expected to lower the SMR hydrogen production rate, for the specified conditions, there is actually a slight increase due to the better ratio of methane and water fed into the reformer and the improved performance of the WGS reaction within the steam reformer. This increase in total reaction stream flow rate also results in a higher required air flow rate through the condenser for appropriate heat rejection to occur and a higher required air flow rate into the mixed tail gas/air stream for complete combustion to occur. All other state points are consistent with the results from the baseline flow sheet and general operation expectations and thus appear reasonable.

Examining the equipment parameters for the differential temperature WGS reactor flow sheet, it can be seen that the higher methane feed rate also results in slightly higher required compressor work, condenser blower work, tail gas blower work, and boiler duty inputs to the system, but also in a lower required SMR heat duty, a higher WGS heat rejection, and a significantly higher heat of combustion from the tail gas. The lower SMR temperature results in a moderately larger required SMR reactor volume due to the lower reaction kinetics, but this is more than compensated for by the the 20% reduction in the WGS reactor volume achieved by the differential WGS reactor compared to the HTS/LTS reactors since the vast majority of the reactor volume in these systems is concentrated in the WGS process. Volume reductions would likely be even larger in reality given the conservative nature of the reactor modeling equations used. While the required heat exchanger area for the recuperative heat exchanger (HX 1) remains relatively constant and the required heat exchanger area for the WGS pre-cooler (HX 2) and air/water heat exchanger (HX 3) decrease moderately, there is a net increase in the total required heat transfer area in the system for the differential temperature WGS reactor flow sheet due to the increased condenser heat duty since the condenser requires the largest amount of heat transfer area.

In terms of the effects that the integration of a differential temperature WGS reactor has on the overall system costs, there is a 3.3% reduction in the capital costs of the system, a 1.63% increase in the operating costs of the system, and a rather significant decrease of 150% in the catalyst costs, as shown in Figure 6.4. The total 6.16% reduction in the overall monthly costs achieved by the differential temperature WGS reactor flow sheet and 2.35% increase in hydrogen production achieved together result in an 8.55% reduction in the overall hydrogen production cost from \$0.98/gge to \$0.90/gge, a significant decrease. Figure 6.5 more directly shows how the breakdown in capital costs of the baseline and differential temperature WGS reactor flow sheets compare to each other. While most of the equipment

capital costs remain fairly similar between the two systems, with the capital costs of a number of pieces of equipment actually increasing slightly due to the increased feed rate of methane into the system, there is a significant reduction in the cost of the WGS reactor system due to the significant reduction in reactor volume. This, when combined with the absence of an intercooler cost and the slight reductions in cost for the WGS pre-cooler and SMR reactor, results in the lower overall capital costs of the differential temperature WGS reactor flow sheet. Figure 6.6 more directly show the breakdown of operating costs of the baseline and differential temperature WGS reactor flow sheets compare to each other. There is actually an overall increase in the operating costs associated with the differential temperature WGS reactor flow sheet compared to the baseline flow sheet primarily due to the increased feed rate of methane into the system, resulting in both higher methane feed costs and slightly higher turbomachinery costs. This is somewhat tempered by the reduction in the SMR operating costs due to the increased heat recovery achieved from the tail gas and the lower required heat input to the SMR as a result of its lowered operating temperature. While higher overall operating costs are generally undesirable, when considered in the broader context of the overall system costs, the reduction in both the capital and catalyst costs and the increase in the hydrogen production rate achieved by the differential temperature WGS reactor flow more than compensate for this and result in a more cost effective process overall. Should higher operating costs be undesirable, the optimization model can be reformulated to account for additional constraints or updated cost information to evaluate a new optimal operation point, making it a generally useful design tool in evaluating both the overall system operation and for defining the inlet condition that a differential temperature WGS reactor should be designed for in the context of optimal system operation.

Table 6.6: Optimal differential temperature WGS reactor flow sheet state points

	State Points														
	1	**2**	**3**	**4**	**5**	**6**	**7**	**8**	**9**	**10**	**11**	**12**	**13**	**14**	**15**
Mass Flow Rate, $\dot{m}$ [kg/s]	0.0577	0.0577	0.200	0.200	0.200	0.200	0.200	0.2577	0.2577	0.2577	0.2577	0.2577	0.2577	0.2577	0.0797
Temperature, T [K]	293.15	522.98	293.15	293.23	453.57	453.57	453.57	472.46	875.81	1144.7	817.43	673.15	535.48	323.15	323.15
Pressure, P [kPa]	101.3	1013	101.3	1013	1013	1013	1013	1013	1013	1013	1013	1013	1013	1013	1013
CH_4 Mole Fraction, y_{CH4}	1	1	0	0	0	0	0	0.2448	0.2448	0.0070	0.0070	0.0070	0.0070	0.0070	0
H_2O Mole Fraction, y_{H2O}	0	0	1	1	1	1	1	0.7522	0.7522	0.3032	0.3032	0.3032	0.2048	0.2048	1
CO Mole Fraction, y_{CO}	0	0	0	0	0	0	0	0	0	0.1085	0.1085	0.1085	0.0100	0.0100	0
H_2 Mole Fraction, y_{H2}	0	0	0	0	0	0	0	0	0	0.5301	0.5301	0.5301	0.6286	0.6286	0
CO_2 Mole Fraction, y_{CO2}	0	0	0	0	0	0	0	0	0	0.0512	0.0512	0.0512	0.1497	0.1497	0
N_2 Mole Fraction, y_{N2}	0	0	0	0	0	0	0	0	0	0	0	0	0	0	0
O_2 Mole Fraction, y_{O2}	0	0	0	0	0	0	0	0	0	0	0	0	0	0	0

	State Points														
	16	**17**	**18**	**19**	**20**	**21**	**22**	**23**	**24**	**25**	**26**	**27**	**28**	**29**	**30**
Mass Flow Rate, $\dot{m}$ [kg/s]	0.1780	0.0219	0.1561	0.3838	0.3838	0	1	1	1	1.4949	1.4949	1.4949	1.4949	0.2277	0.02277
Temperature, T [K]	323.15	323.15	323.15	323.15	313.17	313.17	293.15	303.93	406.81	293.15	303.93	523.38	481.49	293.15	303.93
Pressure, P [kPa]	1013	1013	111.43	111.43	111.43	111.43	101.3	111.43	111.43	101.3	111.43	111.43	111.43	101.3	111.43
CH_4 Mole Fraction, y_{CH4}	0.0088	0	0.0238	0.0106	0.0106	0.0106	0	0	0	0	0	0	0	0	0
H_2O Mole Fraction, y_{H2O}	0	0	0	0	0	0	0	0	0	0	0	0	0	0	0
CO Mole Fraction, y_{CO}	0.0126	0	0.0342	0.0152	0.0152	0.0152	0	0	0	0	0	0	0	0	0
H_2 Mole Fraction, y_{H2}	0.7905	1	0.4300	0.1911	0.1911	0.1911	0	0	0	0	0	0	0	0	0
CO_2 Mole Fraction, y_{CO2}	0.1882	0	0.5119	0.2275	0.2275	0.2275	0	0	0	0	0	0	0	0	0
N_2 Mole Fraction, y_{N2}	0	0	0	0.4389	0.4389	0.4389	0.79	0.79	0.79	0.79	0.79	0.79	0.79	0.79	0.79
O_2 Mole Fraction, y_{O2}	0	0	0	0.1167	0.1167	0.1167	0.21	0.21	0.21	0.21	0.21	0.21	0.21	0.21	0.21

Table 6.7: Optimal differential temperature WGS reactor flow sheet equipment parameters

Equipment Parameter	**Value**
Compressor Work, $\dot{W}_{1-2}$ [kW]	34.49
Pump Work, $\dot{W}_{3-4}$ [kW]	0.2439
WGS Pre-Cooler Blower, $\dot{W}_{22-23}$ [kW]	10.89
Condenser Blower, $\dot{W}_{25-26}$ [kW]	16.27
Tail Gas Blower, $\dot{W}_{29-30}$ [kW]	2.48
Boiler Duty, $\dot{Q}_{6-7}$ [kW]	290.79
SMR Duty, $\dot{Q}_{9-10}$ [kW]	927.67
WGS Heat Rejection, $\dot{Q}_{12-13}$ [kW]	182.53
Tail Gas Heat of Combustion, $\dot{Q}_{tail}$ [kW]	777.88
Recuperative Heat Exchanger Area, $A_{HX1}[m^2]$	9.94
WGS Pre-cooler Area, $A_{HX2}[m^2]$	3.41
Air/Water Heat Exchanger Area, $A_{HX3}[m^2]$	10.96
Condenser Area, $A_{CON}[m^2]$	34.76
SMR Reactor Volume, $V_{SMR}[m^3]$	1.05×10^{-3}
WGS Reactor Volume, $V_{WGS}[m^3]$	0.1995

Table 6.8: Optimal differential temperature WGS reactor flow sheet production cost parameters

Production Cost Parameter	**Value**
Total Capital Costs, C	\$1,577,942.73
Capital Cost Monthly Annuity, A_C	\$12,233.77
Catalyst Cost Monthly Annuity, A_{cat}	\$583.98
Monthly Operating Cost, O	\$33,333.07
Monthly Hydrogen Production Rate, $\dot{m}_{H2,p}$	52,537 kg
Hydrogen Production Cost, $Cost_{H2}$	\$0.896/gge

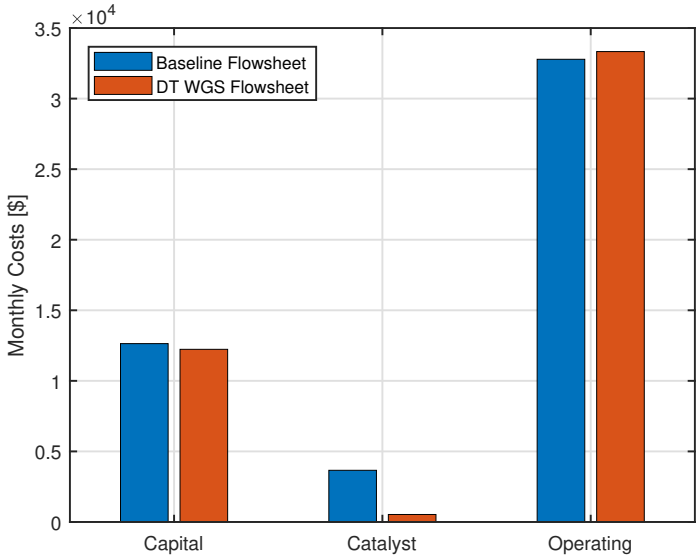

Figure 6.4: Comparison of total monthly costs for baseline and differential WGS reactor flow sheets

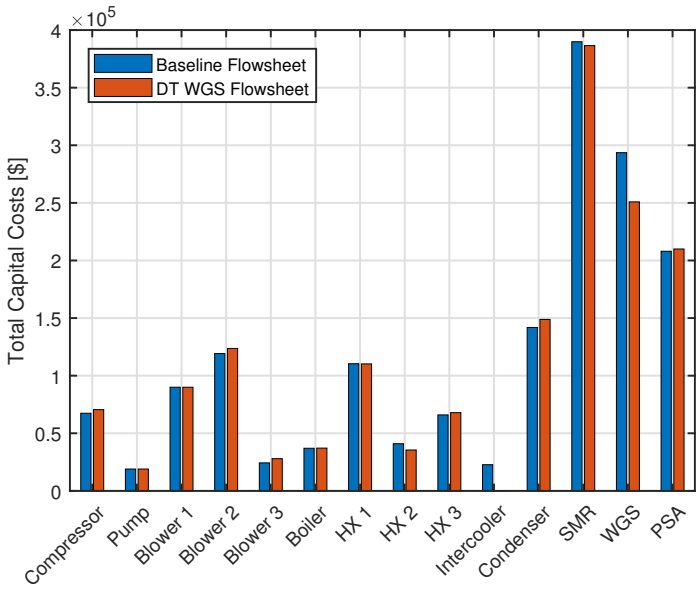

Figure 6.5: Comparison of total capital costs for baseline and differential WGS reactor flow sheets

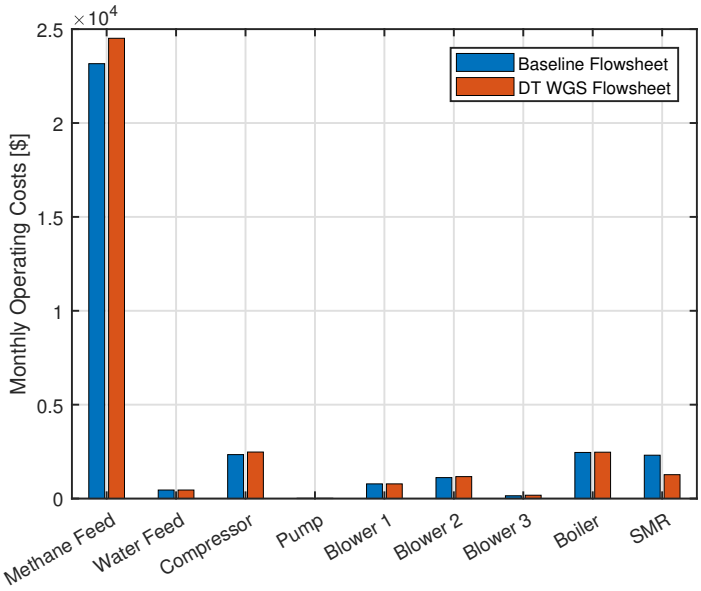

Figure 6.6: Comparison of operating costs for baseline and differential WGS reactor flow sheets

6.6 Optimization Studies Summary

The optimization study results presented in this chapter indicate that the implementation of a differential WGS reactor within the steam methane reforming process is capable of achieving a significant hydrogen production cost reduction of \$0.08/gge, primarily as a result of the decrease in capital and catalyst costs achieved and the increased production capacity that it allows the system to operate at while still maintaining appropriately low product concentrations of CO. In addition to validating that the effective implementation of differential temperature WGS reactors can be used to the economic benefit of the whole steam methane reforming process, these results also provide baseline conversion and temperature profiles that can be used in the development of more detailed component design models such as the ones discussed in Chapters 3 and 4. As an example of this, the conversion and temperature profiles evaluated from the optimal differential temperature WGS reactor flow sheet are shown in Figures 6.7 and 6.8 and compared to the optimal reaction progression for these conditions in 6.9. These results generally indicate that the reactor should operate as close to adiabatically as possible for the first 5.53×10^{-3} m^3 of reactor volume for the inlet condition supplied and then be actively cooled for the remainder of the reactor length to follow the optimal progression as closely as possible. This information, when used in conjunction with the reactor design parameters corresponding to the desired geometry, can be used to develop an appropriate reactor design through an iterative process as I did in the development of a reactor prototype in Chapter 5.

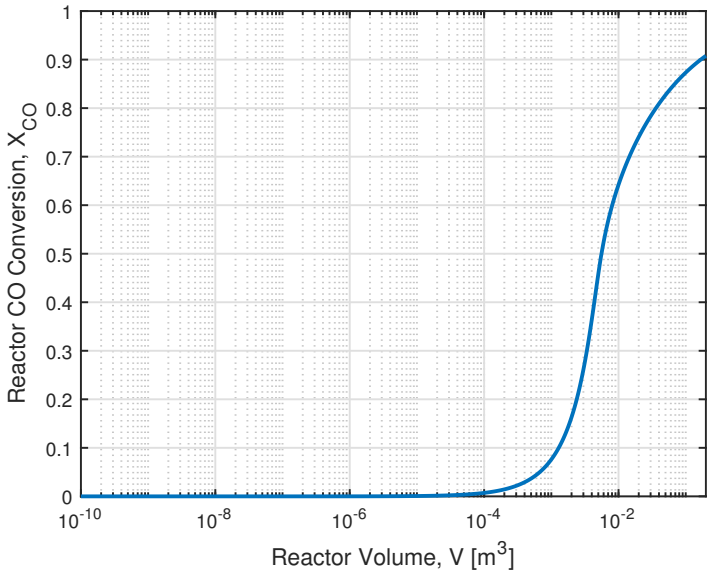

Figure 6.7: Differential temperature WGS reactor conversion profile for optimal system performance

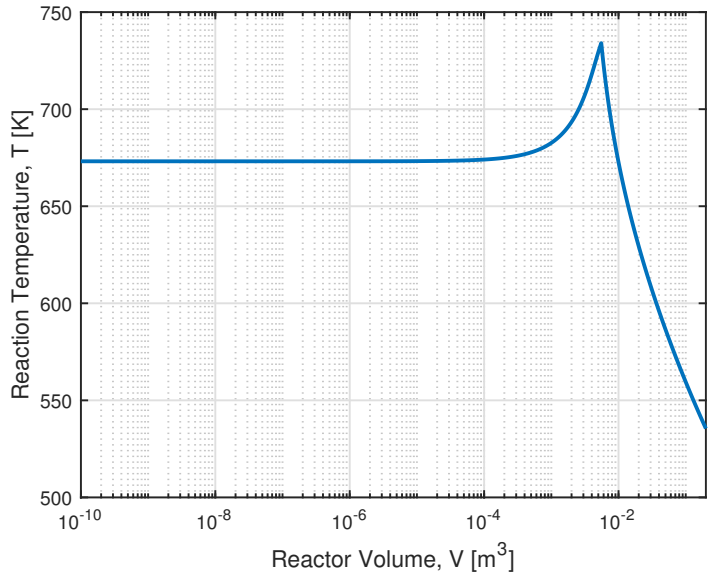

Figure 6.8: Differential temperature WGS reactor temperature profile for optimal system performance

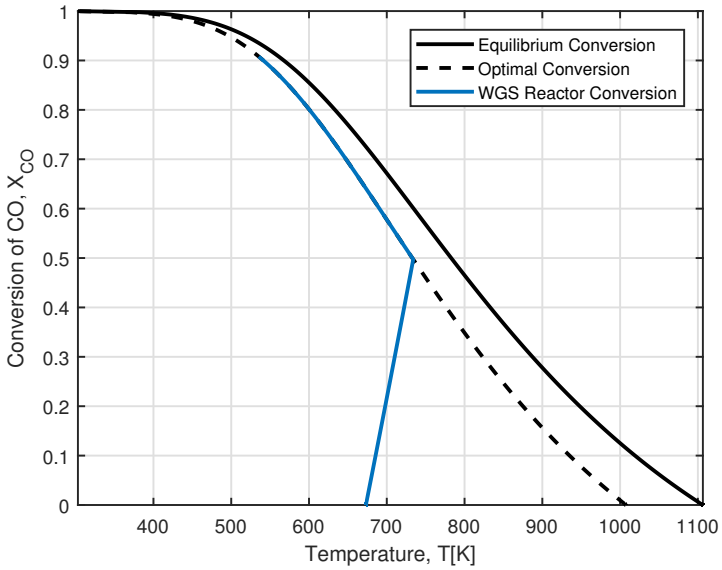

Figure 6.9: Comparison of differential temperature WGS reactor progression to optimal reaction progression for optimal system performance

Chapter 7: Conclusions, Research Contributions, and Future Work

This chapter presents the major conclusions drawn from the component modeling, prototyping, experimental verification, and system optimization efforts presented across this thesis, outlines the major research contributions offered by this study, and discusses major opportunities for future work.

7.1 Conclusions

In the presented study, a 2-D COMSOL Multiphysics model of a differential temperature water-gas shift reactor accounting for momentum, mass, and heat transfer was developed. Comparisons of the predicted CO conversion results from the model and experimental data in the literature indicated good agreement, within an absolute average percent error of 8%, validating the model and giving confidence that the parametric studies performed using the model provide physically meaningful results. The operation of this model under an optimal temperature profile improves reactor performance beyond what standard HTS/LTS reactors are capable of, often achieving 10-25% reductions in the required reactor volume and as much as an 80-90% reduction in the required amount of catalyst under ideal conditions. Given the very conservative nature of the HTS/LTS reactor model used, which assumes 100% catalyst effectiveness and ultimately represent the best possible performance of this reactor system, significantly larger reductions in the required reactor volume and required catalyst amount appear possible. Studies examining the performance of integrated coolant microreactor models suggest that this ideal performance can be reasonably approximated by more realistic cooling conditions, though care must be taken to avoid excessive cooling

of the reaction at the expense of the reaction kinetics.

In the optimization studies performed, a baseline flowsheet using HTS/LTS WGS reactors was developed, optimized, and used to develop a baseline hydrogen production cost for a steam reforming process operating at a distributed production capacity of 1500 kg H_2/day. The predicted capital and operating costs of this system agree within 7.5% and 16.8% of a similar flowsheet developed by the National Renewable Energy Laboratory (NREL), giving confidence that it is producing reasonable production cost estimates. Modifying this flowsheet to use a differential temperature WGS reactor instead of HTS/LTS reactors resulted in a an \$0.08/gge reduction in the hydrogen production cost of the system, a significant decrease which demonstrates the economic benefit that properly implemented differential temperature WGS reactors can have on the overall steam reforming process. Furthermore, the evaluated conversion and temperature profiles of the WGS reaction from this system level optimization study serve as useful baseline results to emulate in more detailed component modeling and design efforts.

As part of an exploratory effort to evaluate the potential application of additive manufacturing to WGS microreactor production, a microreactor prototype featuring channels with characteristic lengths on the order of 1 mm was manufactured from Inconel 718 using a selective laser melting (SLM) process. The thermal-hydraulic performance was experimentally characterized by measuring the heat exchanger effectiveness and pressure drop of the device under non-reacting conditions to further validate the thermal-hydraulic component of the COMSOL model. Notably, the thermal-hydraulic performance of the manufactured prototype appears reasonably well predicted by the thermal-hydraulic portion of the modeling performed in COMSOL Multiphysics, with the experimental and modeled heat exchanger effectiveness values agreeing within an absolute average percent error of 9%, and the experimental and modeled pressure drops agreeing within an absolute average percent error

of 15% across all test points evaluated. While a microreactor prototype was successfully manufactured using SLM, manufacturing and cost restrictions ultimately required the production of an approximately sixth scale device. Restrictions regarding both the size of the powder bed available to manufacture the device in and the size of the powder itself limited the footprint of the overall device and the minimum feature size to values outside of the ranges initially desired. Issues regarding catalyst insertion, removal, and replacement in this prototype and similarly manufactured microreactors also still pose a challenge since there is essentially no access to the internal features of the device once it has been fully formed by the additive manufacturing process. Furthermore, consistent trends in the collected experimental data potentially suggest that the channel dimensions of the prototype slightly differ from the specified dimensions in the part model, which is problematic for the development of microscale devices which require a high degree of manufacturing precision. These are all challenges that still need to be resolved before additive manufacturing can truly be used to its full potential for the production of microreactors.

7.2 Research Contributions

While a number of other groups have studied the performance of differential temperature WGS microreactors, there has not been work generalizing how the improved performance of these reactors translates to improved operation of the entire steam methane reforming process. The work presented in this thesis bridges this gap by implementing the developed component model of a differential temperature WGS microreactor into a flow sheet model of the steam methane reforming process and optimizing the system's performance subject to a common set of operating constraints, demonstrating the notable economic benefits that can be incurred by doing so.

As part of the work that needs to be done to realize the implementation of differential temperature WGS microreactors into actual industrial operation, manufacturing and fabrication techniques to achieve the desired microreactor architectures of these designs must be further refined and developed. In service of this, this thesis also acts as a preliminary study examining the potential that additive manufacturing has for the development of differential temperature WGS microreactors by experimentally demonstrating how the thermal-hydraulic performance of one such prototype is appropriate for the temperature control of the WGS reaction and how the performance of such a device is well predicted by the modeling performed in this study.

7.3 Future Work

While the modeling results in this study suggest that the application of differential temperature microreactors operating under optimal temperature conditions to the WGS reaction can result in significant reductions in the required reactor volume, the model was limited to a 2-D model of single rectangular channels/reactor unit cells due to the extended computation times required by more intricate 3-D models. This suggest an opportunity for the development of more detailed computational models that would better predict the performance of actual reactors. Additionally, further experimental studies are needed to evaluate if the modeling results presented in this study accurately predict improvements in WGS reaction performance during actual operation and to evaluate if the proposed platinum catalyst in this study can successfully weather these conditions for extended periods of time. Furthermore, while an initial additively manufactured prototype was successfully created and tested as part of this study, future work should be done to examine how the resolutions of these devices can be improved, how catalyst can be effectively integrated into

these devices, and how additive manufacturing can be applied toward the development of geometrically optimized reactor designs otherwise not achievable by traditional manufacturing techniques. Finally, while the results of the flow sheet optimization study indicate significant cost reductions in the steam methane reforming process by the implementation of a differential temperature WGS microreactor, there were a number of simplifying assumptions in this analysis which could impact the accuracy of the indicated results. This suggest an opportunity for more detailed economic analyses which could account for phenomena such as pressure drop and heat losses in the operating costs of the system.

Bibliography

[1] E Taibi, R Miranda, W Vanhoudt, T Winkel, JC Lanoix, and F Barth, *Hydrogen from renewable power: Technology outlook for the energy transition*, tech. rep. (International Renewable Energy Agency, Abu Dhabi, 2018), pp. 1–50.

[2] MRF Joseck, *Hydrogen Threshold Cost Calculation*, tech. rep. (2011).

[3] *Hydrogen Production Pathways | Department of Energy.*

[4] *Hydrogen Production: Natural Gas Reforming | Department of Energy.*

[5] R Wegeng, R Diver, and P Humble, "Second law analysis of a solar methane reforming system", Energy Procedia **49**, 1248–1258 (2014) 10.1016/j.egypro.2014.03.134.

[6] A Li, CJ Lim, and JR Grace, "Staged-separation membrane reactor for steam methane reforming", Chemical Engineering Journal **138**, 452–459 (2008) 10.1016/j.cej.2007.06.024.

[7] C Rhodes, GJ Hutchings, and AM Ward, "Water-gas shift reaction: finding the mechanistic boundary", Catalysis Today **23**, 43–58 (1995).

[8] BR Smith J, M Loganathan, and M Shekhar Shantha, "A Review of the Water Gas Shift Reaction Kinetics A Review of the Water Gas Shift Reaction Kinetics", International Journal of Chemical Reactor Engineering **8**, 1–32 (2010).

[9] P Kumar, E Akpan, H Ibrahim, A Aboudheir, and R Idem, "Kinetics and Reactor Modeling of a High Temperature Water-Gas Shift Reaction (WGSR) for Hydrogen Production in a Packed Bed Tubular Reactor (PBTR)", Ind. Eng. Chem. Res **47**, 4086–4097 (2008) 10.1021/ie071547q.

[10] N Kockmann, *Micro Process Engineering : Fundamentals, Devices, Fabrication, and Applications*, 5th ed. (Wiley-VCH, 2006), p. 507.

[11] W Ehrfeld, V Hessel, and H Löwe, *Microreactors: New Technology for Modern Chemistry*, 1st (Wiley-VCH, Apr. 2000), 10.1002/3527601953.

[12] KF Jensen, "Microchemical systems: Status, challenges, and opportunities", AIChE Journal **45**, 2051–2054 (1999) 10.1002/aic.690451003.

[13] KF Jensen, "Flow chemistry-Microreaction technology comes of age", AIChE Journal **63**, 858–869 (2017) 10.1002/aic.15642.

[14] *Technological Advances Could Reduce Effectiveness of Chemical Weapons Convention | Lawrence Livermore National Laboratory.*

[15] SH Huang, P Liu, A Mokasdar, and L Hou, "Additive manufacturing and its societal impact: a literature review", The International Journal of Advanced Manufacturing Technology **67**, 1191–1203 (2013) 10.1007/s00170-012-4558-5.

[16] KV Wong and A Hernandez, "A Review of Additive Manufacturing", International Scholarly Research Network ISRN Mechanical Engineering **2012**, 1–10 (2012) 10.5402/2012/208760.

[17] C Parra-Cabrera, C Achille, S Kuhn, and R Ameloot, "3D printing in chemical engineering and catalytic technology: structured catalysts, mixers and reactors", Chem. Soc. Rev **47**, 209–230 (2018) 10.1039/c7cs00631d.

[18] J Kruth, "Material Incress Manufacturing by Rapid Prototyping Techniques", CIRP Annals **40**, 603–614 (1991) 10.1016/S0007-8506(07)61136-6.

[19] M Twigg, *Catalyst Handbook*, 2nd ed. (CRC Press, 1989).

[20] J Moe, "Design of Water-Gas Shift Reactors", Chem. Eng. Prog. **58**, 33–36 (1962).

[21] RA Van Santen, *Modern Heterogeneous Catalysis: An Introduction* (Wiley-VCH, 2017).

[22] DS Newsome, "The Water-Gas Shift Reaction", Catalysis Reviews **21**, 275–318 (1980) 10.1080/03602458008067535.

[23] C Ratnasamy and JP Wagner, "Catalysis Reviews Water Gas Shift Catalysis Water Gas Shift Catalysis", Catalysis Reviews **51**, 325–440 (2009) 10.1080/01614940903048661.

[24] HF Rase, *Chemical Reactor Design for Process Plants* (Wiley, 1977).

[25] C Callaghan, I Fishtik, R Datta, M Carpenter, M Chmielewski, and A Lugo, "An improved microkinetic model for the water gas shift reaction on copper", Surface Science **541**, 21–30 (2003) 10.1016/S0039-6028(03)00953-1.

[26] MSS Martyn V. Twigg, "Deactivation of supported copper metal catalysts for hydrogenation reactions", Applied Catalysis A: General **212**, 161–174 (2001) 10.1016/S0926-860X(00)00854-1.

[27] H Kušar, S Hočevar, and J Levec, "Kinetics of the water-gas shift reaction over nanostructured copper-ceria catalysts", Applied Catalysis B: Environmental **63**, 194–200 (2005) 10.1016/j.apcatb.2005.09.019.

[28] AM Duarte de Farias, D Nguyen-Thanh, and MA Fraga, "Discussing the use of modified ceria as support for Pt catalysts on water-gas shift reaction", Applied Catalysis B: Environmental **93**, 250–258 (2010) 10.1016/j.apcatb.2009.09.036.

[29] O Thinon, F Diehl, P Avenier, and Y Schuurman, "Screening of bifunctional water-gas shift catalysts", Catlysis Today **137**, 29–35 (2008) 10.1016/j.cattod.2008.01.001.

[30] X Wang, RJ Gorte, and JP Wagner, "Deactivation Mechanisms for Pd/Ceria during the Water-Gas-Shift Reaction", Journal of Catalysis **212**, 225–230 (2002) 10.1006/jcat.2002.3789.

[31] S Hilaire, X Wang, T Luo, RJ Gorte, and J Wagner, "A comparative study of water-gas-shift reaction over ceria supported metallic catalysts", Applied Catalysis A: General **215**, 271–278 (2001).

[32] JM Zalc and V Sokolovskii, "Are Noble Metal-Based Water–Gas Shift Catalysts Practical for Automotive Fuel Processing?", Journal of Catalysis **206**, 169–171 (2002) 10.1006/jcat.2001.3465.

[33] C Ovesen, P Stoltze, J Nørskov, and C Campbell, "A kinetic model of the water gas shift reaction", Journal of Catalysis **134**, 445–468 (1992) 10.1016/0021-9517(92)90334-E.

[34] G Wang, L Jiang, Z Cai, Y Pan, X Zhao, W Huang, K Xie, Y Li, Y Sun, and B Zhong, "Surface Structure Sensitivity of the Water-Gas Shift Reaction on Cu(hkl) Surfaces: A Theoretical Study", Journal of Physical Chemistry B **107**, 557–562 (2003) 10.1021/jp0215567.

[35] C Ovesen, B Clausen, B Hammershøi, G Steffensen, T Askgaard, I Chorkendorff, J Nørskov, P Rasmussen, P Stoltze, and P Taylor, "A Microkinetic Analysis of the Water–Gas Shift Reaction under Industrial Conditions", Journal of Catalysis **158**, 170–180 (1996) 10.1006/JCAT.1996.0016.

[36] AA Gokhale, JA Dumesic, and M Mavrikakis, "On the Mechanism of Low-Temperature Water Gas Shift Reaction on Copper", Journal of the American Chemical Society **130**, 1402–1414 (2008) 10.1021/ja0768237.

[37] LC Grabow, AA Gokhale, ST Evans, JA Dumesic, and M Mavrikakis, "Mechanism of the Water Gas Shift Reaction on Pt: First Principles, Experiments, and Microkinetic

Modeling", Journal of Physical Chemistry C **112**, 4608–4617 (2008) 10.1021/jp7099702.

[38] FG Botes, "Water-gas-shift kinetics in the iron-based low-temperature Fischer-Tropsch synthesis", Applied Catalysis A: General **328**, 237–242 (2007) 10.1016/j.apcata.2007.06.016.

[39] I Fishtik and R Datta, "A UBI–QEP microkinetic model for the water–gas shift reaction on Cu(111)", Surface Science **512**, 229–254 (2002) 10.1016/S0039-6028(02)01689-8.

[40] C Rhodes and GJ Hutchings, "Studies of the role of the copper promoter in the iron oxide/chromia high temperature water gas shift catalyst", Physical Chemistry Chemical Physics **5**, 2719–2723 (2003) 10.1039/b303236c.

[41] RL Keiski, T Salmi, P Niemisti5, J Ainassaari, and VJ Pohjola, "Stationary and transient kinetics of the high temperature water-gas shift reaction", Applied Catalysis A: General **137**, 349–370 (1996).

[42] S Shwe Hla, D Park, GJ Duffy, JH Edwards, DG Roberts, A Ilyushechkin, LD Morpeth, T Nguyen, KP Co, and P Co, "Kinetics of high-temperature water-gas shift reaction over two iron-based commercial catalysts using simulated coal-derived syngases", Chemical Engineering Journal **146**, 148–154 (2009) 10.1016/j.cej.2008.09.023.

[43] Y Choi and HG Stenger, "Water gas shift reaction kinetics and reactor modeling for fuel cell grade hydrogen", Journal of Power Sources **124**, 432–439 (2003) 10.1016/S0378-7753(03)00614-1.

[44] G Germani and Y Schuurman, "Water-gas shift reaction kinetics over μ-structured Pt/CeO2/Al2O3 catalysts", AIChE Journal **52**, 1806–1813 (2006) 10.1002/aic.10764.

[45] A Criscuoli, A Basile, and E Drioli, "An analysis of the performance of membrane reactors for the water–gas shift reaction using gas feed mixtures", Catalysis Today **56**, 53–64 (2000) 10.1016/S0920-5861(99)00262-X.

[46] J Sun, J Desjardins, J Buglass, and K Liu, "Noble metal water gas shift catalysis: Kinetics study and reactor design", International Journal of Hydrogen Energy (2005) 10.1016/j.ijhydene.2005.02.013.

[47] OL Ding and SH Chan, "Water-gas shift reaction-A 2-D modeling approach", International Journal of Hydrogen Energy **33**, 4325–4336 (2008) 10.1016/j.ijhydene.2008.05.087.

[48] WE Tegrotenhuis, DL King, KP Brooks, BJ Golladay, and RS Wegeng, "Optimizing Microchannel Reactors by Trading-Off Equilibrium and Reaction Kinetics through Temperature Management", in 6th international conference on microreaction technology (2002), pp. 1–11.

[49] O Levenspiel, *Chemical Reaction Engineering*, 3rd ed. (Wiley, 1999).

[50] HS Fogler, *Elements of Chemical Reaction Engineering*, 4th ed. (Prentice Hall, 2006).

[51] G Barbieri, A Brunetti, T Granato, P Bernardo, and E Drioli, "Engineering Evaluations of a Catalytic Membrane Reactor for the Water Gas Shift Reaction", Ind. Eng. Chem. Res **44**, 7676–7683 (2005) 10.1021/ie050357h.

[52] G Germani, P Alphonse, M Courty, Y Schuurman, and C Mirodatos, "Platinum/ceria/alumina catalysts on microstructures for carbon monoxide conversion", Catlysis Today **110**, 114–120 (2005) 10.1016/j.cattod.2005.09.017.

[53] A Tonkovich, J Zilka, M LaMont, Y Wang, and R Wegeng, "Microchannel reactors for fuel processing applications. I. Water gas shift reactor", Chemical Engineering Science **54**, 2947–2951 (1999) 10.1016/S0009-2509(98)00346-7.

[54] S Bac, S Keskin, and AK Avci, "Modeling and simulation of water-gas shift in a heat exchange integrated microchannel converter", International Journal of Hydrogen Energy **43**, 1094–1104 (2018) 10.1016/j.ijhydene.2017.09.141.

[55] E Rebrov, S Kuznetsov, M de Croon, and J Schouten, "Study of the water-gas shift reaction on Mo2C/Mo catalytic coatings for application in microstructured fuel processors", Catalysis Today **125**, 88–96 (2007) 10.1016/j.cattod.2007.01.075.

[56] GY Kim, JR Mayor, and J Ni, "Parametric study of microreactor design for water gas shift reactor using an integrated reaction and heat exchange model", Chemical Engineering Journal **110**, 1–10 (2005) 10.1016/j.cej.2004.05.015.

[57] EL Romero and BA Wilhite, "Enhancement of water-gas-shift conversion via externally imposed temperature profiles: Comparison of linear, convex and Gaussian profiles", Chemical Engineering Journal **175**, 433–442 (2011) 10.1016/j.cej.2011.09.050.

[58] T Baier and G Kolb, "Temperature control of the water gas shift reaction in microstructured reactors", Chemical Engineering Science **62**, 4602–4611 (2007) 10.1016/j.ces.2007.04.047.

[59] AJ Capel, S Edmondson, SDR Christie, RD Goodridge, RJ Bibb, and M Thurstans, "Design and additive manufacture for flow chemistry", Lab on a Chip **13**, 4583–4590 (2013) 10.1039/c3lc50844g.

[60] PJ Kitson, MH Rosnes, V Sans, V Dragone, and L Cronin, "Configurable 3D-Printed millifluidic and microfluidic 'lab on a chip' reactionware devices", Lab on a Chip **12**, 3267 (2012) 10.1039/c2lc40761b.

[61] PJ Kitson, S Glatzel, W Chen, CG Lin, YF Song, and L Cronin, "3D printing of versatile reactionware for chemical synthesis", Nature Protocols **11**, 920–936 (2016) 10.1038/nprot.2016.041.

[62] CR Wilke, "A Viscosity Equation for Gas Mixtures", The Journal of Chemical Physics **18**, 517–519 (1950) 10.1063/1.1747673.

[63] SJ Kline and FA McClintock, "Describing Uncertainties in Single Sample Experiments", Mechanical Engineering **75**, 3–8 (1953).

[64] M Penev, G Saur, C Hunter, and J Zuboy, *H2A Production Model H2A Hydrogen Production Model: Version 3.2018 User Guide*, tech. rep. (National Renewable Energy Laboratory, 2018).

[65] S Sircar, WE Waldron, MB Rao, and M Anand, "Hydrogen production by hybrid SMR – PSA – SSF membrane system", Separation and Purification Technology **17**, 11–20 (1999).

[66] J Xu and GF Froment, "Methane Steam Reforming, Methanation and Water-Gas Shift: 1. Intrinsic Kinetics", AIChE Journal **35**, 88–96 (1989).

[67] A Jeong, D Shin, SM Baek, and JH Nam, "Effectiveness factor correlations from simulations of washcoat nickel catalyst layers for small-scale steam methane reforming applications", International Journal of Hydrogen Energy **43**, 15398–15411 (2018) 10.1016/j.ijhydene.2018.06.059.

[68] HA Dirksen and CH Riesz, "Equilibrium in the Steam Reforming of Natural Gas", Industrial and Engineering Chemistry Research **45**, 1562–1565 (1953).

[69] DE Garrett, *Chemical Engineering Economics* (New York, 1989), pp. 255–308.

[70] *Chemical Engineering - Chemical Engineering essentials for the global chemical processing industries (CPI).*

[71] *CatCost, An Estimation Tool to Aid Commercialization and R&D Decisions for Catalytic Materials, Documentation and User Guide*, tech. rep. (National Renewable Energy Laboratory, 2018).

[72] JG Speight, "Hydrogen Production", in *Heavy oil recovery and upgrading* (Gulf Professional, Cambridge, Massachusetts, Jan. 2019) Chap. 15, pp. 657–697, 10.1016/B978-0-12-813025-4.00015-5.

[73] JS Arora, *Introduction to Optimum Design*, 4th ed. (Elsevier, San Diego, 2017).

[74] S Han, "A Globally Convergent Method for Nonlinear Programming", Optimization Theory and Applications **22**, 297–309 (1977).

[75] M Powell, "The Convergence of Variable Metric Methods for Nonlinearly Constrained Optimization Calculations", in *Nonlinear programming 3* (Elsevier, Jan. 1978), pp. 27–63, 10.1016/b978-0-12-468660-1.50007-4.

[76] *Constrained Nonlinear Optimization Algorithms - MATLAB & Simulink.*

APPENDICES

Appendix A: HTS/LTS Packed Bed Reactor Model MATLAB Script

The MATLAB script used to solve the baseline HTS/LTS packed bed reactor model developed in Section 3.1 is attached in this appendix. This script directly implements the plug flow reactor (PFR) relations developed to solve for the conversion profile, temperature profile, and required reactor volume of this system.

Contents

Appendix A: HTS/LTS PFR Model

```
%Thomas Tolley
```

Clear All, Close All, Clear Screen

```
clear all;

close all;

clc;
```

Set Inlet Conditions for HTS

```
m_dot_WGS = 2.525/1000; %Mass flow [kg/s]

y_CO_HTS(1,1) = 0.113; %Inlet mole fraction CO to HTS

y_H2O_HTS(1,1) = 0.244; %Inlet mole fraction H2O to HTS

y_CO2_HTS(1,1) = 0.052; %Inlet mole fraction CO2 to HTS

y_H2_HTS(1,1) = 0.546; %Inlet mole fraction H2 to HTS
```

```
y_CH4_HTS(1,1) = 0.045; %Inlet mole fraction CH4 to HTS

T_HTS(1,1) = 350+273.15; %Inlet temperature to HTS [K]

P_WGS = 5; %Reactor pressure [bar]

R_const = 8.314; %Ideal gas constant [J/mol-K]

X_CO_HTS(1,1) = 0; %Initial CO conversion

V_HTS(1,1) = 0; %Initial reactor volume [m3]

%Molar Masses [kg/mol]

MW_CO = 0.028;

MW_H2O = 0.01802;

MW_CO2 = 0.04401;

MW_H2 = 0.002016;

MW_CH4 = 0.01604;
```

Kinetic Parameters

```
K_0 = 3.7E7; %Frequency factor [mol/kg-s]

E_a = 78.2*1000; %Activation energy [J/mol]

K_CO = 94.4; %CO adsoprtion constant [1/bar]

K_H2O = 12.2; %H2O adsorption constant [1/bar]

K_CO2 = 2.4; %CO2 adsorption constant [1/bar]

K_H2 = 462; %H2 adsorption constant [1/bar]

rho_cat = 1450; %Catalyst density [kg/m3]
```

Calculated HTS Inlet Conditions

```
%Partial Pressures [bar]

P_CO_HTS(1,1) = y_CO_HTS(1,1)*P_WGS;
P_H2O_HTS(1,1) = y_H2O_HTS(1,1)*P_WGS;
P_CO2_HTS(1,1) = y_CO2_HTS(1,1)*P_WGS;
P_H2_HTS(1,1) = y_H2_HTS(1,1)*P_WGS;
P_CH4_HTS(1,1) = y_CH4_HTS(1,1)*P_WGS;

%Concentrations [mol/m3]

c_CO_HTS(1,1) = (P_CO_HTS(1,1)*(1E5))/(R_const*T_HTS(1,1));
c_H2O_HTS(1,1) = (P_H2O_HTS(1,1)*(1E5))/(R_const*T_HTS(1,1));
```

```
c_CO2_HTS(1,1) = (P_CO2_HTS(1,1)*(1E5))/(R_const*T_HTS(1,1));
c_H2_HTS(1,1) = (P_H2_HTS(1,1)*(1E5))/(R_const*T_HTS(1,1));
c_CH4_HTS(1,1) = (P_CH4_HTS(1,1)*(1E5))/(R_const*T_HTS(1,1));
```



```
%Mixture Molar Mass [kg/mol]

MW_HTS(1,1) = y_CO_HTS(1,1)*MW_CO+y_H2O_HTS(1,1)*MW_H2O+...
y_CO2_HTS(1,1)*MW_CO2+y_H2_HTS(1,1)*MW_H2+y_CH4_HTS(1,1)*MW_CH4;

%Molar Flow Rates [mol/s]

F_HTS(1,1) = m_dot_WGS/MW_HTS(1,1);
F_CO_HTS(1,1) = y_CO_HTS(1,1)*F_HTS(1,1);
F_H2O_HTS(1,1) = y_H2O_HTS(1,1)*F_HTS(1,1);
F_CO2_HTS(1,1) = y_CO2_HTS(1,1)*F_HTS(1,1);
F_H2_HTS(1,1) = y_H2_HTS(1,1)*F_HTS(1,1);
F_CH4_HTS(1,1) = y_CH4_HTS(1,1)*F_HTS(1,1);

%Total Volumetric Flow [m3/s]

V_dot_HTS(1,1) = F_HTS(1,1)*R_const*T_HTS(1,1)/(P_WGS*1E5);

%Density [kg/m3]

rho_HTS(1,1) = (P_WGS*1E5*MW_HTS(1,1))/(R_const*T_HTS(1,1));
```

HTS Inlet Specific Heat from NASA Polynomials

```
%CO Values

a_1_CO = 3.57953347E0;
a_2_CO = -6.10353680E-4;
a_3_CO = 1.01681433E-6;
a_4_CO = 9.07005884E-10;
a_5_CO = -9.0442449E-13;

c_p_CO_HTS(1,1) = R_const*(a_1_CO + a_2_CO*T_HTS(1,1) + ...
a_3_CO*T_HTS(1,1)^2 + a_4_CO*T_HTS(1,1)^3 + a_5_CO*T_HTS(1,1)^4);

%H2O Values

a_1_H2O = 4.19864056E0;
a_2_H2O = -2.03643410E-3;
a_3_H2O = 6.52040211E-6;
a_4_H2O = -5.48797062E-9;
a_5_H2O = 1.77197817E-12;

c_p_H2O_HTS(1,1) = R_const*(a_1_H2O + a_2_H2O*T_HTS(1,1) + ...
a_3_H2O*T_HTS(1,1)^2 + a_4_H2O*T_HTS(1,1)^3 + a_5_H2O*T_HTS(1,1)^4);

%CO2 Values

a_1_CO2 = 2.35677352E0;
a_2_CO2 = 8.98459677E-3;
a_3_CO2 = -7.12356269E-6;
a_4_CO2 = 2.45919022E-9;
```

```
a_5_CO2 = -1.43699548E-13;

c_p_CO2_HTS(1,1) = R_const*(a_1_CO2 + a_2_CO2*T_HTS(1,1) + ...
a_3_CO2*T_HTS(1,1)^2 + a_4_CO2*T_HTS(1,1)^3 + a_5_CO2*T_HTS(1,1)^4);

%H2 Values

a_1_H2 = 2.34433112E0;
a_2_H2 = 7.98052075E-3;
a_3_H2 = -1.94781510E-5;
a_4_H2 = 2.01572094E-8;
a_5_H2 = -7.37611761E-12;

c_p_H2_HTS(1,1) = R_const*(a_1_H2 + a_2_H2*T_HTS(1,1) + ...
a_3_H2*T_HTS(1,1)^2 + a_4_H2*T_HTS(1,1)^3 + a_5_H2*T_HTS(1,1)^4);

%CH4 Values

a_1_CH4 = 5.14987613E0;
a_2_CH4 = -1.36709788E-2;
a_3_CH4 = 4.9180599E-5;
a_4_CH4 = -4.84743026E-8;
a_5_CH4 = 1.66693956E-11;

c_p_CH4_HTS(1,1) = R_const*(a_1_CH4 + a_2_CH4*T_HTS(1,1) + ...
a_3_CH4*T_HTS(1,1)^2 + a_4_CH4*T_HTS(1,1)^3 + a_5_CH4*T_HTS(1,1)^4);

%Mixture specific heat [kJ/mol-K]

c_p_HTS(1,1) = ((y_CO_HTS(1,1)*c_p_CO_HTS(1,1)+...
y_H2O_HTS(1,1)*c_p_H2O_HTS(1,1)+y_CO2_HTS(1,1)*c_p_CO2_HTS(1,1)...
+y_H2_HTS(1,1)*c_p_H2_HTS(1,1)+y_CH4_HTS(1,1)*c_p_CH4_HTS(1,1))*(1/1000));
```

HTS Inlet Heat of Reaction

```
%Reference heats of formation [kJ/mol]

h_CO_f = -110.5;
h_H2O_f = -241.8;
h_CO2_f = -393.5;
h_H2_f = 0;

%Heat of reaction at reference state

H_rxn_HTS_ref = (h_CO2_f+h_H2_f)-(h_CO_f+h_H2O_f);

%Reference state specific heats

T_HTS_int(1,1) = 25+273.15; %Reference temperature [K]

c_p_CO_HTS_int(1,1) = R_const*(a_1_CO + a_2_CO*T_HTS_int(1,1) + ...
a_3_CO*T_HTS_int(1,1)^2 + a_4_CO*T_HTS_int(1,1)^3 + ...
a_5_CO*T_HTS_int(1,1)^4);

c_p_H2O_HTS_int(1,1) = R_const*(a_1_H2O + a_2_H2O*T_HTS_int(1,1) + ...
a_3_H2O*T_HTS_int(1,1)^2 + a_4_H2O*T_HTS_int(1,1)^3 + ...
```

```
a_5_H2O*T_HTS_int(1,1)^4);

c_p_CO2_HTS_int(1,1) = R_const*(a_1_CO2 + a_2_CO2*T_HTS_int(1,1) + ...
a_3_CO2*T_HTS_int(1,1)^2 + a_4_CO2*T_HTS_int(1,1)^3 + ...
a_5_CO2*T_HTS_int(1,1)^4);

c_p_H2_HTS_int(1,1) = R_const*(a_1_H2 + a_2_H2*T_HTS_int(1,1) + ...
a_3_H2*T_HTS_int(1,1)^2 + a_4_H2*T_HTS_int(1,1)^3 + ...
a_5_H2*T_HTS_int(1,1)^4);

%Evaluate reaction differential specific heat at reference state

Delta_c_p_HTS_int(1,1) = ((c_p_CO2_HTS_int(1,1)+c_p_H2_HTS_int(1,1))-...
(c_p_CO_HTS_int(1,1)+c_p_H2O_HTS_int(1,1)))*(1/1000);

%Integration to determine heat of reaction

T_range_HTS = T_HTS(1,1)-T_HTS_int(1,1);
T_HTS_int = [T_HTS_int(1,1):T_range_HTS/100:T_HTS(1,1)]';

for i=2:length(T_HTS_int)

    %Change in species energies with respect to reference temperature

    c_p_CO_HTS_int(i,1) = R_const*(a_1_CO + a_2_CO*T_HTS_int(i,1) + ...
    a_3_CO*T_HTS_int(i,1)^2 + a_4_CO*T_HTS_int(i,1)^3 + ...
    a_5_CO*T_HTS_int(i,1)^4);

    c_p_H2O_HTS_int(i,1) = R_const*(a_1_H2O + a_2_H2O*T_HTS_int(i,1) + ...
    a_3_H2O*T_HTS_int(i,1)^2 + a_4_H2O*T_HTS_int(i,1)^3 + ...
    a_5_H2O*T_HTS_int(i,1)^4);

    c_p_CO2_HTS_int(i,1) = R_const*(a_1_CO2 + a_2_CO2*T_HTS_int(i,1) + ...
    a_3_CO2*T_HTS_int(i,1)^2 + a_4_CO2*T_HTS_int(i,1)^3 + ...
    a_5_CO2*T_HTS_int(i,1)^4);

    c_p_H2_HTS_int(i,1) = R_const*(a_1_H2 + a_2_H2*T_HTS_int(i,1) + ...
    a_3_H2*T_HTS_int(i,1)^2 + a_4_H2*T_HTS_int(i,1)^3 + ...
    a_5_H2*T_HTS_int(i,1)^4);

    Delta_c_p_HTS_int(i,1) = ((c_p_CO2_HTS_int(i,1)+...
    c_p_H2_HTS_int(i,1))-(c_p_CO_HTS_int(i,1)+...
    c_p_H2O_HTS_int(i,1)))*(1/1000);

    %Trapezoidal rule to evaluate change in energy

    Int_HTS(i-1,1) = 0.5*(T_HTS_int(i,1)-...
    T_HTS_int(i-1,1))*(Delta_c_p_HTS_int(i,1)+...
    Delta_c_p_HTS_int(i-1,1));

end

%Heat of reaction for inlet to HTS

H_rxn_HTS(1,1) = H_rxn_HTS_ref + sum(Int_HTS);
```

HTS Inlet Reaction Rate Evaluation


```
%Equilibrium expression

K_eq_HTS(1,1) = exp(4577.8/T_HTS(1,1)-4.33);

%Rate constant [mol/kg-s]

k_rds_HTS(1,1) = K_0*exp(-E_a/(R_const*T_HTS(1,1)));

%Reversibility factor

Beta_HTS(1,1) = (P_CO2_HTS(1,1)*P_H2_HTS(1,1))/...
(K_eq_HTS(1,1)*P_CO_HTS(1,1)*P_H2O_HTS(1,1));

%Reaction rate [mol/m3-s]

r_HTS(1,1) = rho_cat*(k_rds_HTS(1,1)*K_CO*K_H2O*P_CO_HTS(1,1)*...
P_H2O_HTS(1,1)*(1-Beta_HTS(1,1)))/((1+K_CO*P_CO_HTS(1,1)+...
sqrt(K_H2*P_H2_HTS(1,1)))^2*(1+sqrt(K_H2O*P_H2O_HTS(1,1))+...
K_CO2*P_CO2_HTS(1,1)));
```

Evaluate Equilibrium Curve of Reaction

```
X_CO_WGS_eq = [0:0.001:0.999]';

for i=1:length(X_CO_WGS_eq)

    %Equilibrium molar flow rates [mol/s]

    F_CO_WGS_eq(i,1) = F_CO_HTS(1,1)-X_CO_WGS_eq(i,1)*F_CO_HTS(1,1);
    F_H2O_WGS_eq(i,1) = F_H2O_HTS(1,1)-X_CO_WGS_eq(i,1)*F_CO_HTS(1,1);
    F_CO2_WGS_eq(i,1) = F_CO2_HTS(1,1)+X_CO_WGS_eq(i,1)*F_CO_HTS(1,1);
    F_H2_WGS_eq(i,1) = F_H2_HTS(1,1)+X_CO_WGS_eq(i,1)*F_CO_HTS(1,1);
    F_CH4_WGS_eq(i,1) = F_CH4_HTS(1,1);

    F_WGS_eq(i,1) = F_CO_WGS_eq(i,1)+F_H2O_WGS_eq(i,1)+...
    F_CO2_WGS_eq(i,1)+F_H2_WGS_eq(i,1)+F_CH4_WGS_eq(i,1);

    %Equilibrium mole fractions

    y_CO_WGS_eq(i,1) = F_CO_WGS_eq(i,1)/F_WGS_eq(i,1);
    y_H2O_WGS_eq(i,1) = F_H2O_WGS_eq(i,1)/F_WGS_eq(i,1);
    y_CO2_WGS_eq(i,1) = F_CO2_WGS_eq(i,1)/F_WGS_eq(i,1);
    y_H2_WGS_eq(i,1) = F_H2_WGS_eq(i,1)/F_WGS_eq(i,1);
    y_CH4_WGS_eq(i,1) = F_CH4_WGS_eq(i,1)/F_WGS_eq(i,1);

    %Equilibrium partial pressures

    P_CO_WGS_eq(i,1) = y_CO_WGS_eq(i,1)*P_WGS;
    P_H2O_WGS_eq(i,1) = y_H2O_WGS_eq(i,1)*P_WGS;
    P_CO2_WGS_eq(i,1) = y_CO2_WGS_eq(i,1)*P_WGS;
    P_H2_WGS_eq(i,1) = y_H2_WGS_eq(i,1)*P_WGS;
    P_CH4_WGS_eq(i,1) = y_CH4_WGS_eq(i,1)*P_WGS;
```

```
    %Equilibrium constant

    K_WGS_eq_graph(i,1) = (P_H2_WGS_eq(i,1)*P_CO2_WGS_eq(i,1))/...
    (P_CO_WGS_eq(i,1)*P_H2O_WGS_eq(i,1));

    %Logic to evaluate if reaction has consumed all of one reactant

    if K_WGS_eq_graph(i,1) <0

        break

    end

    %Equilibrium temperature for each equilibrium constant

    T_WGS_eq(i,1) = (4577.8)/(log(K_WGS_eq_graph(i,1))+(4.33));

end

%Equilibrium conversion levels

X_CO_WGS_eq = X_CO_WGS_eq(1:length(T_WGS_eq));
```

Solve PFR Mass and Energy Balances Simultaneously for HTS

```
Delta_V_HTS = [0 logspace(-10,0,10000)]'; %Set volume step sizes for solution

for i=2:length(Delta_V_HTS)

    %Evaluate mass balance for new molar flow rates at each volume step
    %[mol/s]

    F_CO_HTS(i,1) = F_CO_HTS(i-1,1)-Delta_V_HTS(i,1)*(r_HTS(i-1,1));
    F_H2O_HTS(i,1) = F_H2O_HTS(i-1,1)-Delta_V_HTS(i,1)*(r_HTS(i-1,1));
    F_CO2_HTS(i,1) = F_CO2_HTS(i-1,1)+Delta_V_HTS(i,1)*(r_HTS(i-1,1));
    F_H2_HTS(i,1) = F_H2_HTS(i-1,1)+Delta_V_HTS(i,1)*(r_HTS(i-1,1));
    F_CH4_HTS(i,1) = F_CH4_HTS(1,1);

    %Set logic to stop solution process if molar flow drops below physical
    %value

    if F_CO_HTS(i,1) < 0 | F_H2O_HTS(i,1) < 0

        break

    end

    %Evaluate new mole fractions of each component at each conversion level

    y_CO_HTS(i,1) = F_CO_HTS(i,1)/F_HTS;
    y_H2O_HTS(i,1) = F_H2O_HTS(i,1)/F_HTS;
    y_CO2_HTS(i,1) = F_CO2_HTS(i,1)/F_HTS;
    y_H2_HTS(i,1) = F_H2_HTS(i,1)/F_HTS;
    y_CH4_HTS(i,1) = F_CH4_HTS(i,1)/F_HTS;

    %Evaluate new partial pressures of each component at each conversion
```

```
%level [bar]

P_CO_HTS(i,1) = y_CO_HTS(i,1)*P_WGS;
P_H2O_HTS(i,1) = y_H2O_HTS(i,1)*P_WGS;
P_CO2_HTS(i,1) = y_CO2_HTS(i,1)*P_WGS;
P_H2_HTS(i,1) = y_H2_HTS(i,1)*P_WGS;
P_CH4_HTS(i,1) = y_CH4_HTS(i,1)*P_WGS;

%Evaluate conversion level at each volume step

X_CO_HTS(i,1) = (F_CO_HTS(1,1)-F_CO_HTS(i,1))/F_CO_HTS(1,1);

%Evaluate energy balance for new temperature at each volume step
%[K]

T_HTS(i,1) = ((-H_rxn_HTS(i-1,1)*r_HTS(i-1,1))/...
(rho_HTS(i-1,1)*(c_p_HTS(i-1,1)/MW_HTS(i-1,1))*...
V_dot_HTS(i-1,1)))*Delta_V_HTS(i,1)+T_HTS(i-1,1);

%Evaluate new concentrations at each volume step [mol/m3]

c_CO_HTS(i,1) = (P_CO_HTS(i,1)*(1E5))/(R_const*T_HTS(i,1));
c_H2O_HTS(i,1) = (P_H2O_HTS(i,1)*(1E5))/(R_const*T_HTS(i,1));
c_CO2_HTS(i,1) = (P_CO2_HTS(i,1)*(1E5))/(R_const*T_HTS(i,1));
c_H2_HTS(i,1) = (P_H2_HTS(i,1)*(1E5))/(R_const*T_HTS(i,1));
c_CH4_HTS(i,1) = (P_CH4_HTS(i,1)*(1E5))/(R_const*T_HTS(i,1));

%Evaluate new molar mass at each volume step [kg/mol]

MW_HTS(i,1) = y_CO_HTS(i,1)*MW_CO+y_H2O_HTS(i,1)*MW_H2O+...
y_CO2_HTS(i,1)*MW_CO2+y_H2_HTS(i,1)*MW_H2+y_CH4_HTS(i,1)*MW_CH4;

%Evaluate new volumetric flow at each volume step [m3/s]

V_dot_HTS(i,1) = F_HTS*R_const*T_HTS(i,1)/(P_WGS*1E5);

%Evaluate new density at each volume step [kg/m3]

rho_HTS(i,1) = (P_WGS*1E5*MW_HTS(i,1))/(R_const*T_HTS(i,1));

%Evaluate new specific heats at each volume step [kJ/mol-K]

c_p_CO_HTS(i,1) = R_const*(a_1_CO + a_2_CO*T_HTS(i,1) + ...
a_3_CO*T_HTS(i,1)^2 + a_4_CO*T_HTS(i,1)^3 + a_5_CO*T_HTS(i,1)^4);

c_p_H2O_HTS(i,1) = R_const*(a_1_H2O + a_2_H2O*T_HTS(i,1) + ...
a_3_H2O*T_HTS(i,1)^2 + a_4_H2O*T_HTS(i,1)^3 + a_5_H2O*T_HTS(i,1)^4);

c_p_CO2_HTS(i,1) = R_const*(a_1_CO2 + a_2_CO2*T_HTS(i,1) + ...
a_3_CO2*T_HTS(i,1)^2 + a_4_CO2*T_HTS(i,1)^3 + a_5_CO2*T_HTS(i,1)^4);

c_p_H2_HTS(i,1) = R_const*(a_1_H2 + a_2_H2*T_HTS(i,1) + ...
a_3_H2*T_HTS(i,1)^2 + a_4_H2*T_HTS(i,1)^3 + a_5_H2*T_HTS(i,1)^4);

c_p_CH4_HTS(i,1) = R_const*(a_1_CH4 + a_2_CH4*T_HTS(i,1) + ...
a_3_CH4*T_HTS(i,1)^2 + a_4_CH4*T_HTS(i,1)^3 + a_5_CH4*T_HTS(i,1)^4);
```

```
c_p_HTS(i,1) = ((y_CO_HTS(i,1)*c_p_CO_HTS(i,1)+...
y_H2O_HTS(i,1)*c_p_H2O_HTS(i,1)+...
y_CO2_HTS(i,1)*c_p_CO2_HTS(i,1)+y_H2_HTS(i,1)*c_p_H2_HTS(i,1)+...
y_CH4_HTS(i,1)*c_p_CH4_HTS(i,1))*(1/1000));

%Evaluate new heat of reaction at each volume step [kJ/mol]

T_range_HTS = T_HTS(i,1)-T_HTS_int(1,1);
T_HTS_int = [T_HTS_int(1,1):T_range_HTS/100:T_HTS(i,1)]';

for j=2:length(T_HTS_int)

    c_p_CO_HTS_int(j,1) = R_const*(a_1_CO + ...
    a_2_CO*T_HTS_int(j,1) + a_3_CO*T_HTS_int(j,1)^2 + ...
    a_4_CO*T_HTS_int(j,1)^3 + a_5_CO*T_HTS_int(j,1)^4);

    c_p_H2O_HTS_int(j,1) = R_const*(a_1_H2O + ...
    a_2_H2O*T_HTS_int(j,1) + a_3_H2O*T_HTS_int(j,1)^2 + ...
    a_4_H2O*T_HTS_int(j,1)^3 + a_5_H2O*T_HTS_int(j,1)^4);

    c_p_CO2_HTS_int(j,1) = R_const*(a_1_CO2 + ...
    a_2_CO2*T_HTS_int(j,1) + a_3_CO2*T_HTS_int(j,1)^2 + ...
    a_4_CO2*T_HTS_int(j,1)^3 + a_5_CO2*T_HTS_int(j,1)^4);

    c_p_H2_HTS_int(j,1) = R_const*(a_1_H2 + ...
    a_2_H2*T_HTS_int(j,1) + a_3_H2*T_HTS_int(j,1)^2 + ...
    a_4_H2*T_HTS_int(j,1)^3 + a_5_H2*T_HTS_int(j,1)^4);

    Delta_c_p_HTS_int(j,1) = ((c_p_CO2_HTS_int(j,1)+...
    c_p_H2_HTS_int(j,1))-(c_p_CO_HTS_int(j,1)+...
    c_p_H2O_HTS_int(j,1)))*(1/1000);

    Int_HTS(j-1,1) = 0.5*(T_HTS_int(j,1)-...
    T_HTS_int(j-1,1))*(Delta_c_p_HTS_int(j,1)+...
    Delta_c_p_HTS_int(j-1,1));

end

H_rxn_HTS(i,1) = H_rxn_HTS_ref + sum(Int_HTS);

%Evaluate new reaction rate at each volume step [mol/m3-s]

K_eq_HTS(i,1) = exp(4577.8/T_HTS(i,1)-4.33);

k_rds_HTS(i,1) = K_0*exp(-E_a/(R_const*T_HTS(i,1)));

Beta_HTS(i,1) = (P_CO2_HTS(i,1)*P_H2_HTS(i,1))/...
(K_eq_HTS(i,1)*P_CO_HTS(i,1)*P_H2O_HTS(i,1));

r_HTS(i,1) = rho_cat*(k_rds_HTS(i,1)*K_CO*K_H2O*P_CO_HTS(i,1)*...
P_H2O_HTS(i,1)*(1-Beta_HTS(i,1)))/((1+K_CO*P_CO_HTS(i,1)+...
sqrt(K_H2*P_H2_HTS(i,1)))^2*(1+sqrt(K_H2O*P_H2O_HTS(i,1))+...
K_CO2*P_CO2_HTS(i,1)));

%Evaluate Cumulative Reactor Volume [m3]

V_HTS(i,1) = V_HTS(i-1,1)+Delta_V_HTS(i,1);
```

```
    %Institute logic to break loop if reaction rate drops below threshold
    if r_HTS(i,1)-1E-2  < 0
        break
    end
end
```


Set Inlet Conditions for HTS

```
y_CO_LTS(1,1) = y_CO_HTS(end); %Mole fraction CO
y_H2O_LTS(1,1) = y_H2O_HTS(end); %Mole fraction H2O
y_CO2_LTS(1,1) = y_CO2_HTS(end); %Mole fraction CO2
y_H2_LTS(1,1) = y_H2_HTS(end); %Mole fraction H2
y_CH4_LTS(1,1) = y_CH4_HTS(end); %Mole fraction CH4

T_LTS(1,1) = 200+273.15; %Inlet temperature to LTS [K]

X_CO_LTS(1,1) = 0; %Initial CO conversion

V_LTS(1,1) = 0; %Initial reactor volume [m3]
```

Calculated LTS Inlet Conditions

```
%Partial Pressures [bar]

P_CO_LTS(1,1) = y_CO_LTS(1,1)*P_WGS;
P_H2O_LTS(1,1) = y_H2O_LTS(1,1)*P_WGS;
P_CO2_LTS(1,1) = y_CO2_LTS(1,1)*P_WGS;
P_H2_LTS(1,1) = y_H2_LTS(1,1)*P_WGS;
P_CH4_LTS(1,1) = y_CH4_LTS(1,1)*P_WGS;

%Concentrations [mol/m3]

c_CO_LTS(1,1) = (P_CO_LTS(1,1)*(1E5))/(R_const*T_LTS(1,1));
c_H2O_LTS(1,1) = (P_H2O_LTS(1,1)*(1E5))/(R_const*T_LTS(1,1));
c_CO2_LTS(1,1) = (P_CO2_LTS(1,1)*(1E5))/(R_const*T_LTS(1,1));
c_H2_LTS(1,1) = (P_H2_LTS(1,1)*(1E5))/(R_const*T_LTS(1,1));
c_CH4_LTS(1,1) = (P_CH4_LTS(1,1)*(1E5))/(R_const*T_LTS(1,1));

%Mixture Molar Mass [kg/mol]

MW_LTS(1,1) = y_CO_LTS(1,1)*MW_CO+y_H2O_LTS(1,1)*MW_H2O+...
y_CO2_LTS(1,1)*MW_CO2+y_H2_LTS(1,1)*MW_H2+y_CH4_LTS(1,1)*MW_CH4;

%Molar Flow Rates [mol/s]

F_LTS(1,1) = m_dot_WGS/MW_LTS(1,1);
F_CO_LTS(1,1) = y_CO_LTS(1,1)*F_LTS(1,1);
F_H2O_LTS(1,1) = y_H2O_LTS(1,1)*F_LTS(1,1);
F_CO2_LTS(1,1) = y_CO2_LTS(1,1)*F_LTS(1,1);
```

```
F_H2_LTS(1,1) = y_H2_LTS(1,1)*F_LTS(1,1);
F_CH4_LTS(1,1) = y_CH4_LTS(1,1)*F_LTS(1,1);

%Total Volumetric Flow [m3/s]

V_dot_LTS(1,1) = F_LTS(1,1)*R_const*T_LTS(1,1)/(P_WGS*1E5);

%Density [kg/m3]

rho_LTS(1,1) = (P_WGS*1E5*MW_LTS(1,1))/(R_const*T_LTS(1,1));
```


LTS Inlet Heat of Reaction

```
%CO Values

c_p_CO_LTS(1,1) = R_const*(a_1_CO + a_2_CO*T_LTS(1,1) + ...
a_3_CO*T_LTS(1,1)^2 + a_4_CO*T_LTS(1,1)^3 + a_5_CO*T_LTS(1,1)^4);

%H2O Values

c_p_H2O_LTS(1,1) = R_const*(a_1_H2O + a_2_H2O*T_LTS(1,1) + ...
a_3_H2O*T_LTS(1,1)^2 + a_4_H2O*T_LTS(1,1)^3 + a_5_H2O*T_LTS(1,1)^4);

%CO2 Values

c_p_CO2_LTS(1,1) = R_const*(a_1_CO2 + a_2_CO2*T_LTS(1,1) + ...
a_3_CO2*T_LTS(1,1)^2 + a_4_CO2*T_LTS(1,1)^3 + a_5_CO2*T_LTS(1,1)^4);

%H2 Values

c_p_H2_LTS(1,1) = R_const*(a_1_H2 + a_2_H2*T_LTS(1,1) + ...
a_3_H2*T_LTS(1,1)^2 + a_4_H2*T_LTS(1,1)^3 + a_5_H2*T_LTS(1,1)^4);

%CH4 Values

c_p_CH4_LTS(1,1) = R_const*(a_1_CH4 + a_2_CH4*T_LTS(1,1) + ...
a_3_CH4*T_LTS(1,1)^2 + a_4_CH4*T_LTS(1,1)^3 + a_5_CH4*T_LTS(1,1)^4);

%Mixture specific heat

c_p_LTS(1,1) = ((y_CO_LTS(1,1)*c_p_CO_LTS(1,1)+...
y_H2O_LTS(1,1)*c_p_H2O_LTS(1,1)+y_CO2_LTS(1,1)*c_p_CO2_LTS(1,1)+...
y_H2_LTS(1,1)*c_p_H2_LTS(1,1)+y_CH4_LTS(1,1)*c_p_CH4_LTS(1,1))*(1/1000));
```

LTS Inlet Heat of Reaction

```
%Heat of reaction at reference state

H_rxn_LTS_ref = (h_CO2_f+h_H2_f)-(h_CO_f+h_H2O_f);

%Reference state specific heats

T_LTS_int(1,1) = 25+273.15; %Reference temperature [K]
```

```
c_p_CO_LTS_int(1,1) = R_const*(a_1_CO + a_2_CO*T_LTS_int(1,1) + ...
a_3_CO*T_LTS_int(1,1)^2 + a_4_CO*T_LTS_int(1,1)^3 + ...
a_5_CO*T_LTS_int(1,1)^4);

c_p_H2O_LTS_int(1,1) = R_const*(a_1_H2O + a_2_H2O*T_LTS_int(1,1) + ...
a_3_H2O*T_LTS_int(1,1)^2 + a_4_H2O*T_LTS_int(1,1)^3 + ...
a_5_H2O*T_LTS_int(1,1)^4);

c_p_CO2_LTS_int(1,1) = R_const*(a_1_CO2 + a_2_CO2*T_LTS_int(1,1) + ...
a_3_CO2*T_LTS_int(1,1)^2 + a_4_CO2*T_LTS_int(1,1)^3 + ...
a_5_CO2*T_LTS_int(1,1)^4);

c_p_H2_LTS_int(1,1) = R_const*(a_1_H2 + a_2_H2*T_LTS_int(1,1) + ...
a_3_H2*T_LTS_int(1,1)^2 + a_4_H2*T_LTS_int(1,1)^3 + ...
a_5_H2*T_LTS_int(1,1)^4);

Delta_c_p_LTS_int(1,1) = ((c_p_CO2_LTS_int(1,1)+c_p_H2_LTS_int(1,1))-...
(c_p_CO_LTS_int(1,1)+c_p_H2O_LTS_int(1,1)))*(1/1000);

%Numerical Integration to determine heat of reaction at LTS temperatures

T_range_LTS = T_LTS(1,1)-T_LTS_int(1,1);
T_LTS_int = [T_LTS_int(1,1):T_range_LTS/100:T_LTS(1,1)]';

for i=2:length(T_HTS_int)

    %Change in species energies with respect to reference temperature

    c_p_CO_LTS_int(i,1) = R_const*(a_1_CO + a_2_CO*T_LTS_int(i,1) + ...
    a_3_CO*T_LTS_int(i,1)^2 + a_4_CO*T_LTS_int(i,1)^3 + ...
    a_5_CO*T_LTS_int(i,1)^4);

    c_p_H2O_LTS_int(i,1) = R_const*(a_1_H2O + a_2_H2O*T_LTS_int(i,1) + ...
    a_3_H2O*T_LTS_int(i,1)^2 + a_4_H2O*T_LTS_int(i,1)^3 + ...
    a_5_H2O*T_LTS_int(i,1)^4);

    c_p_CO2_LTS_int(i,1) = R_const*(a_1_CO2 + a_2_CO2*T_LTS_int(i,1) + ...
    a_3_CO2*T_LTS_int(i,1)^2 + a_4_CO2*T_LTS_int(i,1)^3 + ...
    a_5_CO2*T_LTS_int(i,1)^4);

    c_p_H2_LTS_int(i,1) = R_const*(a_1_H2 + a_2_H2*T_LTS_int(i,1) + ...
    a_3_H2*T_LTS_int(i,1)^2 + a_4_H2*T_LTS_int(i,1)^3 + ...
    a_5_H2*T_LTS_int(i,1)^4);

    Delta_c_p_LTS_int(i,1) = ((c_p_CO2_LTS_int(i,1)+...
    c_p_H2_LTS_int(i,1))-(c_p_CO_LTS_int(i,1)+...
    c_p_H2O_LTS_int(i,1)))*(1/1000);

    %Trapezoidal rule to evaluate change in energy

    Int_LTS(i-1,1) = 0.5*(T_LTS_int(i,1)-...
    T_LTS_int(i-1,1))*(Delta_c_p_LTS_int(i,1)+...
    Delta_c_p_LTS_int(i-1,1));

end

%Heat of reaction for inlet to LTS
```

```
H_rxn_LTS(1,1) = H_rxn_LTS_ref + sum(Int_LTS);
```


Intercooler between HTS/LTS

```
%WGS heat rejection [kW]

Q_dot_WGS = m_dot_WGS*(0.5*(c_p_HTS(end)/MW_HTS(end)+...
c_p_LTS(1,1)/MW_LTS(1,1)))*(T_HTS(end)-T_LTS(1,1));
```

LTS Inlet Reaction Rate Evaluation

```
%Equilibrium expression

K_eq_LTS(1,1) = exp(4577.8/T_LTS(1,1)-4.33);

%Rate constant [mol/kg-s]

k_rds_LTS(1,1) = K_0*exp(-E_a/(R_const*T_LTS(1,1)));

%Reversiility factor

Beta_LTS(1,1) = (P_CO2_LTS(1,1)*P_H2_LTS(1,1))/...
(K_eq_LTS(1,1)*P_CO_LTS(1,1)*P_H2O_LTS(1,1));

%Reaction rate [mol/m3-s]

r_LTS(1,1) = rho_cat*(k_rds_LTS(1,1)*K_CO*K_H2O*P_CO_LTS(1,1)*...
P_H2O_LTS(1,1)*(1-Beta_LTS(1,1)))/((1+K_CO*P_CO_LTS(1,1)+...
sqrt(K_H2*P_H2_LTS(1,1)))^2*(1+sqrt(K_H2O*P_H2O_LTS(1,1))+...
K_CO2*P_CO2_LTS(1,1)));
```

Solve PFR Mass and Energy Balances Simultaneously for LTS

```
Delta_V_LTS = [0 logspace(-10,0,10000)]'; %Set volume step sizes for solution

for i=2:length(Delta_V_LTS)

    %Evaluate mass balance for new molar flow rates at each volume step
    %[mol/s]

    F_CO_LTS(i,1) = F_CO_LTS(i-1,1)-Delta_V_LTS(i,1)*(r_LTS(i-1,1));
    F_H2O_LTS(i,1) = F_H2O_LTS(i-1,1)-Delta_V_LTS(i,1)*(r_LTS(i-1,1));
    F_CO2_LTS(i,1) = F_CO2_LTS(i-1,1)+Delta_V_LTS(i,1)*(r_LTS(i-1,1));
    F_H2_LTS(i,1) = F_H2_LTS(i-1,1)+Delta_V_LTS(i,1)*(r_LTS(i-1,1));
    F_CH4_LTS(i,1) = F_CH4_LTS(1,1);

    %Set logic to stop solution process if molar flow drops below physical
    %value

    if F_CO_LTS(i,1) < 0 | F_H2O_LTS(i,1) < 0

        break
```

```
end

%Evaluate new mole fractions of each component at each conversion level

y_CO_LTS(i,1) = F_CO_LTS(i,1)/F_LTS;
y_H2O_LTS(i,1) = F_H2O_LTS(i,1)/F_LTS;
y_CO2_LTS(i,1) = F_CO2_LTS(i,1)/F_LTS;
y_H2_LTS(i,1) = F_H2_LTS(i,1)/F_LTS;
y_CH4_LTS(i,1) = F_CH4_LTS(i,1)/F_LTS;

%Evaluate new partial pressures of each component at each conversion
%level [bar]

P_CO_LTS(i,1) = y_CO_LTS(i,1)*P_WGS;
P_H2O_LTS(i,1) = y_H2O_LTS(i,1)*P_WGS;
P_CO2_LTS(i,1) = y_CO2_LTS(i,1)*P_WGS;
P_H2_LTS(i,1) = y_H2_LTS(i,1)*P_WGS;
P_CH4_LTS(i,1) = y_CH4_LTS(i,1)*P_WGS;

%Evaluate conversion level at each volume step

X_CO_LTS(i,1) = (F_CO_LTS(1,1)-F_CO_LTS(i,1))/F_CO_LTS(1,1);

%Evaluate energy balance for new temperature at each volume step
%[K]

T_LTS(i,1) = ((-H_rxn_LTS(i-1,1)*r_LTS(i-1,1))/...
(rho_LTS(i-1,1)*(c_p_LTS(i-1,1)/MW_LTS(i-1,1))*...
V_dot_LTS(i-1,1)))*Delta_V_LTS(i,1)+T_LTS(i-1,1);

%Evaluate new concentrations at each volume step [mol/m3]

c_CO_LTS(i,1) = (P_CO_LTS(i,1)*(1E5))/(R_const*T_LTS(i,1));
c_H2O_LTS(i,1) = (P_H2O_LTS(i,1)*(1E5))/(R_const*T_LTS(i,1));
c_CO2_LTS(i,1) = (P_CO2_LTS(i,1)*(1E5))/(R_const*T_LTS(i,1));
c_H2_LTS(i,1) = (P_H2_LTS(i,1)*(1E5))/(R_const*T_LTS(i,1));
c_CH4_LTS(i,1) = (P_CH4_LTS(i,1)*(1E5))/(R_const*T_LTS(i,1));

%Evaluate new molar mass at each volume step [kg/mol]

MW_LTS(i,1) = y_CO_LTS(i,1)*MW_CO+y_H2O_LTS(i,1)*MW_H2O+...
y_CO2_LTS(i,1)*MW_CO2+y_H2_LTS(i,1)*MW_H2+y_CH4_LTS(i,1)*MW_CH4;

%Evaluate new volumetric flow at each volume step [m3/s]

V_dot_LTS(i,1) = F_LTS*R_const*T_LTS(i,1)/(P_WGS*1E5);

%Evaluate new density at each volume step [kg/m3]

rho_LTS(i,1) = (P_WGS*1E5*MW_LTS(i,1))/(R_const*T_LTS(i,1));

%Evaluate new specific heats at each volume step [kJ/mol-K]

c_p_CO_LTS(i,1) = R_const*(a_1_CO + a_2_CO*T_LTS(i,1) + ...
a_3_CO*T_LTS(i,1)^2 + a_4_CO*T_LTS(i,1)^3 + a_5_CO*T_LTS(i,1)^4);
```

```
c_p_H2O_LTS(i,1) = R_const*(a_1_H2O + a_2_H2O*T_LTS(i,1) + ...
a_3_H2O*T_LTS(i,1)^2 + a_4_H2O*T_LTS(i,1)^3 + a_5_H2O*T_LTS(i,1)^4);

c_p_CO2_LTS(i,1) = R_const*(a_1_CO2 + a_2_CO2*T_LTS(i,1) + ...
a_3_CO2*T_LTS(i,1)^2 + a_4_CO2*T_LTS(i,1)^3 + a_5_CO2*T_LTS(i,1)^4);

c_p_H2_LTS(i,1) = R_const*(a_1_H2 + a_2_H2*T_LTS(i,1) + ...
a_3_H2*T_LTS(i,1)^2 + a_4_H2*T_LTS(i,1)^3 + a_5_H2*T_LTS(i,1)^4);

c_p_CH4_LTS(i,1) = R_const*(a_1_CH4 + a_2_CH4*T_LTS(i,1) + ...
a_3_CH4*T_LTS(i,1)^2 + a_4_CH4*T_LTS(i,1)^3 + a_5_CH4*T_LTS(i,1)^4);

c_p_LTS(i,1) = ((y_CO_LTS(i,1)*c_p_CO_LTS(i,1)+...
y_H2O_LTS(i,1)*c_p_H2O_LTS(i,1)+...
y_CO2_LTS(i,1)*c_p_CO2_LTS(i,1)+y_H2_LTS(i,1)*c_p_H2_LTS(i,1)+...
y_CH4_LTS(i,1)*c_p_CH4_LTS(i,1))*(1/1000));

%Evaluate new heat of reaction at each volume step [kJ/mol]

T_range_LTS = T_LTS(i,1)-T_LTS_int(1,1);
T_LTS_int = [T_LTS_int(1,1):T_range_LTS/100:T_LTS(i,1)]';

for j=2:length(T_LTS_int)

    c_p_CO_LTS_int(j,1) = R_const*(a_1_CO + ...
    a_2_CO*T_LTS_int(j,1) + a_3_CO*T_LTS_int(j,1)^2 + ...
    a_4_CO*T_LTS_int(j,1)^3 + a_5_CO*T_LTS_int(j,1)^4);

    c_p_H2O_LTS_int(j,1) = R_const*(a_1_H2O + ...
    a_2_H2O*T_LTS_int(j,1) + a_3_H2O*T_LTS_int(j,1)^2 + ...
    a_4_H2O*T_LTS_int(j,1)^3 + a_5_H2O*T_LTS_int(j,1)^4);

    c_p_CO2_LTS_int(j,1) = R_const*(a_1_CO2 + ...
    a_2_CO2*T_LTS_int(j,1) + a_3_CO2*T_LTS_int(j,1)^2 + ...
    a_4_CO2*T_LTS_int(j,1)^3 + a_5_CO2*T_LTS_int(j,1)^4);

    c_p_H2_LTS_int(j,1) = R_const*(a_1_H2 + ...
    a_2_H2*T_LTS_int(j,1) + a_3_H2*T_LTS_int(j,1)^2 + ...
    a_4_H2*T_LTS_int(j,1)^3 + a_5_H2*T_LTS_int(j,1)^4);

    Delta_c_p_LTS_int(j,1) = ((c_p_CO2_LTS_int(j,1)+...
    c_p_H2_LTS_int(j,1))-(c_p_CO_LTS_int(j,1)+...
    c_p_H2O_LTS_int(j,1)))*(1/1000);

    Int_LTS(j-1,1) = 0.5*(T_LTS_int(j,1)-...
    T_LTS_int(j-1,1))*(Delta_c_p_LTS_int(j,1)+...
    Delta_c_p_LTS_int(j-1,1));

end

H_rxn_LTS(i,1) = H_rxn_LTS_ref + sum(Int_LTS);

%Evaluate new reaction rate at each volume step [mol/m3-s]

K_eq_LTS(i,1) = exp(4577.8/T_LTS(i,1)-4.33);

k_rds_LTS(i,1) = K_0*exp(-E_a/(R_const*T_LTS(i,1)));
```

```
    Beta_LTS(i,1) = (P_CO2_LTS(i,1)*P_H2_LTS(i,1))/...
    (K_eq_LTS(i,1)*P_CO_LTS(i,1)*P_H2O_LTS(i,1));

    r_LTS(i,1) = rho_cat*(k_rds_LTS(i,1)*K_CO*K_H2O*P_CO_LTS(i,1)*...
    P_H2O_LTS(i,1)*(1-Beta_LTS(i,1)))/((1+K_CO*P_CO_LTS(i,1)+...
    sqrt(K_H2*P_H2_LTS(i,1)))^2*(1+sqrt(K_H2O*P_H2O_LTS(i,1))+...
    K_CO2*P_CO2_LTS(i,1)));

    %Evaluate Cumulative Reactor Volume [m3]

    V_LTS(i,1) = V_LTS(i-1,1)+Delta_V_LTS(i,1);

    %Institute logic to break loop if reaction rate drops below threshold

    if r_LTS(i,1)-1E-3  < 0

        break

    end

end
```

Compile HTS/LTS Into Single Vector

```
%Evaluate cumulative reactor conversion and volume

for i=1:length(X_CO_LTS)

    X_CO_LTS_cum(i,1) = (F_CO_HTS(1,1)-F_CO_LTS(i,1))/F_CO_HTS(1,1);

    V_LTS_cum(i,1) = V_HTS(end) + V_LTS(i,1);

end

X_CO_WGS = [X_CO_HTS;X_CO_LTS_cum]; %Overall CO conversion

T_WGS = [T_HTS;T_LTS]; %Overall temperature profile

V_WGS = [V_HTS;V_LTS_cum]; %Overall reactor volume

y_CO_WGS = [y_CO_HTS;y_CO_LTS]; %Overall CO mole fraction profile

y_H2O_WGS = [y_H2O_HTS;y_H2O_LTS]; %Overall CO mole fraction profile

y_CO2_WGS = [y_CO2_HTS;y_CO2_LTS]; %Overall CO mole fraction profile

y_H2_WGS = [y_H2_HTS;y_H2_LTS]; %Overall CO mole fraction profile

y_CH4_WGS = [y_CH4_HTS;y_CH4_LTS]; %Overall CO mole fraction profile
```

Published with MATLAB® R2017b

Appendix B: 2-D Microreactor COMSOL Multiphysics Model

This appendix gives a more detailed description of the COMSOL Multiphysics water-gas shift microreactor model developed in Section 3.2 by discussing the physics interfaces used to implement the relevant conservation equations and property relations, the mesh used to solve the 2-D microreactor model geometry and the approach to mesh refinement used, and the solver type used to numerically solve the model.

B.1 Chemistry and Thermodynamics Interfaces

The Chemistry and Thermodynamics physics interfaces are used in conjunction with each other to evaluate the reaction mixture properties and to input the stoichiometry and kinetics of the water-gas shift reaction. By defining a gas system in the Thermodynamics interface consisting of the gas species present in the reacting flow (CO, H_2O, CO_2, H_2, and CH_4) and defining the WGS reaction in the Chemistry interface along with the non-participating CH_4 component, the properties of each individual component defined in the Chemistry interface can be matched to its corresponding properties within the Thermodynamics interface and then used to evaluate the corresponding mixture properties using equations 3.6, 3.12, 3.18, and 3.22. By inputting the Langmuir-Hinshelwood rate expression developed by Germani and Schuurman that is given by equation 2.5 to the defined WGS reaction, the kinetics of the reaction can be fully defined and use to evaluate the total reaction heat generation. Finally, the pressure and temperature results from the Laminar Flow and Heat Transfer interfaces can be linked to the Chemistry interface and used to evaluate the reaction kinetics and fluid properties across the model domain as appropriate.

B.2 Laminar Flow Interface

At the length scales associated with the model geometry analyzed and the process conditions specified, the reaction and coolant streams operate within the laminar flow regime. In COMSOL, separately specified Laminar Flow interfaces can be used to solve for the velocity and pressure distributions through both the reaction and coolant channels. On the Settings tab of each of these interfaces, the physical model is set to solve for compressible flows with Mach numbers less than 0.3 since the density of both the reaction and coolant streams can change with both respect to both pressure and temperature. A reference pressure of 5 bar, the expected operating pressure of the reaction stream, is specified for the Laminar Flow interface used for the reacting stream. A reference pressure of 1 bar is specified for the coolant flow. The reference temperature for both Laminar Flow interfaces is left at the default value of 293.15 K. Porous media domains are enabled in the Laminar flow interface used for the reacting stream to allow for the specification of properties within the porous catalyst phase. As part of the default settings for the Laminar Flow interface, the general form of the Navier-Stokes equations specified in equations 3.10 and 3.14 is automatically applied over the entire specified fluid domain, but can be overridden by applying other domain conditions. Because the flows in both the reaction and coolant domains are both expected to be laminar, no turbulence models are specified.

In the Laminar Flow interface applied for the reacting flow channel of each model, the following additional physics nodes are specified:

- Fluid Properties: This node defines the reaction flow's mixture properties in the open channel phase. The Chemistry and Heat Transfer interfaces are linked to this node to define the density and dynamic viscosity values directly used in the Navier-Stokes equations.

- Initial Values: This node defines the initial guesses for the velocity and pressure distributions in the reaction channel for the solver to begin iterating off of. While specifying accurate values in this node can help the solver converge more quickly, it is difficult to have reasonable guesses for the velocity and pressure distributions before actually solving the system so these values are left at their default values in all models.

- Wall 1: This node defines a no-slip boundary condition along the reactor wall in the model such that the flow velocity goes to 0 at these locations.

- Fluid and Matrix Properties 1: This node defines the reaction flow's mixture properties in the porous catalyst phase and overrides the application of the Navier-Stokes equations within the porous catalyst so that the Brinkman equations defined in equation 3.11 are applied instead. The Chemistry and Heat Transfer interfaces are linked to this node to define the density and dynamic viscosity values directly used in the Brinkman equations. The catalyst porosity is specified as a constant value of $\epsilon = 0.4$ and the permeability, κ, is specified using equation 3.13. These porous catalyst properties are assumed to be isotropic within the model.

- Inlet 1: This node specifies an inlet boundary condition to the reaction channel. A mass flow rate boundary condition, corresponding to the mass flow expected to enter a single reaction channel with a channel width of $W = 80$ mm, is specified. Because the model is formulated using only half of the reaction channel height to take advantage of the symmetry present in the reactors, the specified mass flow rate in this node is half of the entire mass flow expected to flow through a single channel.

- Outlet 1: This node specifies an outlet boundary condition to the reaction channel. Since an inlet flow rate is specified using the Inlet 1 boundary condition, an outlet

pressure condition of 0 Pa is specified at this boundary so that the model directly solves for the pressure drop across the reaction channel.

- Symmetry 1: This node specifies a combined Neumman-Dirichlet boundary condition along the center line of the reaction channel such that the flow velocity in the y-direction goes to 0 (no penetration) and the partial derivative of the flow velocity in the x-direction goes to 0 (the maximum flow velocity occurs along the center line of the reaction channel).

For models including integrated coolant flow, a separate Laminar Flow interface is specified for the coolant channel. In this interface, the same physics nodes are applied with the exception of the Fluid and Matrix Properties node since there is no catalyst layered within the coolant channel. Additionally, instead of the fluid properties being taken from the Chemistry interface, as is done for the reaction channel, the coolant properties are taken from the embedded air properties in COMSOL that are assigned to the coolant domain as a material property.

B.3 Transport of Concentrated Species Interface

For the reaction compositions expected throughout the reaction domain of the model, no individual species is present in a high enough concentration as to be assumed to act as a solvent diluting the remaining species. As a result, the Transport of Concentrated Species interface is specified to evaluate the mass transfer process occurring through the reaction channel. On the Settings tab of this interface, the diffusion model is set to a mixture averaged approach such that the multi-component diffusion coefficients are evaluated from each species pair diffusion coefficient using equation 3.17. Porous media domains are enabled to allow for the specification of properties within the porous catalyst phase. The dependent

variables that the interface solves for are set to the mass fractions of each chemical species flowing through the reaction channel and the mass constraint is set as the mass fraction of hydrogen. The mass constraint sets which chemical species in the interface are solved for using the mass conservation equations discussed in Section 3.2.3 and which single chemical species is evaluated from a mass constraint requiring the total mass fraction of the mixture to sum to a value of 1. Selecting hydrogen, which has the highest concentration of the species considered, helps reduce the error associated with this solution method. As part of the default settings for the Transport of Concentrated Species interface, the general form of the convection-diffusion equation specified in equation 3.16 is automatically applied over the entire reaction domain, though the transport properties and generation term can change based on the application of other domain conditions.

In the Transport of Concentrated Species interface applied for the reacting flow channel of the model, the following additional physics nodes are specified:

- Transport Properties: This node defines the reaction flow's mixture properties in the open channel phase. The binary diffusion coefficients calculated for each species pair in the Chemistry interface are entered in the Diffusion section of this node. The Chemistry and Heat Transfer interfaces are linked to this node to define additional fluid properties such as the mixture density and the molar mass of each species and the Laminar Flow interface is linked to this node so that the calculated velocity field can be used to evaluate the convective mass transfer process.

- Initial Values: This node defines the initial guesses for the mole fractions of each species throughout the reaction channel for the solver to begin iterating off of. While specifying accurate values in this node can help the solver converge more quickly, it is difficult to have reasonable guesses for the mole fraction profiles of each species before actually solving the system. As a result, the guess values for each species are

set as the inlet mole fraction values.

- No Flux 1: This node defines a no-flux boundary condition along the reactor wall within the model such that there is no mass transfer through the wall.

- Porous Media Transport Properties 1: This node defines the reaction flow's mixture properties in the porous catalyst phase and modifies the convection-diffusion equation to use the effective diffusion coefficient defined in equation 3.19. The binary diffusion coefficients calculated for each species pair in the Chemistry interface are input in the Diffusion section of the node. The porosity of the catalyst is input for the matrix properties and the tortuosity model is chosen to evaluate the effective diffusion coefficient through the porous catalyst with the tortuosity set to a value of $\tau = \epsilon^{-1}$ to match equation 3.19. The Chemistry and Heat Transfer interfaces are linked to this node to define additional fluid properties such as the mixture density and the molar mass and the Laminar Flow interface is linked to this node so that the calculated velocity field can be used to evaluate the convective mass transfer process.

- Inflow 1: This node specifies inlet mole fractions for each of the species entering the reaction channel.

- Outflow 1: This node specifies an outlet boundary condition for the mass transfer process in the reaction channel by assuming that there is no diffusive flux through the channel outlet such that only convective mass transfer occurs.

- Reaction Sources 1: This node modifies the application of the convection-diffusion equation in the porous catalyst phase for each species to include a consumption/generation term due to the chemical reaction facilitated by the presence of the catalyst. The consumption/generation term for each species is taken directly from the reaction rate calculated in the Chemistry interface, which is linked to this node. The reacting

volume is specified as the volume of the entire porous catalyst phase as opposed to the pore volume.

- Symmetry 1: This node specifies a no-flux boundary condition along the center line of the reaction channel such that there is no mass transfer through the center line of the reaction channel.

B.4 Heat Transfer in Fluids Interface

The physics nodes used in the Heat Transfer in Fluids interface varies for each microreactor model significantly based on if the reaction is controlled via boundary conditions (i.e. the adiabatic and prescribed wall temperature models) or integrated coolant channels. Regardless of which model type is used, the heat transfer process through the open channel and porous catalyst phases of the reaction channel must be evaluated. On the Settings tab of this interface, the thickness of the model geometry is set as $W = 80$ mm, the reference temperature is left at the default value of 293.15 K, and porous media domains are enabled to allow for the specification of properties within the porous catalyst phase. As part of the default settings for the Heat Transfer in Fluids interface, the general form of the energy conservation specified in equation 3.21 is automatically applied over the entire reaction domain, though the transport properties and generation term can change based on the application of other domain conditions.

In the Heat Transfer in Fluids interface applied for the adiabatic reactor model, the following physics nodes are specified:

- Fluid 1: This node defines the reaction flow's mixture properties in the open channel phase. The Chemistry interface and pressure field calculated using the Laminar Flow interface are linked to this node to define the fluid reacting flow mixture properties,

including the thermal conductivity and specific heat at constant pressure. The calculated velocity field from the Laminar Flow interface is similarly linked to this node so that it can be used to evaluate the convective heat transfer process.

- Initial Values: This node defines the initial guess for the temperature distribution across the model for the solver to begin iterating off of. While specifying accurate values in this node can help the solver converge more quickly, it is difficult to have reasonable guesses for the temperature profile before actually solving the system. As a result, the guess value is set as the inlet temperature for each simulation.

- Thermal Insulation 1: This node defines an insulation boundary condition along the reactor wall within the model such that there is not heat transfer through the wall. This boundary condition is automatically applied for each model considered, but can be overridden by applying other boundary conditions.

- Porous Medium 1: This node defines the reaction flow's mixture properties in the porous catalyst phase and modifies the energy conservation equation to use the effective thermal conductivity of the porous catalyst phase defined in equation 3.23. The porosity, thermal conductivity, specific heat, and density of the catalyst are all input and the volume averaged effective thermal conductivity model is selected. The Chemistry interface and pressure field calculated using the Laminar Flow interface are linked to this node to define the fluid reacting flow mixture properties, including the thermal conductivity and specific heat at constant pressure. The calculated velocity field from the Laminar Flow interface is similarly linked to this node so that it can be used to evaluate the convective heat transfer process.

- Temperature 1: This node specifies the inlet temperature of the reaction stream entering the reaction channel.

- Outflow 1: This node specifies an outlet boundary condition for the heat transfer process in the reaction channel by assuming that there is not conductive heat flux through the channel outlet such that only convective heat transfer occurs.

- Heat Source 1: This node modifies the application of the energy conservation equation in the porous catalyst phase to include a heat generation term due to the exothermic reaction facilitated by the presence of the catalyst. The material type is specified as non-solid and heat source is linked to the Chemistry interface to use the heat generation evaluated from the reaction rate and heat of reaction.

- Symmetry 1: This node specifies a no-flux boundary condition along the center line of the reaction channel such that there is no heat transfer through it.

In the prescribed wall temperature models, all of the physics nodes used for the adiabatic model are also applied, but an additional temperature node corresponding to the optimal temperature profile (Temperature 2) is applied over a portion of the reactor wall length, partially overriding the Thermal Insulation 1 node. The desired temperature boundary condition set in the Temperature 2 node is developed using an interpolation function and discrete data points obtained from the optimal temperature profile evaluated using the method described in Section 3.3.

The integrated coolant model applies all of the physics nodes used for the adiabatic model, but uses a modified geometry, requiring the additional physics nodes as well:

- Solid 1: This node specifies the solid material properties for the wall separating the reaction and coolant channels of the microreactor model and applies the general form of the heat equation listed in 3.24 to evaluate the heat transfer through the wall. The volume reference temperature is set as the reaction inlet temperature and pressure is set using the pressure field calculated from the Laminar Flow interface used for

the reaction channel flow. The wall material is set as Inconel 718 and its properties, including its thermal conductivity, specific heat, and density, are specified as functions of temperature from data in Engineering Equation Solver (EES) using interpolation functions.

- Fluid 2: This node defines the coolant flow's properties. The Laminar Flow interface used for the coolant flow is linked to this node to define the coolant pressure, which is used to evaluate the the thermal conductivity and specific heat at constant pressure of the coolant fluid. All coolant properties are taken from embedded air properties in COMSOL that are assigned to the coolant domain as a material property. The calculated velocity field from the coolant Laminar Flow interface is similarly linked to this node so that it can be used to evaluate the convective heat transfer process.

- Temperature 2: While the Temperature 2 node in the prescribed wall temperature model is used to define the optimal temperature progression boundary condition along the reactor wall, it defines the coolant inlet temperature in this model.

- Outflow 2: This node specifies an outlet boundary condition for the heat transfer process in the coolant channel, similar to the Outflow 1 node for the reaction channel.

- Symmetry 2: This node specifies a second symmetry condition along the center line of the coolant channel such that there is no heat transfer through it.

B.5 Mesh Description and Mesh Refinement Study

Given the nature of the model geometry specified, it is known that there will be relatively little variation for many of the variables in the direction transverse to the flow. As a result, a mesh consisting of rectangular elements, as shown in Figure B.1, is used in the

implemented COMSOL model to reduce computation time. The mesh was made using a Mapped mesh node, which allows the user to specify a desired number of elements on a boundary to manually generate a grid of elements. This is done separately for the height of each of the coolant, reactor wall, catalyst, and reacting flow domains and along the entire model length. For the fluid flow domains, symmetric distributions with arithmetic growth sequences were specified to make the mesh density higher near the model boundaries to account for the more rapid changes in velocity that occur in these locations. A higher mesh density was specified for the catalyst layer to account for the more rapid change in variables that occurs due to the reaction taking place.

To verify that the solutions generated using the COMSOL model are sufficiently independent of the mesh used to solve the model and to avoid using computationally expensive models which take a long time to run, a mesh refinement study was performed and used to incrementally evaluate a mesh where the change in the outlet CO mole fraction (y_{CO}) from the model changed by less than %0.1 with continued refinement. This was done by specifying a mesh parameter as a Global Definition which was used to set the number of nodes along the height and length of each domain and then using a Parametric Sweep to incrementally increase this parameter to increase the mesh density of the entire model. The average outlet CO mole fractions from the solutions generated at each mesh density were then compared to each other to evaluate the point at which it changed by less than %0.1 and then this mesh was set as the standard model mesh for the majority of simulations. The presented COMSOL solutions in this study are the solutions evaluated using this mesh. Details regarding the number of elements used in this mesh are presented in Table B.1.

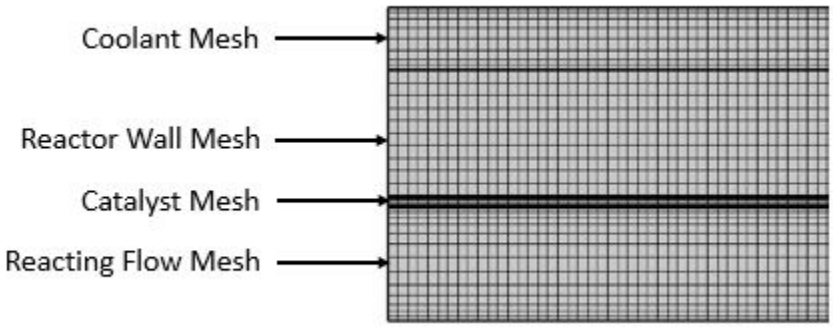

Figure B.1: Closeup of mesh used in COMSOL model

Table B.1: Implemented mesh in COMSOL model

Model Boundary	**Number of Elements**
Reacting Flow Height	15
Catalyst Layer Height	15
Reactor Wall Height	10
Coolant Flow Height	10
Reactor Length	5000

B.6 Solver Type

To solve the system of conservation and and property equations applied to the model using the physics interfaces described in Sections B.1 through B.4, I used the default stationary solver selected by COMSOL. Because the 2-D model geometry requires a relatively small mesh to solve the problem, COMSOL defaults to the fully-coupled PARDISO direct solver which attempts to solve all of the compiled equations for each node for each iteration simultaneously. Compared to iterative solvers, this can require a significant amount of

RAM as each variable being solved for must be stored in memory during the solution process. This was generally not an issue as the 2-D model had a reasonably small number of mesh elements and the computer used to run the simulations had 120 GB of RAM available. I selected a relative tolerance of 1×10^{-5} as the convergence criteria to stop the solver to as opposed to the default value of 1×10^{-3} to ensure sufficient solution accuracy.

In addition to the default solver described above, I frequently used the Auxiliary Solver in the Study Extensions section of the solver settings to perform parametric sweeps of non-geometric parameters such as flow rates and inlet temperatures and as a method of more efficiently supplying initial guesses to models that had convergence issues. The Auxiliary Solver is quite robust and is capable of using previously found solutions in the sweep as initial guesses for later solutions. This was very useful as studies operating at lower reactor inlet temperatures frequently converged without any issues, but convergence issues were often observed for models operating at higher inlet temperatures when solved without the Auxiliary Solver. I also frequently added Parametric Sweeps to the conducted studies, which can be used to perform parametric studies of geometric parameters which require remeshing the model geometry between each iteration.